UNIVERSITY OF
BIRMINGHAM

Laser-based manufacturing routes for functionalizing surfaces

by

Jean-Michel Romano

May 2019

A thesis submitted to
the University of Birmingham
for the degree of Doctor of Philosophy

Department of Mechanical Engineering
School of Engineering
College of Engineering and Physical Sciences
University of Birmingham

Abstract

Robust functional surfaces are of a growing industrial interest for a range of optical, easy-to-clean, anti-icing and non-fouling applications. At the same time, nature is a great source of inspiration for micro/nano-scale surface structures with tailored functional properties. There are a number of competing technologies for producing such structures but ultrashort laser processing is emerging as one of the most promising for fabricating bio-inspired surfaces. However, the technology has limitations and its capabilities have to be augmented to achieve the required high-throughput in manufacturing products that incorporate functional surface topographies. Therefore, this research investigates a promising process chain that combines synergistically the capabilities of laser texturing with complementary surface engineering and replication technologies. Several large-area laser texturing techniques are investigated, namely Direct Laser Writing (DLW), Laser-Induced Periodic Surface Structures (LIPSS) and microlenses-induced Photonic Jet (PJ) texturing. The research advances the knowledge in laser-based surface functionalization and also in factors affecting the functional response and durability of laser structured surfaces.

Acknowledgments

What a journey it has been! During my three years as PhD student, I have met incredible persons who contributed directly or indirectly to my research. Now is the time to acknowledge them appropriately.

Primarily, I am grateful to Prof. Stefan Dimov for accepting me in his research group. I valued his guidance and the freedom that he gave me in orientating my research. I would like to acknowledge my colleagues from the School of Engineering and the Laser group. My gratitude goes to my teammate Antonio García Girón for the years spent together in the lab and outside working hours, where he had to listen to my French humor and my musical taste.

I am thankful to Prof. Hanshan Dong for the valuable discussions and the fruitful collaborative work with the School of Metallurgy and Materials; I also take the opportunity to thank Behnam Dashtbozorg and Shaojun Qi for your constant support. I would like to thank Rachel Sammons from the School of Dentistry for the valuable discussions and for training me in microbiological characterization. I acknowledge as well Shangfeng Du and Ahmad El-Kharouf for the access to equipment in the School of Chemical Engineering. I thank Olivier Delléa from the CEA-Liten for the deposition of microspheres and my colleague Rajib Ahmed for his skills in simulations and his advices in paper editing. I thank Ralf Helbig from the Leibniz Institute for Polymer Research for his valuable expertise in bio-inspired surfaces and the non-fouling characterizations performed in this work.

I am grateful to Prof. Ben Whiteside from the Centre for Polymer Micro and Nano Technology for welcoming me in Bradford where I carried out a research exchange on micro injection

molding, with the precious support of Mert Gülçür. I am also grateful to Virginia Gotor, Andrés Escartín and Francisco Javier Ester for granting Antonio and me with the access to the research facilities at BSH Electrodomésticos in Zaragoza. I would like to thank the researchers in BSH and especially Jorge Fantova Sarasa who contributed to the manufacturing of injection molded parts. I also had the pleasure to meet Prof. José Ignacio Peña and had the opportunity to use his lab at the Universidad de Zaragoza, during my research exchange in Spain. Finally, I thank Elmar Bonaccurso and Vittorio Vercillo for your welcoming in Airbus in Munich and the fruitful collaboration.

I would like to acknowledge the European Commission and the Marie Skłodowska-Curie Actions for the financial support to my research. In these tumultuous times, I truly believe that withdrawal is not a solution but that we have to foster intercultural and multidisciplinary interactions. I learned and met great persons within our research consortium on laser texturing and surface functionalization and my research would not have been possible without them. My thoughts are with the other PhD students of the Laser4Fun project: Melissa Sikosana, Antonio García Girón, José Cardoso, Daniel Huerta, Vittorio Vercillo, Gagandeep Singh Joshi, Fotis Fraggelakis, Luigi Capuano, Marek Mezera Sabri Alamri, Alfredo Aguilar Morales, Tobias Stark. There should be no misunderstanding, on top of our hard work and accomplishments, there was indeed a lot of fun, especially during our adventures in Bordeaux, Berlin, Dresden, Zaragoza and Amsterdam. I'll never forget the trip to Bari, for many reasons including the amazing live concert of Prof. Gert-willem Römer and Prof. Andrés Lasagni.

I have to thank several persons that I met during my graduate studies at the Technical University Dresden and the Karlsruhe Institute of Technology and who eventually led me to pursue this PhD experience: Prof. Andrés Lasagni, Stephan Hunze, Mateusz Chlipala and Mathias Heckele.

Moreover, I warmly thank Prof. Philippe Tanguy for inspiring me during our years spent at Total.

Last but not least, this journey would not have been possible without the support of my family and friends. To my parents, thank you for encouraging me to follow my dreams. *Merci Maman pour ton attention et ta bienveillance. Merci Papa pour me pousser toujours de l'avant et me rappeler de* "*faire attention*". *J'ai des pensées affectueuses pour mes frères et sœurs, Marie, Cynthia et Julien, ainsi que ma petite nièce Séraphine.* I am thinking especially at my friends who were there for me for important moments of my life, I know you will recognize yourselves in this few lines. I cannot cite everyone as I don't want to double the printing costs, but Anne, Pierre-Georges, Guillaume, Léonard and Yann, you are part of them. Thank you, Nashira and Ana Maria for having been such wonderful flatmates, I loved our trips and that we were there for each other. Thanks to Pauline, Sylvain and Jean-Luc for our evenings at the Flapper, the Bacchus, the Prince of Wales and the Shakespeare; and to Aymeric, Vincent and Benoit for being great climbing partners. To my *parceros*, Ana Maria, Ana, Lorea, Roberto and Antonio: long live the "Consultancy". You are amazing.

Table of Contents

Page

List of Tables

Page

List of Figures

Page

Chapter 1

Chapter 2

Chapter 3

Chapter 4

Chapter 5

Chapter 6

Chapter 7

Nomenclature

Chapter 1 & 2

LIPSS	Laser-Induced Periodic Surface Structures
PJ	Photonic Jet
SLIPS	Slippery Liquid-Infused Porous Surfaces
LASER	Light Amplification by Stimulated Emission of Radiation
τ	Pulse length
FWHM	Full Width at Half-Maximum
ω_0	Laser spot size radius
Z_R	Rayleigh length
λ	Laser wavelength
M^2	Beam quality factor
f	Focal length of a lens
d	Beam diameter prior to a lens
Θ	Beam divergence
DLW	Direct Laser Writing
E_p	Pulse energy
P	Average optical power
f	Pulse repetition rate
P_{peak}	Peak power
φ	Fluence
φ_0	Fluence per pulse
r	Radial distance from the propagation axis
DLIP	Direct Laser Interference Patterning

<u>Specific to: DLW</u>

N	Number of pulses
D	Ablated crater diameter
S	Incubation coefficient
L	Ablated crater depth
α^{-1}	Optical penetration depth or optical length
Φ_{th}	Fluence threshold for strong ablation regime
γ	Electron heat diffusion length

<u>Specific to: LIPSS</u>

FLIPSS	Femtosecond LIPSS
SSP	Surface Plasma Polaritons

LSFL	Low Spatial Frequency LIPSS
HSFL	High Spatial Frequency LIPSS

Specific to: PJ

DLC	Dry Laser Cleaning
2r	Microsphere's diameter
D	Focal distance

Specific to: Wetting properties

θ_Y	Young's contact angle
γ_{LV}	Interfacial tensions liquid-vapor
γ_{SV}	Interfacial tensions solid-vapor
γ_{SL}	Interfacial tensions solid-liquid
θ_W	Wenzel's contact angle
r_W	Wenzel roughness or factor
CB	Cassie-Baxter
θ_{CB}	Cassie-Baxter's contact angle
φ_{CB}	Fraction of the solid in contact with the liquid
V	Liquid drop volume
r	Radius of liquid drop
θ_H	Contact angle hysteresis
α	Tilting angle
θ_{max}	Maximum contact angle in the "tilted plate" method
θ_{min}	Minimum contact angle in the "tilted plate" method
θ_{adv}	Advancing contact angle
θ_{rec}	Receding contact angle
σ	Surface energy
σ^D, σ^D_S, σ^D_L	Dispersive component of surface energy, globally or of solid or of liquid
σ^P, σ^P_S, σ^P_L	Polar component of the surface energy, globally or of solid or of liquid

Chapter 3

LIPSS	Laser-Induced Periodic Surface Structures
LSFL	Low Spatial Frequency LIPSS
FFT	Fast Fourier Transform
λ	Central wavelength
ω_0	Laser spot radius at $1/e^2$
d	Pulse-to-pulse distance
h	Hatch distance
N	Effective number of pulses

φ_0	Fluence per pulse
φ	Accumulated fluence
f	Pulse repetition rate
P	Average power
E	Pulse energy
v	Scanning speed
θ	Static contact angle
θ_{eq}	Static contact angle, after ageing
β	Time constant

Chapter 4

LIPSS	Laser-Induced Periodic Surface Structures
LSFL	Low Spatial Frequency LIPSS
2D-FFT	Two-dimensional Fast Fourier Transform
Ra	Average roughness
λ	Central wavelength
$\omega 0$	Laser spot radius at $1/e^2$
ZR	Rayleigh length
M2	Beam quality factor
h	Hatch distance
v	Scanning velocity
f	Pulse repetition rate
d	Pulse-to-pulse distance
N	Effective number of pulses
O	Pulse overlap
P	Average power
$\phi 0$	Fluence per pulse
ϕ	Accumulated fluence
CA	Static contact angle
Λ	LIPSS periodicity
α	LIPSS orientation
Δz	Out of focus distance

Chapter 5

PN	Photonic Nanojet
LIPSS	Laser-Induced Periodic Surface Structures
E. coli	Escherichia coli
HCP	Hexagonal Close-Packed
CPLA	Contacting Particle-Lens Array

λ	Central wavelength
n	Refractive index
r	Sphere radius
DLC	Dry Laser Cleaning
FE	Finite Elements
FWHM	Full Width at Half Maximum
ω_0	Laser spot radius at $1/e^2$
$\omega(z)$	Laser spot radius at focal offset
Z_R	Rayleigh length
δ	Pulse-to-pulse distance
σ	Hatching distance
CA	Static contact angle
PFPE	Perfluoropolyether
LB	Lysogeny broth
UV	Ultra Violet
OD	Optical Density
PFA	Paraformaldehyde
x	Microsphere-to-wavelength ratio
w_g	Focal spot size (geometrical regime)
w_d	Focal spot size (dipole regime)
C	Constant of transition between the geometrical/dipole regimes
w	PN's focal spot size
k	Electromagnetic wave number
D	PN's paraxial focal length
L	PN's length
I_{max}	PN's peak intensity
NI	Near-Infrared
Λ	Grating's spacing
φ	Observation angle
θ	Incident angle

Chapter 6

L	Liquid
S	Surface
σ_S	Overall surface energy of solid surface
σ_L	Overall surface tension of liquid
σ_{SL}	Interfacial tension between solid and liquid
θ_Y	Young's contact angle
θ_W	Wenzel's contact angle
r_W	Wenzel's roughness ratio

CB	Cassie-Baxter
θ_{CB}	Cassie-Baxter's contact angle
φ_{CB}	Cassie-Baxter's filling ratio
PJ	Photonic Jet
LIPSS	Laser-Induced Periodic Surface Structures
PP	Polypropylene
FFT	Fast Fourier Transform
θ	Static contact angle
θ_{adv}	Advancing contact angle
θ_{rec}	Receding contact angle
θ_H	Contact angle hysteresis
σ	Overall surface energy
σ^D	Dispersive contribution to the surface energy
σ^P	Polar contribution to the surface energy
R, φ	Polar coordinates
W_{SL}	Work of adhesion
ΔG_{SL}	Free energy of adhesion
Sa	Arithmetical mean height (Areal roughness parameter)
Sz	Maximal height (Areal roughness parameter)
F	ratio between measured and projected topographies, also called true-to-nominal area ratio
…*	… in Wenzel state
r_{Weq}	Equivalent Wenzel's roughness ratio
Sq	Root mean square height (Areal roughness parameter)
Sk	Core roughness depth (Areal roughness parameter)
Sdr	Developed interfacial area ratio (Areal roughness parameter)
Sku	Kurtosis (Areal roughness parameter)
Ssk	Skewness (Areal roughness parameter)

Chapter 7

LIPSS	Laser-Induced Periodic Surface Structures
S phase	Expanded austenitic surface layer due to e.g. carburising or nitriding
DC	Direct Current
S…	Stainless Steel plates
C…	Low-temperatures plasma carburised stainless steel plates
PP	Polypropylene
Sa	Arithmetical mean height (Areal roughness parameter)
Δz	Maximum peak-to-valley height
FFT	Fast Fourier Transform
HV	Hardness in Vickers

gf	Gram-force

Chapter 8

LIPSS	Laser-Induced Periodic Surface Structures
PJ	Photonic Jet
DLW	Direct Laser Writing
E. coli	Escherichia coli

List of Publications and Presentations

Parts of the work described in this thesis have been published in papers, listed below in reverse chronological order.

Journal papers submitted/accepted for publication directly from this doctoral research

1. **Romano J.-M.**, Fantova-Sarasa J., Concheso C., Gulcur M., Dashtbozorg B., Garcia-Giron A., Penchev P., Dong H., Whiteside B.R., Dimov S.S. (----) Effects of tool wear on hydrophobic polymer surfaces replicated using plasma treated and laser-textured stainless steel inserts, *Tribology – Materials, Surfaces & Interfaces* (*Submitted on 23/04/2019, Manuscript Number TRB685*).
2. **Romano J.-M.**, Helbig R., Fraggelakis F., Garcia-Giron A., Werner C., Kling R., Dimov S.S. (2019) Springtail-inspired triangular laser-induced surface textures on metals using MHz ultrashort pulses, *Journal of Micro and Nano Manufacturing, 7(2), 024504*, doi:10.1115/1.4043417.
3. **Romano J.-M.**, Ahmed R., Garcia-Giron A., Penchev P., Butt H., Delléa O., Sikosana M., Helbig R., Werner C., Dimov S.S. (2019) Subwavelength Direct Laser Nanopatterning via Microparticle Arrays for Functionalizing Metallic Surfaces, *Journal of Micro and Nano Manufacturing, 7(1), 010901*, doi:10.1115/1.4042964.
4. **Romano J.-M.**, Gulcur M., Garcia-Giron A., Martinez-Solanas E., Whiteside B.R., Dimov S.S. (2019) Mechanical durability of hydrophobic surfaces fabricated by injection moulding of laser-induced textures, *Applied Surface Science, 476, 850-860*, doi:10.1016/j.apsusc.2019.01.162.
5. **Romano J.-M.**, Garcia-Giron A., Penchev P., Dimov S.S. (2018) Triangular laser-induced submicron textures for functionalising stainless steel surfaces, *Applied Surface Science, 440, 162–169*, doi:10.1016/j.apsusc.2018.01.086.

Proceeding papers submitted/accepted for publication directly from this doctoral research

1. **Romano J.-M.**, Garcia-Giron A., Penchev P., Gulcur M., Whiteside B.R., Dimov S.S. (2019) Lotus-leaf inspired surfaces: hydrophobicity evolution of replicas due to mechanical cleaning and tool wear, *Proceedings of 3rd World Congress on Micro and Nano Manufacturing (WCMNM) - Tribology session, 289-292*.
2. **Romano J.-M.**, Ahmed R., Garcia-Giron A., Penchev P., Delléa O., Dimov S.S. (2018) Towards large area submicron surface texturing by femtosecond laser irradiation of microparticle arrays, *Proceedings of 2nd World Congress on Micro and Nano Manufacturing (WCMNM) - Himalaia H2020 project session, 309-312*, doi:10.3850/978-981-11-2728-1_10.

3. **Romano J.-M.**, Garcia-Giron A., Penchev P., Dimov S.S. (2018) Triangular self-organized surface textures produced by femtosecond laser irradiation on stainless steel and titanium alloy, *Proceedings of 2nd World Congress on Micro and Nano Manufacturing (WCMNM) - Laser Processing I, 103-106*, doi:10.3850/978-981-11-2728-1_09.

Awards as a result of this research

Honorable mention paper award, for "Towards large area submicron surface texturing by femtosecond laser irradiation of microparticle arrays" by **Romano J.-M.**, Ahmed R., Garcia-Giron A., Penchev P., Delléa O., Dimov S.S., at *2nd World Congress on Micro and Nano Manufacturing (WCMNM), September 2018, Portoroz, Slovenia*.

Conference presentations arising from this doctoral research

1. **Romano J.-M.**, Garcia-Giron A., Penchev P., Gulcur M., Whiteside B.R., Dimov S.S. (2019) Lotus-leaf inspired surfaces: hydrophobicity evolution of replicas due to mechanical cleaning and tool wear, *3rd World Congress on Micro and Nano Manufacturing (WCMNM), September 2019, Raleigh, NC, USA.*
2. **Romano J.-M.**, Garcia-Giron A., Penchev P., Gulcur M., Whiteside B.R., Dimov S.S. (2019) Lotus-leaf inspired surfaces: hydrophobicity evolution of replicas due to mechanical cleaning and tool wear, *Polymer Process Engineering (PPE), Polymer Interdisciplinary Research Centre, July 2019, Bradford, United Kingdom.*
3. **Romano J.-M.**, Garcia-Giron A., Penchev P., Dimov S.S. (2018) Mechanical abrasion of superhydrophobic polymeric surfaces fabricated by laser texturing and injection moulding, *3rd Laser4Fun Summer School on Laser Micro/Nanostructuring and Surface Tribology, University of Bari, October 2018, Bari, Italy*.
4. **Romano J.-M.**, Ahmed R., Garcia-Giron A., Penchev P., Delléa O., Dimov S.S. (2018) Towards large area submicron surface texturing by femtosecond laser irradiation of microparticle arrays, *2nd World Congress on Micro and Nano Manufacturing (WCMNM) - HIMALAIA H2020 project session, September 2018, Portoroz, Slovenia*.
5. **Romano J.-M.**, Garcia-Giron A., Penchev P., Dimov S.S. (2018) Triangular self-organized surface textures produced by fs laser irradiation on stainless steel and titanium alloy, *2nd World Congress on Micro and Nano Manufacturing (WCMNM) - Laser Processing I, September 2018, Portoroz, Slovenia*.
6. **Romano J.-M.**, Ahmed R., Garcia-Giron A., Penchev P., Delléa O., Butt H., Dimov S.S. (2018) Subwavelength laser texturing using microsphere-assisted photonic jet array, *19th Laser Precision Microfabrication (LPM) – Laser surface micro/nano structuring, June 2018, Edinburgh, United Kingdom*.
7. **Romano J.-M.**, Dong H., Dimov S.S. (2018) Laser-textured masters for high-throughput replication of functional surfaces, *Manufacturing Research Group seminar, University of Birmingham, January 2018, Birmingham, United Kingdom*.

8. **Romano J.-M.**, Garcia-Giron A., Dimov S.S. (2017) Laser-based process chain for mass-scale surface functionalisation of polymer parts, *Poster session at workshop of EU H2020 project Laser4Fun, November 2017, Zaragoza, Spain*.
9. **Romano J.-M.**, Dong H., Dimov S.S. (2017) [1)] Laser-based process chain for mass-scale texturing of polymer parts, [2)] Laser structuring below the micron: triangular LIPSS and photonic nanojets, *2nd Laser4Fun Summer School on Advanced Laser Processing, University of Twente, August 2017, Enschede, The Netherlands*.
10. **Romano J.-M.**, Dong H., Dimov S.S. (2017) Large-area triangular-shaped fs-LIPSS on stainless steel, *39th Conference on Advanced Manufacturing (MATADOR) – Laser Micro/Nano Manufacturing 4, July 2017, Manchester, United Kingdom*.
11. **Romano J.-M.**, Dong H., Dimov S.S. (2017) Laser-textured masters for high throughput replication of hydrophobic surfaces, *5th Industrial Laser Applications Symposium (ILAS) – Ultra-Short Pulse, March 2017, Grantham United Kingdom*.
12. **Romano J.-M.**, Dong H., Dimov S.S. (2016) Fabrication of laser-textured masters/moulds for mass replication on polymers with antibacterial properties, *Manufacturing Research Group seminar, University of Birmingham, October 2016, Birmingham, United Kingdom*.
13. **Romano J.-M.**, Penchev P., Dimov S.S. (2016) Laser processing of bulk metallic glasses, *1st Laser4Fun Summer School on Short Pulsed Laser Micro/Nanostructuring of Surfaces & 5th International Summer School on Trends and new developments in Laser Technology, Fraunhofer IWS, August 2016, Dresden, Germany*.
14. **Romano J.-M.**, Penchev P., Dimov S.S. (2016) Bulk metallic glasses: enabling technology for micro manufacturing, *International Conference on Industrial Laser Processing (JNPLI) – Micro-Machining, June 2016, Liege, Belgium*.

Related publications during this doctoral research

1. Vercillo V., Tonnicchia S., **Romano J.-M.**, Garcia-Giron A., Aguilar-Morales A., Alamri S., Dimov S.S., Lasagni A.F., Bonaccurso E. (----) Design Rules for Laser Patterned Icephobic Metallic Surfaces for Aeronautic Applications *(in preparation)*.
2. Dashtbozorg B., **Romano J.-M.**, Garcia-Giron A., Li X.Y., Sammons R.L., Dimov S.S., Dong H. (----) Low Temperature Plasma Nitriding and Pulsed Laser Patterning for Durable Textured Surfaces *(in preparation).*
3. Dashtbozorg B., Li X.Y., **Romano J.-M.**, Garcia-Giron A., Sammons R.L., Dimov S.S., Dong H. (----) Response of Metastable S Phase Layer formed on AISI 316L to Ultrashort Pulsed Laser Texturing, *Applied Surface Science (Submitted on 09/08/2019).*
4. Garcia-Giron A., **Romano J.-M.**, Batal A., Michałek A., Penchev P., Dimov S.S. (2020) Experimental investigation of processing disturbances in laser surface patterning, *Optics and Lasers in Engineering, 126, 105900*, doi: 10.1016/j.optlaseng.2019.105900.

5. Baruffi F., Gulcur M., Calaon M., **Romano J.-M.**, Penchev P., Dimov S.S., Whiteside B.R., Tosello G. (2019) Correlating nano-scale surface replication accuracy and cavity temperature in micro-injection moulding using in-line process control and high-speed thermal imaging, *Journal of Manufacturing Processes, 47, 367-381*, doi: 10.1016/j.jmapro.2019.08.017.

6. Garcia-Giron A., **Romano J.-M.**, Batal A., Dashtbozorg B., Dong H., Martinez-Solanas E., Urrutia Angos D., Walker M., Penchev P., Dimov S.S. (2019) Durability and wear resistance of laser-textured hardened stainless steel surfaces with hydrophobic properties, *Langmuir, 35(15), 5353-5363*, doi: 10.1021/acs.langmuir.9b00398.

7. Huerta-Murillo D., García-Girón A., **Romano J.-M.**, Cardoso J.T., Cordovilla F., Walker M., Dimov S.S., Ocaña J.L. (2019) Wettability modification of laser-fabricated hierarchical surface structures in Ti-6Al-4V titanium alloy, *Applied Surface Science, 463, 838-846*, doi:10.1016/j.apsusc.2018.09.012.

8. Garcia-Giron A., **Romano J.-M.**, Liang Y., Dashtbozorg B., Dong H., Penchev P., Dimov S.S. (2018) Combined surface hardening and laser patterning approach for functionalising stainless steel surfaces, *Applied Surface Science, 439, 516-524*, doi:10.1016/j.apsusc.2018.01.012.

9. Garcia-Giron A., **Romano J.-M.**, Liang Y., Dashtbozorg B., Dong H., Penchev P., Dimov S.S. (2018) Combined Surface Hardening and Laser Patterning for Producing Wear Resistant Hydrophobic Surfaces, *Proceedings of 2nd World Congress on Micro and Nano Manufacturing (WCMNM) - Surface Functionalization, 75-78*, doi:10.3850/978-981-11-2728-1_16.

10. Joshi G.S., Dashtbozorg B., **Romano J.-M.**, Garcia-Giron A., Gaudiuso C., Dong H., Dimov S.S., Ancona A., Carbone G. (2018) Experimental investigation of the tribological and wettability properties of laser-textured martensitic steel surfaces, *Proceedings of the 19th International Symposium on Laser Precision Microfabrication (LPM), JLMN-18-049, 1-5*.

11. Cardoso J.T., Garcia-Girón A., **Romano J.-M.**, Huerta-Murillo D., Jagdheesh R., Walker M., Dimov S.S., Ocaña J.L. (2017) Influence of ambient conditions on the evolution of wettability properties of IR-, ns- laser textured aluminum alloy, *RSC Advances, 7, 39617*, doi:10.1039/C7RA07421B.

Chapter 1

General introduction

1.1 Motivation

Nature is a rich source of inspiration, where a broad variety of surfaces exhibits very interesting functional properties. For that reason, researchers are fascinated by the field of biomimicry and the replication of biological systems. Indeed, innovative solutions could be transferred to industrial applications such as in tribology, optic, implant or packaging (Ivanović et al., 2018; Mann et al., 2014, 2016).

Wetting, in particular, is a surface property defining its interaction with fluids. A tailored wetting is critical to many fields, e.g. surface engineering, coatings or frictional/lubricated contacts (Asthana and Sobczak, 2000; Bhushan and Jung, 2008; Kalin and Polajnar, 2013). Surfaces can exhibit different wetting properties, such as liquid attraction (high wetting, also called hydrophilicity in the case of water as liquid phase) or, on the contrary, liquid repulsion (low wetting or hydrophobicity). In some extreme cases, superhydrophobic behaviour can be observed when water beads up and rolls off, without wetting the surface. Perhaps some of the most remarkable superhydrophobic examples found in nature are the plant leaves. In particular, the "Lotus effect" describes the outstanding self-cleaning properties of the leaves of *Nelumbo nucifera*, also known as the sacred Lotus (Barthlott and Neinhuis, 1997). Water hardly wets the Lotus leaf, forming water drops, collecting and evacuating dirt particles while they roll off the surface, leaving immaculate leaves. Such wetting behaviour is partially due to a complex compound of micro- and nano- scale surface structures (see Fig. 1) associated with tailored surface chemistry (Neinhuis and Barthlott, 1997; Bhushan et al., 2009).

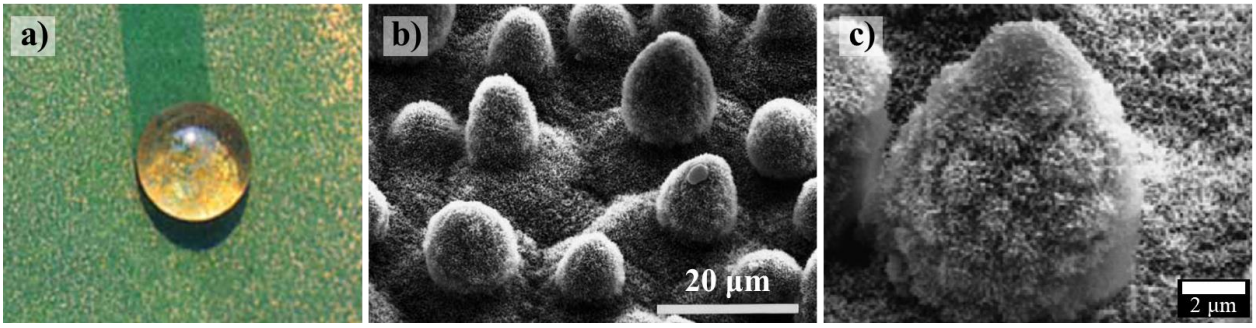

Figure 1. Example of superhydrophobic surface textures found in nature: a) cleaning of loam dust by a water drop on a Lotus leaf (Barthlott and Neinbuis, 1998), copyright (1998), reproduced with permission from WILEY-VCH Verlag GmbH. Details of a *Nelumbo nucifera* (Lotus) leaf surface structures at the b) micro- and c) nanoscale. b) Reprinted by permission from Springer Nature: (Barthlott and Neinhuis, 1997), copyright (1997). c) Republished with permission of The Royal Society of Chemistry, from (Koch et al., 2009), copyright (2009).

Therefore, the fabrication of hierarchical surface structures with controlled micro and nano scale topographies is attracting a growing interest (Feng et al., 2002; Patankar, 2004; Koch et al., 2009; Liu et al., 2010). Such complex topographies can be produced employing different micro/nano texturing approaches or combination of them. In general, they can be divided into wet processes, e.g. etching, anodization, coating (Daglar et al., 2014; Kim et al., 2015; Lee et al., 2007; Nakashima et al., 2011); and selective micro/nano-scale processes, such as lithography, conventional or electro-discharged micromachining and imprinting (Falah Toosi et al., 2016; Sivasubramaniam and Alkaisi, 2014; Vilhena et al., 2017; Wang et al., 2018). Laser ablation i.e. Direct Laser Writing (DLW) is another selective micro-scale structuring/patterning technique that can be deployed for surface texturing of various materials, from metals (Nolte et al., 1997), glass (Rosenfeld et al., 1999), ceramics (Sola et al., 2011) to plastics (Sohn et al., 2008). Another complementary laser-enabled approach is the generation of so called Laser-Induced Periodic Surface Structures (LIPSS) that allows micro-to-nano-scales surface features with random or periodic arrangements to be fabricated (see Fig. 2) (Fraggelakis et al., 2019, 2017; Mezera et al., 2018; Wu et al., 2009). LIPSS are usually wavy or quasi linear ripples and the fabrication of

highly regular LIPSS over relatively large area has been reported (Gnilitskyi et al., 2017; Skoulas et al., 2017). Nevertheless, the large-area fabrication of uniform submicron surface structures was shown to be beneficial for many applications such as anti-icing, anti-counterfeiting, tribological and microbiological (Bonse et al., 2018; Caffrey et al., 2012; Cunha et al., 2016; Kietzig et al., 2011b; Vorobyev and Guo, 2015).

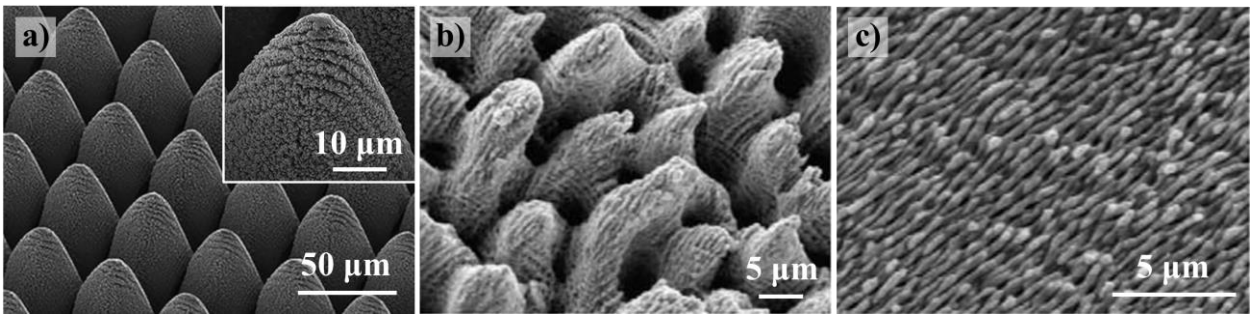

Figure 2. Example of ultrashort laser texturing: a) Lotus-leaf inspired topography on cupper-based substrate (Han et al., 2018), CC BY 3.0, published by The Royal Society of Chemistry; b) Multi-scale and c) ripple-like laser-induced surface structures on stainless steel, reprinted from (Wu et al., 2009), copyright (2009), with permission from Elsevier.

To enable the high throughput production of such laser-fabricated surface structures, several direct and indirect methods can be deployed. Especially, the direct laser texturing methods usually involve the use of laser sources with specific technical characteristics, e.g. increased pulse repetition rates, pulse energies and beam deflection dynamics (Fraggelakis et al., 2017; Mincuzzi et al., 2016). While, indirect surface texturing methods are mostly based on the use of replication masters, e.g. roll-to-roll (Ng et al., 2016) or injection moulding processes (Pina-Estany et al., 2018; Stormonth-Darling et al., 2014; Yoo et al., 2009). The cost-effectiveness of replication methods is directly related to the number of replicas produced during the life span of the master. To extend the lifetime or to facilitate the separation of parts from the masters, different approaches have been considered, in particular, further surface treatments such as hardening, alloying or coating (Aizawa, 2013; Crema and Lucchetta, 2014).

Any wear or surface damage would be detrimental to the specially produced topographies and therefore to their respective functional responses. While functional surfaces in nature can exhibit self-healing properties (Murphy and Wudl, 2010; Wong et al., 2011), this is still to be developed for most engineered surfaces and the wear resistance of functional surfaces remains an active research field (Han et al., 2018; Roessler and Lasagni, 2018; Wang et al., 2017; Gong et al., 2016; Tang et al., 2015). A more in-depth understanding of interdependencies between surface structures and their functional responses will underpin the design of improved surface structures and also can attenuate the deterioration of their expected surface functionalities during the product's lifetimes.

1.2 Research aims and objectives

The overall aim of this research is to investigate the functional response of laser-fabricated surfaces structures. Inspired by functional surfaces observed in nature, the wetting properties of laser-based textured polymeric surfaces with dimensions in the submicron and micron scale are studied. To that aim, a process chain combining surface engineering, laser texturing and injection moulding is investigated. In particular, the research is focused on large-area laser texturing of regular submicron surface structures. Indeed, such textures, i.e. much smaller than the laser spot size, could find many applications, e.g. to achieve anti-bacterial / non-fouling, optical and wetting properties. Although such process chain could be economically viable for enabling the mass production of functional polymeric surfaces, it is necessary for the replication masters to withstand several hundred thousand to million injection cycles. Therefore, the durability of laser textured replication master deserves to be investigated. Finally, the effects of wear and other damages of textured polymer replicas occurring during their use on their functional surfaces

should be considered, too. In order to fulfil these aims, the main research objectives are as follows:

i) *To develop laser-based surface texturing technologies for creating bio-inspired micro/nano scale topographies on masters for polymer replication.* A range of laser-based topographies, such as submicron surface structures mimicking Springtail cuticles or hierarchical micro/submicro-scale topographies inspired by Lotus leaves, will be manufactured. Especially, this will include:

a. High-throughput fabrication of hexagonal-arranged submicron surface features by two direct laser texturing processes;

b. A single-pass process using a circularly polarized beam to demonstrate the fabrication of triangular LIPSS;

c. Fabrication of arrays of submicron holes employing microlens-induced Photonic Jet (PJ);

d. Fabrication of hierarchical micro/submicro-scale topographies using DLW;

e. Demonstrating regularity and homogeneity of such topographies over relatively large areas on stainless steel substrates;

f. Replication of various surface structures on polypropylene parts employing injection moulding systems.

ii) *To investigate the functional properties of laser-textured surfaces.* The surface functionalities of laser-textured steels and polypropylene replica will be characterised, especially in term of their wetting properties. Some optical and non-fouling characteristics will also be highlighted, too.

iii) *To evaluate the durability of superhydrophobic behaviour of laser textured surfaces.* The effects of wear and other surface damages on superhydrophobic properties of textured

polypropylene parts will be investigated. Firstly, the evolution of their functional response will be assessed by conducting mechanical cleaning cycles based on standardized routines for testing durability of coatings. Secondly, the tool wear and surface damage occurring during injection moulding cycles will be analysed to determine their detrimental effects on the superhydrophobic properties of textured replicas. The use of plasma carburised masters for enhanced wear resistance will be investigated, too.

1.3 Thesis organization

The thesis is composed of eight chapters. Following the General introduction (**Chapter 1**), **Chapter 2** provides an overview of state-of-the-art techniques for laser texturing, with background information on wetting theories and a review of interesting functional surfaces found in the nature.

Chapter 3 describes the similarities between the hexagonal arrangement of submicron features fabricated by near-infrared LIPSS processing and springtail (Collembola) cuticles. Substrates made of stainless steel and titanium alloy are laser-processed. The processing efficiency of stainless steel substrate is investigated by employing ultrashort laser with higher repetition rates, in the MHz range.

Chapter 4 presents the further optimisation of LIPSS processing on stainless steel surfaces to achieve hexagonal arrangement of submicron features with superhydrophobic and light scattering properties. A processing window is identified for uniform processing of large areas. In particular, the effects of pulse energy, pulse-to-pulse distance and focal plane offsets on morphologies of resulting laser-induced submicron structures are studied.

Chapter 5 presents the surface texturing of stainless steel surfaces employing the Photonic Jet (PJ) technique. A processing domain for producing uniform arrays of holes on relatively large areas is identified. In particular, the effects of pulse energy, effective number of pulses and focal plane offsets on the deposited monolayer of microlenses and the resulting submicron ablation are investigated. The wetting, optical and non-fouling characteristics of such surface structures are also presented.

Chapter 6 reports micro-injection moulding of polypropylene parts with different laser-induced topographies that incorporate submicron to microscale features. Controlled mechanical abrasion of the textured polypropylene surface is performed and the evolution of 3D areal parameters with the wetting properties is investigated.

In **Chapter 7**, a process chain combining low-temperature plasma carburising of stainless steel, ultrashort laser texturing and injection moulding is presented. The surface damage on textured inserts occurring during the injection moulding process and its effect on wetting properties of polypropylene replica are investigated.

Finally, **Chapter 8** summarises the contribution to knowledge, the general conclusion of the carried out research and an outlook for future research directions.

Chapter 2

Literature review

This chapter is covering some of the latest development in functional surfaces. Some insights in water-repellent surfaces found in nature are presented. Different laser-based micromanufacturing techniques are introduced. Fundamentals of liquid-solid interfaces and surface characterization techniques are presented. Finally, some applications and limitations of laser-textured superhydrophobic surfaces are discussed.

2.1 Bio-inspired functional surfaces

2.1.1 Nature as inspiration: self-organized features

Nature has long been an endless source of inspiration for scientists and engineers, who attempted to transfer their observations into the design of technical components. Some recent examples include the optimization of stress distribution in lightweight design, inspired from mechanical self-optimisation of trees (Mattheck and Tesari, 2004) or aerodynamic concept cars, inspired from the morphology of *Ostracion cubicus* (tropical boxfish) (Kozlov et al., 2015). Surfaces, in particular, often present intriguing physical features. Among famous examples are the fractal geometries (Mandelbrot, 1982) that are observed e.g. in the spirals of *Helianthus* (sunflower) seeds (Senior, 1989), the curd of *Brassica oleracea botrytis* (Romanesco cauliflower) (Kieffer et al., 1998) or the nucleation of ice grains (Magono and Lee, 1966). Other examples exist in nature, such as ridges or ripple-like surface structures, that will be considered in **Chapters 3 to 5**. Such self-organized phenomena have been studied across many disciplines (Ayrton, 1910; Hoyle, 2006; Larison et al., 2015), from landscape topography, human body, animal skin or plant leaf (see Fig. 3).

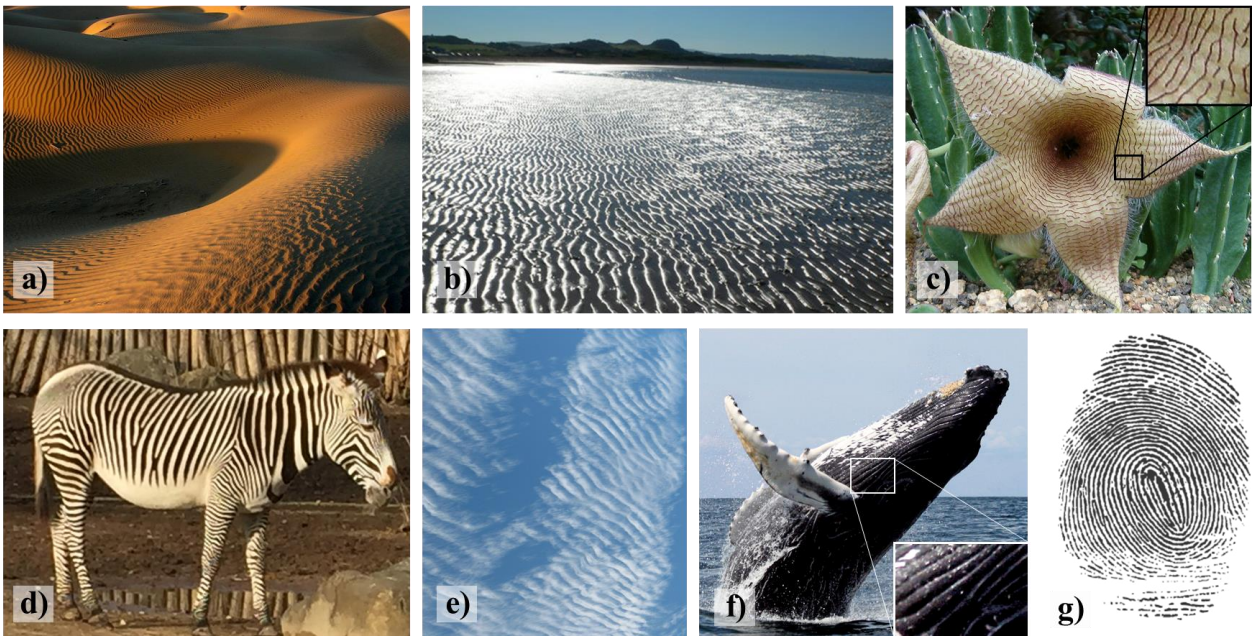

Figure 3. Example of ripples observed in the nature: a) Aeolian sand dunes in the Rocky Mountains (Subramanian, 2009), copyright CC BY 2.0. b) Bottom of a river during low tide (Evans, 2007), copyright CC BY-SA 2.0. c) *Stapelia gigantea* (Carrion flower) (BotBln, 2006), copyright CC BY-SA 2.0. d) *Equus grevyi* (Imperial zebra). Picture taken in the zoological garden of Mulhouse, France, 2019. e) *Altocumulus undulatus* (middle-altitude clouds) (O'Beirne, 2009), copyright CC BY-SA 3.0. f) *Megaptera novaeangliae* (Humpback whale) (Welles, 2007), copyright CC BY 3.0. g) Papillary ridge (friction ridge skin) of human fingerprint (Cyrillic, 2006), copyright CC BY-SA 3.0.

More generally, a complex mix of macro, micro and nano-scale surface structures is often observed in nature. Such multi-scale structures can provide exceptional functional properties to the surfaces. This section offers a non-exhaustive review of surfaces found in nature, with a main focus on the dimensions of surface structures with wetting properties.

2.1.2 Legs and feet

Various animals and insects, e.g. spider, fly, beetle, benefit from adhesion-enhanced properties on their feet. This effect is due to a structural surface, with more or less complexity depending on the body mass to be supported (Bhushan, 2007). Among all examples, the geckos are the most emblematic, as their feet are well-known for their high, yet reversible, dry adhesive

characteristics and also superhydrophobic and self-cleaning properties (Autumn et al., 2002; Bhushan, 2007; K. Liu et al., 2012). The Gecko toes are composed of hierarchical features (see Fig. 4): i) 1-2 mm linear lamellae, ii) covered with 110 μm long hairs (setae), iii) which are split into smaller microhairs (1-2 μm in diameter and 20-30 μm in length), finally iv) terminating in nanohairs (spatulae) of 100-200 nm in diameter and 2-5 μm in length (Bhushan, 2007; Jeong and Suh, 2009; Swiegers et al., 2012). The high adhesion and friction forces are due to van der Walls forces between the spatulae and the wall to climb. The reversible adhesion is permitted by a combined effect of the flexibility of the hierarchical features, the natural tilting of the setae and the rolling-out movements of the foot (Tian et al., 2006). The same flexibility contributes to the self-cleaning properties of the gecko feet, as dust particles can be accommodated in the interstices of the lamellae or setae, protecting the functionality of spatulae, and can be removed by hyperextension of the toes (Hu et al., 2012; Mengüç et al., 2014).

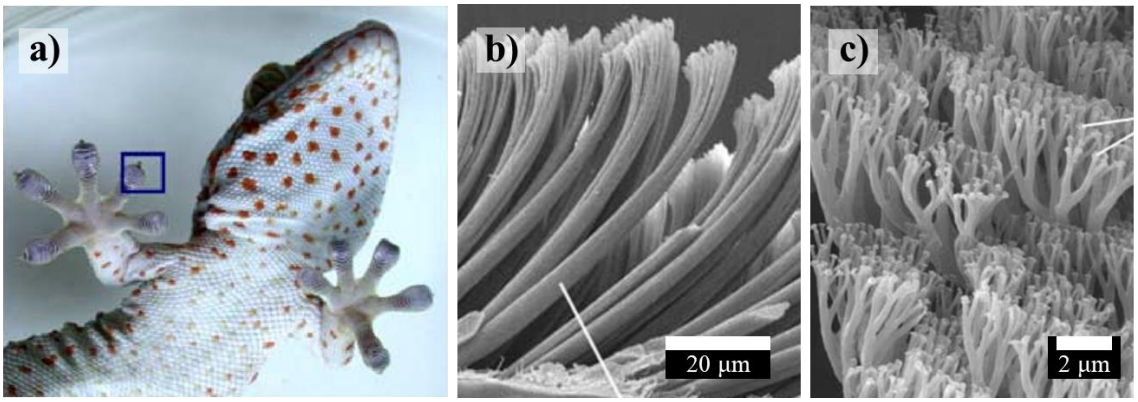

Figure 4. a) Picture of *Gekko gecko* (tokay gecko). Details of the hierarchical structures of the b) setae and c) spatulae. Reprinted from (Gao et al., 2005), copyright (2005), with permission from Elsevier.

Finally, other insects have the capacity to walk on the surface of ponds, such as the water strider that have legs covered with 50 μm long hairs of some hundred nanometers in diameter (Gao and Jiang, 2004; S. Wang et al., 2015).

2.1.3 Wings and feathers

Wings enable insects and animals to fly and can exhibit striking colors and patterns, that are useful for finding a mate or for fooling predators. Therefore, to preserve the special properties of their wings, some insects developed structural features with anisotropic superhydrophobic and self-cleaning properties, as it is the case for most butterflies with wings having overlapping scales of 35-70 μm in width and 55-150 μm in length (G. Sun et al., 2009).

Furthermore, butterfly wings usually show a broad range of colors. The colors can be caused by pigments and/or by structural colors, i.e. due to the interaction of sun light with, usually, lamellar nanostructures (see Fig. 5). The most famous example is probably the brilliant blue observed on the Morpho species, whom wing scales are covered by i) ridges with 0.5-1.4 μm pitch distance with ii) lamellar structures of 2-10 layers of around 50-150 nm pitch distance (Kinoshita et al., 2002; Watanabe et al., 2004). Other species, such as the birdwing butterflies, exhibit different structural colors such as blue, green, yellow or orange, by tailoring the height (around 1.4-3.3 μm) and pitch distance (around 170-215 nm) of sharp ridges with 9-14 lamellar textures (Wilts et al., 2015).

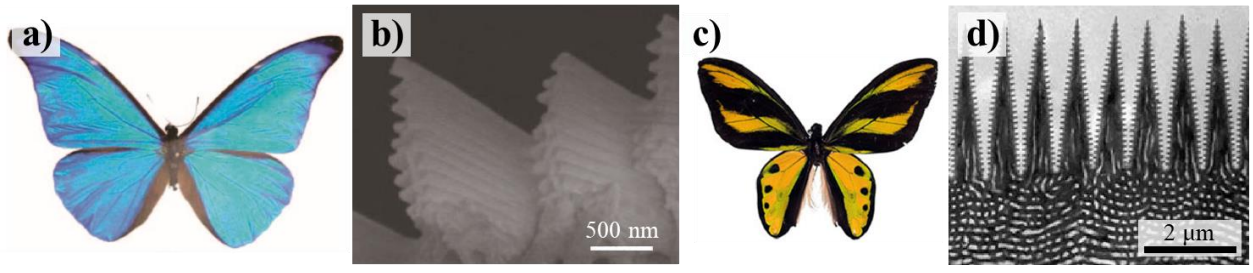

Figure 5. Picture and detail of lamellar structures for a-b) *Morpho Rhetenor* (Morpho butterfly) (Watanabe et al., 2004), reprinted with permission, copyright (2005) The Japan Society of Applied Physics; and c-d) *Ornithoptera Tithonus* (tithonus birdwing) (Wilts et al., 2015), copyright (2015), with permission from The Royal Society.

Apart from ridges/lamellar textures, other types of topographies are observed on structural-colored wing scales. For example, the green color of swallowtail butterflies is provided by close-packed spherical cavities of 4-6 μm in diameter and 0.5-3 μm in depth (see Fig. 6), reflecting the blue-yellow wavelengths of the sun light (Vukusic et al., 2000, 2001). Also, submicron spongy structures are acting as photonic crystals and giving a cyan clue structural color to kingfishers (around 185-210 nm feature sizes) (Stavenga et al., 2011) and iridescence colors to peacocks (3-12 layers of close-packed 130-140 nm spherical features for blue/yellow colors) (Yoshioka and Kinoshita, 2002).

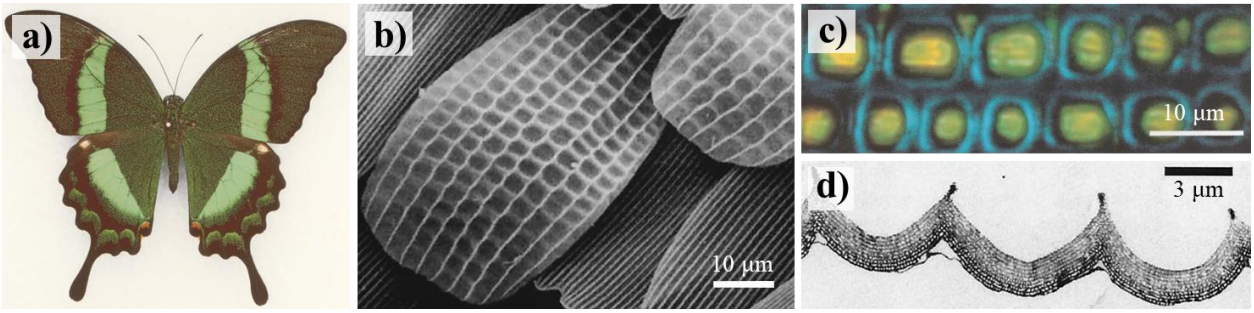

Figure 6. a) Picture of *Papilio Palinurus* (emerald swallowtail butterfly). b) Scales covered by microcavities. c) Blue and yellow color reflected in the cavities. d) Details of microcavities. Reprinted with permission from (Vukusic et al., 2001), copyright (2001) ©The Optical Society (OSA).

Other insects, such as dragonflies (Song et al., 2007) and cicadae (M. Sun et al., 2009), possess visually transparent and superhydrophobic wings. In particular, the glasswing butterfly has anti-reflective properties for camouflage purposes, thanks to wings that are structured with irregular nanopillars with 400-600 nm in height and radius of 40-60 nm (Binetti et al., 2009; Siddique et al., 2015). As for cicada, the wings are covered by nanopillars (see Fig. 7), arranged typically in hexagonal arrays and distant from 170-180 nm, with height of around 200-400 nm and 30 nm tip radius (Zhang et al., 2006; Ivanova et al., 2012; Pogodin et al., 2013). Apart from anti-reflective properties (Xie et al., 2008), such sharp nanostructures were found to be bactericidal, i.e. killing

bacteria by mechanically breaching through their membranes (Ivanova et al., 2012; Hasan et al., 2013; Pogodin et al., 2013).

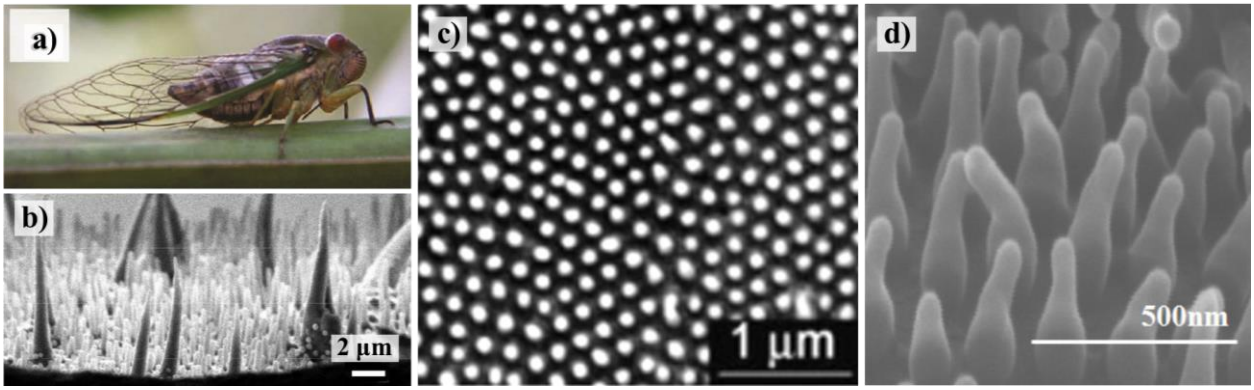

Figure 7. Various specimens of Cicada wing. a) Picture of *Psaltoda claripennis* (Ivanova et al., 2012), reproduced with permission from WILEY-VCH Verlag GmbH, copyright (2012). b) Multiscale features of *Megapomponia intermedia*'s wing. Reprinted with permission from (Kelleher et al., 2016), copyright (2016) American Chemical Society. c) Hexagonal arrays of nanopillars covering wings of *Cryptympana atrata Fabricius* (Zhang et al., 2006), reproduced with permission from WILEY-VCH Verlag GmbH, copyright (2006). d) Detail of nanopillars (species non specified) (Hong et al., 2009), copyright (2009), © IOP Publishing Ltd, reproduced with permission.

2.1.4 Eyes of mosquitos and moths

Compound eyes of insects were mostly studied for their antireflective properties. The glare-free movements of the moth eyes, for example, are due to its quasi-ordered hexagonally close-packed parabolic protrusions, approximately 250 nm in height and distant of 200 nm from each other (Dewan et al., 2011; Gonzalez and Gordon, 2014; Müller et al., 2016). Similarly, the compound eyes of mosquitos are anti-reflective, but also superhydrophobic and anti-fogging (S. Wang et al., 2015). Indeed, even when the mosquitos are exposed to moist environments, their vision remain unaltered as no water drop nucleates on their eyes. These properties are attributed to a dual scale topography made of hexagonally arranged micro and nano convex features (see Fig. 8). The superhydrophobic properties are attributed to the eye's microstructure, composed of close-

packed microbumps of around 20 μm in diameter, while condensation is prevented by non-close-packed nanobumps of around 10 nm in diameter (Gao et al., 2007).

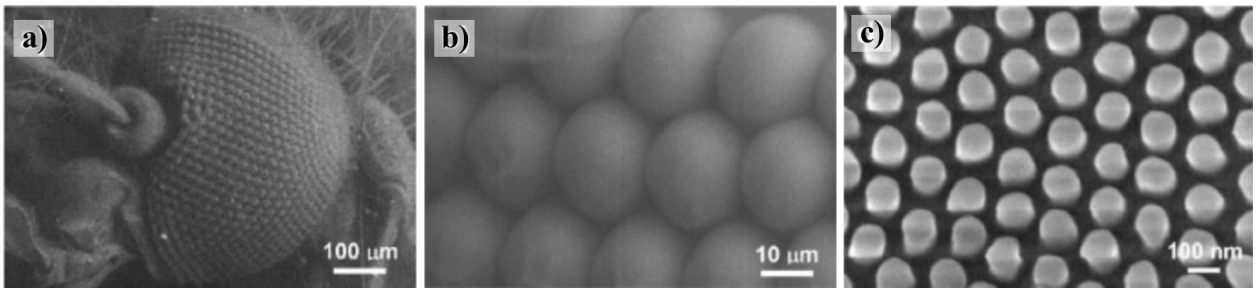

Figure 8. Detail of ommatidium of *Culex pipiens* (mosquito): a) eyes, b) hexagonally close-packed ommatidia, c) hexagonally non-close-packed nipples (Gao et al., 2007), reproduced with permission from WILEY-VCH Verlag GmbH, copyright (2007).

Other compounds eyes are worth being cited for their microstructures, such as the deepwater fishes (Warrant and Locket, 2004) or the lobsters (Tichý and Willingale, 2018) which can see in dim light underwater.

2.1.5 Body skins and elytra

Some living creatures, e.g. chameleon, can tune their body's pigments and nanostructures to generate structural colors in response to external stimulations such as temperature, pH, chemicals, mechanical force or electromagnetic field (Swiegers et al., 2012). Many examples of multiscale surface features are observed on body skins and elytra, providing them interesting functional properties. As example, the abdomen and dorsal skin of *Lucasium steindachneri* (box-patterned gecko) are made of i) spherical micro-bumps of 100-300 μm in diameter and 50 μm in height and ii) sharp hairs (4 μm length and 10-30 nm tip radius); providing the gecko with superhydrophobic, self-cleaning and antibacterial properties (Watson et al., 2015).

Desert beetles, such as the tenebrionid beetle *Stenocara sp.*, have two wing cases (elytra) with water vapor harvesting properties (Parker and Lawrence, 2001). Due to a heterogenous mix of hydrophilic (peaks) and superhydrophobic regions (valleys) (see Fig. 9), the surface extracts water from early-morning fog, that forms droplets on the body of the beetle and roll down towards the beetle's mouth. The valleys are covered by wax and microstructured by a hexagonal array of flattened ~10 μm-diameter hemispheres (Parker and Lawrence, 2001).

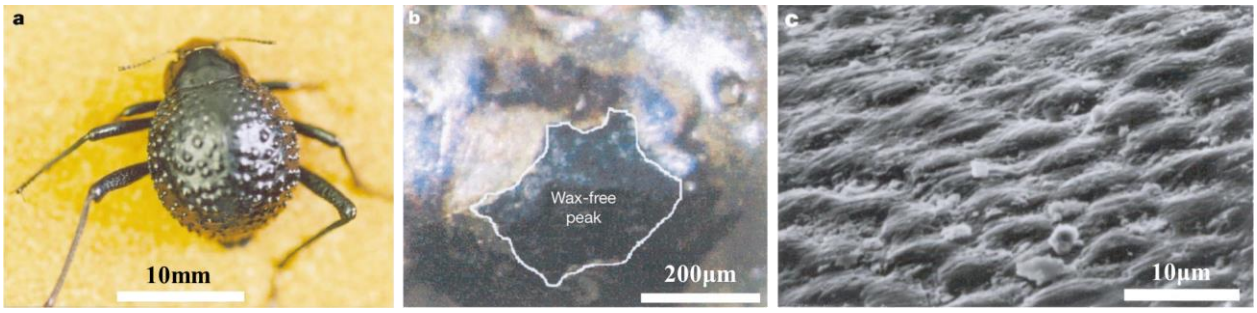

Figure 9. a) Picture of *Stenocara sp*. (Tenebrionidae desert beetle) which elytra (wing cases) covered by near-random arranged peak and valleys. b) Wax is covering the elytra except on the peaks (darker matte region on the picture). c) Microstructures, on the sides and bottom of the valleys. Reprinted by permission from Springer Nature: (Parker and Lawrence, 2001), copyright (2001).

Furthermore, omniphobic properties were observed on the skin of some springtails (Hensel et al., 2013a, 2013b, 2016), which peak-and-valley topographies seem also to offer protection to mechanical damages (Helbig et al., 2011). Different hierarchical structured skin can be observed (Nickerl et al., 2013), usually composed of 3 levels, such as i) disperse hairs, ii) top-flattened microscale peak-and-valleys and iii) submicron granules in rhombic or hexagonal alignments, that are interconnected together by ridges for enhanced mechanical robustness (see Fig. 10). The omniphobic properties of such springtails, even upon full immersion into liquid, are provided by the overhanging (re-entrant) features formed by the submicron granules (Hensel et al., 2013a, 2013b).

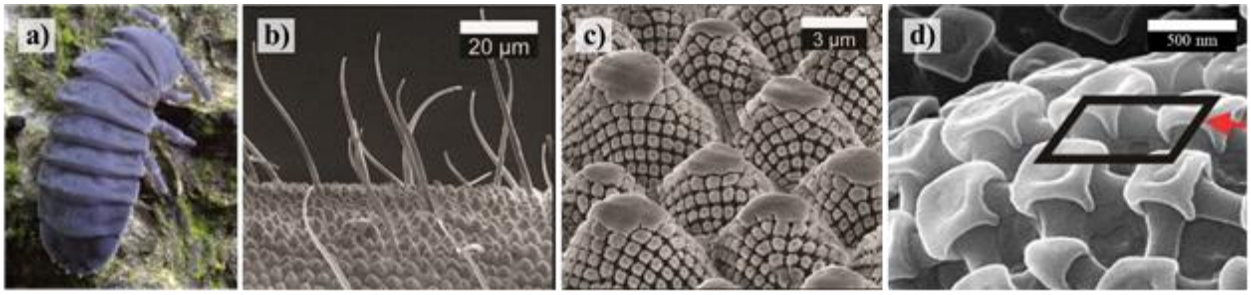

Figure 10. a) Picture of *Tetrodontophora bielanensi* (European giant springtail) (Chereshen'ka, 2016), copyright CC BY-SA 4.0. Details of hierarchically structured skin: b) feathered hairs, c) secondary granules (Hensel et al., 2013b), copyright CC BY-NC-ND 3.0, covered by d) rhombic arrangement of primary granules (Helbig et al., 2011), copyright CC BY.

Furthermore, structural colors can be seen on the wing cases of multiple beetles species. Golden colors are observed on longhorn (F. Liu et al., 2009) and tortoise beetles (Vigneron et al., 2007). Green or metallic colors are seen on weevil beetles (Galusha et al., 2008; Parker et al., 2003) and Carabidae beetles (Galusha et al., 2008; Luna et al., 2013). Most of these structural colors are due to a spongy textured skin, referred to as photonic crystals, which can have different arrangements (tetrahedral-like, honeycomb-like or others). In the case of the weevil beetle, hexagonal- and staircase-like arrangements with an average lattice size of around 450 nm are providing a near-angle independent green colour (Galusha et al., 2008) (see Fig. 11).

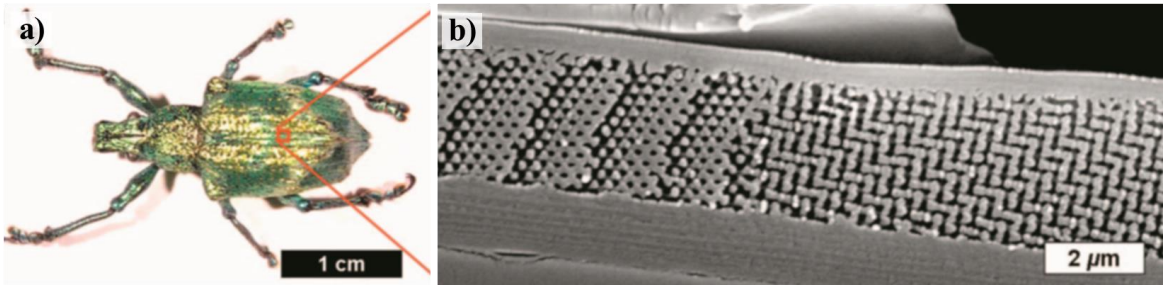

Figure 11. a) Picture of *Lamprocyphus augustus* (weevil beetle). b) Photonic crystals observed in cross section of dorsal scales. Reprinted with permission from (Galusha et al., 2008), copyright (2008) by the American Physical Society.

2.1.6 Fish scales and shells

The shark skin has attracted many interests due to the different functional properties of various species. Indeed, different shark species exhibit a broad spectrum of surface functionalities, from bioluminescence, resistance to abrasion, enhanced hydrodynamics or fouling-resistance towards ectoparasites (Ferrón and Botella, 2017). Different microstructures can be observed on the same species, such as on the large near-shore hunters, which combined surfaces with either enhanced hydrodynamic or abrasive resistance properties (see illustration in Fig. 12). In particular, shark skin riblets led to many studies for their fluid-drag reduction advantage (Ball, 1999; Dean and Bhushan, 2010) and their non-fouling properties (Mann et al., 2014).

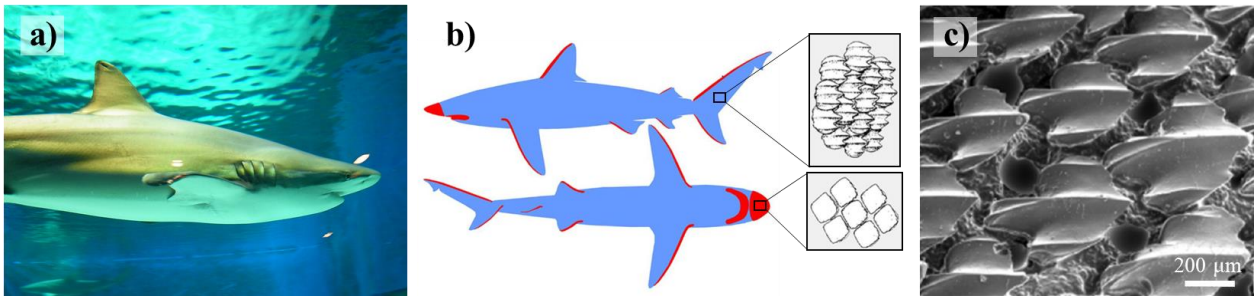

Figure 12. a) Picture of *Carcharhinus brachyurus* (Copper shark) (Azuma, 2012), copyright CC BY-SA 2.5, and b) illustration of hydrodynamic (blue) and abrasive resistant (red) surface structures (Ferrón and Botella, 2017), copyright CC BY 4.0. c) Replicas of shark skin riblets of *Squalus acanthias* (Spiny dogfish shark) (Jung and Bhushan, 2009), copyright (2009), © IOP Publishing Ltd, reproduced with permission.

More generally, some fishes have, in addition to drag reduction effects, self-cleaning properties in oil-polluted water. Indeed, due to the fish scale composition and the presence of a thin layer of mucus, the surface is hydrophilic and superoleophobic in water (M. Liu et al., 2009). Observations of fish scales revealed a multiscale surface structure (see Fig. 13) composed of i) arrays of sector-like scales with diameter of 4-5 mm, ii) oriented papillae with dimensions of 100-300 µm over 30-40 µm and iii) a fine-scale roughness (M. Liu et al., 2009). The complex

microstructures, combined with heterogeneous chemical composition, enabled the formation of a composite interface on fish scales with the oil-repellent properties (S. Wang et al., 2015).

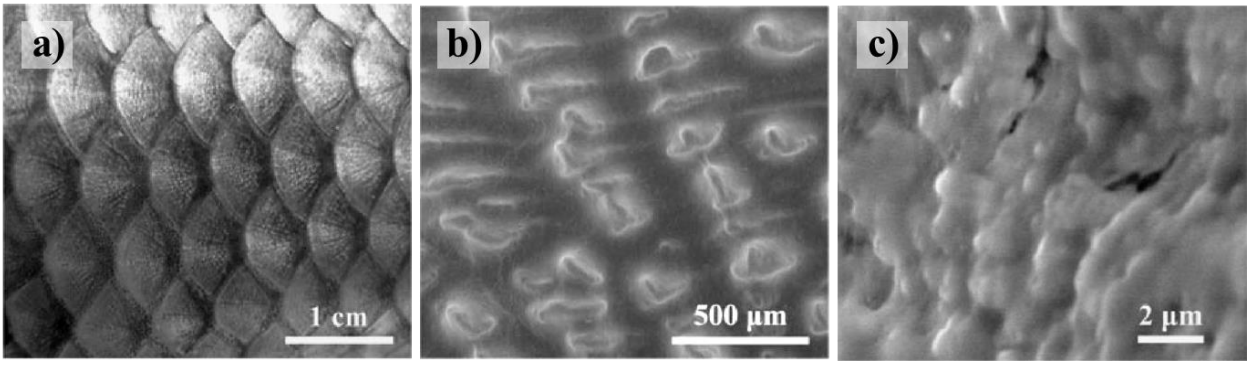

Figure 13. Multiscale surface structures of fish scales such as on *Carassius carassius* (crucian carp) (S. Wang et al., 2015): a) Fish scales at the millimetre range with b) oriented papillae at the micrometre range and c) detail on its surface roughness (M. Liu et al., 2009), reproduced with permission from WILEY-VCH Verlag GmbH, copyright (2009).

Similar underwater superoleophobic behaviours were also observed on other surfaces, e.g. on clam shell (X. Liu et al., 2012) or mucilage (secretion) of Aloe vera (Shome et al., 2018).

Other species of fish, such as the neon tetra (*Paracheirodon innesi*), can also exhibit structural colors, as e.g. with the cyan and yellow colors of neon tetra fishes that have scales covered with lateral stripes with 160 nm spatial distance for cyan color and around 200 nm for yellow color (Cong et al., 2011).

2.1.7 Plant leaves, flower petals and moulds

A broad variety of plants exhibited water-repellent properties, which were associated to their epidermis (outmost boundary layer between the plant and the environment) and cuticle (protecting wax layer) (Neinhuis and Barthlott, 1997). In particular, various surface structures

were observed on plants, e.g. smooth, hairy or papillose epidermis combined with dendritic, tubulous or platelike wax crystals.

Among all plant leaves, the lotus leaf has attracted much attention due to its exceptional low-adhesive superhydrophobic properties. The highly isotropic water-repellency and self-cleaning properties observed on the lotus leaves resulted in calling such extreme low wetting behavior the "Lotus effect" (Barthlott and Neinhuis, 1997). The lotus leaf floats on water (see Fig. 14) and eventual dirt particles are washed away by water drops, leaving the upper side of the leaf dry and clean. The Lotus effect is due to a combination of surface chemistry (wax) and micro/nano surface structures (Feng et al., 2002), composed of i) non-close-packed convex papillae with approximate dimensions of 4-12 μm in diameter and 5-15 μm in height (estimated values); and ii) randomly oriented wax tubules, usually 100-200 nm in diameter and 0.3-1.1 μm in length (Koch et al., 2009). The back side of the leaf, on the contrary, exhibits complete wetting with water and underwater superoleophobicity due to a different surface structure, made of i) close-packed tabular-shaped papillae with approximately 30-50 μm in length, 10-30 μm in width and 4 μm in height; and ii) nanogroove structures with size of 200-500 nm that are exempt of 3D wax crystals (Cheng et al., 2011).

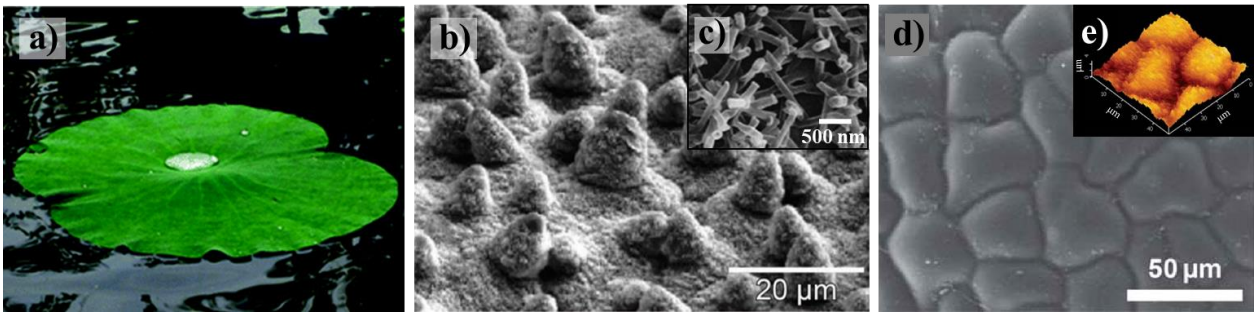

Figure 14. a) Picture of *Nelumbo nucifera* (lotus leaf) floating on water. Detail of upper side of leaf surface, covered with b) papillae and c) 3D wax tubules. Detail of lower side of leaf textured with d) tabular papillae and e) submicron structures. Republished with permissions of The Royal Society of Chemistry: a,d,e) from (Cheng et al., 2011), copyright (2011) and b,c) from (Koch et al., 2009), copyright (2009).

Hierarchical micropapillae similar to the upper side of lotus leaves have been observed on rice leaves. However, the papillae of *Oryza sativa* (rice) leaves are arranged linearly, providing an anisotropic water repellent effect (Feng et al., 2002).

Other states of hydrophobicity are observed on plants, e.g. petals of flower are known to retain spherical water drops on their surface. An illustrative example is usually the high-adhesive superhydrophobic property of the rose petals (Bhushan and Her, 2010). In opposition to the Lotus effect, the "Petal effect" designates superhydrophobicity where water drops are not rolling off but remain pinned to the surfaces (Feng et al., 2008). The papillae of red roses are quite different from the ones observed on the lotus and rice leaves (see Fig. 15). They are close-packed, with average diameter of 16 μm and height of 7 μm, and covered by nanogrooves of about 730 nm in width (Feng et al., 2008). In addition to particular wetting properties, rose petals exhibit structural color due to the periodic nanogrooves (Feng et al., 2010). The structural colors enhance the brightness of the colors already provided by pigments (S. Wang et al., 2015).

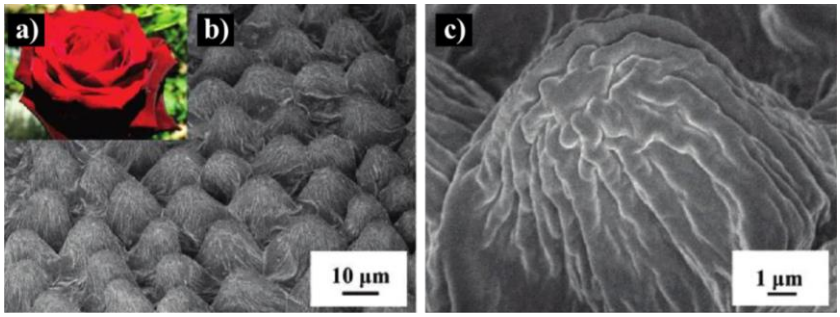

Figure 15. a) Picture of *Rosea Rehd* (red rose) petals. b) Details of micropapillae and c) nanogrooves present on the petals. Reprinted with permission from (Feng et al., 2008). Copyright (2008) American Chemical Society.

The Lotus or Petal effects are not necessarily long lasting after a full immersion of the leaves in liquids. However, some extreme cases of dryness are observed in nature. Indeed, the Salvinia leaf has the special characteristic to stay dry while immerged, as the surface can retain a stable

air layer even after a long-term immersion in water. Such air retention is observed on *Salvinia molesta* which is covered with 3D hierarchical hairs, about 2 mm long and ending in a whisker shape. The leaf is mostly superhydrophobic due to wax nanocrystals, yet the ends of the hairs are flat and free from wax, therefore hydrophilic (Barthlott et al., 2010). The so called "Salvinia effect" is due to a complex surface geometry combining hydrophobic and -philic areas, where the water is either repelled or pinned. Paradoxically, the stability of the air layer is provided by the water bonding at hydrophilic pinning points.

Moreover, in order to better control their wetting properties, some surfaces in nature developed secretions, leading to natural lubricant-impregnated surfaces or so called Slippery Liquid-Infused Porous Surfaces (SLIPS). For example, the *Nepenthes* pitchers are carnivorous plants with typical mug-shaped leaves that ingeniously attract and retain preys. The upper part of the pitcher, called peristome, is fully hydro- and lipophilic (Gorb and Gorb, 2006; Bauer and Federle, 2009). Once the insect, attracted by flagrance, steps on the peristome, it inexorably slips and falls at the bottom of the pitcher, which is filled with some digestive liquids. A lid is closing the pitcher, preventing the insect to climb up the steep waxy peristome walls and to escape. The insect "aquaplaning" effect on the peristome is enabled by a nectar, secreted originally in pores and covering the whole peristome due to capillary effect (Bohn and Federle, 2004, Chen et al., 2016). Such anisotropic properties are lost in dry conditions but are activated by rain and condensation (Bauer et al., 2008). The peristome of a *Nepenthes alata* (see Fig. 16) is hierarchically textured with i) regular ridges of about 460 μm in width, ii) regular microgrooves, with spacing of about 50 μm and iii) arc-shaped microcavities, with the arches tips pointing towards the outside of the pitcher (Chen et al., 2016).

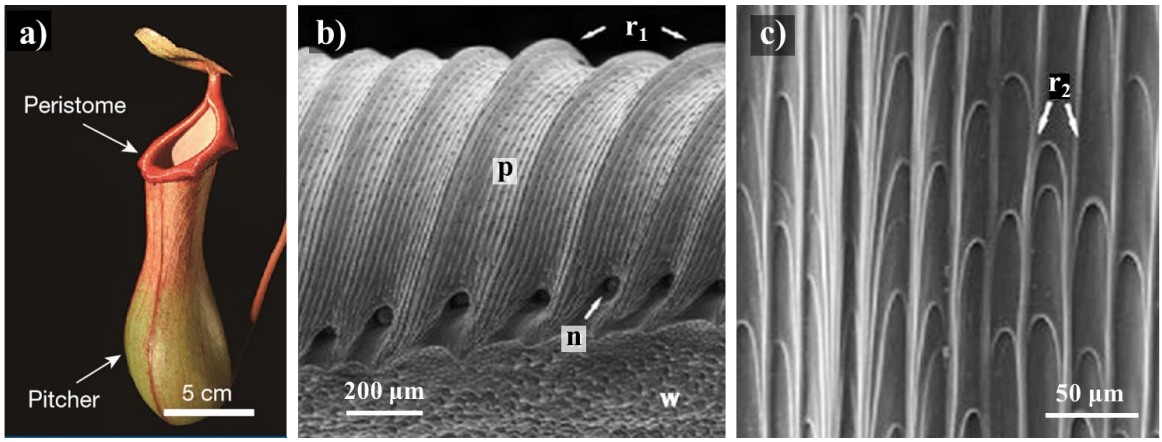

Figure 16. a) Picture of *Nepenthes alata* (carnivorous pitcher plant). Reprinted by permission from Springer Nature: (Chen et al., 2016), copyright (2006). b-c) Detail of peristome surface (p) textured by hierarchical parallel grooves (r_1, r_2). The inner wall surface (w) is covered with wax and secretion exiting pores (n) (Bauer and Federle, 2009), copyright (2009), with permission from Taylor & Francis.

Other cases of functional surfaces are worth mentioning, as for example the sun burn protection of some leaves, enabled by highly reflective properties due to a hair layer on their surface. Such high reflective properties, combined with superhydrophobicity, are observed on poplar leaves which have one side covered by dense ribbon-like hollow hairs, with dimensions of about 14 µm in diameter and 200 µm in length (Ye et al., 2011).

Last but not least, some petals (Glover and Whitney, 2010), fruits (Vignolini et al., 2012) and moulds (Inchaussandague et al., 2010) have also demonstrated iridescent colours, due to thin-film interference or photonic crystals (Sun et al., 2013). In particular, *Diachea leucopoda*, a unicellular slime mould, have a peridium (outer surface of a sporangium or fungus) with some very specific features (see Fig. 17). The peridium is 300-700 nm thick and textured in arrays of bumps with 5 µm in height and 10 µm in diameter, but its structural colors are due to interference between the sun light and inhomogeneous sandwich of air layers of around 10 nm thickness (Inchaussandague et al., 2010).

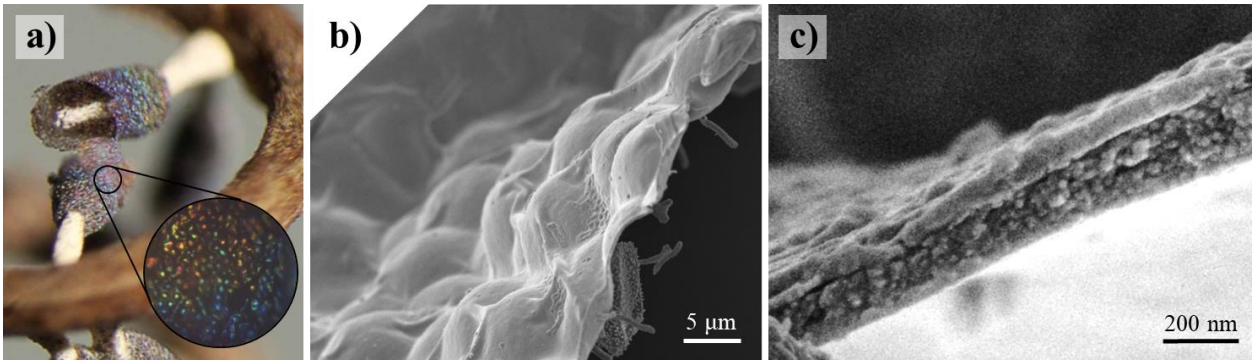

Figure 17. a) Picture of *Diachea leucopoda* (slime mould). b-c) Details of peridium's surface topography and subsurface air layers. Reprinted with permission from (Inchaussandague et al., 2010), copyright (2010) © The Optical Society (OSA).

2.2 Laser-based surface texturing

Science fiction authors long imagined the laser beam technology. In *The War of the Worlds*, written in 1898 by H.G. Wells, a Martian weapon is described as an "invisible, inevitable sword of heat", something that could be nowadays referred to as a near-infrared laser beam, to some extent. Since the first development of laser in the 1960s, laser technology has become reality for a broad variety of applications including barcode scanners, telecommunication, medical surgery and industrial processing (Perkowitz, 2010).

2.2.1 Laser as a manufacturing tool

Based on the idea that amplification of light could be achieved by pumping an active medium in an optical resonator, the principle of LASER (Light Amplification by Stimulated Emission of Radiation) was notarized in 1957 by Gould and the first working laser was built in 1960 by Maiman (Maiman, 1960; Hintze, 2006). Several fundamental physical principles enable a laser beam. When an atom is in excited state, at least one electron is at a higher-energy state, but

usually spontaneously falls back to its ground-energy state, while releasing a photon (spontaneous emission). A photon travelling through an excited atom will not be absorbed but causes the electron at higher-energy state to fall down to its lower-energy state, by emitting a second photon identic to the first one, in term of wavelength, direction, phase and polarization. Therefore, the outcome of a laser device (laser beam) is a coherent monochromatic electromagnetic wave.

The beam is usually linearly polarized, however, a half waveplate can rotate the linear polarisation angle while a quarter waveplate can transform a linear polarisation into a circularly polarized light i.e. a polarisation rotating along the axis of propagation (see Fig. 18).

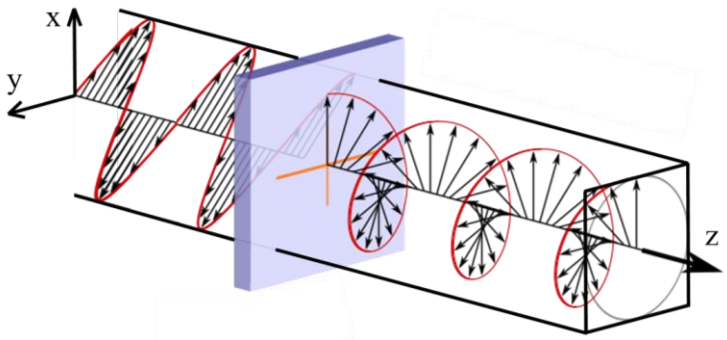

Figure 18. Illustration of a quarter waveplate transforming a linear polarization into a left-handed circular polarization, adapted from (Ryazanov, 2015).

Depending on the construction of the laser, the continuous wave can be pulsed, allowing to increase the optical intensities (peak power, as defined below). The pulse length τ is usually considered at full width at half-maximum (FWHM) i.e. the duration of the power density profile where the intensity reaches half the peak value. The beam delivery system can use further optical devices such as stack of lenses to focus the beam in a smaller spot size and therefore increase further the power density. For Gaussian-shaped beams, the spot size diameter $2\omega_0$ is considered at $1/e^2$ of the intensity distribution (see Fig. 19). The depth of focus can be considered as twice

the Rayleigh length, $Z_R = \pi \omega_0^2 / (\lambda M^2)$, where λ is the laser wavelength and M^2 is the beam quality factor. The minimum spot size achievable is theoretically limited by the optical diffraction limit of light and is given by: $2\omega_0 = 4 M^2 (\lambda / \pi) (f / d)$, where f is the focal length of the lens and d is beam diameter prior to the lens (Spencer, 1982).

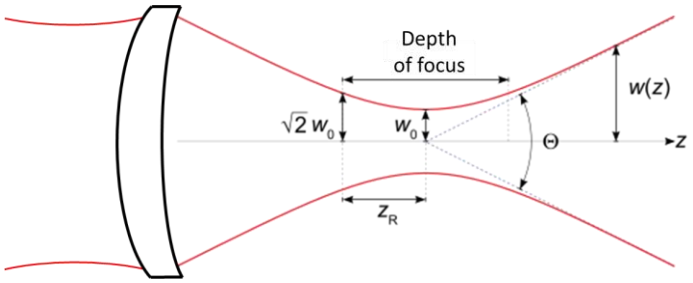

Figure 19. Beam propagation of a laser beam through a focussing lens. The angle Θ represents the divergence of the beam (Hermans, 2009), copyright CC BY-SA 3.0.

Different technologies exist to process areas, either by moving the sample relatively to the beam or vice versa. For example, galvo scanners can allow the deflection of the laser beam over relatively large areas, typically in the order of a few cm^2. In such cases, telecentric lenses are useful to keep the same focal plane and a constant incident angle over the 'field of view' (see Fig. 20a). Then, computerized control of the deflection allows to modify various processing parameters such as scanning speed, distance between scanning lines or their orientations (see Fig. 20b).

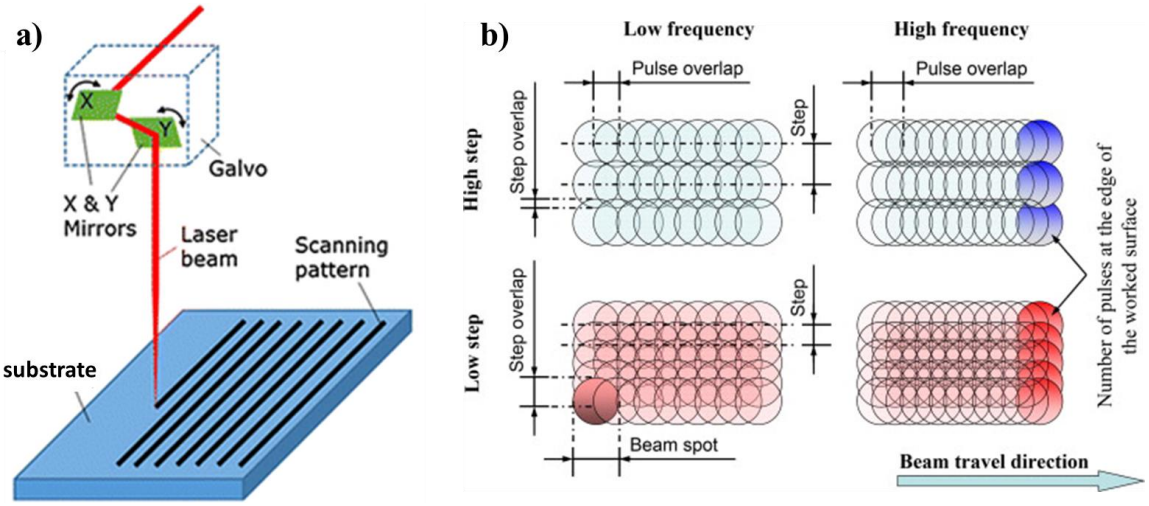

Figure 20. a) Example of scanning strategy for laser surface texturing. The focal position is kept on the surface across the field of view. Reprinted by permission from Springer Nature: from (Yue et al., 2017), copyright (2017). b) Effect of processing parameters on the deposition of pulses over the area. Reprinted from (Leone et al., 2013), copyright (2013), with permission from Elsevier.

Several laser-texturing approaches are described in the following: Direct Laser Writing (DLW), Laser-Induced Periodic Surface Structures (LIPSS) and Photonic Jet (PJ) texturing. All laser-matter interactions involved in these laser techniques are based on the deposition of localized or accumulated energy onto a substrate. The energy per pulse is $E_p = P / f$, where P is the average optical power and f is the pulse repetition rate (frequency). Note that the average power differs from the peak power which is $P_{peak} = 0.94\ E_p / \tau$ (RP Photonics Consulting GmbH, 2019a). The average power can be measured for example by calorimetric methods using a thermopile, which converts the heat generated by the laser irradiation into an electric signal. The fluence φ is calculated with the relation $\varphi(r) = \varphi_0 \exp(-2r^2 / \omega_0^2)$, where r is the distance from the beam spot center. The fluence per pulse φ_0 is the density of energy and usually considered as $\varphi_0 = E_p / (\pi\ \omega_0^2)$, however a factor 2 can be occasionally applied for Gaussian beams (RP Photonics Consulting GmbH, 2019b).

2.2.2 Direct Laser Writing (DLW)

When the fluence received by the substrate is sufficient enough, the surface can go through melting and/or ablation i.e. vaporization (Hamad, 2016). The pulse length allows to classify different processing regimes: long pulses (millisecond range), short pulses (nanosecond range), ultrashort pulses (picosecond and femtosecond range). Typically, ultrashort pulsed laser can minimize thermal effects to the substrate and avoid melting, cracks and redeposition of debris (see Fig. 21).

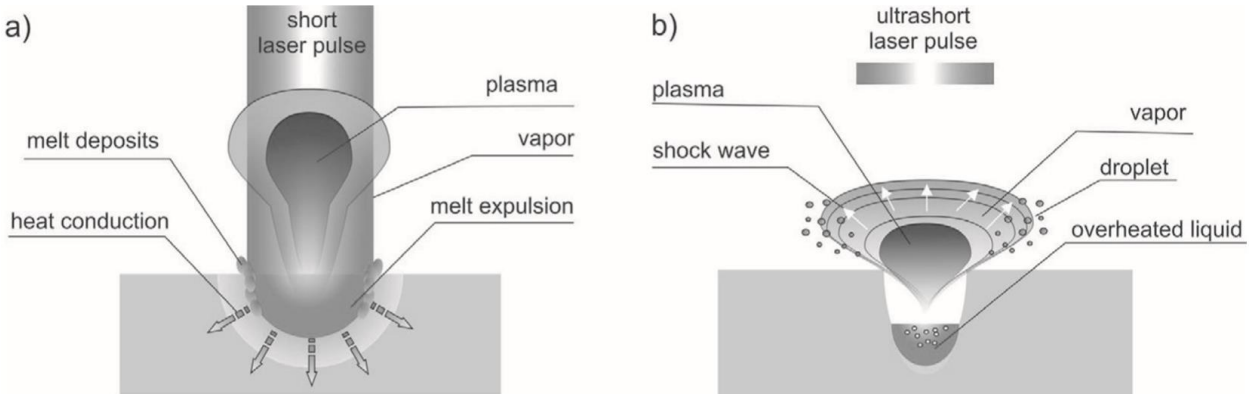

Figure 21. Effects of a) short and b) ultrashort pulsed laser processing on a substrate. Reprinted from (Leitz et al., 2011), copyright (2011), with permission from Elsevier.

When a metallic substrate is exposed to ultrashort pulses, several effects take place during a time scale usually larger than the pulse duration (see Fig. 22). By the action of the electromagnetic radiation, several non-linear optical processes occur (Hamad, 2016). Photons interact with the atoms of the substrate and dissociate the matter into electrically-charged particles (photo-ionization). In essence, the photons are absorbed by the electrons, i.e. the photons disappear and their energy is transferred to the electrons. The excited electrons can reach higher excitation states (multi-photon absorption) and/or escape the atom's potential barrier (tunnel ionization). A chain reaction follows up, caused by the attraction and repellence of the electrically-charged particles, leading to collisions and thus more ions (avalanche ionization). After 100 fs, the

electrons are reaching their thermal equilibrium (thermalization). Then, the energy transfer from electron to the lattice last a few picoseconds (energy transfer) (Hamad, 2016). A simplified two-temperature model was developed to calculate the evolution of temperature of the electrons and the lattice in metals (Anisimov et al., 1974), with good agreements with empirical data (Nolte et al., 1997; Byskov-Nielsen et al., 2011). When using pico- or nanosecond pulses, further thermodynamic and photochemical mechanisms occur. Such effects might not be negligible for train of femtosecond pulses, especially at high repetition rate. The substrate can start melting after a few to a hundred picoseconds (Vorobyev and Guo, 2013). After some tens or hundreds picoseconds, laser ablation occurs (von der Linde et al., 1997) and solid fragments, liquid drops, vapors and an expanding plasma plume are released from the substrate. The mechanisms underlaying ablation are multiple, such as explosive boiling, evaporation, spallation (ejection of particles) or fragmentation (Vorobyev and Guo, 2013). The plume is composed of various elements such as ions, atoms or nanoparticles. Finally, energy is dissipated into the substrate (Bäuerle, 2011; Hamad, 2016).

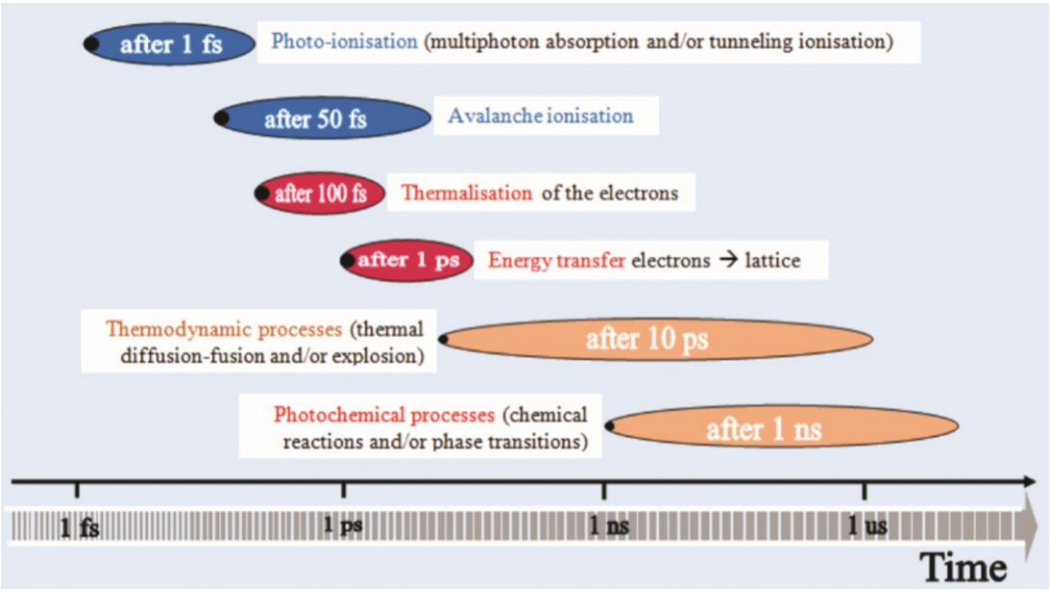

Figure 22. Timeline of effects occurring in a substrate upon an ultrashort pulsed irradiation (Hamad, 2016), copyright CC BY 3.0.

To vaporize a volume of material, a threshold of energy density has to be overcome. Such ablation threshold depends on multiple parameters such as material properties, laser wavelength and pulse length, but can be assessed experimentally following a simple procedure (Liu, 1982). For example, for a single 150 fs and 775 nm laser pulse, the ablation threshold were calculated at 0.21, 0.28, 0.58 J/cm^2 for stainless steel, titanium and copper, respectively (Mannion et al., 2004). For multiple pulses (N pulses), the ablated diameter D can be calculated by: $D = \omega_0 [2 \ln(\varphi_0 / (\varphi_{th} N^{S-1}))]^{1/2}$, by applying an incubation coefficient S estimated at 0.86, 0.83, 0.87 for stainless steel, titanium and copper, respectively (Mannion et al., 2004). The ablated depth L per pulse can be estimated depending on the fluence level. In the gentle ablation regime ($\varphi_0 < 1$ J/cm^2), $L = \alpha^{-1} \ln(\varphi_0 / \varphi_{th})$ where α^{-1} represents the optical penetration depth (optical length) (Nolte et al., 1997). The ablation threshold and optical length could be estimated at 0.13, 0.08, 0.55 J/cm^2 and 20.2, 29.8, 42.7 nm for stainless steel, titanium and copper, respectively (Mannion et al., 2004). When using higher pulse fluence than a threshold Φ_{th}, the removal rate increases. Such strong ablation regime is characterized by the electron heat penetration depth (heat diffusion length) γ and $L \approx \gamma \ln(\varphi_0 / \Phi_{th})$. Similarly, the threshold and heat penetration depth were estimated at 1.25, 1.41, 3.19 J/cm^2 and 52.2, 71.5, 103.0 nm in the strong ablation regime, for stainless steel, titanium and copper, respectively (Mannion et al., 2004).

The material removal process occurring when steering a laser over a surface is commonly referred to as Direct Laser Writing (DLW). By tailoring the fluence per pulse, the spatial between the pulses and the number of over-scans, cavities, trenches or more complex geometries can be fabricated (see Fig. 23) (Chichkov et al., 1996; Schille et al., 2011; Martínez-Calderon et al., 2016). The temporal distance between the pulses, defined by the pulse repetition rate and the

scanning speed, can also alter the targeted geometry (Schille et al., 2014; Ahmmed et al., 2015; Mannion et al., 2004; Fraggelakis et al., 2017).

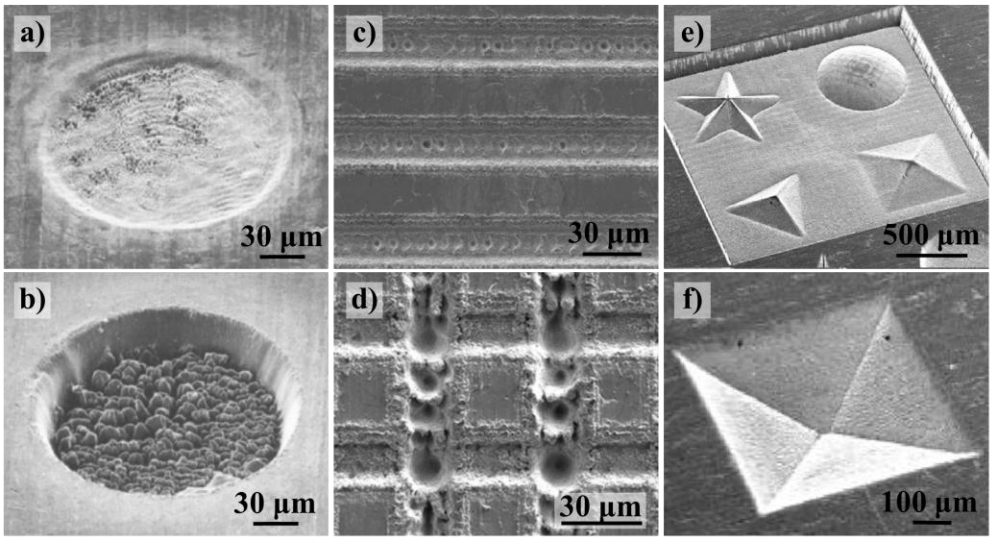

Figure 23. Examples of femtosecond DLW on stainless steel: a-b) Single spot. Reprinted by permission from Springer Nature: (Chichkov et al., 1996), copyright (1996). c-d) Grooves and trenches. Reprinted from (Martínez-Calderon et al., 2016), copyright (2016), with permission from Elsevier, and e-f) 3D geometries. Reproduced from (Schille et al., 2011), with the permission of the Laser Institute of America.

2.2.3 Laser-Induced Periodic Surface Structures (LIPSS)

Laser-Induced Periodic Surface Structures (LIPSS) are surface damages, often referred to as ripples or nanoripples, and typically observed when processing substrates with a polarized laser beam. Such surface damages were discovered soon after the building of the first laser source (Birnbaum, 1965) and are often periodic or quasi periodic wavy ripples, similarly to the ones observed in the nature (see Fig. 3). In the field of laser micro fabrication, laser-induced damages such as LIPSS are usually considered as unfavorable side-effects that have to be minimized for enhanced surface finish. However, in the field of nanofabrication and surface texturing, LIPSS are of a growing interest for fabricating surface structures of various shapes and dimensions,

especially in the subwavelength range (Moradi et al., 2013; Nayak and Gupta, 2010; Vorobyev and Guo, 2015).

Such laser-induced surface structures can be generated either on the substrate's surface, i.e. without material removal, or at the bottom and sides of the ablated area. The time scales involved in their generation is estimated in the nanosecond range, i.e. long after the end of the pulse duration (Vorobyev and Guo, 2013). The mechanisms underlaying the LIPSS formation are still an active research topic, as all concepts fail to explain thoroughly the different LIPSS morphologies observed on various materials. Usually, the femtosecond LIPSS (FLIPSS) require multiple irradiation close to the ablation regime. Therefore, the absorption of the successive laser pulses is contingent to surface defects that are already present on the surface or sparsely generated by the first few laser pulses; and occurs under non thermal equilibrium between the electrons and the lattice (Vorobyev and Guo, 2013). The predominant concepts associated with the generation of LIPSS are:

- *Surface-scattered wave*: Modulation of deposited energy due to interference between the incident laser beam and "surface-scattered waves" originating at surface defects. (Emmony et al., 1973).
- *Efficacy factor* (Sipe): Due to surface roughness, inhomogeneous absorption of energy occurs in the sub-surface, localised underneath the surface roughness (Sipe et al., 1983; Clark et al., 1989).
- *Surface Plasma Polaritons* (SPP): Modulation of deposited energy due to interference between the incident laser beams and SPP. SPP are electromagnetic waves, excited by the photons of the incident beam, and propagating at the surface of electrically conductive substrates (Keilmann and Bai, 1982; Bonse et al., 2009; Huang et al., 2009).

- *Thermocapillary forces*: Rapid melting and re-solidification of the surface associated with thermal gradients, generating Marangoni flows or convection roll movements, or similar convection flows as the ones observed on fluid surfaces during heat transfer (Kirichenko, 2009; Tsibidis et al., 2016; Fraggelakis et al., 2019).

Various LIPSS morphologies can be fabricated depending on the substrate material and the laser processing conditions, in particular the laser wavelength (Bashir et al., 2012) and the polarisation i.e. electric field vector (Graf and Muller, 2015), to name only a few. The fabricated surface structures, especially FLIPSS, can be covered by a nanoroughness, sometimes referred to as nanopores, nanobubbles or nanoforest (Vorobyev and Guo, 2013; Ahmmed et al., 2015). As femtosecond lasers typically have a Gaussian intensity profile, the deposition of energy over the surface plays a major role for the fabrication of uniform LIPSS (Vorobyev and Guo, 2013; Lehr and Kietzig, 2014). While it is possible to optimize the processing parameters to fabricate only one specific LIPSS morphology, it is very common to observe combination of LIPSS. Among the LIPSS morphologies, at least 3 categories can be described:

- *Low Spatial Frequency LIPSS* (LSFL) are usually wavy ripples and, in certain cases, very regular gratings. Such LIPSS morphologies are the focus on the research reported in the **Chapters 3 to 7**. On metals, such surface structures have usually an overall orientation perpendicular to the polarization of the incident beam and a statistical peak-to-peak-distance (referred to as periodicity) close to but slightly lower than the laser wavelength (Bashir et al., 2012). In some cases, the periodicity could be decreased by tilting the incident angle of the laser beam (Wang and Guo, 2006) or by controlling the environment conditions (Golosov et al., 2011; Jiao et al., 2013). The manufacture of LSFL occurs usually in a processing window of a few to a

few hundred pulses with fluences slightly below or around the ablation threshold (Vorobyev and Guo, 2013). Figure 24 shows different stages of colonization of ripples over a surface when increasing the fluence per pulses: the ripples are initiated in some areas, then merge together to cover the surface, until they evolve to other LSFL periodicities or to later-stage LIPSS (Hong et al., 2014). Inventive single-pass solutions were able to generate complex LSFL, by employing e.g. the dynamic rotation of the polarization (Graf and Muller, 2015; Jwad et al., 2018), a complex 2D vector field (azimuthal, radial, spiral) (Ouyang et al., 2015; Skoulas et al., 2017) or a dual-pulse approach (usually cross-polarized pulses delayed from a few picoseconds) (Fraggelakis et al., 2018; Q. Liu et al., 2018). Last but not least, multi scanning methods using cross-polarized directions were also used. In such cases, previously generated LIPSS shouldn't be erased and, usually, lower number of pulses and fluences are applied in the second scanning step (Shinoda et al., 2009; Gregorčič et al., 2016).

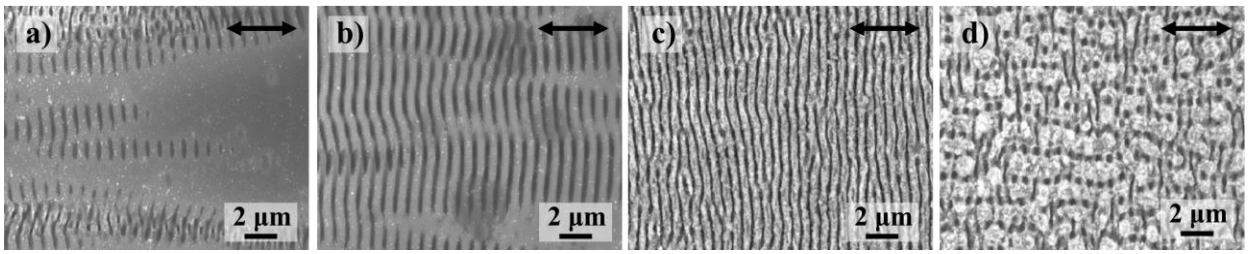

Figure 24. Evolution of ripples-LSFL on silicon wafer with the increase of laser fluence. Reprinted from (Hong et al., 2014), copyright (2014), with permission from Elsevier. The arrow represents the polarisation.

- *High Spatial Frequency LIPSS* (HSFL) are usually ripples with very similar properties than the LSFL, except that they differ in sizes and relative orientation to the polarization (see Fig. 25). Indeed, HSFL are usually much smaller than half the laser wavelength and oriented along the polarisation i.e. perpendicularly to LSFL (Qi et al., 2009; Bonse et al., 2012; Yasumaru et al., 2017). However, parallel subdivision of LSFL can also occur, creating ultimately HSFL perpendicular to the polarisation (Hou et al., 2011; L. Jiang et al., 2012). Large area of HSFL are

usually fabricated using hundreds of pulses with fluences below the ablation threshold (Dufft et al., 2009). Combination of LSFL and HSFL can be fabricated, in which cases the HSFL are located perpendicularly and in between the ripple-like LSFL (Aguilar-Morales et al., 2018).

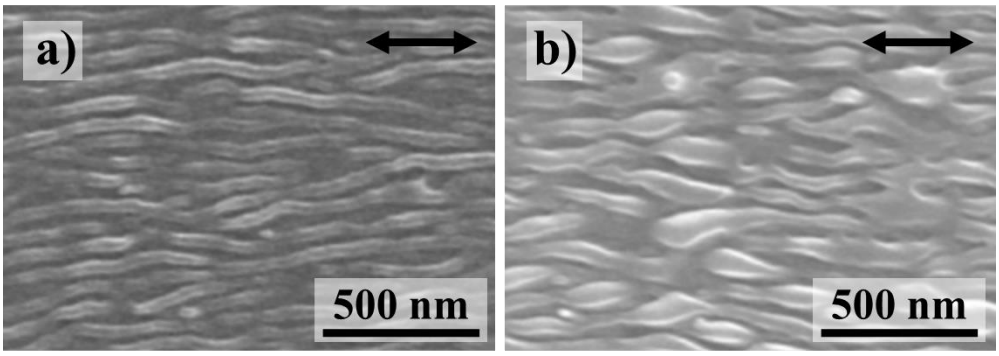

Figure 25. Examples of HSFL on pure titanium with the increase of laser fluence. Reprinted from (Yasumaru et al., 2017), copyright (2017), with permission from Elsevier. The arrow represents the polarisation.

- *Late-stage LIPSS*, such as grooves, spikes, microbumps and columnar structures, appear usually by combining high number of pulses and high fluences. Figure 26 shows typical evolution of late-stage LIPSS with the increased of accumulated fluence. In particular, grooves can be fabricated parallelly to the polarisation with periodicities much larger than the laser wavelength. Such grooves exhibit either a smooth surface finish or can be covered by LSFL (Wu et al., 2009; Tsibidis et al., 2015). Further accumulation of fluence can result in more random structures, such as the hierarchical columnar structures (Wu et al., 2009). In other cases, microbumps of different diameters can be generated. Heat accumulation phenomena, due to increased repetition rate, were shown to enhance the formation of microbumps (Bauer et al., 2015; Fraggelakis et al., 2017) and to inhibit the presence of nanoroughness (T. Jiang et al., 2012). Such surface structures can raise above the original surface, due to combination of scattering and material flow (Zuhlke et al., 2013).

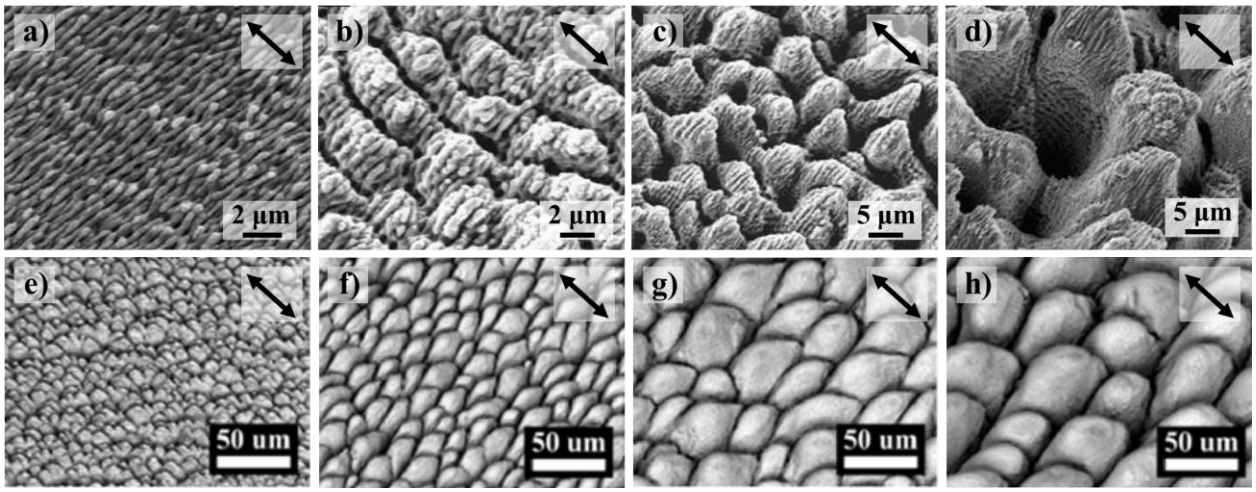

Figure 26. Evolution of late-stage LIPSS on stainless steel with the accumulated fluence: a-d) from LSFL to dual scale columnar structures and e-h) from spikes to microbumps. Note the difference of scales. The arrow represents the polarisation. a-d) Reprinted from (Wu et al., 2009), copyright (2009), with permission from Elsevier. e-h) Reprinted with permission from (Fraggelakis et al., 2017), copyright (2017) ©The Optical Society (OSA).

2.2.4 Photonic Jet (PJ)

The research on Photonic Jet originated probably from the microelectronic and spatial industry. Indeed, foreign particles down to the submicron scales were detrimental to final products and several techniques were developed to remove them from surfaces (Tam et al., 1992; Mittal, 1994). In particular, Dry Laser Cleaning (DLC) involved short and ultrashort pulses with fluences much lower than the damage threshold of the substrate. In the case of small particles less than a few micrometers in size, the gravitational forces are less than the adhesions forces, such as Van de Waals, capillary and electrostatic forces (Tam et al., 1992). The main removal mechanisms involved during DLC were identified as:

- *Thermal expansion.* Upon short pulse irradiation, a rapid absorption and thermal expansion can occur within the substrate or the particles, depending on their respective absorption to the laser wavelength. The thermal expansion is usually in the order of a few nm for

about 10 ps and leads to a strong acceleration force that enable the particle detachment (Tam et al., 1992; Arnold, 2003).

- *Liquid evaporation.* Humidity from ambient air may result in capillary condensed water underneath particles. Upon ultrashort pulse irradiation, the particles are ejected by the momentum created by the explosive evaporation of water (Vereecke et al., 1999). Indeed, ambient humidity showed a strong effect on the particle removal efficacy, suggesting even steam laser cleaning as a safer removal technique, due to the lower fluences required (Mosbacher et al., 2000, 2001).

As a consequence of research on DLC, unusual surface damages were identified. A manufacturing route was developed employing the observed optical phenomena that occur in the vicinity of the irradiated microspheres. Indeed, in some cases, peak of intensities are observed due to the interference between the incident beam and the scattered field around a sphere (McCloskey et al., 2010). In particular, Photonic Jet (PJ) or Nanojet refers to non-evanescent beams emerging from the shadow-side of the microspheres. A focal spot can be generated beyond the optical diffraction limit of light (Abbe, 1873; Chen et al., 2004; Lecler et al., 2005), usually as small as a third of the irradiated wavelength (Heifetz et al., 2009). However, to determine the optical phenomena around a microsphere, the conventional rules of geometrical optics are not valid anymore and two extreme cases are usually considered (see Fig. 27).

- *Lorentz-Mie regime*. For large microspheres ($2r/\lambda >> 1$), a generalized Lorentz-Mie theory can be applied (Han et al., 2014) and the key factors affecting the PJ are: i) the refractive index contrast i.e. the ratio of refractive indexes between the microsphere and the ambient environment and ii) the ratio of microsphere's diameter ($2r$) over the irradiated wavelength (λ) (McCloskey et al., 2010).

- *Dipole regime*. In the case particle's size much smaller than the wavelength ($2r/\lambda<<1$), the actual shape of the particle or the refractive index contrast are less critical. Maxima of intensity can be reached in the front or rear focal planes (Arnold, 2003) or on the sides of the particles (Münzer et al., 2001).

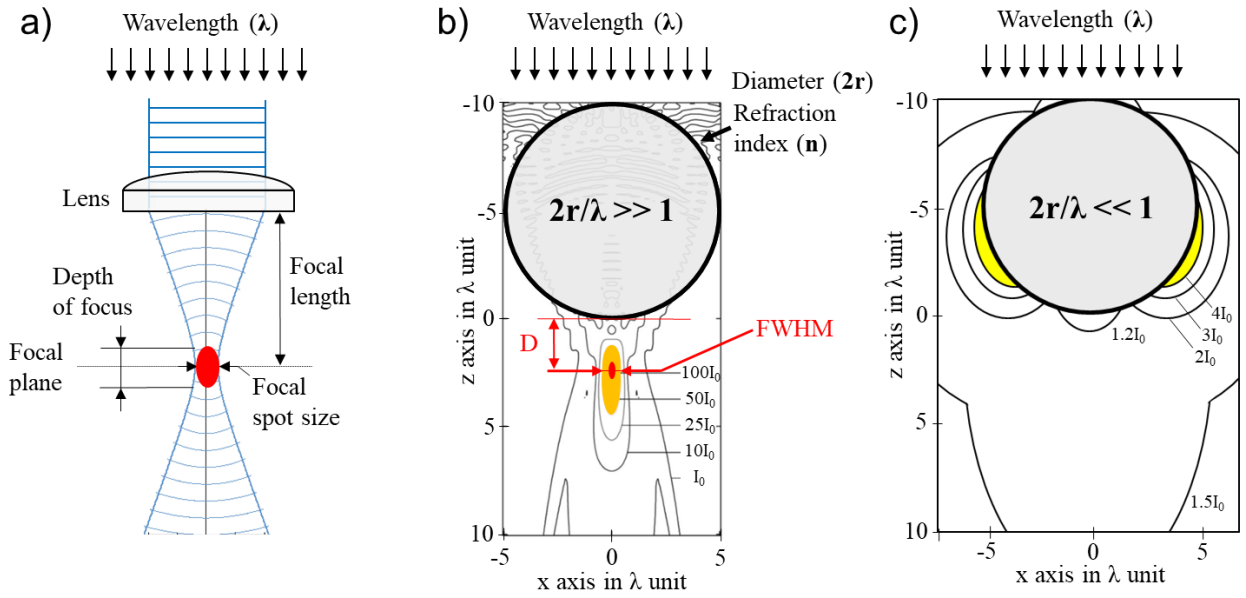

Figure 27. Schematic of focal enhancement in different regimes: a) optical geometry, b) Lorentz-Mie and c) dipole regime. a) Adapted from (Etoombs, 2011), copyright CC BY 3.0 and from (Hermans, 2009), copyright CC BY-SA 3.0. b) Case 2r=5 λ, n=1.3. Adapted with permission from (Lecler et al., 2005), copyright (2005) ©The Optical Society (OSA). c) Case 2r=0.4 λ, n=1.58. Adapted with approximative values from (Münzer et al., 2001) with permission from WILEY-VCH Verlag GmbH, copyright (2001).

Numerous modelling of near-field optical enhancement were reported in the literature, especially in the Lorentz-Mie regime. The resulting PJ can be analyzed in term of focal distance (D) and spot size at full width at half-maximum (FWHM). Depending on the refractive index contrast, focal spot sizes were calculated between 0.8 λ and 0.15 λ and located in the shadow-side of the particle (Huang et al., 2002; Leitz et al., 2010; Pereira et al., 2008). The transition between the Lorentz-Mie and dipole regime, occurring for particles of size close to the wavelength, was

sparsely investigated in the literature, without clear trend for the case $2r = \lambda$ (see Table 1). This case will be the focus of **Chapter 5**.

Table 1. PJ modeling in the literature (non-exhaustive, * estimations).

Refractive index contrast (-)	**Wavelength** λ (nm)	**Ratio sphere-wavelength** 2r/λ (-)	**Focal distance** D (μm)	**Focal spot** FWHM (nm)	**Reference**
1.50	1000	4-35	0.15	600	(Abdurrochman et al., 2014)
1.59	400-800	0.6-1.3	N.A.	N.A.	(Afanasiev et al., 2015)
1.63	365	2.7	>0	N.A.	(Berthod et al., 2017)
1.40	800	1.3	>0	325	(Cai and Piestun, 2006)
1.60	520	1.9-9.6	1.0*-2.5*	300*-400*	(Ferrand et al., 2008)
1.47	400	0.9	<0	N.A.	(Grojo et al., 2014)
1.51*	248	2	~0*	200	(Guo et al., 2007, 2008; Li et al., 2009)
1.20	633	3.2	1.54	340	(Han et al., 2014)
1.6	248	1.9-3.8	>0*	38-46*	(Huang et al., 2002)
1.6	248	1.9-3.8	~1	80*-100*	(Huang et al., 2003)
~1.6*	248	4	~1*	100*	(Huang et al., 2005)
1.3-1.63	N.A.	2-5	0-2.5λ	<λ*	(Lecler et al., 2005)
1.57	1064	0.94-4.70	~0.4*	~150-330	(Leitz et al., 2010)
1.34-2.00	300	3.3	<r*- ~0.5*	<λ*	(C. Li et al., 2005)
1.59	400	2.5-20	0.1*-0.7*	130-210	(X. Li et al., 2005)
~1.6*	365	1.4-5.5	>r*	60-140	(Li et al., 2013)
1.5*	248	2.0	~0*	80	(Lu et al., 2000)
1.68	400	2.5-15	~0.05*	140-230	(McCloskey et al., 2010)
1.6	800	0.4-3.2	N.A.	N.A.	(Mosbacher et al., 2001)
1.58	800	0.4-2.1	~0.3	600*	(Münzer et al., 2001)
0.2*	800	0.25	N.A.	N.A.	(Nedyalkov et al., 2007)
1.6	193	2.6	N.A.	160*	(Pereira et al., 2008)
1.78	248	4	~0.15*	N.A.	(Piparia et al., 2006)
0.96	515	2.5	<0*	N.A.	(Sedao et al., 2012)
~1.6*	248	4	>0*	100*	(Wang et al., 2004)
1.47	365	1.4-14	>0*	N.A.	(Wu et al., 2007)
1.5	800	1.25	N.A.	N.A.	(Zhou et al., 2006)

Regarding laser processing employing microspheres' diameters close to the laser wavelength, many works reported the use of short pulses, especially for lasers with wavelengths between 248 and 800 nm (Huang et al., 2002; Mosbacher et al., 2001; Münzer et al., 2001; Watanabe et al., 2001). In some cases, the effect of femtosecond pulses was investigated, however constrained to wavelengths in the range from 400 to 800 nm (see Table 2). Overall, craters with submicron diameters were reported, independently of the combinations of materials (microsphere/substrate), sphere's diameters and/or the laser wavelength. Compared to conventional laser processing using micro-scale focal spots (DLW), PJ-assisted processing enabled the ablation of substrate at lower fluence threshold and for materials usually transparent at the irradiated wavelength (Cai and Piestun, 2006; Zhou et al., 2006). Moreover, ultrashort pulses often induced thermal effects resulting in e.g. rim or bulges around the ablated craters (Nedyalkov et al., 2007) or convex bumps above the surface (Huang et al., 2002; McLeod and Arnold, 2008). The formation of nanobumps were explained by thermo- (Marangoni effect) and chemico- (gradient of chemical composition and surface energies) capillary forces (Lu et al., 2003).

Table 2. Experimental results found in the literature, using ultrashort PJ-assisted laser ablation (non-exhaustive, * estimations).

Materials particle/ substrate	**Pulse length**	**Laser wavelength** λ (nm)	**Ratio sphere-wavelength** 2r/λ (–)	**Ablated diameter** ∅ (µm)	**Reference**
PS / PMMA	50fs	400-800	0.6-2.5	0.43*	(Afanasiev et al., 2015)
SiO_2 / Glass	60fs	800	1.3	~0.3	(Cai and Piestun, 2006)
PS / Si	10ps	1064	0.9-4.8	~0.3-1	(Leitz et al., 2010)
SiO_2 / GST film on PC	100fs	800	28.75	0.4	(Lin et al., 2006)
PS / Si	150fs - 30ps	400-800	0.4-4.3	0.2-0.4	(Mosbacher et al., 2001)
PS / Si and Glass	100fs	800	0.3-2.1	~0.1-0.4	(Münzer et al., 2001)
Au / Au, Si and Glass	100fs	800	0.25	~0.1*-0.2*	(Nedyalkov et al., 2007)
SiO_2 on Glass / Si	6.7ps	515	2.5	0.3*-0.8*	(Sedao et al., 2012)
SiO_2 / Copper	100fs	800	8.5	0.4*-2.0*	(Vestentoft et al., 2005)
SiO_2 / Glass	100fs	800	1.25	0.5*	(Zhou et al., 2006)

PJ-assisted laser processing is a promising high-throughput texturing technique. In some cases, up to 6 million features could be fabricated in parallel (Li et al., 2009). Prior to laser processing, an homogeneous hexagonally close-packed monolayer is deposited onto the substrate. Therefore, the resulting nanoholes or nanobumps are hexagonally aligned with a spacing defined by the microspheres' diameter (see Fig. 28). Multiple laser pulses could either increase the depths of nanoholes (Sedao et al., 2012) or smoothen nanoholes' bulges (Abdurrochman et al., 2014; Kallepalli et al., 2013). A major issue in large-area texturing is the DLC effect, triggered among other by ablation of material below the microspheres. Large-area texturing was therefore enhanced by maintaining artificially the microspheres in contact with the surface (O'Connell et

al., 2010; Khan et al., 2010, 2011; Sedao et al., 2012) or processing with a non-orthogonal incident angle (Münzer et al., 2001; Guo et al., 2007; Li et al., 2009; Wang et al., 2004).

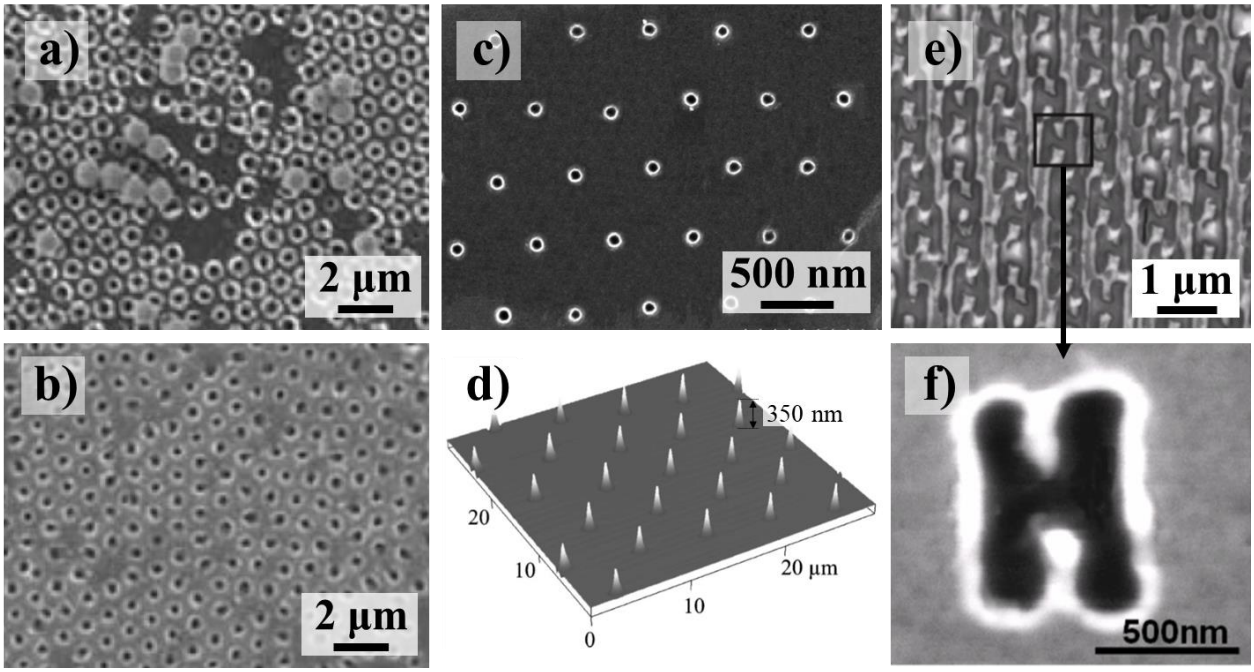

Figure 28. Examples of PJ-assisted texturing: a-b) multipulse refining of array of holes (Kallepalli et al., 2013), copyright (2013) © IOP Publishing Ltd. Reproduced with permission. All rights reserved; c) nanoholes, reprinted from (Li et al., 2013), with the permission of AIP Publishing, copyright (2013); d) nanopillars, reprinted from (Wysocki et al., 2003), with the permission of AIP Publishing, copyright (2003); e-f) angular processing for user-defined nanopatterns (Li et al., 2009), copyright (2009) © IOP Publishing Ltd Reproduced with permission. All rights reserved. The $2r/\lambda$ factors are around a-b) 5, c) 1.6, d) 24 and e-f) 4. All examples are on silicon, except on silver for c).

2.2.5 Other laser-based texturing techniques

Other selective laser texturing approaches are of interest for large-area functionalization of surfaces, such as the Direct Laser Interference Patterning (DLIP) techniques (Aguilar-Morales et al., 2018; Alamri et al., 2019a). Compared to DLW, DLIP employs significantly larger spot sizes and the laser ablation is triggered by intensity maxima of a multi-beam interference pattern. Such technique is also very versatile, as the shape and periodicity of the interference pattern can be tailored (Lasagni et al., 2010, 2011; Helbig et al., 2016; Rosenkranz et al., 2016).

The DLW was shown to be an attractive method to engineer hierarchical structures, even using nanosecond pulses due to solidified melted and recast materials (Emelyanenko et al., 2015; Gregorčič et al., 2016; Ta et al., 2015). Moreover, when employing the DLW and DLIP techniques with a polarised beam, LIPSS are usually created as well (Aguilar-Morales et al., 2018; Alamri et al., 2019b; Long et al., 2015a). Nevertheless, several laser techniques can be combined to complexify the surface structures, e.g. combinations of DLW with LIPSS (Martínez-Calderon et al., 2016; Huerta-Murillo et al., 2019) or DLIP techniques (Huerta-Murillo et al., 2017; Cardoso et al., 2018). Last but not least, further dry or wet processes, such as plasma-, chemical-etching or anodization, can also be used to add a nanoroughness on micro-scale topographies (Abdulhussein et al., 2016; Lee et al., 2007; Park et al., 2012; Yoo et al., 2009; Zhang et al., 2019).

Polymer replica of laser-fabricated surface structures were reported mainly by curing of poly(dimethylsiloxane) (PDMS) (Caffrey et al., 2012; Liu et al., 2016; Nayak et al., 2013; Noh et al., 2010). However, other replication techniques were successfully employed on laser-textured masters : embossing (Falah Toosi et al., 2016; Rank et al., 2016), roll-to-roll embossing (Rank et al., 2019) and micro injection moulding (Pina-Estany et al., 2018). Hair-like structures could be fabricated on polymer replica by the careful control of the cooling and demoulding processes (Bekesi et al., 2010; Stormonth-Darling et al., 2014). Soft metals such as cupper could be hot embossed with DLW-processed tungsten masters, too (Jiang et al., 2016).

2.3 Superhydrophobic applications of laser surface structures

2.3.1 Introduction to wetting theories

The wetting property of surfaces is key issue in surface engineering. When a liquid gets in contact with a solid, two simplified extreme wetting behaviors can be observed. The full wetting of a surface, occurring when the liquid spreads out to form a film over a surface, is relevant to applications such as lubrification, coating, printing and adhesive bonding (Yuan and Lee, 2013; Völkermeyer et al., 2013). On the contrary, the full drying of a surface is when liquid does not wet the surface. The liquid adopts an almost spherical shape and the formed droplets would roll off the surfaces easily due to gravity, providing self-cleaning properties (Barberoglou et al., 2009; Li et al., 2007).

In the early 1800s, Thomas Young first theorized the equilibrium of a sessile drop of liquid resting on an ideal, flat and chemical homogeneous solid surface (Young, 1805). The Young's contact angle θ_Y represent the angle between the liquid-solid interface and the tangent line to the liquid-vapor interface. The state of mechanical equilibrium was defined in the Young's equation $\gamma_{LV} \cos \theta_Y = \gamma_{SV} - \gamma_{SL}$ where γ_{LV}, γ_{SV} and γ_{SL} referred to the interfacial tensions liquid-vapor, solid-vapor and solid-liquid, respectively. Full wetting of surfaces can be characterized by Young's contact angle close to zero. In the case where the liquid is water (see Fig. 29), the surface is denominated hydrophilic when the water contact angle is forming an angle lower than 90° and hydrophobic for angles larger than 90°.

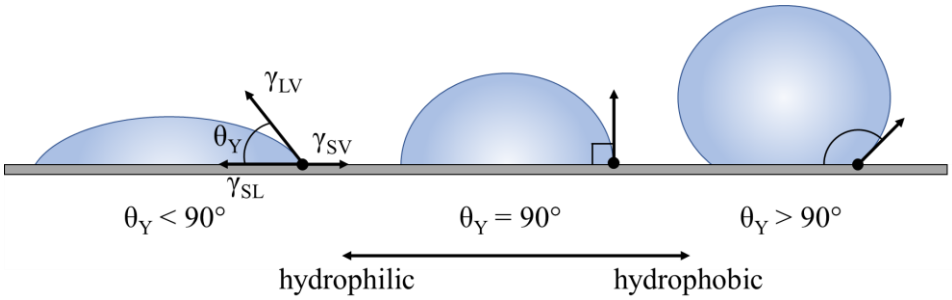

Figure 29. Illustration of Young's contact angles for hydrophilic and hydrophobic surfaces. Reprinted (adapted) by permission from Springer Nature: (Yuan and Lee, 2013), copyright (2013).

The Young's wetting model for ideal surfaces was adapted to rough surfaces by Wenzel (Wenzel, 1936, 1949), taking in account the increased solid-liquid interface. The Wenzel contact angle θ_W could be calculated by the equation: $\cos \theta_W = r_W \cos \theta_Y$, where r_W is a dimensionless factor, known as Wenzel's roughness or factor and referring to the ratio between the developed surface area and the nominal area. For an ideal flat surface, the Wenzel factor is equal to 1 and the Young's contact angle equals the Wenzel's contact angle. The Wenzel factor becomes larger than 1 when the surface roughness increases and, as a consequence, the Wenzel's model predicts that an increase in roughness leads to lower or higher water contact angles depending on the hydrophilic or -phobic nature of the flat surface (see Fig. 30).

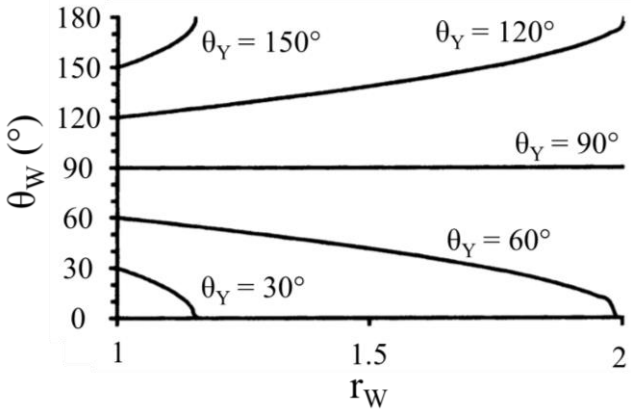

Figure 30. Influence of roughness factor r_W on the contact angle according to Wenzel's model. Reprinted by permission from Springer Nature: (Nosonovsky and Bhushan, 2005), copyright (2005).

However, the formation of cavities (air trapping effect) can be observed for very rough, high porous surfaces or high aspect ratio surface features. Limited by the Wenzel model, Cassie and Baxter considered in 1944 a composite solid-liquid-air interface to describe such air cushions below the liquid drops (Cassie and Baxter, 1944, 1945). This effect is usually referred to "fakir" or Cassie-Baxter (CB) state (Quéré, 2002; Kietzig et al., 2011a; Kim et al., 2016a). According to the CB model, the contact angle θ_{CB} can be calculated using $\cos \theta_{CB} = - 1 + \varphi_{CB} (\cos \theta_Y + 1)$, where φ_{CB} represents the fraction of solid in contact with the liquid. The CB state happens to be metastable and imbibition or capillarity effects can be triggered by e.g. vibrations, impact or squeezing (Papadopoulos et al., 2013). Further wetting can lead to intermediate CB-Wenzel (heterogeneous) regimes or homogeneous (full) Wenzel state (see Fig. 31). The mixed CB-Wenzel wetting states often exist and can be classified into "lotus", "petal" or "gecko" wetting states, depending on the wetting of micro structures and/or nano structures and/or porosities (S. Wang et al., 2015). The transition regime between the CB and Wenzel states has been continuedly studying since the last decades (Lafuma and Quere, 2003; Quéré, 2008) and further effects such as the pressure drop (Afferrante and Carbone, 2010) or thermodynamics (Marmur, 2003, 2006; Marmur and Valal, 2010) have also been considered. Further studies modelled different surface structures and were able to some extend to predict their wetting behavior (Kubiak and Mathia, 2014; Nosonovsky and Bhushan, 2005; Kietzig et al., 2011a; Wu et al., 2009; Cai et al., 2018; Kim et al., 2016a; Bittoun and Marmur, 2012).

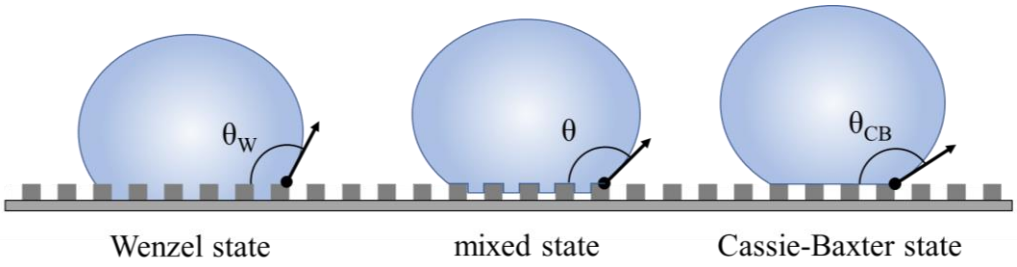

Figure 31. Illustration of the wetting of rough surfaces according to the Wenzel and Cassie-Baxter models. Adapted with permission from (Dettre and Johnson, 1964). Copyright (1964) American Chemical Society.

To assess the wetting state of a liquid towards a surface, the most used technique is the sessile drop technique, that consists in measuring the static contact angle of a specific volume of liquid deposited on the levelled surface (Yuan and Lee, 2013). To that mean, a Young-Laplace fitting method is usually used to extract the profile of the drop on the solid, taking in account the deformation due to external forces such as ambient gas phase (temperature, humidity) and gravity (Cardoso et al., 2015; Krüss GmbH, n.d.). The volume of liquid used in the sessile drop technique is influencing the static contact angle measurements because of the drop settling effects and variation in contact area between solid and liquid (Noordmans and Busscher, 1991). Therefore, volumes of 6 to 7 µl have been commonly used (Kietzig et al., 2011b; Cardoso et al., 2017) even if, in some cases, smaller (1-3 µl) (Kietzig et al., 2009, 2011a; Wu et al., 2009; Cardoso et al., 2015) or larger (8-12 µl) (Jagdheesh et al., 2016, 2017; Chun et al., 2016; Jang et al., 2017) volumes have also been reported. It is not trivial to correlate the volume of the drop with the contact area of the drop with the solid as it is dependent on the contact angle and the Wenzel or CB or mixed wetting regime. The geometric formula $V = 4 \pi r^3 / 3$ can be applied to calculate the radius r of an ideal spherical drop of volume V in levitation in air. The radius of a 3 µl spherical water drop, for example, is estimated around 1 mm (Cardoso et al., 2015).

In general, superhydrophobic surfaces refer to surfaces on which sessile drops of water have static contact angles larger than 150° (S. Wang et al., 2015). However, the wetting state is not identified by the static contact angle only and it is usual to measure the contact angle hysteresis θ_H. Therefore, a superhydrophobic surface can also be described as having a static water contact angle higher than 150° combined with a low roll-off angle or a low water contact angle hysteresis (Kietzig et al., 2009; Jagdheesh et al., 2016; Kubiak and Mathia, 2014). To measure the contact angle hysteresis, two methods are usually used (see Fig. 32). For example, the "tilted plate" method requires first, the deposition of a sessile drop on the levelled surface and then, the controlled rotation of the surface (Macdougall and Ockrent, 1942). Tilting the surface induces a deformation of the drop and the contact angles of both sides of the drop have to be monitored. When the liquid drop is just about to start sliding or rolling, at an inclination α (the tilting angle), the difference between the two contact angles, θ_{max} and θ_{min}, is considered to be the contact angle hysteresis. The elliptical distorsion and asymmetry of such method on the contact angle hysteresis have been discussed (Extrand and Kumagai, 1995). Note that when the tilting angle is reached, the liquid drop can either start to slide (in mixed or full Wenzel regime) or to roll (in mixed or CB state).

A second common procedure to measure the contact angle hysteresis, called the needle-in-drop experiment, requires the dynamic variation of the volume of the drop and the monitoring of quasi-static contact angles (Yuan and Lee, 2013). By expanding and contracting the liquid, the advancing and receding contact angles, θ_{adv} and θ_{rec} respectively, can be monitored. Using the needle-in-drop method, the contact angle hysteresis is the difference between the advancing and receding contact angles. To have reliable results, specific test conditions were elaborated, in term

of volume of liquid and number of expanding/contracting cycles (Korhonen et al., 2013) or distortion-free measurements (Wong and Tricoli, 2018).

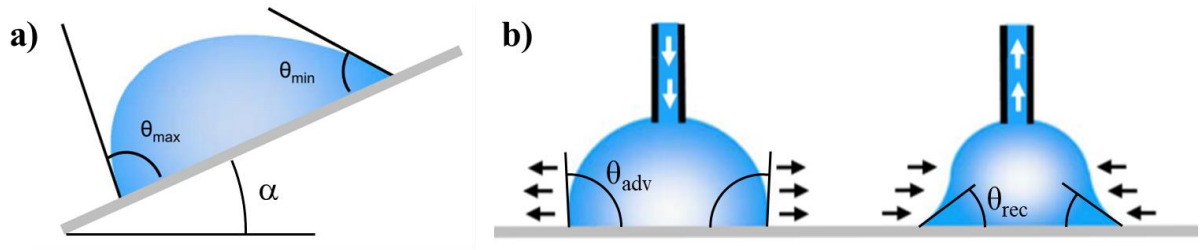

Figure 32. Illustration of the "tilted plate" and "needle-in-drop" methods, used to quantify the contact angle hysteresis. Reprinted by permission from Springer Nature: (Yuan and Lee, 2013), copyright (2013).

For certain liquid-repellent applications, such as anti-icing surfaces, it is relevant to characterize the dynamic behaviour of a drop impacting on a surface (Mishchenko et al., 2010). When a liquid drop comes in contact with a superhydrophobic surface, the sequential list of events is as follow: impact/contact, spreading, retraction, drop repulsion, bouncing/non-contact (see Fig. 33). During the bouncing test, performed by droping a given volume from a specific height, different factors can be monitored such as the bouncing height, the maximum spreading, the duration of contact or the critical drop velocity at which drop pinning occurs (Jung and Bhushan, 2008; Mishchenko et al., 2010; Bahadur et al., 2011).

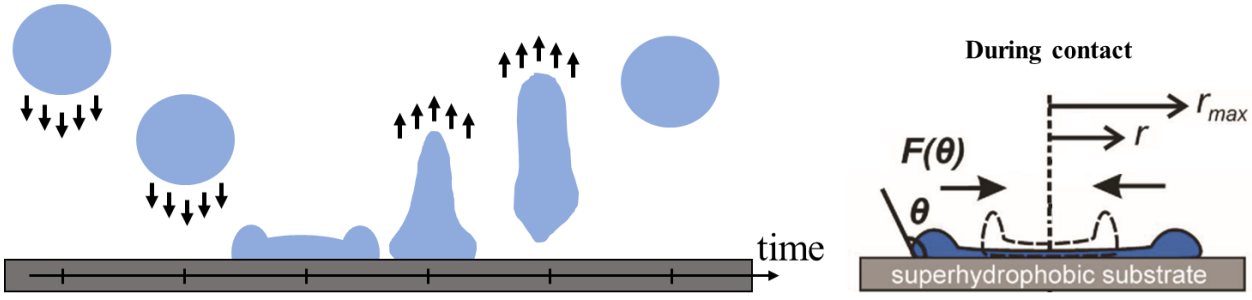

Figure 33. Illustration of the sequences during a bouncing test, with details on the maximum spreading on impact on a superhydrophobic surface. Adapted with permission from (Bahadur et al., 2011). Copyright (2011) American Chemical Society.

Moreover, the wetting of surfaces can be characterized independently of the liquid used for the experimentations, allowing a more holistic approach. The surface energy of the solid surface is quantified and, subsequently, the wetting behaviour of any liquid of known surface tension can be predicted for this surface. For example, low energy surfaces have been reported to have superomniphobic properties i.e. repelling water but also liquid with low surface tension such as oils (Dufour et al., 2011). Surface energies can be qualitatively assessed by Dyne level testing (Dyne Technology Ltd., n.d.). This method involves using liquids with known surface tensions and assessing visually the wetting or non-wetting of the liquids on the surface. In addition, the surface energy of a solid can be calculated from a set of liquids and their contact angles. Several quantitative methods exist (Krüss GmbH, 1999) based on different models, such as Zisman's one-component model (Zisman, 1964; Jie-Rong and Wakida, 1997) or the van Oss' three-component model (Van Oss et al., 1989). Another particular model is used in the Fowkes methodology, which is a two component surface energy model, dissociating the surface energy σ into a dispersive σ^D and a polar σ^P component, where $\sigma = \sigma^D + \sigma^P$ (Fowkes, 1964). It is highly relevant to quantify the polar and dispersive components of a surface, as the amount of hydrogen bonds between a water drop in contact with a surface is strongly correlated with the hydrophilic (high number of hydrogen bonds) or hydrophobic (lower amount of bonds) behavior of the surface (Good and Van Oss, 2013). The components can be calculated using the relation $\gamma_{SL} = \sigma_S + \sigma_L - 2 (\sigma^D_S + \sigma^D_L)^{1/2} - 2 (\sigma^P_S + \sigma^P_L)^{1/2}$ combined with the Young's equation (Owens and Wendt, 1969). This two-component model requires static contact angle measurements using only two liquids: water and diiodomethane. The system of equations can be solved, as diiodomethane can be considered apolar i.e. without polar component ($\sigma^P_L=0$).

2.3.2 Examples of functional applications

Many laser-fabricated surfaces successfully reproduced surface structures observed in the nature, such as the topographies from Lotus leaf and Rose petal (Long et al., 2015a), lizard skin (Hermens et al., 2017), snake skin (Greiner and Schäfer, 2015; Alamri et al., 2019b) and fish scale (Yin et al., 2016). Several bio-inspired functional properties could be enabled from surface microstructuring:

- *Self-cleaning.* The Lotus effect was reproduced on laser-textured surfaces, i.e. water drops could easily roll off the surfaces and remove dirt particles from the surface (Barberoglou et al., 2009; Jagdheesh et al., 2016; Ngo and Chun, 2017, 2018). The remaining stains after liquid evaporation (coffee-stain effect) could be reduced, too (Ta et al., 2016).

- *Condensation control*. Tailored microstructures were reported to influence the liquid condensation, in term of droplet sizes and distribution, with application for improved heat transfer performance and reduced ice nucleation (Miljkovic and Wang, 2013; Mishchenko et al., 2013).

- *Anti-icing*. Laser-fabricated surfaces exhibited beneficial anti-icing properties (Römer et al., 2009a). Superhydrophobic surfaces could prevent ice formation, by decreasing the time of contact of impacting water drops (Bahadur et al., 2011; Mishchenko et al., 2010) however could also enhance ice accretion (Y. Liu et al., 2018) and ice adhesion (Kulinich et al., 2011; Nosonovsky and Hejazi, 2012).

- *Underwater superoleophobicity*. Surfaces structures fabricated with ultrashort pulses exhibited underwater oil-repellent properties (Yong et al., 2018) with potential application to submarines (Yin et al., 2016).

- *Biology*. The cell attachment of osteoblast and fibroblast could be tailored on laser-textured titanium implants (Fadeeva et al., 2010). Furthermore, non-fouling properties i.e. bacterial repellence or retention were observed on laser-textured surfaces depending on the considered bacteria, substrate composition and surface topography (Cunha et al., 2016; Fadeeva et al., 2011; Guenther et al., 2016; Helbig et al., 2016; Rajab et al., 2017, 2018, 2019; Rosenkranz et al., 2016; Valle et al., 2015).

- *Tribology*. Laser surface texturing has been investigated from boundary to hydrodynamic lubrification regimes, providing decreased friction coefficients in some regimes, depending on the combination of materials in contact, lubrification and surface structures (Etsion, 2004, 2005; Stark et al., 2019; Bonse et al., 2018).

- *Optical properties*. Laser-textured surfaces could generate antireflection and blackening effect, by increased light absorption (Faucon et al., 2014; Ou et al., 2016; Vorobyev and Guo, 2011), but also colorization due to surface oxidation (Lu et al., 2017) or light scattering (Fraggelakis et al., 2019).

- *Anti-fingerprint*. Few research seems to be reported on this topic, but microtextured surface could inhibit the traces of fingerprint onto surfaces (Wu et al., 2011; Belhadjamor et al., 2018).

2.3.3 Limitations of laser-textured functional surfaces

2.3.3.1 Ageing of wetting properties

When metallic substrates are laser-textured, a complex mix of surface structures and surface chemistries are generated. Following the texturing process, no more topographical change takes

place, except for eventual processing debris to be removed using e.g. jet of compressed air. However, the wetting properties of laser-textured surfaces usually evolve over time. Such ageing process was demonstrated for nanosecond and femtosecond laser texturing of stainless steel (Kietzig et al., 2009; Garcia-Giron et al., 2018a). Indeed, following the laser processing, exposure to air leads to progressive oxidation of the surface. The storage conditions influence therefore such phenomenon and controlling the ambient atmosphere allows to accelerate or inhibit the ageing process (Long et al., 2015b; Kim et al., 2016b; Cardoso et al., 2017; Jagdheesh et al., 2017). For instance, long-term superhydrophilicity was demonstrated by nanosecond laser texturing in controlled atmosphere (Guan et al., 2015).

However, the changes in surface oxidation cannot explain the superhydrophilic-to-superhydrophobic transition that is observed after ageing of laser-textured metallic substrates. Indeed, metals and metal oxides have generally high surface free energies that result in a hydrophilic behavior (Drzymala, 1994). Laser-processed metallic substrates exhibit initially superhydrophilic properties, just after the laser patterning (Kietzig et al., 2009). Therefore, other effects, which have not yet been fully understood, take place during the ageing process. One main ageing mechanism identified in the literature is the spontaneous adsorption of airborne hydrocarbons i.e. organic elements from air that form a layer of nonpolar molecules on the surface (Boinovich et al., 2016; Long et al., 2015b). Other mechanisms have been considered, too, such as the partial deoxidation of the laser-induced oxides (Ta et al., 2015) or the adsorption of water molecule (Huerta-Murillo et al., 2019).

The surface chemistry reaches a superhydrophobic steady state usually after a week time but a low-temperature annealing (100-200°C) can accelerate the ageing process (Chun et al., 2016; Ngo and Chun, 2017). On the contrary, immersion of the laser-textured substrates in boiling

water could inhibit such wetting transition, leading to superhydrophilic behavior of metallic substrates (Ngo and Chun, 2018). Such organics compounds have weak bonds to the surface and can be easily cleaned away. Nevertheless, the adsorption of organic compounds could be regenerated e.g. by vacuum processing (Jagdheesh et al., 2017). The long-term stability of superhydrophobic surfaces was also investigated, up to one year after laser processing (Gregorčič et al., 2018).

2.3.3.2 Mechanical durability of textured surfaces

Another major concern of textured surfaces is their limited mechanical resistance. Indeed, any contact with the external environment, such as impact, rubbing, scratches and even finger contact, can be detrimental to the fragile surface textures and the eventual surface chemistry (Wang et al., 2017). As a result, many research has been conducted to enhance the material physico-chemical or tribo-mechanical properties (Milionis et al., 2016; Scarratt et al., 2017). In particular, additional chemical modification or etching was beneficial for the life span of superhydrophobic surfaces (She et al., 2013; Su and Yao, 2014; N. Wang et al., 2015; Wang et al., 2017). The multi-scale topographies act as protection for the nanoscale features or roughnesses or chemical coatings (Verho et al., 2011).

Similarly, for laser-textured surfaces, a chemical post-treatment or coating demonstrated more durable superhydrophobicity (Boinovich et al., 2017, 2018; Emelyanenko et al., 2015; Han et al., 2018; Tang et al., 2015). Several initial surface structures were investigated such as laser-induced roughness/porous surfaces, channel-like patterns, cross-like channels or Lotus leaf-like hierarchical peak and valleys. Recently, the surface engineering techniques were combined to

laser texturing to fabricate more durable superhydrophobic surfaces, without coatings (Garcia-Giron et al., 2018a, 2019).

Improved design of the surface topographies can enhance the mechanical stability. To that aim, the deterioration of topographies was investigated, e.g. the abrasion of recast material surrounding laser-textured microdimples (Mishra and Polycarpou, 2011). Understanding of the shear stresses on the surface structures could also improve the design of surface structures. For instance, the shape of pillar structures can be tailored, to allow bending instead of breakage (Hensel et al., 2016). Further improvements could be achieved through better design of materials, such as functionalisation via soft nanorod-polymer composites (Elliott et al., 2015). Another approach to inhibit damages to the functional surfaces is the renewal of the surface structures and/or coating upon damages. Nature is providing numerous examples of self-healing capacities and the same concepts could be applied to engineered surfaces, e.g. by encapsulation of hydrophobic agents (Li et al., 2010; Jin et al., 2013).

Chapter 3

Springtail-inspired triangular laser-induced surface textures on metals using MHz ultrashort pulses

Technical Brief, published

Romano J.-M. [(1)], Helbig R. [(2)], Fraggelakis F. [(3,4)], Garcia-Giron A. [(1)], Werner C. [(2)], Kling R. [(3)], Dimov S.S. [(1)] (2019) Springtail-inspired triangular laser-induced surface textures on metals using MHz ultrashort pulses, Journal of Micro and Nano Manufacturing, 7(2), 024504.

[(1)] Department of Mechanical Engineering, School of Engineering, University of Birmingham, B15 2TT Birmingham, United Kingdom
[(2)] Max Bergmann Center of Biomaterials, Leibniz Institute of Polymer Research, 01069 Dresden, Germany
[(3)] ALPhANOV, Technological Centre for Optics and Lasers, Optic Institute of Aquitaine, 33400 Talence, France
[(4)]CELIA, University of Bordeaux – CNRS – CEA UMR5107, 33405 Talence, France

Authors' contributions: J.-M. Romano is the first and main author of this publication. He laser-fabricated the metallic samples and imaged their structural colors and superhydrophobic properties. Dr. R. Helbig provided the specimen of springtail and Dr. F. Fraggelakis contributed with the laser texturing using MHz repetition rates. J.-M. Romano wrote the manuscript that was reviewed by A. Garcia-Giron, Dr. R. Helbig, Dr. F. Fraggelakis, and our supervisors Prof. C. Werner, Prof. R. Kling and Prof. S.S. Dimov.

Abstract

Considering the attractive surface functionalities of springtails (Collembola), an attempt at mimicking their cuticular topography on metals is proposed. An efficient single-step manufacturing process has been considered, involving Laser-Induced Periodic Surface Structures (LIPSS) generated by near-infrared femtosecond laser pulses. By investigating the influence of number of pulses and pulse fluence, extraordinarily uniform triangular structures were fabricated on stainless steel and titanium alloy surfaces, resembling the primary comb-like surface structure of springtails. The laser-textured metallic surfaces exhibited hydrophobic properties and light scattering effects that were considered in this research as a potential in-line process monitoring solution. The possibilities to increase the processing throughput by employing high repetition rates in the MHz-range are also investigated.

3.1 Introduction

Nature offers numerous inspirations for the manufacturing of smart surfaces. Springtails are good examples, as their cuticle are made of complex topographies with superior omniphobic and anti-adhesive surface functionalities (Hensel et al., 2016; Helbig et al., 2011). Especially, cuticles with hierarchical alignment of two to three levels are observed (Nickerl et al., 2013):

a) bristle-like or hairy (tertiary) structures with length of some tens of microns;
b) a micron-scaled papillose (secondary) structure, which is not present on all species;
c) a submicron-scaled alignment of small granules with interconnecting ridges (called primary structure).

Recently, laser micro manufacturing has reached a new milestone, enabling the controlled generation of highly regular Laser-Induced Periodic Surface Structures (LIPSS) on metals (Gnilitskyi et al., 2017) and hexagonally-aligned submicron triangular features could be fabricated (Romano et al., 2018a). Such surface structures resembles the hexagonal comb-like pattern (see Fig. 34) observed on the submicron level of half of evaluated springtail species (Nickerl et al., 2013). LIPSS exhibit promising self-cleaning and decorative properties (Vorobyev and Guo, 2015) and triangular LIPSS could therefore contribute to the transfer of some springtail surface properties onto manmade surfaces.

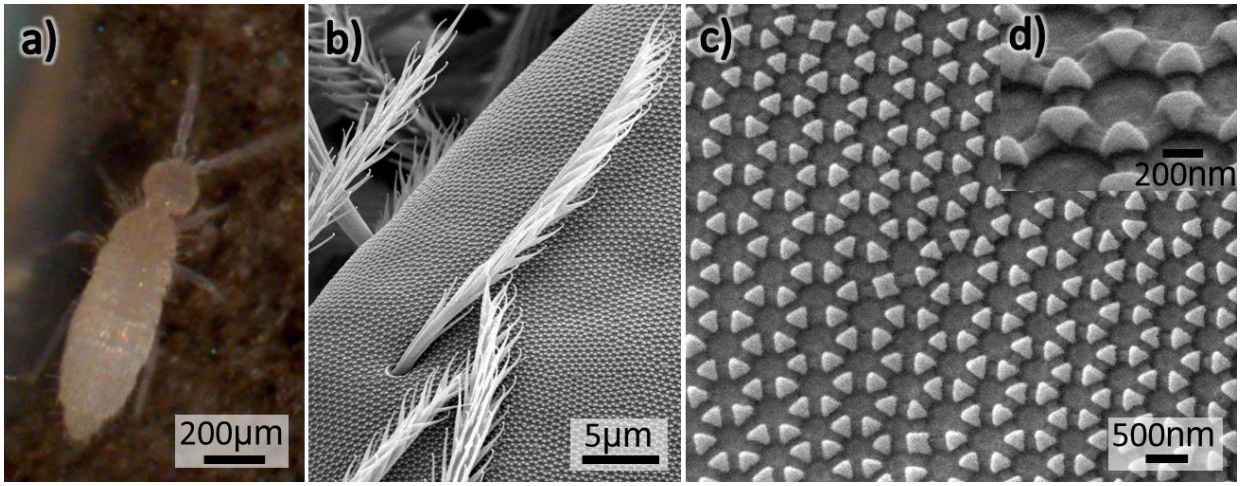

Figure 34. Springtail: specimen of *Sinella tenebricosa* (a) with micro- (b) and submicro-scale (c) close up. Tilted view of a hexagonal arrangement of granules and ridges (d).

While LIPSS have a self-organizing nature, a plethora of morphologies can be generated. In particular, the so-called low-spatial frequency LIPSS (LSFL) are a type of LIPSS that are usually quasi-periodic in the shape of wavy ripples, nanogratings or nanobubbles. Their generation can be tailored depending on irradiated materials, laser wavelength, beam polarization, fluence and number of pulses (Graf and Muller, 2015). More complex LIPSS morphologies, such as diamond-shaped LSFL, were generated in multi-step processes requiring several cross-polarized scans of the surface (Cunha et al., 2016). Other single-scan processes, involving radial polarized

beam, dynamic rotation of the polarization or double cross-polarized pulses, could induce complex but controlled LIPSS morphologies such as rhombic shapes (Skoulas et al., 2017; Fraggelakis et al., 2019).

To enable scale up manufacture of triangular LIPSS, several aspects should be addressed, such as high processing time and the development of in-line monitoring solutions. In this research, a conventional circular-polarized beam delivery set-up is used in a single raster scan mode to investigate their generation on stainless steel and titanium samples. Near-infrared femtosecond laser pulses with Gaussian-shaped intensity with high repetition rates in the MHz range are used to generate uniform springtail-inspired triangular LIPSS over large areas. Surface functionalities in term of wetting and light scattering, as well as its use as an in-line monitoring method, are discussed.

3.2 Experimental set-up

Stainless steel (X6Cr17, Aceros Bergara, Sant Just Desvern, Spain) and Titanium alloy (Ti-6Al-4V, VSMPO, Verkhnaya Salda, Russia) in the form of 0.7 mm- and 2 mm-thick plates and as-received roughness of 35 nm and 450 nm, respectively, are used in this research. The metallic substrates are processed using ultrashort laser pulses with 1032 nm central wavelength (λ) and 310 fs pulse duration (Satsuma, Amplitude Systemes, Pessac, France). The beam was right-hand circularly polarized and deflected over the surface at normal incidence (RhoTor RTA, Newson NV, Derndermonde, Belgium). The spot diameter ($2\omega_0$) is estimated experimentally to be 30 μm at $1/e^2$. The experimental set-up and raster scan strategy are depicted in Figure 35, where the pulse-to-pulse distance (d) equals the scanning speed (v) over the pulse repetition rate (f).

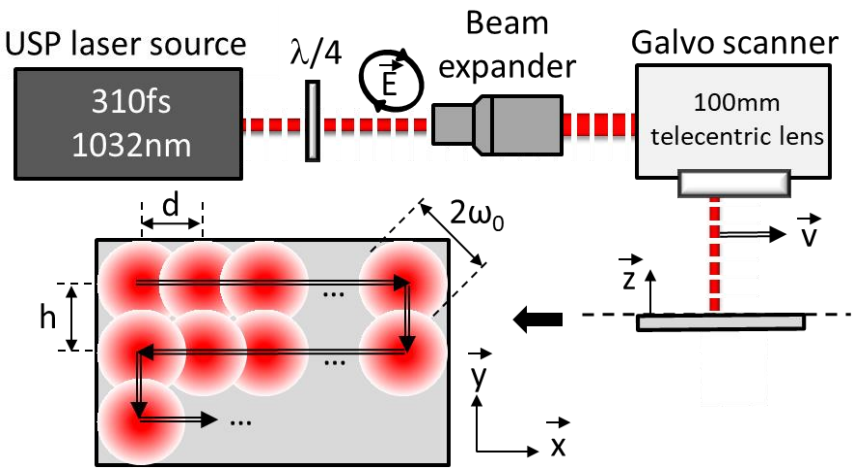

Figure 35. Beam line components and raster scan strategy.

The following results are based on a preliminary study where a single raster scan was used to generate triangular LIPSS on steel surfaces (Romano et al., 2018a). Uniform triangles were obtained over relatively large area by varying the fluence per pulse (φ_0) and the number of pulses (N). By estimating the effective number of pulses per unit area (as in Eq. 3.1), an accumulated fluence (φ) can also be calculated (see Eq. 3.2). The processing parameters used in the investigation are listed in Table 3.

$$N = \pi\, \omega_0^2 / (d\, h) \tag{3.1}$$

$$\varphi = N\, \varphi_0 = N\, P / (f\, \pi\, \omega_0^2) \tag{3.2}$$

Table 3. Laser processing parameters.

Parameters	**Units**	**Value**	
		min	**max**
Repetition rate (f)	MHz	0.25	2
Power (P)	W	0.01	5
Pulse Energy (E)	µJ	0.05	3.50
Fluence per pulse (φ_0)	mJ/cm^2	10	500
Scanning speed (v)	m/s	0.1	5
Hatch distance (h)	µm	1	20

Laser texturing was performed in atmospheric conditions. Any processing debris were removed by using compressed air. LIPSS morphologies were inspected using optical microscope (Alicona G5) and scanning electron microscope (ESEM Philips XL-30). The LIPSS periodicities were measured on Fast Fourier Transform (FFT), performed with the Gwyddion software. Samples were stored in polyethylene bags and wetting properties were measured with 6 µl Milli-Q water on an optical tensiometer (Attension Biolin Scientific Theta T2000-Basic+).

3.3 Results

3.3.1 Fabrication of springtail-inspired LIPSS

The surface texturing in this research was specifically designed for generating uniform submicron-scale LIPSS over large areas. Therefore, a processing window with enough pulse overlap was chosen where no rim effect due to the Gaussian energy distribution could be noticed, i.e. in the present case for h and d inferior to $\omega_0/3$. Accumulated fluence above materials' damage threshold was used to generate different LIPSS morphologies by varying the fluence per pulse and the number of pulses (see Fig. 36). All generated LIPSS in this study have multi-directional spatial periodicities that are due to the used circular polarization. These LIPSS are mainly so-called low spatial frequency LIPSS, with periodicities ranging from 0.85 to 0.98 λ.

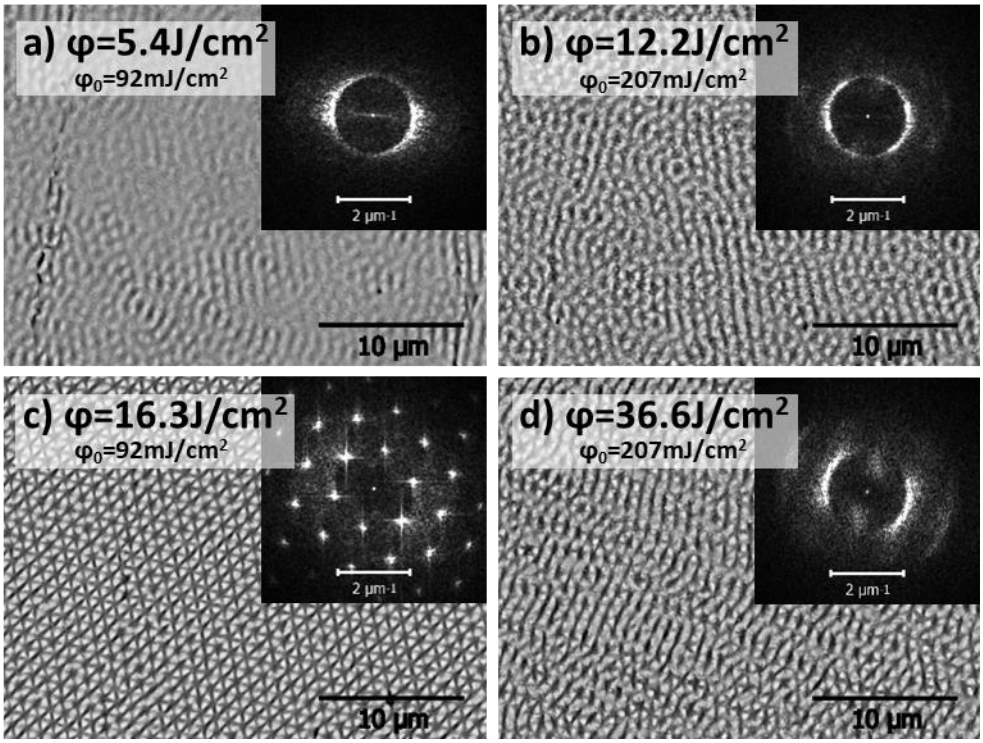

Figure 36. SEM pictures and corresponding FFTs illustrating the LIPSS evolution with fluence increase (h = 2 µm) on X6Cr17, for N = 59 (a-b) and N = 177 (c-d).

The LIPSS seem to go through sharp morphological transitions under specific irradiation conditions, containing surprisingly uniform hexagonal alignments. While the mechanisms underlying LIPSS formations are yet to be fully understood, with such concepts put forward as surface-scattered interferences (Young et al., 1983) or resonance of surface plasmon polaritons (Bonse et al., 2009), circular polarisation is the main underlining reason for creating such hexagonal alignments (Romano et al., 2018a). A cartography of the low spatial frequency LIPSS is therefore presented in Figure 37. The mapping was done by varying the fluence per pulse and the number of pulses while keeping the other parameters constant, especially the repetition rate at 250 kHz. Uniform triangular LIPSS were produced within a processing window of 118 to 353 pulses at fluences from 71 to 144 mJ/cm^2.

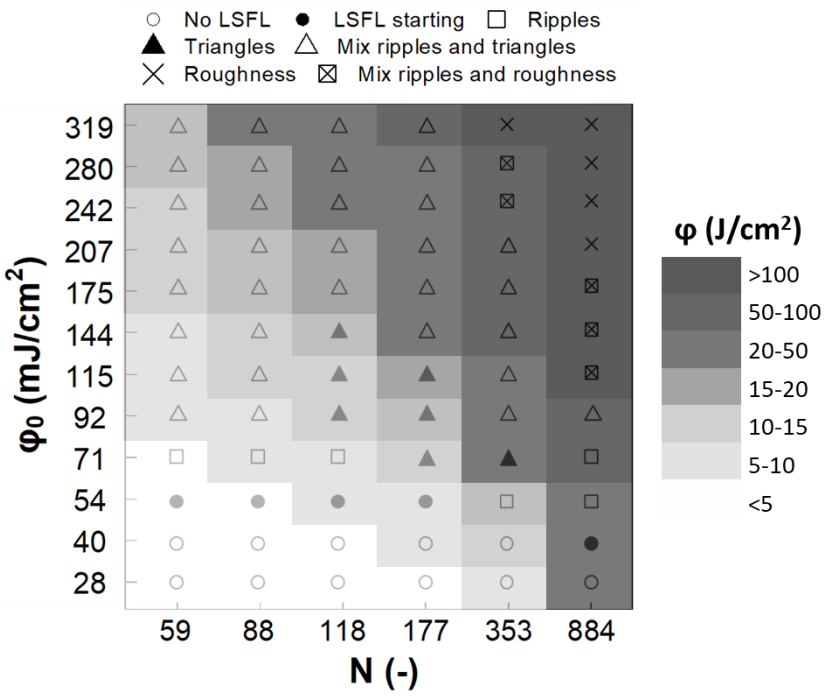

Figure 37. Evolution of LIPSS morphologies on X6Cr17 with number of pulses and fluence per pulse.

The uniformity of the surface structures was observed at different micro and sub-micron scales (see Fig. 38). The hexagonally aligned LIPSSs that were generated in the selected processing window were composed of different types of self-organised structures, as depicted in Figure 38c. For these specific processing parameters, LSFL are shaped as comb-aligned triangles with sides between 450 and 650 nm and a periodicity of 930 nm. Between the triangles, orthogonal gratings of around 80 nm periodicity could be observed. Finally, the surface was also randomly covered by nanobubbles with diameters estimated to be in the range from 40 to 150 nm. Similar triangular LIPSS were fabricated on titanium alloy substrates, which indicates that such morphologies could be achieved on other metals, too (see Fig. 39). However, the relatively rougher surface finish seems to alter the overall quality of the hexagonal arrangement.

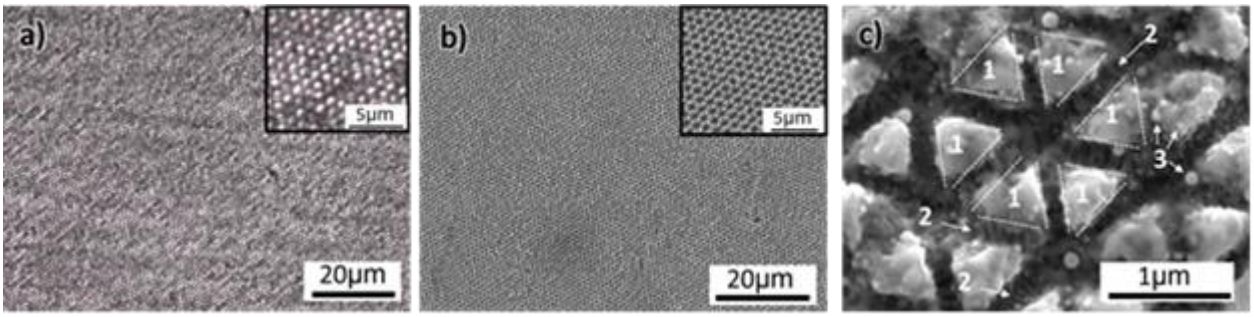

Figure 38. Optical microscope views (a) and SEM pictures (b-c) of a large-area hexagonal arrangement of triangular-LIPSS (zone 1) on X6Cr17. High spatial frequency LIPSS (zone 2) and nanobubbles (zone 3) are also highlighted.

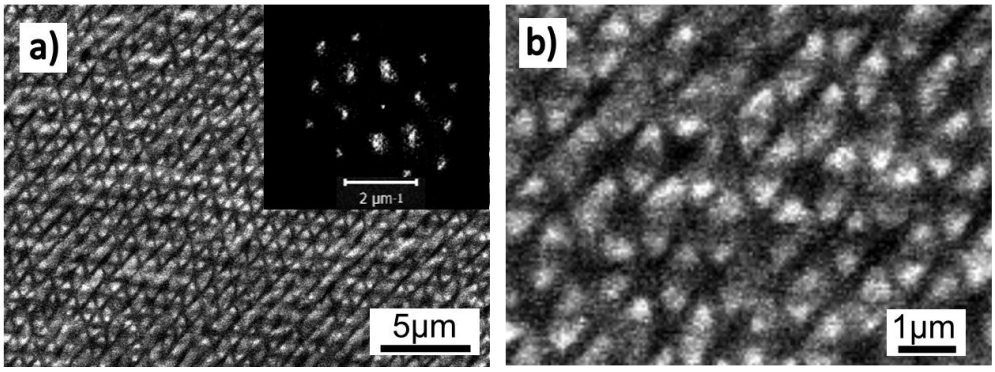

Figure 39. SEM pictures with corresponding FFT (a) and detailed view (b) of triangular LIPSS on Ti-6Al-4V (h = 2 µm, φ_0 = 54 mJ/cm^2, N = 442, φ = 23.9 J/cm^2).

The highest processing rate attained in the investigated processing window was 1.5 mm^2/s. Higher processing rates could be achieved by increasing both the beam deflection speed and the pulse repetition rate. To match the same range of pulse numbers while using velocities above 1m/s, repetition rates in the MHz regime had to be deployed. At 1 MHz, uniform triangular LIPSS were still observed, however with some distortions appearing. Up to 2 MHz it was possible to achieve relatively uniform triangular LIPSS on steel substrates. Thus, the processing rate could therefore be increased to 10 mm^2/s. Nevertheless, at such high repetition rates, a potential heat accumulation can occur (Fraggelakis et al., 2017) and this may explain partially some “melted-like” effects on the hexagons and the observed groove-like structures (see Fig. 40).

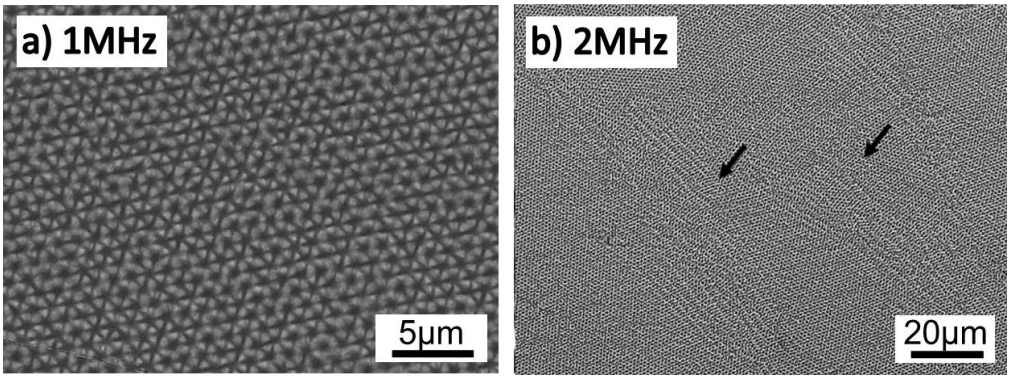

Figure 40. MHz processing of triangular LSFL on X6Cr17 at fixed h = 2 µm, φ_0 = 100 mJ/cm^2, for 118 pulses at 1 MHz (a) and 141 pulses at 2 MHz (b).

3.3.2 Surface functionalization

The uniform triangular LIPSS presented in this study could be fabricated over areas up to 40 x 40 mm^2, suggesting that the entire field of view of galvo scanners equipped with telecentric lenses could be fabricated in a single-step process. A surface of 500 mm^2 presented in Figure 41a exhibited visually uniform light scattering effect. White light was producing rainbow colours depending on the illumination and observation angles. Rhombic-shaped LIPSS were shown to produce such diffracting colours in 2 symmetric directions (Skoulas et al., 2017). In the case of submicron hexagonal arrangements, under normal illumination, light was diffracted in 6 main directions, as the Fourier Transforms (see Fig. 36c and 39a) were suggesting. Furthermore, logos of smaller dimensions could be produced with a similar structural colorization (see Fig. 41b).

The wettability of the textured metallic substrates was analysed in term of the static water contact angle. The textured samples became hydrophilic right after laser processing and the static contact angle (θ) followed a progressive grow (see Eq. 3.3) and then stabilising at a maximum value (θ_{eq}) (Kietzig et al., 2009):

$$\theta(t) = \theta_{eq} \cdot (1 - e^{-t}/\beta) \quad (3.3)$$

where β is a time constant. Both steel and titanium alloy samples exhibited similar ageing behaviours. For stainless steel, the maximum contact angle was measured at more than 155° after 7 days of storage in ambient air (Romano et al., 2018a) or after the same amount of time in plastic bags (see Fig. 41c-d). It should be noted that after ageing all LIPSS structures in this study exhibited the same isotropic superhydrophobic state with static contact angles higher than 150° and low rolling off angles (<10°).

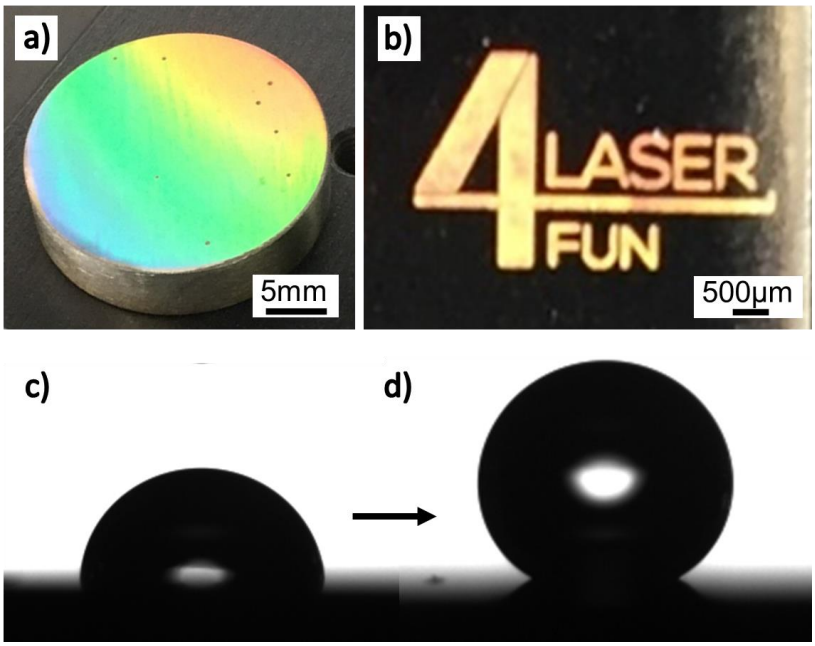

Figure 41. The uniform structural colours of triangular LIPSS over large area (a) and micro-scale logo writing (b). The contact angle of 6 µl water drops on untextured (c) compared to textured (d) X6Cr17.

The triangular LIPSS fabricated using MHz repetition rates, as described in Section 3.3.1, had similar wetting properties as those produced employing kHz processing, even on samples with non-hexagonal aligned textures. Only the optical properties were affected either because the beam dynamics were not correctly adjusted for the higher scanning speeds, or the triangular LIPSS became locally misaligned (see Fig. 42).

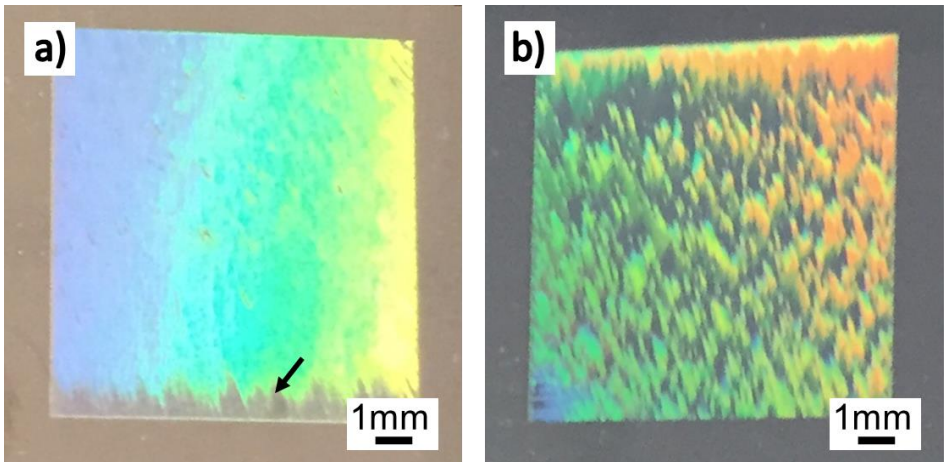

Figure 42. The visual inspection of the structural colours fabricated, at fixed φ_0 = 100 mJ/cm^2, on X6Cr17 by 118 pulses at 1 MHz, φ = 11.8 J/cm^2 (a) and 141 pulses at 2 MHz, φ = 14.1 J/cm^2 (b).

3.3.3 Comparison to the springtail cuticle

The springtails presented in the introduction (*Sinella tenebricosa*, Botanical Garden, Dresden, Germany) exhibit a hierarchical surface structure whereas the smallest structure level represents the most interesting morphological features for anti-wetting and anti-bioadhesion applications. Figure 34c illustrates these submicron-scaled structure with, in average, equilateral triangles of 265 nm side length and a comb size (i.e. spatial periodicity) of 500 nm. Using 1032 nm ultra short laser pulses, the comb-aligned triangles were two times larger than the springtail (see Section 3.3.1). Reducing the laser wavelength (Gnilitskyi et al., 2017) or preliminary surface texturing (Romano et al., 2019a) may generate smaller spatial LSFL periodicities that are closer to the springtail dimensions. Smaller dimensions are foreseen to lead to lower initial bioadhesion (Helbig et al., 2016), for instance.

Nevertheless, up-scaling the springtail comb-pattern to periodicities in the range from 850 nm to 1 µm can enable light-scattering effects that are not present on the springtail cuticles. Therefore,

tailored triangular LIPSS could find potential applications in decoration and/or anti-counterfeiting, too. In addition, potential in-line optical or scattering monitoring techniques were used for linear LSFL (Simões et al., 2018; Tian et al., 2017) and could be developed to ensure that the triangular LIPSS process is kept in control during MHz processing. Indeed, the 3 symmetrical scattering directions, as shown on the FFTs on Fig. 36c and 39a, could be easily monitored e.g. by the correct angular positioning of a collimated light source and a range of photodiode. Deviation from the 3-directional scattering profile, as seen on the FFT, would mean triangles are not anymore produced.

Finally, it is worth mentioning that the textured surfaces were not omni- or lyophobic, as it is usually the case for springtails, due to the presence of overhanging granules (Hensel et al., 2016). LIPSS, especially LSFL, are not yet known to generate such undercuts.

3.4 Conclusion

Triangular LIPSS were fabricated on metallic surfaces using circularly polarized near-infrared femtosecond laser pulses in a one-step process. The large area surface texturing with such LIPSS was investigated on stainless steel and titanium substrates by varying the number of pulses and fluence in a narrow, however repeatable, processing window. It was shown that processing rates up to 10 mm^2/s were achievable by employing a MHz laser processing. At the same time the limitations of such high dynamics processing were highlighted. The resulting triangular LIPSS resemble, to some extent, the cuticle topography of some springtails' species that incorporate twice smaller triangular hexagonally-aligned structures. Superhydrophobicity were demonstrated on laser textured metals that could be deployed for engineering easy-to-clean surfaces. Light

scattering could be useful to display structural colours and for inline monitoring of LIPSS processing.

Acknowledgments

The work was carried out within the H2020 “European ESRs Network on Short Pulsed Laser Micro/Nanostructuring of Surfaces for Improved Functional Applications” (Laser4Fun) under the ITN Marie Skłodowska-Curie grant agreement No. 675063 (www.laser4fun.eu), the H2020 FoF programme “High-Impact Injection Moulding Platform for mass-production of 3D and/or large micro-structured surfaces with Antimicrobial, Self-cleaning, Anti-scratch, Anti-squeak and Aesthetic functionalities” (HIMALAIA), and of the UKIERI DST programme “Surface functionalisation for food, packaging, and healthcare applications”.

The authors greatfully acknowledge Christoph Neinhuis for the permission of collecting specimen of *Sinella tenebricosa*, a non endangered or protected species, from the tropical greenhouse of the Dresden Botanical Garden, Germany."

Chapter 4

Triangular laser-induced submicron textures for functionalising stainless steel surfaces

Journal Paper, published

Romano J.-M. [(1)], Garcia-Giron A. [(1)], Penchev P. [(1)], Dimov S.S. [(1)] (2018) Triangular laser-induced submicron textures for functionalising stainless steel surfaces, Applied Surface Science, 440, 162–169.

[(1)] Department of Mechanical Engineering, School of Engineering, University of Birmingham, B15 2TT Birmingham, United Kingdom

Authors' contributions: J.-M. Romano is the first and main author of this publication and conceived the idea of using a circular-polarized laser beam to fabricate triangular-shaped LIPSS in a single raster scanning step. He designed the experiments, manufactured and characterised the samples' topographies and wetting properties. Dr. P. Penchev contributed with the calibration of the laser beam. A. Garcia-Giron assisted with the sample manufacturing and characterisation. J.-M. Romano wrote the manuscript that was reviewed by A. Garcia-Giron and Prof. S.S. Dimov.

Highlights

- The large area uniformity of laser-induced sub-micron features is studied.
- Triangular LIPSS are fabricated in single-pass laser texturing.
- Triangular LIPSS in hexagonal arrangement leads to multi-directional light scattering and superhydrophobicity.
- The focus offset effects on surface morphology and functionality is assessed.

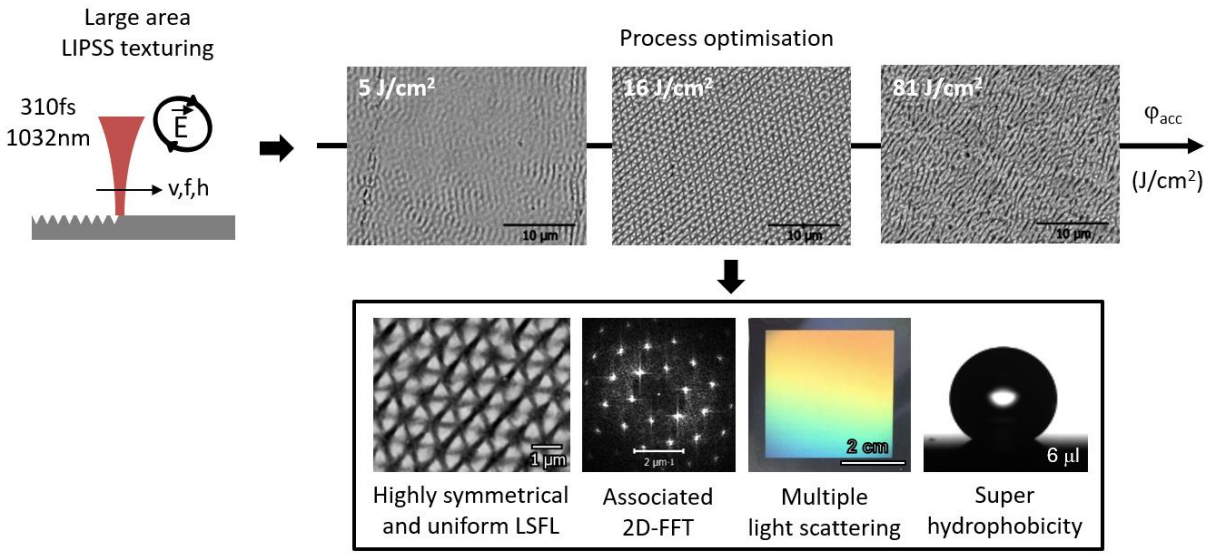

Figure 43. Graphical abstract.

Keywords: LIPSS, Femtosecond laser, Large area, Uniformity, Wettability, Light scattering.

Abstract

Processing technologies that engineer surfaces with sub-micron topographies are of a growing interest to a range of optical, hydrophobic and microbiological applications. One of the promising technologies for creating such topographies employs ultra-short laser pulses to produce laser-induced periodic surface structures (LIPSS) that often result in non-regular, quasi-periodic nanoripples and nanopillars. In this research near infrared ultra-short pulses of 310 fs with a circular polarisation was used to texture ferritic stainless steel workpieces. A single-step process was designed to generate low spatial frequency LIPSS (LSFL) over relatively large areas. Apart from highly regular and homogeneous parallel lines with approximately 900 nm periodicity extraordinarily uniform triangular-LSFL in hexagonal arrangements was created. The generation of such LSFL was found to be highly repeatable but very sensitive to the used laser processing settings. Therefore, the sensitivity of triangular-LSFL formation to the used laser processing settings, i.e. pulse to pulse distance, pulse fluence and focal plane offsets, were investigated in regard to the resulting morphologies and functional properties, i.e. structural colors and super-hydrophobicity. Finally, the capability of this technology for producing uniform triangular-shaped LSFL on relatively large surface areas of stainless steel plates was studied.

4.1 Introduction

The interest and research activities in the field of laser-induced periodic surface structures (LIPSS) have been growing in recent years due to their promising applications for surface functionalisation. In particular, such surface engineering technology has been used for decorative purposes (Dusser et al., 2010), anti-counterfeiting (Yao et al., 2012) and improved solar cell

efficiency (Nayak et al., 2011) due to the resulting structural coloring, broadband light absorption, antireflection and blackening effects. In addition, surfaces processed in this way exhibit a superhydrophobic behaviour that finds applications in self-cleaning (Vorobyev and Guo, 2015) and anti-icing (Kietzig et al., 2011b). Another area is biomedical, i.e. dental and orthopaedic implants, where LIPSS textured surfaces have been used to influence biocompatibility (Liang et al., 2012), cell proliferation (Schlie et al., 2012) and also bacterial adhesion and biofilm formation (Fadeeva et al., 2011; Cunha et al., 2016). Furthermore, LIPSS texturing of hard coatings has also been investigated for tribological applications (Bonse et al., 2017).

These applications can require surface topographies with dimensions in the sub-micron range. Therefore, ultra-short laser pulses are used to generate a plethora of low spatial frequency LIPSS (LSFL), such as nanoroughness, nanopillars and nanogratings, with periodicities much lower than the laser spot size. There are many factors affecting their generation such as irradiated material and laser wavelength (Bashir et al., 2012), beam polarisation (Graf and Muller, 2015), fluence per pulse and number of pulse (Ahmmed et al., 2015), but also the irradiation environment (Jiao et al., 2013) and irradiation angle (Wang and Guo, 2006). LSFL are usually orientated perpendicular to the incident linear polarisation and have a spatial periodicity close to the laser wavelength (Bashir et al., 2012). In the case of circular polarisation, several cases can be observed: wavy ripple-like LSFL generated at 45° orientation (Graf and Muller, 2015; Varlamova et al., 2011). With the increase of the total energy dose per unit area, referred to as accumulated fluence, early-stage LIPSS undergo a sharp change in periodicity and uniformity (Yang et al., 2012). When both peak fluence and accumulated fluence increase, more complex, hierarchical LIPSS referred to as micro-bumps can be obtained (Fraggelakis et al., 2017). Bumpy

surfaces are shown to be a consequence of heat accumulation at high average power and repetition rates (Bauer et al., 2015).

Such complex LIPSS can be generated with linear polarised femtosecond laser pulses by tailoring a compound mix of LIPSS in the sub-micron range (Ji et al., 2015). Furthermore multi-scale topographies can be obtained by using a pre-processed surface (Tsutsumi et al., 2008). The fabrication of rhombic-shaped LIPSS can be achieved using promising single-step laser processes using a dynamic rotation of polarisation (Graf and Muller, 2015) or a cylindrical vector beams generated with a radial polarisation converter (Skoulas et al., 2017). Another approach is the two-step processing employing a train of pulses or multiple passes with varying relative orientation of the scans in regard to the polarisation direction that lead to square- or diamond-shaped LIPSS. Superimposition of LIPSS can occur with significantly less fluence per pulse than that used in the initial pulses (Cunha et al., 2016; Dar et al., 2017; Gregorčič et al., 2016).

The texturing of larger surfaces with such self-organised quasi-periodic nanofeatures is essential to broaden the use of this technology for surface functionalisation in a number of promising application areas. Such large-area texturing has been investigated by employing different processing strategies, e.g. the use of moving discrete spot laser irradiation to merge LIPSS (Lehr and Kietzig, 2014; Reif et al., 2015) or through pulse overlapping (Ardron et al., 2014; Cruz et al., 2014; Fraggelakis et al., 2017; Gemini et al., 2017; Mincuzzi et al., 2016). High repetition rates combined with high scanning speed, in the order of MHz and m/s respectively, has also been shown to enable area processing with sufficient pulse fluence and pulse overlap to generate uniform LIPSS in one pass; the uniformity being then obtained by optimising the distance between scanned lines (Cruz et al., 2014). However, potential local non-uniformities of LIPSS

are known to occur as a result of preceding polishing step (Ardron et al., 2014; Preusch et al., 2016), grain boundaries (Römer et al., 2009b) and surface defects (Ardron et al., 2014). Uniformity of LIPSS generation can potentially be improved using pre-processed gratings (Huang et al., 2009; Tsutsumi et al., 2008).

In this paper, the LIPSS generation on stainless steel plates in ambient air is presented. A single-step femtosecond laser process (one pass) is investigated using high scanning speed and pulse frequency, up to 1 m/s and 500 kHz, respectively, to enable high-throughput processing. The generation of uniform large-area LIPSS with Gaussian intensity laser beam is studied. In addition to wavy and relatively disorganised LSFL reported in literature (Graf and Muller, 2015; Skoulas et al., 2017; Varlamova et al., 2011), this research presents a single-step texturing with highly regular linear-LSFL and triangular-like LSFL in hexagonal arrangements employing a conventional beam delivery set-up with circular polarisation. The functional properties of processed surfaces in terms of light scattering and wettability are also investigated together with process robustness, in particular the sensitivity of the texturing process to variations in the focal position.

4.2 Material and methods

Commercially available X6Cr17 ferritic stainless steel plates with 0.7 mm thickness and average roughness of R_a = 35 nm are used in this research.

The texturing was performed using a femtosecond laser source (Satsuma from Amplitude Systemes) with the following technical characteristics, a central wavelength, λ, of 1032 nm,

310 fs pulse duration, a maximum pulse repetition rate of 500 kHz and 5 W average power. The beam line incorporates a beam expander and a quarter waveplate to convert the s-type linear polarisation of the laser source into a circular one. A galvo scan head (RhoThor RTA) equipped with a 100-mm focal length telecentric lens is used to deflect the laser beam over the surface. The spot diameter $2\,\omega_0$ at $1/e^2$ is 30 μm.

Initially, the field textured were limited to $3 \times 3\ mm^2$ in order to study the LSFL generation. Then, larger areas up to $40 \times 40\ mm^2$ were processed without stitching in order to investigate the surface wettability and optical properties. The theoretical depth of focus is 1.1 mm, in particular twice the Rayleigh length $Z_R = \pi\,\omega_0^2 / (\lambda\,M^2)$, where M^2 is better than 1.2 for the used laser source.

The samples were positioned normal to the incident beam and fixed onto a 5-axis motorised stage that allows three linear and two angular movements. All texturing trials were performed in atmospheric conditions.

The textured areas were processed line by line, using a bidirectional raster scanning strategy (see Fig. 44). The distance between scan lines is defined as hatch distance, h, ranging from 1 μm to 10 μm. The scanning is executed with a variable velocity, v, from 100 mm/s to 1500 mm/s and pulse repetition rates, f, from 50 kHz to 500 kHz. The distance between two consecutive spot centres is therefore given by:

$$d = v / f \qquad (4.1)$$

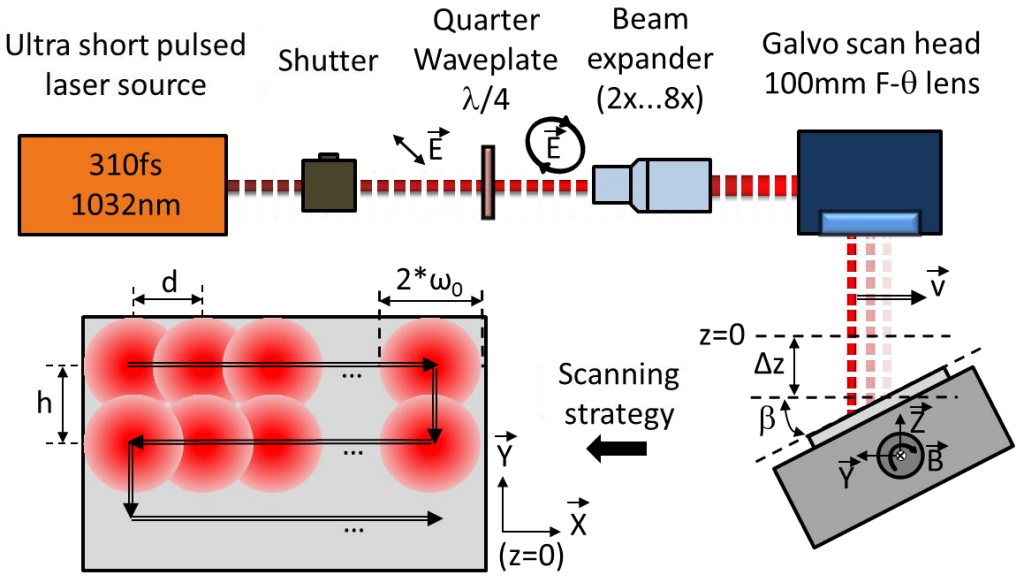

Figure 44. Beam line components and scanning strategy.

The effective number of pulses per beam spot is calculated by $2\omega_0/d$ while the effective number of pulses per unit area, N, is:

$$N = \pi \omega_0^2/(d\ h) \quad (4.2)$$

The overlap, O, between two consecutive circular pulses can be approximated by the geometrical equation (Cardoso et al., 2017):

$$O = (\pi \omega_0)^{-1} \{2 \omega_0 \cos^{-1}[d / (2 \omega_0)] - d (1 - [d / (2\omega_0)]^2)^{1/2} \} \quad (4.3)$$

Surfaces were textured with varying average power, P, and pulse repetition rates, f, and thus the pulse fluence could be calculated as $\varphi_0 = P / (\pi \omega_0^2 f)$ $\varphi_0 = P/(\pi\omega_0{}^2 f)$. The effective accumulated fluence per unit area, φ, can then be approximated as follows:

$$\varphi = N \varphi_0 = P / (f\ d\ h) \quad (4.4)$$

The sub-micron textures of processed surfaces were analysed using a tabletop scanning electron microscope (SEM) (Hitachi TEM3030Plus).

The wetting properties were characterised using the sessile droplet method employing Attension Theta Optical Tensiometer. In particular, Milli-Q waterdrops of 6 µl were dispensed under atmospheric conditions onto the textured surfaces and the average value of the static contact angle (CA) was obtained after stabilisation. No chemical product was used to clean the laser processed samples and any debris were removed by using compressed air.

4.3 Results and discussion

4.3.1 Process optimisation for uniform Low Spatial Frequency LIPSS

The first part of the research reported in this paper was focused on optimising a single pass laser process for texturing large areas with low spatial frequency LIPSS (LSFL) that are referred to as LIPSS from this point on in the paper. As typically these types of self-organised structures occur below and around the ablation threshold, the first objective was to find the LIPSS threshold. This was achieved by adjusting the pulse energy while keeping the other processing parameters constant, i.e. scanning speed of 500 mm/s and pulse repetition rate of 250 kHz. The scanning strategy to achieve a high overlap was initially used to minimise the rim effect of the Gaussian intensity beam as illustrated in (Tan and Venkatakrishnan, 2006). In particular, the pulse to pulse distance was the same over the surface ($d = h = 2\ \mu m$, $N = 177$, $O = 92\ \%$) and the LIPSS threshold was found to be at $\varphi_0 = 28\ mJ/cm^2$. By increasing fluence and varying the scanning

speed various types of surface structures were produced. Typical micrographs illustrating the evolution of LIPSS are shown in Figure 45. The first stage of LIPSS induced by the circularly polarised beam were observed at low levels of accumulated fluence, i.e. around 5 J/cm^2 (see Fig. 45a) corresponding to 0.65 μJ pulses at 1500 mm/s. The periodicity, Λ, given by the 2D-FFT laid below the laser wavelength, i.e. at around 800 to 900 nm. The quasi circular Fourier Transform confirmed the LIPSS morphology with no specific periodic direction.

By varying pulse energy and scanning speed, and hence the pulse-to-pulse distance, intermediate stages of LIPSS were observed progressively where the ripples were self-organised in a very consistent and uniform manner (see Fig. 45c). In particular, the resulting LIPSS morphology looked like triangles where the ripples were divided in triangular-like sub-sections. A long-range hexagonal arrangement is indicated by the 2D-FFT that depicts distinctly 3 directions of periodicity with an angular shift of around 60°.

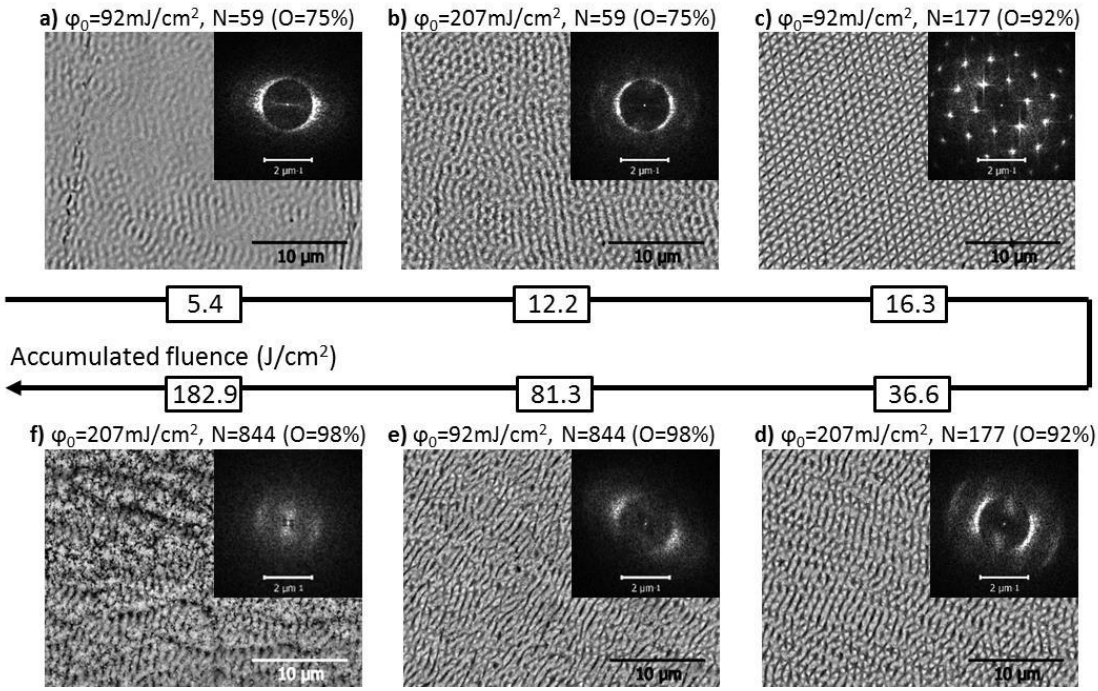

Figure 45. The LIPSS evolution with the increase of accumulated fluence with 250 kHz and 2 µm hatching settings.

The increase of accumulated fluence at the early stages led to the formation of LIPSS with more defined ripples with the same range of periodicity (see Fig. 45a-b). However, the highly uniform triangular-LIPSS are continuously erased at the later stages of their evolution. In particular, the merger of triangular-LIPSS into ripples was observed that led to a mix of triangles and ripples. 2D-FFTs of LIPSS shown in Figures 45d-e indicate a continuous alignment into ripple-like LIPSS. At higher accumulated fluence, sub-micron roughness can be observed on ripples (see Fig. 45e) until covering all LIPSS (see Fig. 45f).

By varying the fluence per pulse and scanning speed while keeping the other parameters constant, a cartography of the LIPSS morphologies was drawn as shown in Figure 46. The processing window for generating uniform triangular-LIPSS was identified, especially pulse

fluence from 71 to 144 mJ/cm^2 and 118 to 353 pulses were used to achieve an accumulated fluence in the range from 10.8 to 25.2 J/cm^2.

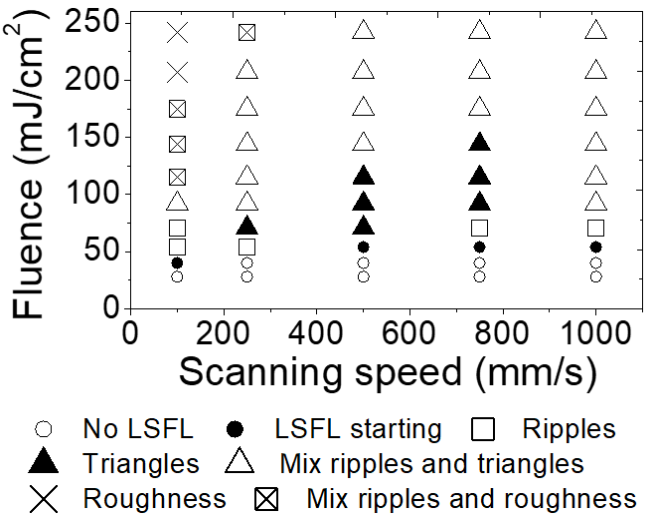

Figure 46. LIPSS morphologies as a function of scanning speed and pulse fluence with 250 kHz and 2 μm hatching settings.

A thorough analysis of the LIPSS periodicity and orientation was carried out by varying the pulse fluence while frequency, scanning speed and hatching distance were fixed at 250 kHz, 500 mm/s and 2 μm, respectively. The LIPSS periodicities vary between 0.84 and 0.98 μm but remain below 1.03 μm, the laser wavelength, as depicted in Figure 47a. At φ_0 = 54 mJ/cm^2, the ripple-like LIPSS have a periodicity (Λ) of 0.85 μm and an orientation (α) of -15°. With pulse fluence in the range from 71 to 91 mJ/cm^2 triangular-LIPSS are generated with multi-directional periodicities, ranging from 0.90 to 0.98 μm. Wavy ripple-like LIPSS with 0.85 μm periodicity are observed at higher pulse fluence. Variations of pulse fluence seem to influence the triangular-LIPSS formation. In particular, when φ_0 increased from 71 to 92 mJ/cm^2, the overall hexagonal orientation (α_1, α_2, α_3) underwent a general shift of 6° clockwise and the third periodicity Λ_3 decreased from 0.98 to 0.93 μm. Figure 47b provides more details about the measurements of Λ and α in the carried out FFT analysis. The orientations, α, of the triangular-LIPSS showed a

surprising consistency compared to the other LIPSS morphologies, especially the α spread was from +/- 1° to 4° compared to +/- 17° and +/- 38° at 54 and 207 mJ/cm^2, respectively.

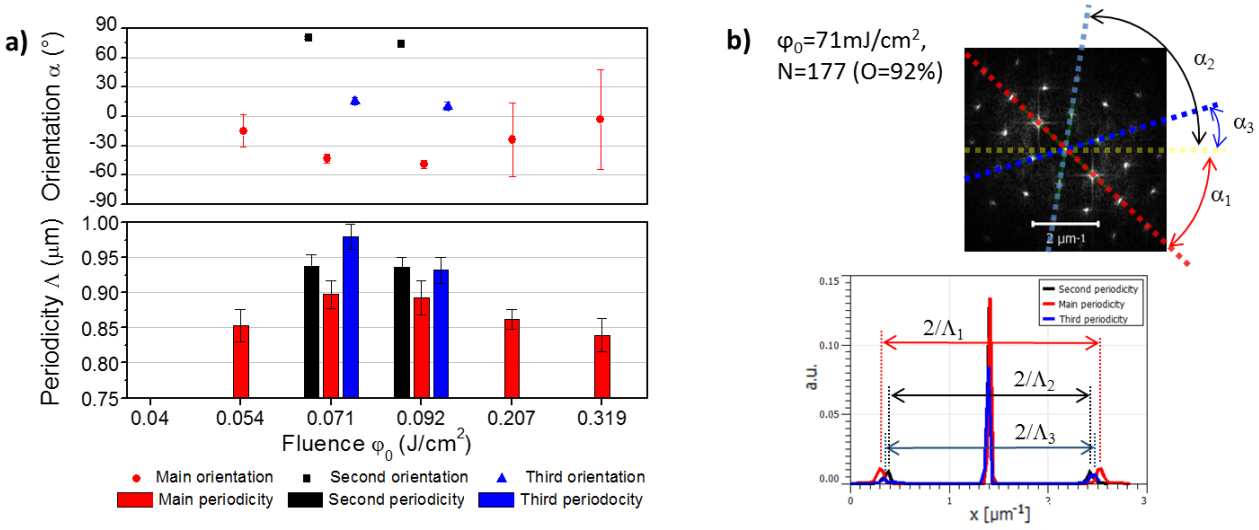

Figure 47. Evolution of LIPSS periodicity and orientation with the pulse fluence with 250 kHz, 500 mm/s and 2 μm hatch (a). Example of 2D-FFT analysis in the case of φ_0 = 71 mJ/cm^2 (b).

The second part of the research investigated the influence of other processing parameters. In particular, experiments were performed for each parameter separately while the average power and the scanning speed were kept constant in order to find the optimum process settings and also to study their effects on LIPSS texturing.

The influence of hatch distance when varied in the range from between 1 to 20 μm was investigated. The surface was not entirely covered with LIPSS when hatching of 10 μm and higher were used and only early stage LIPSS with periodicity of 0.94 μm at - 17° appeared in the centre of the laser track. At the same time 2 distinct ripple directions were observed when the hatch distance was decreased to bring the LIPSS textured laser track together, and a periodicity of 0.92 μm at - 53° was mixed with the periodicity resulting at higher spacing (see Fig. 48a). At 3 μm hatching, 3 more periodicities were added to the 2 earlier ones, i.e. 0.98 μm / 6°,

1.50 μm / 57° and 0.97 μm / 71°, and LIPSS with triangular shapes began to appear but without a clear homogeneity (see Fig. 48b). At h = 2 μm (0.87 μm / - 47°, 0.97 μm / 11°, 0.93 μm / 77°) the triangular-LIPSS were very uniform as stated earlier while a further decrease of hatch distance led to a disappearance of uniformity and only the main periodicity at - 42° remained (see Fig. 48c). Based on this empirical analysis a hypothesis could be drawn on the triangular-LIPSS formation mechanism, in particular the triangles would appear in the transition phase between early linear-LIPSS oriented at - 17° and later LIPSS at - 42°, where sufficient accumulated fluence leads to a separation of the ripple-like LIPSS into triangles.

The variation of pulse repetition rates, i.e. the use of 10, 50, 100, 250 and 500 kHz, didn't allow the triangular-LIPSS to be retained and this could be attributed to some significant changes both in pulse energy and pulse-to-pulse distance. In addition, no surface damage was detected at 10 kHz while early-stage ripple-like LIPSS of single periodicity of 0.92 μm at -17° were observed at 50 kHz (see Fig. 48d). The process settings at f = 100 kHz (N = 71, φ_0 = 68 mJ/cm^2) resulted in highly uniform and regular linear-LIPSS with periodicity of 0.90 μm and orientation at 40° (see Fig. 48e). While process settings in Figure 45b are similar to those in Figure 48e, φ of 12.2 and 12.6 J/cm^2, respectively, LIPSS morphologies differs, especially resulting in uneven ripples and aligned ripples with a spatial periodicity of Λ = 0.90 μm, correspondingly. This effect may be due to different time delays in delivering trains of pulses (Barberoglou et al., 2013) and to different pulse-to-pulse distance (Yao et al., 2012). The LIPSS in Figure 48e was used to compare the surface functionalities of linear- and triangular-LIPSS in this research. A further increase of pulse repetition rate led to the loss of straight lines uniformity and the generation of ripple-like LIPSS (see Fig. 48f).

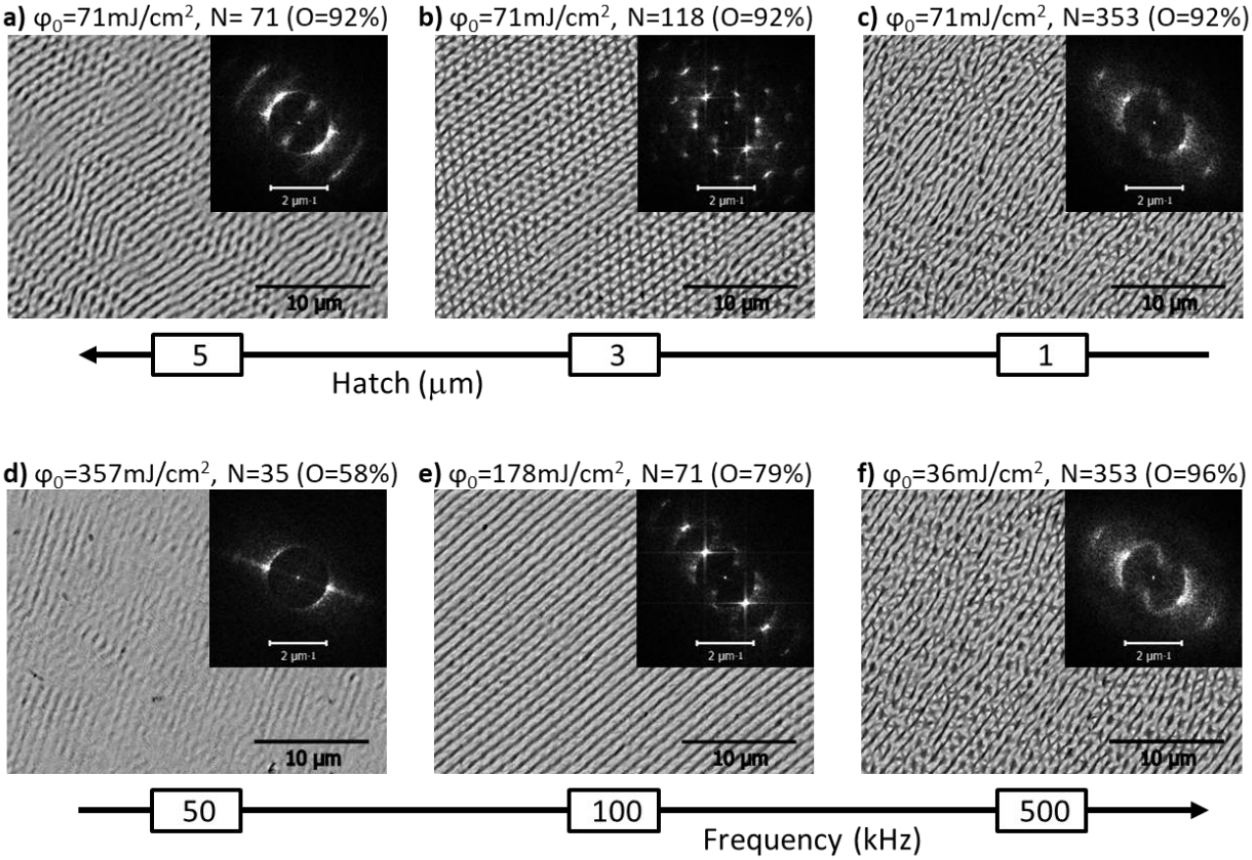

Figure 48. The LIPSS evolution: (a-c) with the decrease of hatching distance with fixed pulse frequency of 250 kHz, scanning speed of 500 mm/s and pulse fluence of 71 mJ/cm^2; and (d-f) with the increase of pulse repetition rate at fixed φ of 12.6 J/cm^2.

The influence of scan repetitions over the processed area was analysed by increasing them from 1 to 10 while using the following process settings: $\varphi_0 = 92$ mJ/cm^2 and N = 177. A clearly defined hexagonal 2D-FFT signifying a uniform triangular arrangement of LIPSS was obtained after the first scan only and then disappeared after the second one (see Fig. 49a-c). In particular, the main periodicity decreased from $\Lambda \sim 0.87$ to 0.74 µm while the orientation shifted from $\alpha \sim$ -46° to ~ -26°. An additional test was performed at a lower fluence per pulse ($\varphi_0 = 54$ mJ/cm^2), just above the LIPSS threshold, where LIPSS appeared only on some very localised surface defects but it was not possible to texture the whole area that was scanned (see Fig. 49d). The increase in scan numbers led to ripple-like LIPSS texturing, with a decrease in the periodicity

without changing significantly the periodicity orientation (see Fig. 49e-f). Figures 49a and 49e depict that the use of similar accumulated fluence (respectively 16 and 19 J/cm^2) but with different pulse fluence and number of pulses can result in different LIPSS, i.e. triangular- and ripple-like LIPSS, respectively.

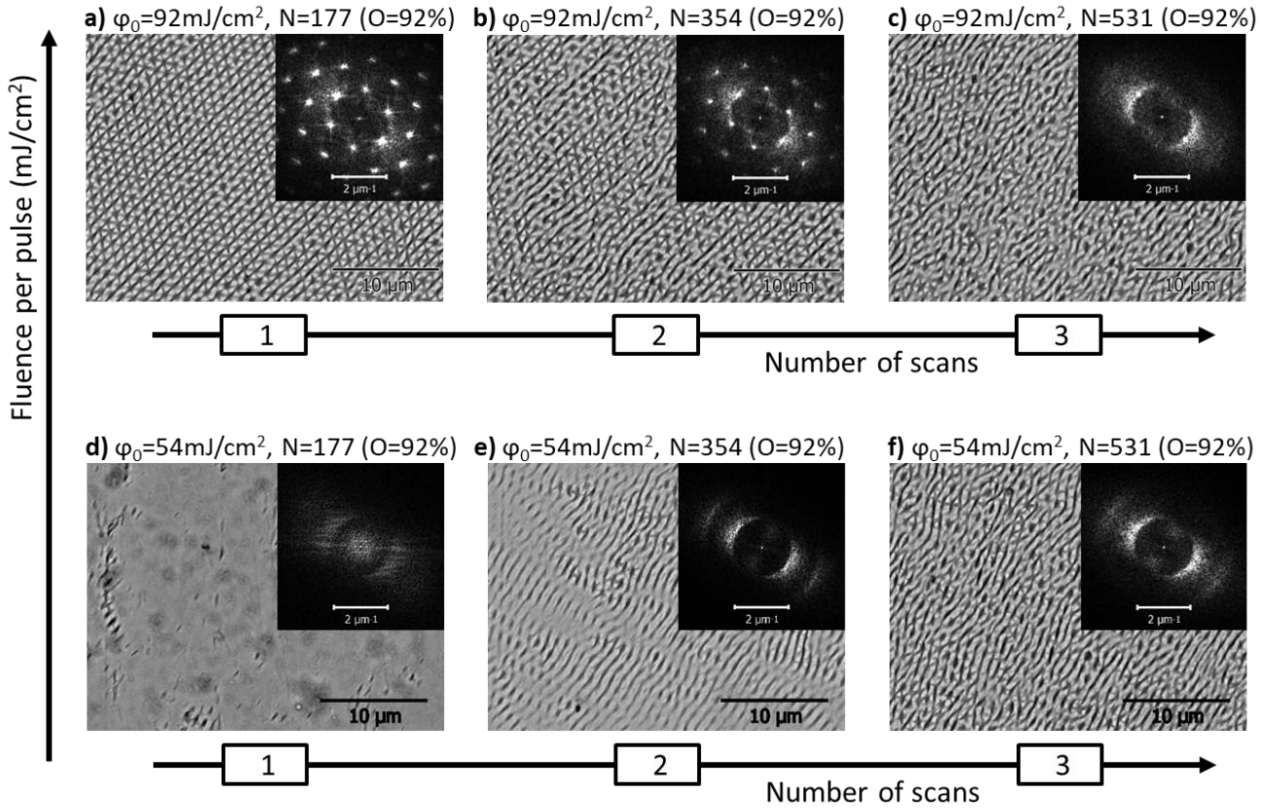

Figure 49. The LIPSS evolution with the scan number increase: (a-c) φ_0 of 92 mJ/cm^2; (d-f) φ_0 of 54 mJ/cm^2.

4.3.2 Formation of LIPSS in hexagonal arrangements

There is still no consensus on the mechanism of quasi-periodic ripples-like LIPSS formation. LIPSS induced with linear polarisation has been widely considered to result from the interference of incident laser beams with surface-scattered waves generated by rough surfaces (Young et al.,

1983). The excitation and resonance of surface plasmon polaritons (Bonse et al., 2009) might also play a significant role in the LIPSS generation.

Hexagonal self-organisation of nanoparticles was observed by irradiating TiO_2 thin films and silver nanoparticles with green CW circularly polarised light (Baraldi et al., 2017). It is suggested that the mesoporous characteristic of TiO_2 facilitates the movement of nanoparticles. The migration of nanoparticles may be the result of the same phenomena as that observed in this research. In particular, the scanning of substrates with circularly polarised laser beams can generate hexagonal-shaped arrangements in specific conditions. The symmetries induced by such hexagonal arrangements may then lead to triangular-shaped LIPSS formation.

As LIPSS are evolving with the increase of pulse numbers, simulation of the electric field distribution after linearly polarised irradiation onto submicron grooves, representing early stage linear-LIPSS, was investigated by several researchers (Hou et al., 2011; Ji et al., 2015). Ji et al. used a linearly polarised femtosecond laser to fabricate a complex mix of cross-periodic LIPSS on Si substrates. It was experimentally demonstrated that the first pulses generated typical linear-LIPSS but with the increase of pulse numbers a perpendicular sub-division of LIPSS occurred while the periodicity was similar. The simulation the electric field distribution after irradiation of linear-LIPSS suggested that the phenomena could be attributed to local maxima in the electric field distribution inside their grooves (Ji et al., 2015). However, Hou et al. reported a parallel subdivision of LIPSS that decreased the LIPSS periodicity by half. This experimental observation was confirmed by referring to the surface-scattered wave theory and simulating the electric filed distribution after irradiation and reflection from linear-LIPSS grooves (Hou et al., 2011). Similar to what was observed and simulated with linearly polarised irradiation, circular

polarisation could lead to a more complex sub-division of LIPSS. Thus, a simulation of circularly polarised beam irradiation onto early-stage LIPSS may provide some insights into the complex maxima patterns of the electric field distribution and potentially to explain the hexagonal arrangement of triangular-LIPSS.

Another aspect to consider in regard to the triangular-LIPSS formation that can affect the process repeatability is the potential misalignment of the quarter waveplate. As reported by Varlamova et al., a slight misalignment can lead to elliptical polarisation instead of a circular one and this may have a significant impact on the LIPSS generation and may lead to different LIPSS morphologies (Varlamova et al., 2007). In this work, a slight shift of the linear-LIPSS arrangements was observed during the early-stage LIPSS generation and also in the evolution of the triangular-LIPSS. However, the mechanism driving the LIPSS hexagonal arrangement has to be investigated further in both empirical and theoretical studies.

4.3.3 Surface functionality

Surface functionalities of two LIPSS types were analysed in this research, i.e. triangular- and linear-like LIPSS depicted in Figures 46b and 48e, respectively. The wettability of a representative 16 mm^2 area was measured after stabilisation of the water drop on the textured surface. Following the laser texturing, the samples exhibited superhydrophilic behaviour, which lasted approximately 1-2 days while the samples were store in ambient conditions, and then they became gradually superhydrophobic and reached a steady state after one week. Starting with a static contact angle of 96.0° +/- 3.5° prior to laser texturing, values of 145.7° +/- 0.8° and 157.1° +/- 1.6° were achieved for linear- and triangular-LIPSS, respectively (see Fig. 50a-b at

$\Delta z = 0$). The time dependent wettability of femtosecond LIPSS was reported by research groups (Gemini et al., 2017; Kietzig et al., 2009; Skoulas et al., 2017; Zhang et al., 2016), however the phenomenon remains largely not fully understood. Modification of surface chemistry together with activation and adsorption of hydrocarbon molecules by the resulting organic layer could explain this phenomenon (Gemini et al., 2017; Kietzig et al., 2009; Yasumaru et al., 2017). The storage condition of the laser-textured samples also plays an important role in the aging process (Cardoso et al., 2017).

While both LIPSS morphologies had a similar hydrophobic behaviour, the hexagonal arrangement of triangular LIPSS may benefit from its more complex morphologies, the multiple axis of symmetry and well-defined uniformity in different ways. The wetting behaviour of ripple-like LIPSS have been reported to show an anisotropic behaviour, where the water drop tends to elongate itself in the LIPSS direction (Cunha et al., 2013). While no water drop elongation has been observed in the present work, the three axes of symmetry of the triangular-LIPSS may minimise any anisotropic effect and also may lead to a multi-directional self-cleaning functionalisation.

The optical properties of both LIPSS morphologies were investigated, too, using a single white LED light source. The light scattering was observed for different combinations of light incident and observation angles. While such structural colors are widely reported to be dependent on the orientation of linear-LIPSS or on more randomly distributed ripples-like LIPSS (Dusser et al., 2010; Yao et al., 2012) or rhombic-shaped LIPSS (Skoulas et al., 2017), the multiple axes of symmetry of the triangular-LIPSS may exhibit structural colors in multiple directions and further

research is currently ongoing to investigate potential applications of this technology in decoration and anti-counterfeiting.

4.3.4 Influence of focal position on surface functionality

Large surfaces may have localised defects or slight variation in planarity that may influence greatly early stage LIPSS formation, and thus to lead to ripples instead of uniform lines or triangles. Changes in LIPSS generation when processing out of focus or with incident beam that was not normal to the processed surface were widely reported by research groups, especially in term of their homogeneity, morphology and periodicity (Wang and Guo, 2006; Zhang et al., 2016).

The effect of focal position variations on LIPSS formation was investigated on two LIPSS morphologies studied in this research (the triangular- and linear-LIPSS shown in Figures 46b and 48e). In particular, out of focus texturing was performed with offsets of 50, 100, 150, 200, 250, 300, 500, 750 and 1000 μm in both positive and negative direction from the focal point. The resulting surface functionalities are depicted in Figures 50a-b.

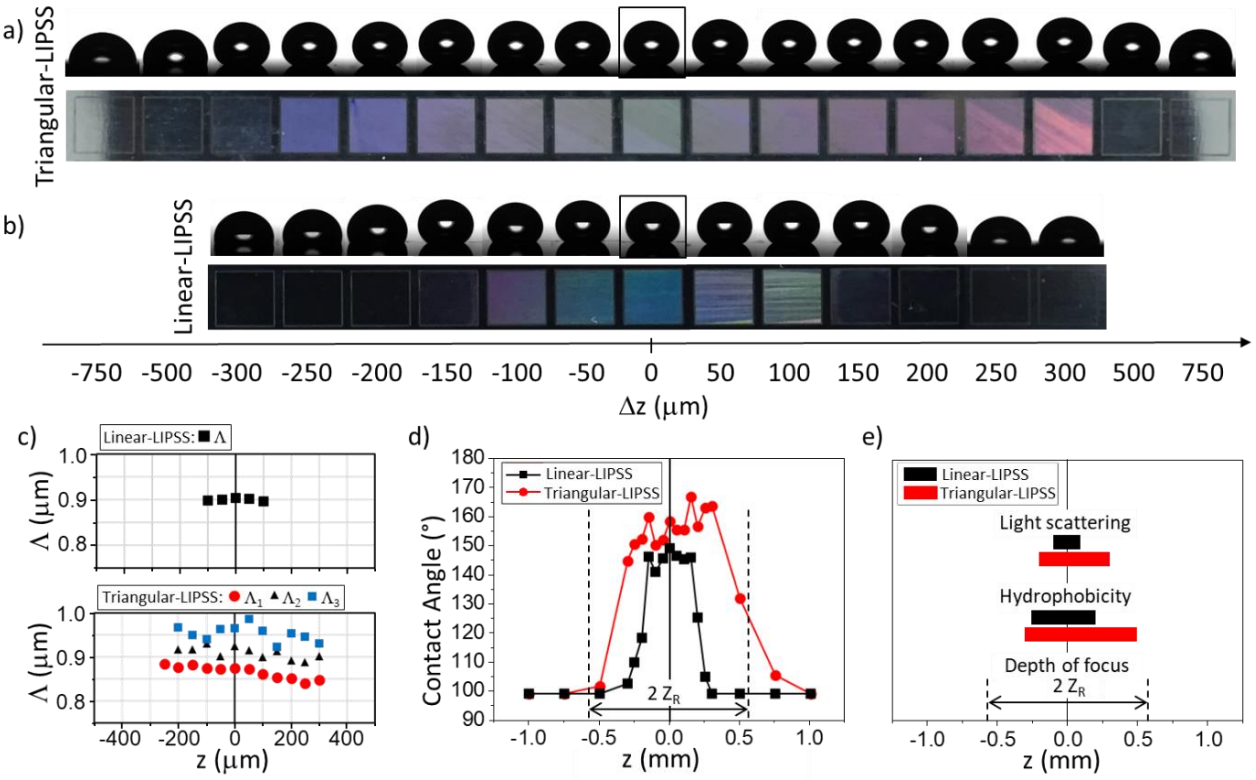

Figure 50. The influence of focal plane offsets on (a) triangular-LIPSS and (b) linear-LIPSS and their evolution in (c) LIPSS periodicity and (d-e) surface functionalities.
Note: the measurements were conducted 1 week after laser-processing.

When off focus processing is carried out, the beam size, pulse overlap and pulse fluence are inherently modified. However, the main periodicities of LIPSS processed off focus remain relatively constant for both the linear-LIPSS (Λ = 0.90 μm) and the triangular LIPSS (Λ_1 = 0.84 to 0.88 μm) as depicted in Figure 50c. Non-uniform LIPSS were observed when Δz was higher than 200 and 500 μm, for linear- and triangular-LIPSS, respectively. It is worth mentioning that triangular-LIPSS were not generated at z = -250 μm and only non-uniform ripples were observed but the surface functionality was not affected.

To assess the depth of focus for the structural coloring, a binary state was considered by visually observing the sample at different combination of lighting and observation angles. Contact angles are measured after surface stabilisation like described in Section 4.3.3 and presented in

Figure 50d. The laser processed surface is considered functionalised when contact angle changes are higher than +/- 10 % of the reference value for unprocessed surfaces.

The results in Figure 50e show that if the offset is within the theoretical depth of focus (estimated at 1.1 mm in Section 4.2), the surface properties cannot be maintained for both LIPSS types. No structural coloring was observed when Δz was higher than 200 and 550 μm, for the linear- and triangular-LIPSS, respectively. The surface wettability was the same that on unprocessed samples when Δz was higher than 450 and 800 μm, for linear- and triangular-LIPSS, respectively. Hence, the depth of focus associated with the hydrophobic property is higher than that for structural coloring.

4.4 Conclusion

The successful generation of uniform Laser-Induced Periodic Surface Structures (LIPSS) was demonstrated on ferritic stainless steel employing a one-step processing approach in air with a circularly polarised femtosecond laser source. Low Spatial Frequency LIPSS (LSFL) were produced exhibiting highly uniform distinct triangular-shapes in hexagonal arrangement over relatively large surface areas. A texturing approach was designed by investigating the effects of pulse fluence and both scanning speed and repetition rates. In addition, the sensitivity of this approach to off focus processing in generating LIPSS was studied. The triangular-LIPSS were demonstrated for a narrow, however highly repeatable laser processing window at a rate of approximately 1 mm^2/s. Such LIPSS exhibited light scattering and superhydrophobic properties, with contact angles as high as 157° after surface stabilisation through storage at ambient

conditions. Using constant processing parameters and an optimised scanning strategy, the depth of focus associated with investigated functional properties, i.e. structural colors and hydrophobicity, was determined. The approach studied in this research represents a new concept in large-area ultrafast laser structuring, where the accumulated fluence was a key factor in achieving a uniform texturing and thus functionalisation of metallic plates with some planarity deviations.

Acknowledgments

The research reported in this paper was carried out within the framework of European Commission H2020 ITN programme “European ESRs Network on Short Pulsed Laser Micro/Nanostructuring of Surfaces for Improved Functional Applications” (Laser4Fun) under the Marie Skłodowska-Curie grant agreement No. 675063 (www.laser4fun.eu). In addition, the work was supported by two other H2020 FoF programmes, i.e. the projects on “Modular laser based additive manufacturing platform for large scale industrial applications” (MAESTRO) and “High-Impact Injection Moulding Platform for mass-production of 3D and/or large micro-structured surfaces with Antimicrobial, Self-cleaning, Anti-scratch, Anti-squeak and Aesthetic functionalities” (HIMALAIA). The authors would like also to acknowledge the support and assistance of Behnam Dashtbozorg and Shaojun Qi from the School of Metallurgy and Materials at the University of Birmingham, in the sample preparation and the SEM characterisation.

Chapter 5

Subwavelength Direct Laser Nanopatterning via Microparticle Arrays for Functionalizing Metallic Surfaces

Journal Paper, published online

Romano J.-M. [(1)], Ahmed R. [(1,2)], Garcia-Giron A. [(1)], Penchev P. [(1)], Butt H. [(1,3)], Delléa O. [(4)], Sikosana M. [(5)], Helbig R. [(5)], Werner C. [(5)], Dimov S.S. [(1)] (2019) Subwavelength Direct Laser Nanopatterning via Microparticle Arrays for Functionalizing Metallic Surfaces, Journal of Micro and Nano Manufacturing, 7(1), 010901.

[(1)] Department of Mechanical Engineering, School of Engineering, University of Birmingham, B15 2TT Birmingham, United Kingdom
[(2)] Bio-Acoustic MEMS in Medicine (BAMM) Laboratory, School of Medicine, Stanford University, Palo Alto, CA 94304, USA
[(3)] Department of Mechanical Engineering, Khalifa University, Abu Dhabi, PO Box 127788, United Arab Emirates
[(4)] Laboratoire des Composants pour le Conversion de l'Energie (L2CE), Laboratoire d'Innovation pour les Technologies des Energies Nouvelles et des nanomatériaux (CEA/LITEN), 38000 Grenoble, France
[(5)] Max Bergmann Center of Biomaterials, Leibniz Institute of Polymer Research, 01069 Dresden, Germany

Authors' contributions: J.-M. Romano is the first and main author of this publication, who designed this study of large-area submicro-texturing using microspheres with diameter close to the laser wavelength. Dr. R. Ahmed implemented the simulations and contributed with the overall design of the paper. Dr. O. Delléa provided the samples deposited with the monolayer of microspheres. J.-M. Romano performed the laser texturing and characterisation of topography and wetting properties, with assistance of A. Garcia-Giron and Dr. Pavel Penchev. M. Sikosana and Dr. R. Helbig conducted the microbacterial tests, under supervision of Prof. C. Werner. J.-M. Romano wrote the manuscript that was reviewed by A. Garcia-Giron, Dr. R. Ahmed, Dr. O. Delléa and Dr. R. Helbig, under supervision of Prof. S.S. Dimov.

Abstract

Functionalized metallic nano-features can be selectively fabricated via ultrashort laser processing, however the cost-effective large-area texturing, intrinsically constrained by the diffraction limit of light, remains a challenging issue. A high-intensity near-field phenomenon that takes place when irradiating micro-sized spheres, referred to as Photonic Nanojet (PN), was investigated in the transitional state between geometrical optics and dipole regime to fabricate functionalized metallic subwavelength-features. Finite element simulations were performed to predict the PN focal length and beam spot size, and nano-feature formation. A systematic approach was employed to functionalize metallic surface by varying the pulse energy, focal offset and number of pulses to fabricate controlled array of nanoholes and to study the generation of triangular and rhombic Laser-Induced Periodic Surface Structures (LIPSS). Finally, large-area texturing was investigated to minimize the dry laser cleaning effect and improve homogeneity of PN-assisted texturing. Tailored dimensions and densities of achievable surface patterns could provide hexagonal light scattering and selective optical reflectance for a specific light wavelength. Surfaces exhibited controlled wetting properties with either hydrophilicity or hydrophobicity. No correlation was found between wetting and microbacterial colonization properties of textured metallic surfaces after 4 h incubation of *E. coli*. However, an unexpected bacterial repellency was observed.

5.1 Introduction

Techniques for selective micro- and nanopatterning of metallic surfaces have attracted a growing interest due to their novel optical (Gnilitskyi et al., 2017; Müller-Meskamp et al., 2012; Skoulas

et al., 2017), wettability (Huerta-Murillo et al., 2019; Palneedi et al., 2018; Romano et al., 2018a), and anti-microbiological (Anselme et al., 2010; Cunha et al., 2016; Helbig et al., 2016; Whitehead et al., 2005; Yi et al., 2018) applications. Several non-lithographic techniques were suggested to fabricate subwavelength-size patterns, such as single and multi-beam direct laser interference patterning (Ahmed et al., 2017a; Bieda et al., 2016) or polarization-based laser-induced periodic surface structures (LIPSS) (Young et al., 1983). In the last 10 years, a promising nanofabrication route involving microparticles as near field focal enhancement systems was developed (Heifetz et al., 2009; Yang et al., 2006). This method benefits from the near field optical phenomena, called Photonic Nanojet (PN), that allows a beam focusing beyond the optical diffraction limit of light (Abbe, 1873; Chen et al., 2004; Lecler et al., 2005). However, a preliminary step is required to apply the PN technology for surface texturing, i.e. the deposition of a microspheres' monolayer on a substrate. Self-assembly processes such as Langmuir-Blodgett techniques can be applied for microspheres' deposition into hexagonal close-packed (HCP) monolayers, also called contacting particle-lens arrays (CPLA) (Delléa et al., 2014). Then, a laser-irradiation of CPLA results in an array of non-evanescent beams emerging from the shadow-side of microspheres, with diameters as small as the third of the irradiated wavelength and a length of two wavelengths (Heifetz et al., 2009). Such a method was applied to laser-fabricate subwavelength holes and convex bumps (Huang et al., 2002; McLeod and Arnold, 2008), even on materials with low absorption at a given wavelength (λ) (Abdurrochman et al., 2014; Theppakuttai and Chen, 2003). Various attempts to tailor the PN optical properties were reported, including changing the refractive index (n) and the shape and diameter ($2r$) of microspheres and also the illumination conditions (Heifetz et al., 2009; Guo et al., 2008; McCloskey et al., 2010; Han et al., 2014; Grojo et al., 2014).

However, large-area texturing for functionalizing surfaces by direct laser ablation remains a challenge. This is mostly due to the detachment of microspheres after any single laser pulse irradiation and this could be explained with the substrate ablation or dry laser cleaning (DLC) effect (Arnold, 2003; Mosbacher et al., 2000; Vereecke et al., 1999; Zheng et al., 2001). Contrary to laser cleaning where the laser-induced marking is an undesirable side-effect, to achieve large-area PN texturing the marking must be maximized while minimizing the microspheres' detachment. Several techniques were proposed to address this issue, usually by preserving CPLA by covering it with a transparent material (O'Connell et al., 2010; Khan et al., 2010, 2011; Sedao et al., 2012). Maintaining CPLA in contact with the substrate allowed multi-pulse processing and thus to texture larger areas homogeneously and at the same time to increase the aspect ratio of the resulting nanoholes (Sedao et al., 2012).

In this research, a novel approach for submicron large-area texturing of metallic surfaces is presented and their multifunctional aspects are described with applications in nano-scale optics, wettability and microbiology. Especially, a near-infrared ultrashort laser irradiation of transparent silica microspheres deposited onto stainless steel plates was investigated. The microspheres were used as CPLA and their sizes were equal to the irradiation wavelength. FE simulations were conducted to predict the PN focal length and the full width at half maximum (FWHM) spot size at the substrate surface while varying laser wavelengths and spheres' radii. Direct laser nanofabrication of nanobumps, nanoholes and LIPSS was investigated and was compared to DLC effect towards large-area texturing. Finally, potential surface functionalities of nanoholes and LIPSS were studied for selective hexagonal scattering, tunable optical reflection, wettability, and microbiology applications.

5.2 Material and methods

5.2.1 Sample preparation and laser set-up

Silica microspheres were deposited in a hexagonal close-packed monolayer onto X6Cr17 stainless steel plates by employing a patented method (Tebby and Dellea, 2011) based on the Langmuir-Blodgett technique. The laser irradiation was performed with a near-infrared ultrashort pulsed laser source (Satsuma, Amplitude Systemes) with a pulse length of 310 fs and a central wavelength of 1032 nm. The laser beam had a circular polarization and was steered over the substrate using a 3D scan head (RhoThor RTA) equipped with a 100 mm F-theta telecentric lens. The beam spot size, $2\ \omega_0$ at $1/e^2$, was adjusted to 30 µm diameter at the focal point with a beam expander. Spot sizes at focal offset were calculated following the relation $\omega(z) = \omega_0 [1 + (z / Z_R)^2]^{1/2}$ with $Z_R = \pi \omega_0^2 / \lambda$. Pulse fluences were estimated by dividing the pulse energy by the spot area $\pi \omega^2$. For post-fabrication of LIPSS, the pulse-to-pulse distance (δ) is the ratio of the scanning speed over the repetition rate and the number of pulse equivalent was calculated according to the formula $N = \pi \omega_0^2 / (\sigma \delta)$, with σ the hatching distance. The remaining spheres and any debris resulting from the laser irradiation were removed using an ultrasonic bath in ethanol for 15 min.

5.2.2 Microscopic imaging

The SEM micrographs were produced using a scanning electron microscope (Hitachi TEM3030Plus) with secondary electron detector and low vacuum. Fourier transforms (2D-FFT) of the images were performed in Gwyddion imaging tool. In addition, the 3D topographies were

measured using an atomic force microscope (AFM, Dimension 3100, Bruker) equipped with AFM probes (PPP-RT-NCHR, Nanosensors) in tapping-mode.

5.2.3 Optical characterization

A broadband light source (400-1100nm, Ocean Optics 2000+) and a spectrophotometer (resolution 0.1-100 FWHM, Ocean Optics HL 2000) were used to characterize the surfaces' optical properties. Broadband light normally illuminated the metallic nanopatterns and the reflected light was captured though an objective (x20) in reflection mode. Near-field hexagonal scattered/diffracted light was measured through a hemispherical screen (semi-transparent white, 30 mm in diameter). Far-field scattered/diffracted rainbow patterns were performed with an image screen (white A4 paper) setup.

5.2.4 Wettability

The wetting properties were analyzed employing an optical tensiometer (Attension Biolin Scientific Theta T2000-Basic+) and purified (Milli-Q, Merck) water was used as probe liquid. All tests were performed under ambient conditions. Static contact angles (CA) of 6 μl drops were measured after stabilization employing the sessile drop technique. The CA hysteresis was calculated using the needle-in-drop method and measuring the advancing and receding CA evolution of 6 μl at 0.5 μl/s.

5.2.5 Microbiology

The textured metallic samples were replicated by a two-step process. First, negative surface structures were obtained from a master with an epoxy resin (Araldit CY212, Plano) via thermal polymerization. Second, the final replicas were produced by employing the epoxy resin master with a perfluoropolyether (PFPE) prepolymer via UV induced polymerization (Fluorolink MD40, Solvay). Bacterial colonization and bacterial adhesion on textured substrates were assessed with *E. coli* (strain W 3110), after 4 h incubation in lysogeny broth media (LB, Sigma-Aldrich) at 37°C (overnight culture adjusted to optical density (OD) ~ 0.4 in fresh LB before). The bacteria were fixed in paraformaldehyde (PFA), then rinsed with phosphate buffer solution and distilled water (milliQ, Merck) and gently dried with nitrogen. Subsequently, the samples were sputter coated with a 10 nm gold layer (SCD 050 sputter coater, Balzers) and imaged with a SEM XL30 (ESEM/FEG, FEI). The adherent bacterial cells were counted on SEM images using the cell counter tool in ImageJ (NIH). The experiment was performed two times and a total of 14 images (~ 150000 μm^2) per sample were examined.

5.3 Results and discussion

5.3.1 FE and computational modelling

Computational modelling techniques for particle light scattering were developed, in particular by employing numerical simulation or analytical methods based on the generalized Lorentz-Mie theory (Arnold, 2003; McCloskey et al., 2010). Such techniques were often applied for particles with much larger sizes than the wavelength and the focal spot sizes were calculated to be in the

range from 0.8 λ down to 0.15 λ depending on the refraction indexes of the particles and the propagation medium (Huang et al., 2002; Leitz et al., 2010; Pereira et al., 2008). Depending on the ratio 2 r / λ (x) three different cases could be distinguished. For x >> 1, the generic rules of geometrical optics apply and the Snell-Descartes' law should be used to obtain the approximate focal spot size (w_g) as follows (Arnold, 2003):

$$w_g \approx r\,[(4 - n^2)^3 / (27\, n^4)]^{1/2} \tag{5.1}$$

For spheres much smaller than the wavelength, x << 1, the close-packed monolayer behaves as a densely homogenous one and the dipole approximation estimated the spot sizes (w_d) in the dipole regime similar to the sphere radii (Arnold, 2003), i.e. $w_d \approx r$, which is comparable with some reported simulation results (Münzer et al., 2001). Seldom, the intermediary range between geometrical and dipole regime, i.e. x ≈ 1, was considered and so the focal spot size could be estimated between 0.14 λ and 0.40 λ (Cai and Piestun, 2006; Leitz et al., 2010; Li et al., 2013). For this third case, Arnold (Arnold, 2003) introduced a constant of transition $C = [(n^2 - 1)\, w_g] / [(n^2 + 1)\, r]$ thus unifying the analytical approximation of geometrical and dipole focal enhancement so that the focal spot size (w) could be approximated as follows:

$$w = (w_d + C\, k^2\, r^2\, w_g) / (1 + C\, k^2\, r^2) \tag{5.2}$$

where $k=2\pi/\lambda$ is the electromagnetic wave number.

To understand the near-field focal enhancement via microspheres, FE based computational modelling was performed in COMSOL Multiphysics (v5.3a). A planar wave (1030 nm) propagates through an air medium and focused through silica microspheres. To take into account optical interferences of the spheres, a close-packed 2D array of 5 spheres was considered. The

continuity and scattering boundary conditions were considered for the spheres and the domain boundaries. The diameter 2 r of the microspheres was varied, and respectively, the domain of simulation (8r x 10r). Near-field electric field intensity distributions upon normal irradiation of microspheres of different sizes were investigated by varying x from 0.5 to 8. The microspheres are considered as a homogeneous, non-absorbent medium with refractive index of 1.50 at 1030 nm wavelength (Radhakrishnan, 1951, p. 2). The near-field focused light intensity as a function of microsphere size (x = 1.0, 1.9, and 2.9) are depicted in Figure 51a. The increase of microspheres' sizes led to an increase of the focused light intensity and PN size. For periodic microsphere arrays, the maximum focused light intensity was observed at the center due to the Gaussian distribution nature of the illuminated plane wave.

The resulting PN was analyzed by means of peak intensity (I_{max}), paraxial focal length (D) and beam spot size (FWHM at I_{max}). The PN length (L) was estimated as the distance from the substrate surface until the intensity reaches $I_{max} / 2$ as shown in Figure 51a, by plotting the evolution of intensity along the vertical axis (see Fig. 51b). The intensity and beam spot size at the point of contact between the microspheres and the substrate was considered, too. Figure 51c showed peak intensity of PN as a function of normalized microsphere size at maximum and surface position. A pre-condition for the near field optical phenomena associated with PN is the electric field propagation along the vertical axis to reach a peak intensity outside the microsphere. Based on the simulation results this pre-condition is met at $x \approx 1.5$ and x larger than 2 (see Fig. 51d). Therefore, the PN geometrical optic regime is considered established for x strictly larger than 2. For this regime, the relative peak intensity increased with the size of the sphere (see Fig. 51c-d). However, while the peak intensity is reached at the substrate surface when x = 2, a further increase of x led to a reduction of the surface peak intensity compared with

the max values, especially up to approximately 50 % for $x > 6$. Another well-established PN trend depicted in Figure 51d is that both the focal point and the PN length decrease with the decrease of microspheres' sizes (Itagi and Challener, 2005; Lecler et al., 2005) until the focal point becomes coincident with the contact point between the microspheres and the substrate for $x = 2$. Interestingly, the simulation illustrated that a further decrease of x led to an increase of the focal distance, when $x = 1.5$, before a rapid decrease down to negative values where the peak intensity was reached inside the microspheres. This was attributed to a transition state between the geometrical optic and dipole regimes. For the dipole regime ($x << 1$), electrical fields are predicted to reach a peak intensity not anymore along the vertical axis but sideways (Münzer et al., 2001). The FE simulation exhibited local intensity peaks shifted sidelong the paraxial axis for the transition state of $x \approx 1$ and the focal point is close to the microsphere's center. Half maximum intensity was reached outside the microsphere, at a paraxial distance of ~ 0.2 λ, which is considered as a PN tail. Furthermore, considering characteristics of Gaussian intensity profiles, the PN tail reached an intensity of I_{max} / e^2 at a paraxial distance of approximately 0.7 λ for $x \approx 1$. Even if the peak intensity is not reached on the substrate, the intensity at the surface may still exceed the ablation threshold for a given material, opening the way for PN-assisted manufacturing applications.

A subwavelength-size damage may appear on substrate surface when the PN energy density is sufficiently high while the PN beam size is smaller than the irradiating wavelength. The analytical approximation for the focal spot size in Equation 5.2 converted to FWHM by a factor of $(2 \ln 2)^{1/2}$ correlated well to the simulation of PN beam size for x lower than 1.5, with FWHM smaller than 0.5 λ. Although the analytical model predicts a constant increase of beam size with the increase of x, the FWHM reached a plateau at around 0.5 λ in the FE simulation, in particular

for x larger than 1.5 (see Fig. 51e). A similar stagnation was also reported by McCloskey et al. (McCloskey et al., 2010). While the PN FWHM appeared consistently in the subwalength range, with a minimum at ~ 0.2 λ, the FWHM at the surface position remained in the subwavelength range only for x from 0.5 to 4. Therefore, when PN are used in direct contact with substrates, two fabrication regimes can be discussed. At first regime, an increase of microspheres' sizes inherently leads to larger surface beam sizes and hence a lower intensity at the surface. This effect may be comparable to performing laser processing out of focus, but only to some extent, as any change in the PN beam shape may induce different surface damage morphologies. The simulation results' trend for microspheres much larger than the wavelength used in contact mode may confirm experimental observation of volcano-shaped surface damages (McLeod and Arnold, 2008; Mosbacher et al., 2001). Several studies investigated how to bring the focal point back to the surface, with a vertical offset of the microspheres (Li et al., 2013; Piglmayer et al., 2002; Vestentoft et al., 2005) or a non-orthogonal incident irradiation (Münzer et al., 2001; Guo et al., 2007; Li et al., 2009), and this aspect is therefore not considered further in this study. At second regime, the irradiation of particles smaller than the wavelength leads to FWHM at the surface position that are in the subwalength range, but with the lowest peak intensity and PN length. Thus, this constrains the fabrication process to low aspect ratio nanofeatures and therefore should be investigated further.

Employing CPLA for large area texturing, the HCP nature of the deposited monolayer induces a surface damage with hexagonal periodicity equal to the microspheres' size. However, the dimension of the surface damages compared to their periodicity has to be considered. The irradiation density, i.e. the ratio of the area covered by PN spots with intensity larger than half maximum over the whole substrate, can be used as an indicator for the achievable feature sizes

and periodicity (see Fig. 51f). A general trend between the analytical and simulation results was observed, the irradiation density increasing with the decrease of x. The analytical approach predicts an asymptotic minimum at ~ 2 % for very large x and a maximum irradiation density of ~ 30 % can be achieved as x tends to 0. Contrarily, the simulations revealed a local maximum of ~ 20 %, reached when x is equal to 1. There are similar trends in approximation and simulation results but there are discrepancies, too, because the analytical approach does not take into account whether the beam spot sizes are at the substrate surface or not. For PN spots on the surface, the density is also increasing for lower x. The ratio FWHM/2r reached more than 50 % when 2 r is smaller than λ, indicating that the density achievable with the PN technology can be sufficient for large-area sub-wavelength surface texturing when using CPLA with microspheres smaller than the wavelength.

In this research the case when x is equal to 1 is selected to investigate the PN texturing process experimentally. Especially, this PN processing case is used to validate the technology for producing dense nanoscale features while the irradiation conditions are far from optimum. In particular, these PN texturing conditions lead to the lowest peak intensity and intensity at the surface (see Fig. 51c), and a PN tail of a few hundred nanometers (see Fig. 51d), however with a relatively high irradiation density with subwavelength-sized FWHM in a λ-periodic HCP (see Fig. 51f).

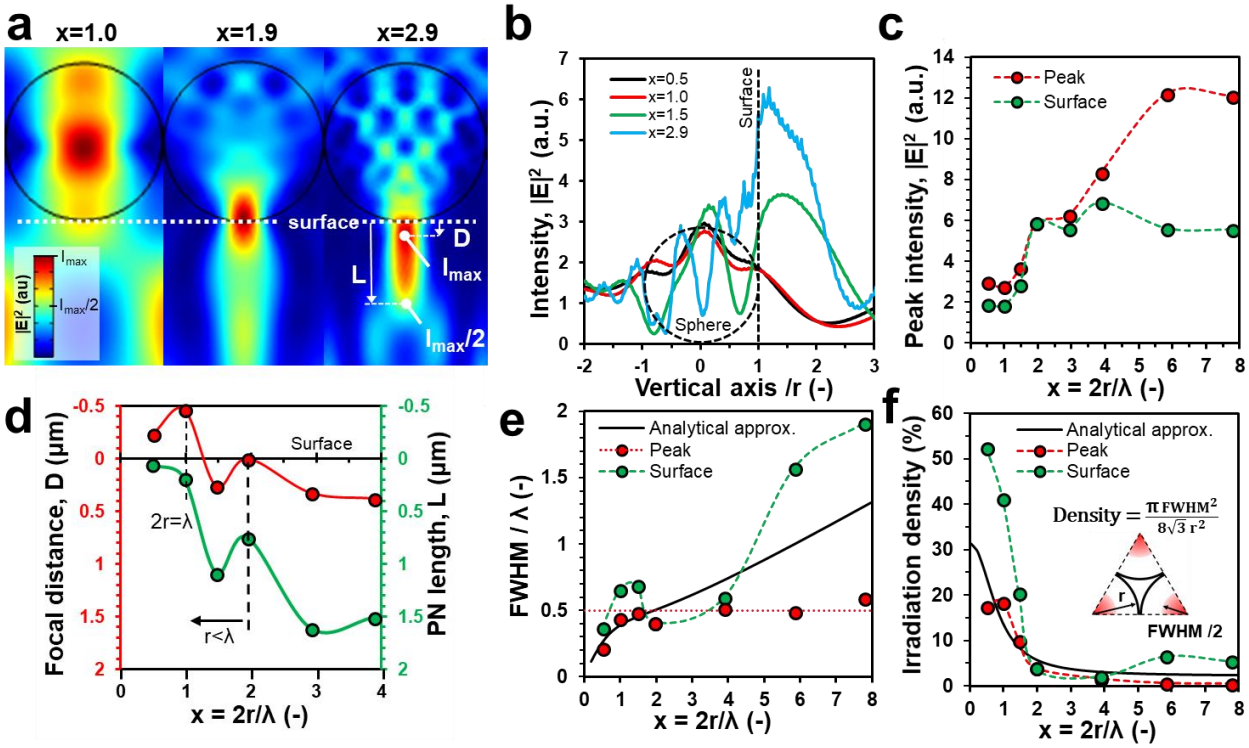

Figure 51. The modelling results of light focusing through silica microspheres. Irradiation wavelength was fixed at 1030 nm while the microspheres' radii were varied. (a) Intensity mapping for three cases of x = 2 r / λ, especially equal to 1.0, 1.9 and 2.9. The color scales are independent for each case, in particular from blue (low intensity) to red (peak intensity). (b) The intensity evolution along the vertical axis, normalized with the sphere's radius for four cases of x. The dashed circle and line indicate the normalized sphere's dimension and surface position. (c) Peak intensity estimations for the considered cases of x from 0.5 to 8. (d) Paraxial focal length and PN length as a function of x. The red colored area suggests combinations of wavelength and radius where the focal point is outside microspheres. (e) FWHM normalized in regard to the irradiation wavelength for the considered x values. (f) Irradiation surface density calculated for a close-packed array of spheres as a function of x. Estimations are taken at the peak intensity positions z = z(I_{max}) on the substrate surface. Analytical PN waist were plotted according to (Arnold, 2003).

5.3.2 PN-assisted surface texturing

5.3.2.1 Subwavelength laser ablation

Ultra-short laser pulses in the near-infrared (NI) range (310 fs, 1032 nm) were used to irradiate a dense monolayer of 1 µm-diameter SiO_2 spheres deposited onto stainless steel substrates (see Fig. 52a). The laser beam was steered over the surface using a galvanometer scanner and

was focused with a 100 mm F-θ-lens. The NI irradiation with a 30 µm beam spot creates an array of PN tails that can lead to surface damage when the pulse energy is sufficiently high, resulting in the ejection of parts of the CPLA (see Fig. 52b-c). Each PN resulting from such CPLA irradiation can be considered as a Gaussian nanobeam, with FWHM and $1/e^2$ spot sizes of 0.46 λ and 0.74 λ, respectively. Various surface morphologies could be achieved depending on pulse energy and pulse numbers. A selection of PN-processed surfaces is presented in Figures 52d-g. As a result of a repeated irradiation with a pulse energy close to the damage threshold, convex nanobumps were fabricated (see Fig. 52d). Huang et al. attributed the generation of such surface features to the Marangoni convection induced by PN sidelong the paraxial axis and achieved λ / 2 - diameter nanobumps on silicon wafers by irradiating a 1-µm-diameter CPLA with UV-nanosecond laser pulses (Huang et al., 2005). In this research, slightly smaller nanobumps, in particular with diameters and heights of ~ λ / 3 and ~ 30 nm, respectively, were generated with near-infrared (NI) 310 fs pulses. While a single shot was sufficient to create the nanobumps with nanosecond pulses, multiple irradiations, in particular 100 pulses at 10 kHz, were required to produce them with femtosecond pulses, and apparently as a result of some cumulative effects.

Beyond the damage threshold of the substrate, the surface was locally ablated under the microspheres and an array of nanoholes were generated. First, a surface damage was observed with single pulses of 0.9 µJ at the focal point and then up to 1 mm focal offset. The nanoholes were circular in shape with a distance between each other corresponding to CPLA periodicity. The minimum diameter was ~ λ / 6, i.e. ~ 175 nm. The increase of pulse energy resulted in larger holes' diameters, up to 1 µm, and thus to form honeycomb structures. For positive or negative surface structures, the aspect ratio remained limited at ~ 1:10, as depicted by two representative AFM cross-sections in Figures 52k-l. The microspheres' sizes were close to the irradiation

wavelength ($x \approx 1$) in this research and these processing conditions differ from those used by other researchers for direct NI femtosecond nanopatterning. In particular, wavelengths in the range from 400 to 800 nm were utilized to fabricate nanoholes of ~ 0.3 λ diameter and several 10nm in depth on silicon and glass substrates (Münzer et al., 2001; Zhou et al., 2006).

The intensity distribution of the laser beam had a direct influence on the homogeneity of fabricated nanoholes' arrays. A single pulse could produce an array of ~ 260 nanoholes with diameters from 255 to 940 nm (see Fig. 52h). An increase of pulse energy results in ~ 730 nanoholes with similar average diameter but with a broader dispersion, from 120 nm to 1.23 μm (see Fig. 52i). Such high pulse energies were detrimental to the nanoholes' homogeneity and this was mostly due to the laser beam Gaussian intensity profile. PN induced thermal-effects after irradiations with femtosecond laser pulses were reported on glass (Zhou et al., 2006), silicon wafers (Mosbacher et al., 2001; Nedyalkov et al., 2007) and metallic substrates (Nedyalkov et al., 2007). Especially, they led to the fabrication of nanoholes larger than the CPLA periodicity and thus clogging contiguous nanoholes. However, by tailoring the focal offset, larger CPLA areas could be irradiated and also the use of laser beams with a top-head Gaussian profiles could enable the fabrication of nanoholes with much smaller spread of diameters. In this work, arrays of nanoholes were produced with a focal offset up to 2 mm. Especially, it was possible with the use of 1mm focal offset to produce ~ 1700 nanoholes with an average diameter 310 nm and a spread from 160 to 780 nm (see Fig. 52j).

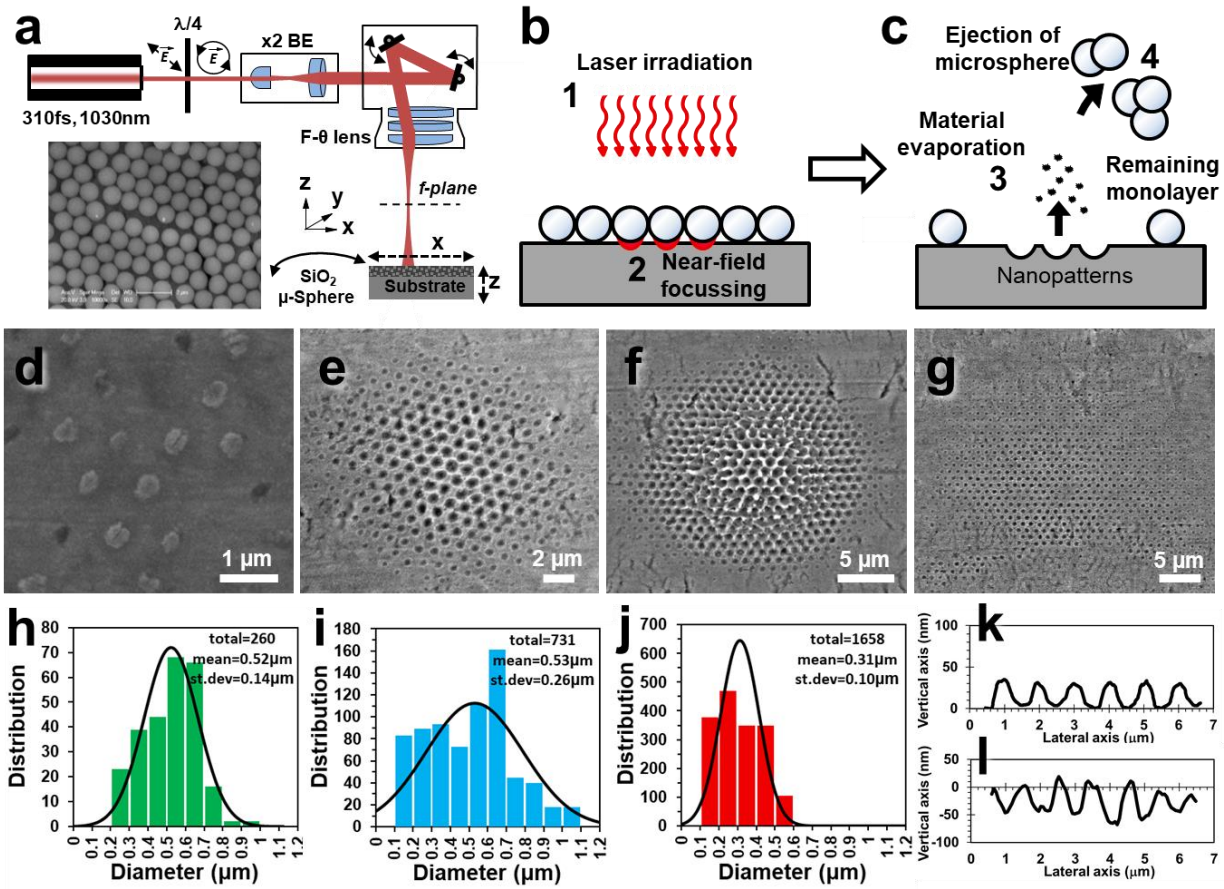

Figure 52. A direct laser ablation based nanopattering by irradiating a HCP CPLA of 1 μm-diameter spheres with a NI 30 μm-diameter Gaussian fs-laser beam. (a) The used experimental setup for processing substrates with a focal offset. (b-c) The schematic steps of the texturing process. The microspheres are partially removed from the textured area and its surroundings. Micrographs of morphologies achieved with 310 fs laser pulses at 1032 nm wavelength: (d) nanobumps fabricated employing a 2 mm focal offset and 100 irradiations at 1.3 μJ; array of nanoholes fabricated with a single irradiation of (e) 1.3 μJ at focus, (f) 6.3 μJ at focus and (g) 6.3 μJ at 1 mm focal offset, respectively. (h-j) Distributions of nanoholes' diameters corresponding to (e-g). The nanoholes are gathered in clusters of 0.1 μm and a normal distribution is extrapolated from the distribution. Profiles of nanobumps (k) and honeycomb structures (i) are given with two representative AFM cross sections.

5.3.2.2 Large area texturing

Parallel nanostructuring refers to the fabrication of nanofeatures over an area significantly bigger than a single-pulse laser spot. The large area covering with PN-induced nanofeatures is intrinsically limited due to the detachment of microspheres after any single laser pulse

irradiation. This is similar to the effect referred to as Direct Laser Cleaning (DLC) that was investigated by many researchers both empirically (Mosbacher et al., 2000) and theoretically (Arnold, 2003). Especially, DLC is the result of a mechanical ejection triggered by the rapid thermal expansion of the irradiated microspheres. The evaporation of condensed humidity at the interface sphere-substrate may also increase DLC effect (Vereecke et al., 1999).

DLC takes place below the ablation threshold and therefore only cracks and delamination of the CPLA could occur without any surface damage, until a sufficient fluence is reached to eject the microspheres. The reported ejection velocities (Grojo et al., 2006) are in the order of 10 m/s and this could explain why there was no increase of nanoholes' aspect ratios with the pulse repetition rates investigated in this research. A pulse energy of 2 µJ and processing with 1.5 mm focal offset were required to start cracking the microspheres' monolayer. A further increase of pulse energy up to 4.8 µJ resulted in a partial removal of microspheres without damaging the substrate surface. At the same time laser processing closer to the focal point and also with higher pulse energies led inevitably to surface damage. The CPLA delamination and ejection of microspheres can be attributed to ablation dynamics, especially the removal of microspheres above nanotextured areas.

A focal offset of the incident laser beam was beneficial for fabricating more homogeneous array of nanoholes, however the tail of the Gaussian beam broadens the area affected by DLC. A multi-pulse approach had the same DLC effect, possibly due to a cumulative effect. Similarly, a higher pulse energy increased not only the thermal effect and nanoholes' sizes but also the DLC area as shown in Figure 53a. The filling ratio, in particular the ratio between the surface area covered with nanofeatures and the total processed area, was optimized by applying various

scanning strategies, especially by varying the pulse-to-pulse distance to achieve moon-shaped arrays of nanoholes, as shown in Figure 53b. For example, the maximum filling ratio of 46 % was reached with 3.6 μJ pulses at focus and a pulse-to-pulse distance slightly smaller than the laser spot diameter (see Fig. 53c). A further reduction of pulse-to-pulse distance led to non-circular arrays of nanoholes and decreased the filling ratio to ~ 30 % (see Fig. 53d-e) until the LIPSS outset threshold was reached and PN-induced nanoholes were converted into ripples-like LIPSS (see Fig. 53f-g).

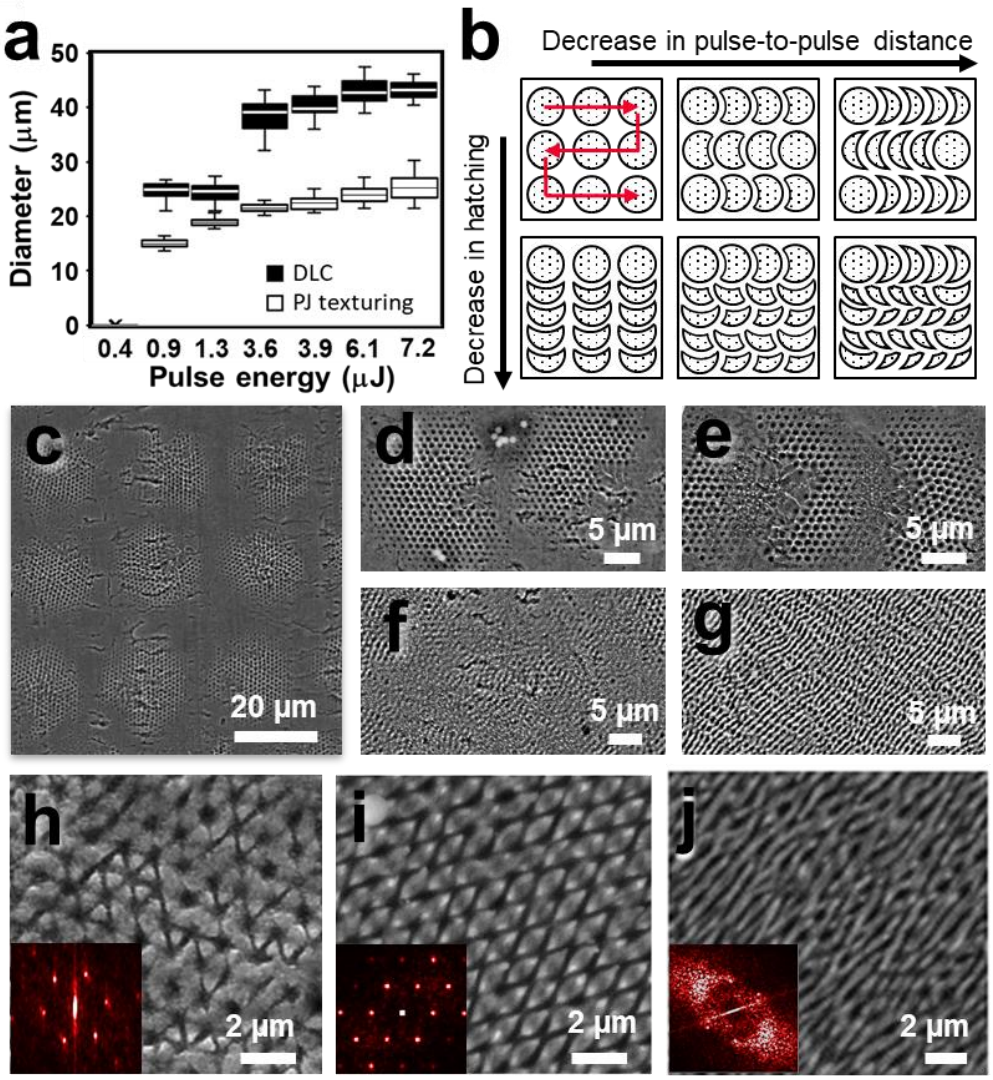

Figure 53. A large area texturing with nanoholes after near-infrared irradiation (λ = 1032 nm, circular polarization, 30 μm focal spot size) of a CPLA of 1-μm-spheres. (a) The diameters of DLC spots compared with the diameter of those covered with PJ-induced holes, as a function of pulse energy at focus. Mean diameters and their standard deviation were calculated based on 5 measurements. (b) Schematic representation of textured areas that result from varying hatching and pulse-to-pulse distances, σ and δ, respectively. Micrographs depict the effects on surface morphologies when varying σ and δ, in particular: (c) σ = δ = 25 μm, (d) δ = 22.5 μm and σ = 25 μm, (e) δ = 15 μm and σ = 25 μm, (f) σ = δ = 10 μm and (g) σ = δ = 5 μm, with 3.6 μJ pulses at focus. LIPSS generation upon multiple irradiations of pre-fabricated arrays of nanoholes: (h) hexagonal LIPSS fabricated at 1mm focal offset by 100 2.5 μJ pulses. Further evolution of LIPSS over nanoholes fabricated with 3.9 μJ pulses at focus: (i) rhombic-shaped LIPSS after 28 0.5 μJ pulses at focus and (j) ripples-like LIPSS after 177 1.5 μJ pulses at focus. The Fourier transformed micrographs indicating LIPSS periodicity and orientation are depicted in the insets.

5.3.2.3 LIPSS generation with tailored periodicity

Further irradiation of nanoholes fabricated with single-pulses with fluences in the range from 0.18 to 0.29 J/cm^2, as shown in Figure 52g, did not lead to additional material removal but resulted in some improvements of nanoholes' rims, as already reported (Abdurrochman et al., 2014; Kallepalli et al., 2013). The irradiation intensity was sufficient to displace the microspheres from their initial locations and thus to prevent the fabrication of nanoholes with higher aspect ratio unless preventing such displacements (Sedao et al., 2012). Albeit the fluences used for nanoholes' fabrication were not sufficient to reach the substrate's ablation threshold after the CPLA removal, multiple irradiations led to surface structures referred to as LIPSS (Young et al., 1983). Cumulative fluence of ~ 1.8 J/cm^2 was sufficient to trigger the generation of LIPSS over the arrays of nanoholes. Further cumulative effects after reaching ~ 2.9 J/cm^2 were the spreading of LIPSS over the whole surface and thus to join the array of nanoholes. At a fluence of ~ 11 J/cm^2 the formation of triangular surface morphologies was initiated (see Fig. 53h) and, compared with the generation of such triangular LIPSS without CPLA (see Chapter 4), only half of the necessary cumulative fluence was required (Romano et al., 2018a). Thus, pre-fabricated surface patterns could be used to lower the cumulative fluence required for LIPSS generation.

Despite LIPSS being wavelength-dependent periodic surface structures, the 1μm periodicity of the CPLA was retained. Various regular LIPSS morphologies were generated by varying pulse numbers and fluence, in particular triangular and rhombic LIPSS (see Fig. 53h-i), which could be of interest for a single-step LIPSS fabrication. The periodicity remained consistent with the pre-fabricated array of nanoholes until the cumulative fluence was sufficient to break down the

established λ-periodic triangular features into ~ 0.82 λ-periodic ripple-like LIPSS (see Fig. 53j). Considering the case in Figure 53h (λ periodic), such triangular LIPSS with ~ 0.87 λ periodicity were achieved with similar irradiation conditions where the triangular surface morphology was attributed to the use of a circular-polarized laser beam (Romano et al., 2018a). A pre-fabricated array of nanoholes can potentially enable the generation of triangular nanofeatures with varying sizes and periodicity.

5.3.3 Surface functionalization

5.3.3.2 Optical properties

The sub-wavelength features fabricated on stainless steel were characterized through light illumination in reflection mode. A broadband light source was used to illuminate the textured surfaces at angles from 0 to 180° by controlling the rotation with a step motor. A spectrophotometer was positioned normal to the patterned surface for intensity measurements within the visible spectrum, i.e. a wavelength range from 400 to 700 nm.

The optical response of stainless steel surfaces fabricated with different pulse energies, pulse numbers and effective pulse-to-pulse distances were studied. A 0.9 μJ-single pulse irradiation resulted in a surface morphology with reflection properties close to 100 % with only a slight decrease to around 85 % in the violet-blue range (see Fig. 54a). Higher pulse energies led to a decrease of the overall reflection spectrum as a result of the high filling ratio (see Fig. 54b). In single pulse processing, the reflection properties could be finely tailored in the range from 100 to 80 % by varying the pulse energy from 0.9 to 6.6 μJ. An increase in pulse numbers led to an

overall decrease of reflection properties that can be attributed to the respective progressing changes in LIPSS morphologies (see Fig. 54a-b). Overall, the reflection of wavelengths in the violet-blue range was lower compared to green and red lights (see Fig. 54c).

A decrease of pulse-to-pulse distance while keeping the hatch distance the same led to a decrease of overall reflection spectrum except for the red light that remained unchanged. Similarly, the decrease of pulse-to-pulse and hatch distances led to surface morphologies that were less reflective except the increase for the red light. A local maximum reflection was obtained for wavelengths in the range from 500 to 520 nm (see Fig. 54d-e). Wider coverage with LIPSS ($\sigma = \delta = 5$ μm) resulted in a constant reflection of ~ 8 % for wavelengths in the range from 500 to 700 nm while there was a full absorption of violet-blue range (see Fig. 54e-f).

Broadband light scattering properties of the sub-wavelength features were investigated by employing near and far-field optical setups. For near-field measurements, the sample was normally illuminated and the scattered light was captured through a hemispherical surface (4 cm diameter). For far-field measurements, the sample was illuminated through an angular setup (Ahmed et al., 2017b). Far-field diffraction patterns were captured through an image-screen setup. The two-dimensional fast Fourier transforms (2D-FFT) in Figures 53h-j were indicative of hexagonal-shaped far field diffraction patterns. Similar 2D-FFT and diffraction patterns were previously reported for hexagonal arrangements of microstructures (Ahmed et al., 2017c; Romano et al., 2018a). In agreement with 2D-FFT of nanoholes' arrays, hexagonal scattering patterns were observed in the surrounding of the non-diffracted broadband light (zero-order) (see Fig. 54g). Since the diffraction angle increases with the wavelength, multiple rainbow patterns were visible covering the range from blue to red. Analogously to diffraction gratings, the

diffraction distances from the center spot were larger for the red light compared with the blue one, accordingly to Bragg's law ($\lambda / \Lambda = 2 \sin \varphi$, where λ is the considered wavelength, Λ the grating's spacing, φ the angle from the surface plane) (Ahmed et al., 2017d). The angle-resolved far-field images indicated that PN-assisted nano-fabrication enables broad-range (up to $\theta = 70°$) diffraction patterns (see Fig. 54h). However, lower tilt angle ($\theta = 10°$) illumination shows bright far-field diffraction compared with higher tilted angle illumination ($\theta = 80°$), due to omnidirectional light scattering from the edge of the micro-patterns at the bigger angle ($\theta = 80°$).

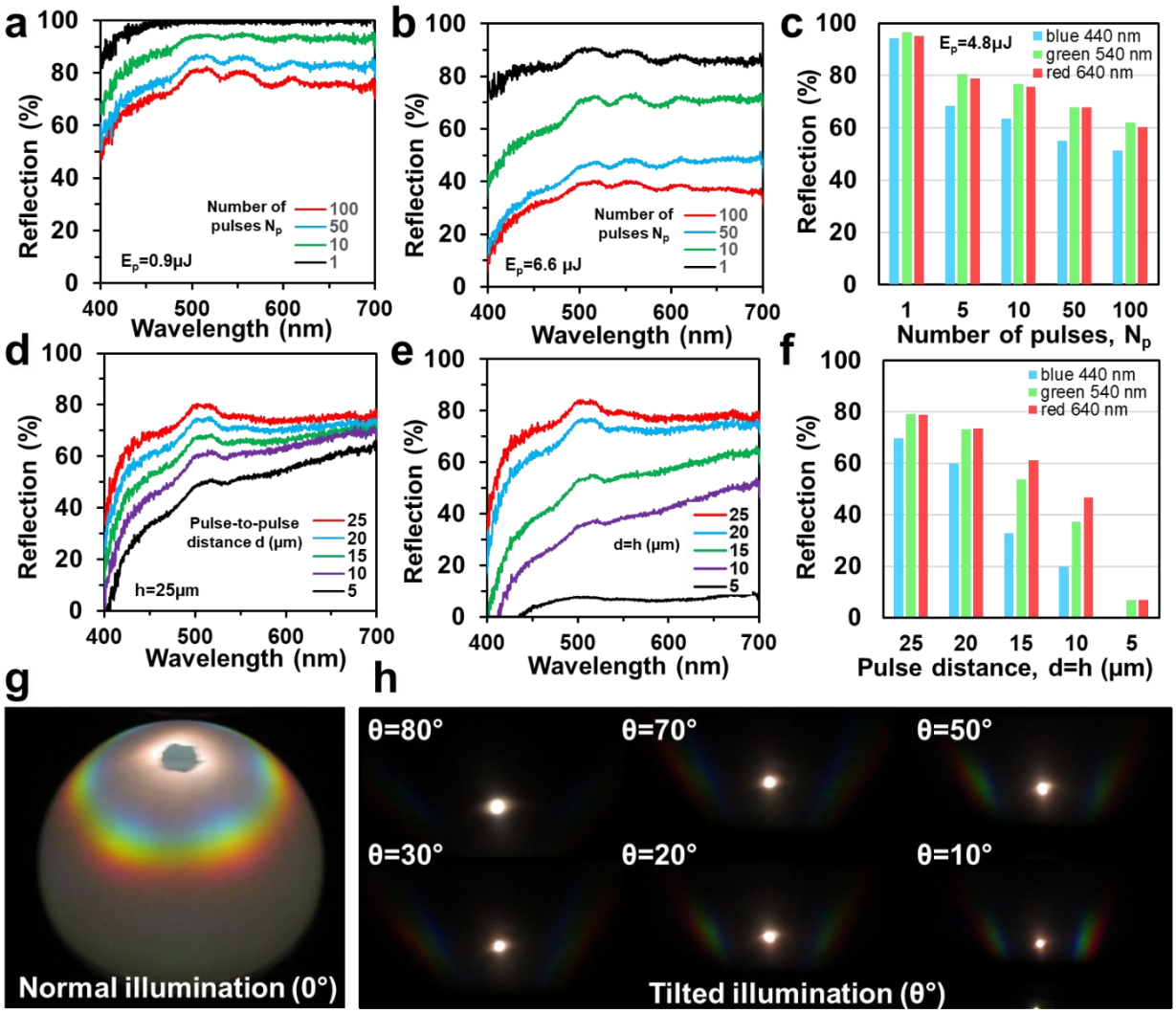

Figure 54. Optical characterization of nanotextured stainless steel. The evolution of broadband reflection with the increase of pulse numbers with two different pulse energies (a) 0.9 μJ and (b) 6.6 μJ. (c) The reflection evolution for three selected wavelengths, 440 nm (blue), 540 nm (green) and 640 nm (red), with pulse numbers (constant pulse energy of 4.8 μJ). The evolution of reflection properties with the pulse-to-pulse distance for (d) fixed σ = 25μm and (e) σ = δ. (f) The reflection evolution for selected blue, green, red wavelengths, with the pulse-to-pulse distance σ = δ. (g) Light scattering properties under normal illumination of the surfaces, projected on a 30 mm-hemispherical semi-transparent surface. (h) Light scattering properties under different illumination angles, from 10 to 80°.

5.3.3.2 Wettability and microbiological properties

Wettability properties of nanopatterned surfaces were investigated with 6 µl of water (n = 3) after prior surface cleaning, with sonication in ethanol solution and air flow drying. While non-textured stainless steel had a static water contact angle (CA) around 90° (between hydrophobic and hydrophilic), nanotexturing had two opposite effects on wetting depending on the pulse-to-pulse distance used during laser processing (see Fig. 55a). If the process results in arrays of nanoholes, such as for $\sigma = \delta$ larger than 15 µm, the static contact angle decreases leading to a hydrophilic surface, with CA down to 59°. If the process results in LIPSS the CA values increased, the surface became apparently hydrophobic, with CA of 101°. In addition to the static CA, dynamic contact angle measurements were conducted for $\sigma = \delta$ equal to 5 µm. Although LIPSS seemed to be hydrophobic (increased static and advancing contact angle), the receding contact angle remained close to the reference receding CA (see Fig. 55b), which leads to sticking droplets on the surface due to the high CA hysteresis (see Fig. 55c).

In microbial experiments, samples with a structural transition from nanoholes towards LIPSS were compared regarding their bioadhesion properties. The experiments were performed with a lab strain of *E. coli* (W 3110) by incubation for 4 h in nutrition rich media. Instead of the originally nanostructured stainless steel samples, identical polymeric replicas were prepared for the bacterial assays, which allowed us to keep the original surface clean and available for further studies. It was shown recently that structural periodicities close to the cells size, similar to the 1 µm period of the PN-structures, support bacterial surface colonization and are, therefore, detrimental to the inhibition of bioadhesion (Helbig et al., 2016). However, many nanotextured samples did not show an increased amount of initially adhered bacterial cells compared to the

non-textured reference (see Fig. 55d-f). One sample type even exhibited a significantly lower bacterial colonization after 4 h compared to unstructured surfaces (see Fig. 55e). In particular, this sample type processed at $\sigma = \delta$ equal to 10 µm represents a transition from the hexagonally ordered nanoholes fabricated with larger pulse-to-pulse distances and self-organized subwavelength structures (LIPSS) fabricated with lower pulse-to-pulse distances (see Fig. 53c-g). While the bacterial assays did not show a similar monotonous trend as the static wetting measurements, interestingly, a strong increase in bacterial adhesion could be observed for the ripples-like LIPSS. SEM images in Figure 55f show that transition is accompanied by a smoothening of the surface, but periodic surface features are still visible, whereas the roughness on the LIPSS structure seems to be more pronounced.

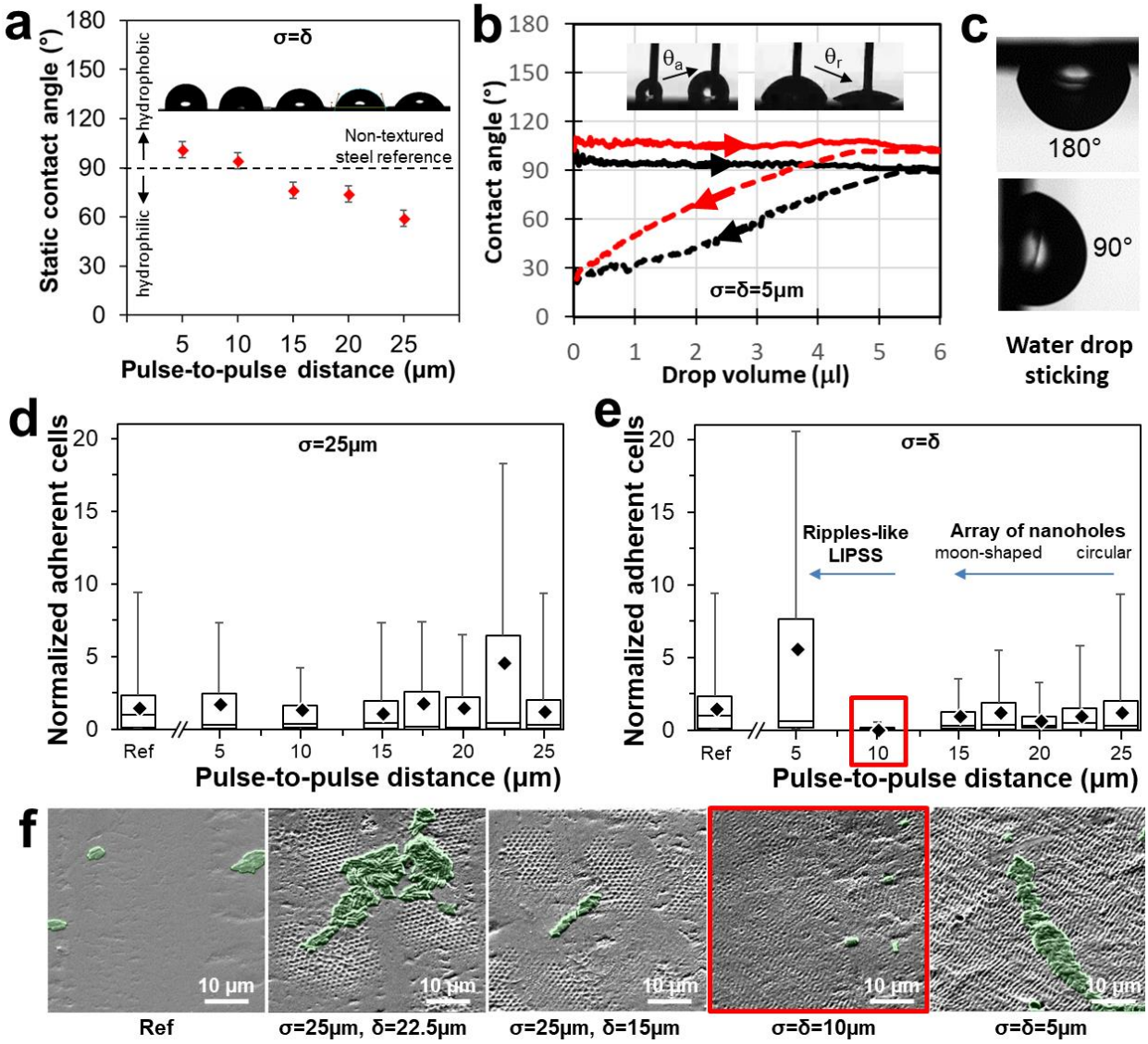

Figure 55. Wettability and microbiological characterizations of subwalength surface structures. (a) The evolution of static water CA with the pulse-to-pulse distance (σ = δ) on stainless steel. (b) Advancing and receding water CA for polished and σ = δ = 5 μm textured stainless steel. (c) A tilting test illustrating the sticking effect of water drops onto the σ = δ = 5 μm textured stainless steel. (d) The evolution of normalized adherent *E. coli* cells after 4 h incubation on PFPE replicas with the fabricated pulse-to-pulse distance, for (d) σ = 25 μm and (e) σ = δ. Data are shown in box-whisker plots with half of all data points within the box and 100 % within the whiskers; black diamonds in the boxes indicate mean values and the black horizontal line the median value (n = 14). (f) Representative SEM images of adhered E. coli on replica of (from left to right): non-structured reference, σ = 25 μm and δ = 22.5 μm, σ = 25 μm and δ = 15 μm, σ = δ = 10 μm, σ = δ = 5 μm. The adhered *E. coli* cells are highlighted in green halos.

5.4 Conclusion

Microsphere-assisted nanopatterning was performed with a femtosecond near-infrared laser. A hexagonal close-packed monolayer of 1-μm-diameter silica spheres was deposited onto stainless steel and then used to generate dense arrays of PN with spot sizes smaller than the beam wavelength. The simulation results were used to estimate the near-field enhancements obtainable with microsphere sizes close to the irradiation wavelength. The minimum PN beam size was calculated to be ~ 470 nm at the surface. Nanobumps, array of nanoholes and honeycomb structures were fabricated with periodicity equal to the microspheres' sizes. Nanoholes' arrays with 1μm spacing and a minimum diameter of 120 nm were generated by employing a single pulse irradiation. Thermal side effects associated with the femtosecond pulsed PN were observable for high fluences with detrimental impact on nanoholes' homogeneity. A beam focal offset was beneficial for the single-pulse fabrication of homogeneous nanoholes, however microspheres were removed from the immediate vicinity of textured areas. Multiple pulses could not improve the typically 1:10 aspect ratio but led to a range of surface self-organized structures (LIPSS). Interestingly, the fluence threshold for LIPSS generation was reduced and the LIPSS periodicity could be tailored according to the microspheres' sizes. The nanoholes' filling ratio could be optimized by employing pulse-to-pulse distances and thus to minimize the DLC effect in single-pulse processing. LIPSS could also be generated to close gaps between islands of nanoholes' array. Multiple characterization of surface functionalities were performed for different arrays of nanoholes and LIPSS. Surfaces exhibited efficient broad range light scattering (up to $\theta = 70°$). Surface reflection and scattering properties could be tailored and specific visible wavelength range could be absorbed. The wetting of the textured surfaces responded differently for array of holes than for LIPSS, showing a monotonous decrease of the static contact angle

from 100° for LIPSS down to 60° for hexagonal-arranged nanoholes, correlating with the gradually change of process parameters. No similar comprehensive trend could be found in microbial adhesion tests, but there was a significant decrease in bacterial surface colonization after 4h on surfaces situated in the transition between nanohole and LIPSS structures. This could open a new pathway for future studies to evaluate the PN-assisted technology for inhibition of bacterial adhesion.

Acknowledgment

The authors would like to acknowledge Tarek Alashraf at Leibniz-IPF, in processing micrographs for counting the attached bacteria.

Funding

This work was carried out within the framework of the H2020 ITN programme “European ESRs Network on Short Pulsed Laser Micro/Nanostructuring of Surfaces for Improved Functional Applications” under the Marie Skłodowska-Curie grant agreement No. 675063 (www.laser4fun.eu). In addition, the work was supported by two other H2020 FoF programmes, i.e. the projects on “Modular laser based additive manufacturing platform for large scale industrial applications” (MAESTRO) and “High-Impact Injection Moulding Platform for mass-production of 3D and/or large micro-structured surfaces with Antimicrobial, Self-cleaning, Anti-scratch, Anti-squeak and Aesthetic functionalities” (HIMALAIA).

Chapter 6

Mechanical durability of hydrophobic surfaces fabricated by injection moulding of laser-induced textures

Journal Paper, published

Romano J.-M. [(1)], Gulcur M. [(2)], Garcia-Giron A. [(1)], Martinez-Solanas E. [(3,4)], Whiteside B.R. [(2)], Dimov S.S. [(1)] (2019) Mechanical durability of hydrophobic surfaces fabricated by injection moulding of laser-induced textures, Applied Surface Science, 476, 850–860.

[(1)] Department of Mechanical Engineering, School of Engineering, University of Birmingham, B15 2TT Birmingham, United Kingdom
[(2)] Centre for Polymer Micro & Nano Technology, Faculty of Engineering and Informatics, School of Engineering, University of Bradford, Bradford BD7 1DJ, United Kingdom
[(3)] ATRIA Innovation, C/Alaún 14, nave 5, 50197, Zaragoza, Spain
[(4)] BSH Home Appliances, Av. de la Industria 49, 50016 Zaragoza, Spain

Authors' contributions: J.-M. Romano is the first and main author of this publication. J.-M. Romano designed the experiments and laser-textured the inserts. M. Gulcur assisted with the sample preparation and preliminary optimisation of the micro injection moulding, that was then performed by J.-M. Romano, under supervision of Prof. B.R. Whiteside. E. Martinez-Solanas provided support for the mechanical abrasion test, which was conducted by J.-M. Romano and A. Garcia-Giron. J.-M. Romano characterised the topographies and wetting properties with assistance of A. Garcia-Giron. J.-M. Romano wrote the manuscript, that was reviewed by M. Gulcur and A. Garcia-Giron, under supervision of Prof. B.R. Whiteside and Prof. S.S. Dimov.

Highlights

- The mechanical durability of textured surfaces is studied.
- Laser-induced topographies were replicated onto polypropylene surfaces.
- The surface energy and the Wenzel/Cassie-Baxter state of the textured surfaces were quantified.
- The hydrophobicity decreased with the progressive abrasion of the topographies.
- Standardised 3D areal parameters were correlated with surface wettability.

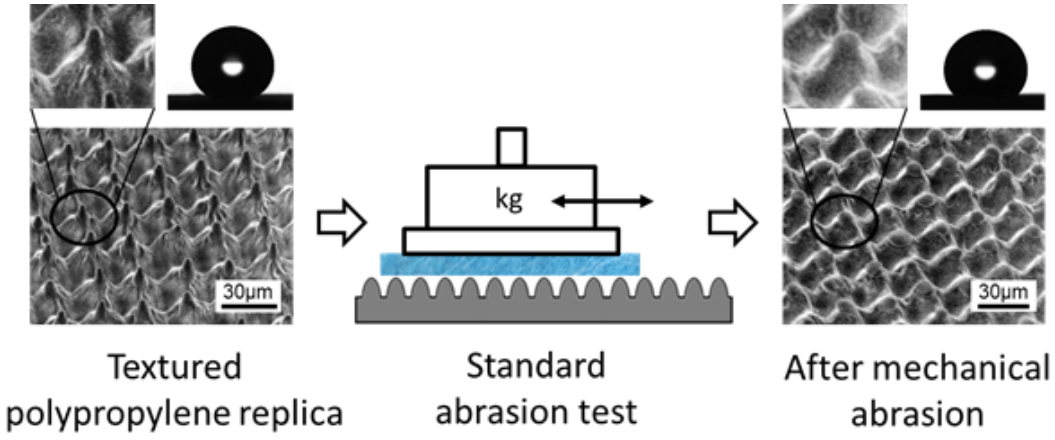

Figure 56. Graphical abstract.

Keywords: Laser texturing, Injection moulding, Wettability, Cleaning, Durability, Areal parameters.

Abstract

The paper reports an investigation on the mechanical durability of textured thermoplastic surfaces together with their respective wetting properties. A range of laser-induced topographies with different aspect ratios from micro to nanoscale were fabricated on tool steel inserts using an ultrashort pulsed near infrared laser. Then, through micro-injection moulding the topographies were replicated onto polypropylene surfaces and their durability was studied systematically. In particular, the evolution of topographies on textured thermoplastic surfaces together with their wetting properties were investigated after undergoing a controlled mechanical abrasion, i.e. reciprocating dry and wet cleaning cycles. The obtained empirical data was used both to study the effects of cleaning cycles and also to identify cleaning procedures with a minimal impact on textured thermoplastic surfaces and their respective wetting properties. In addition, the use of 3D areal parameters that are standardised and could be obtained readily with any state-of-the-art surface characterisation system are discussed for monitoring the surfaces' functional response.

6.1 Introduction

The design and manufacture of thermoplastic surfaces with tailored wettability is of increasing interest. While good wettability is important for many fields, e.g. coating and adhesion (Völkermeyer et al., 2013), the opposite effect is sought in producing easy-to-clean surfaces (Belhadjamor et al., 2018; Stoehr et al., 2016). Such surfaces exhibit low surface energy and repel liquids. The thermodynamic equilibrium of a liquid (L) wetting a solid surface (S) is given by the Young's equation (Young, 1805):

$$\sigma_S = \sigma_{SL} + \sigma_L \cos \theta_Y \quad (6.1)$$

wherein σ_S is the overall surface energy of a solid surface, σ_L - the overall surface tension of a wetting liquid, σ_{SL} - the interfacial tension between a solid and a liquid, and θ_Y - the liquid contact angle. When water is brought into contact with a solid that has a lower surface energy, the contact area of water with the solid is minimised. In particular, spherical drops with high contact and low roll-off angles can be observed. Such effects are witnessed in nature, e.g. on Lotus leaves or on legs of Microvelia, and can be partially attributed to specific surface topographies that are at micro and nano scales (Quéré, 2008). Numerous attempts to reproduce such bioinspired hydrophobic surface structures have been reported (Koch et al., 2009). One growing means to manufacture surfaces with a tailored wettability is the use of ultra-short pulsed lasers (Kietzig et al., 2009; Long et al., 2015a). This route to fabricate micropatterns, nanoripples or dual-scale structures has been investigated by many researchers. However, the evolution of their respective surface chemistry in ambient air or storage conditions is less studied while it is of prime importance in retaining the attractive surface functionality for as long as possible (Kietzig et al., 2011b; Martínez-Calderon et al., 2016; Cardoso et al., 2017). At the same time another indirect route for enhancing the hydrophobic properties of chemically stable polymers is gaining importance, especially through the use of well-established replication processes to transfer laser-fabricated surface textures/structures on tooling inserts onto thermoplastic parts (Caffrey et al., 2012; Falah Toosi et al., 2016; Nayak et al., 2013).

Wenzel and Cassie-Baxter models describe equilibrium states and define the functional dependence between the equilibrium contact angle of a plane surface, θ_Y, and the contact angle

of a structured one, θ_W. Especially, Wenzel introduces in the model the roughness ratio ($r_W \geq 1$) that is the fraction of developed/processed areas of a solid over its nominal one (Wenzel, 1936):

$$\cos \theta_W = r_W \cos \theta_Y \quad (6.2)$$

As it is well-known, Equation 6.2 confirms that for hydrophobic materials the surface roughness increases the hydrophobicity. In the superhydrophobic regime, when the water contact angle is higher than 150°, the Cassie-Baxter (CB) model (Cassie and Baxter, 1944) describes the entrapment of air pockets onto the surface structures/textures:

$$\cos \theta_{CB} = -1 + \varphi_{CB} (\cos \theta_Y + 1) \quad (6.3)$$

where the filling ratio ($\varphi_{CB} \leq 1$) distinguishes the fraction of solid that is in contact with the liquid. The Cassie-Baxter state is usually metastable and a potential imbibition can lead to Wenzel state, i.e. wetting of the surface structures (Kietzig et al., 2011a).

To assess the functional response of easy-to-clean surfaces, their cleanability has to be investigated. During the products' lifetime, any damage to surface topographies will inevitably impact their wetting behaviour, i.e. contact angle values, and thus will affect the desirable functional surface response. Therefore, any mechanical abrasion and surface wear play a very important role in assessing products' durability as a whole. In addition, no standardized cleanability test exists to validate the product durability and usually water contact angle measurements are taken after harsh mechanical abrasion to judge about the surfaces' functional degradation (Han et al., 2018; Gong et al., 2016; Bai et al., 2016; N. Wang et al., 2015).

This paper reports an investigation on the mechanical durability of textured thermoplastic surfaces. Laser-induced topographies with different aspect ratios from micro to nanoscale were

fabricated on mould inserts employing an ultrashort pulsed laser. Then, polypropylene replicas were produced through micro-injection moulding. In this way, hierarchical surface topographies exhibiting the Cassie-Baxter state were "imprinted" on thermoplastic replicas. Their durability was assessed by performing cleaning cycles in reciprocating mode and thus to quantify the impact of mechanical abrasion on surface topology and its wetting property. Finally, the interdependencies between standardised 3D areal parameters and surface functionality, i.e. wettability, were analysed to identify correlations between them.

6.2 Materials and methods

6.2.1 Laser texturing of inserts

A mould steel bar with grade 1.4021 (Uddeholm Stavax ESR) was machined to produce inserts with dimensions ∅10 mm x 7 mm. The insert surfaces were polished to 40 nm (Sa). The process chain is illustrated in Figure 57a. Then, the inserts were textured by employing a laser source with pulse length of 310 fs and wavelength of 1032 nm (Amplitude Systemes Satsuma). A 3D scan head (RhoThor RTA) was used to steer a spot diameter of 30 µm in the focal plane (see Fig. 57b). In this way, different laser-based texturing techniques were employed to fabricate a broad range of micro/nano scale topographies on the steel inserts. In the case of microsphere-assisted "Photonic Jet" (PJ) texturing, a preliminary step was required, involving the deposition of a hexagonal closely-packed monolayer of 1 µm SiO_2 microspheres onto a hydrophilic sacrificial substrate using the Langmuir-Blodgett technique and its transfer onto the insert using a highly transparent adhesive (Nitto CS9862UA). Irradiating of such surface preparation resulted in microsphere-assisted direct laser ablation and the fabrication of array of submicron holes.

Furthermore, Laser-Induced Periodic Surface Structures (LIPSS) processing was used to produce a regular 1D submicron grating with a periodicity close to the laser wavelength, using a linear laser polarisation and high pulse overlap strategy to form homogeneous linear-like ripples on the insert surface. Finally, micro scale ablation was used to manufacture lotus-inspired morphologies with different aspect ratios and grid structures by varying the spatial distance between intersecting grooves. The process settings used to laser texture eight inserts (detailed in Table 4) were selected based on reported results (Kietzig et al., 2009; Martínez-Calderon et al., 2016; Romano et al., 2018a; Römer et al., 2009b; Sedao et al., 2012; Vorobyev and Guo, 2015) and some preliminary trials. After the laser texturing operation, the inserts were first sonicated in ethanol bath for 15 min and then rinsed with water and air dried.

Table 4. The process settings used to laser texture steel inserts.

Nr.	Description	Power (W)	Rep. Rate (kHz)	Speed (mm/s)	Pitch (μm)	Focal offset (mm)	Layer (-)	Strategy
0	Untextured	-	-	-	-	-	-	-
1	Array of holes	0.245	100	1000	10	-1	1	Horizontal
2	LIPSS	0.330	500	2000	2	0	1	Horizontal
3	Lotus1	1.975	250	500	25	0	10	Grid
4	Lotus2	1.975	250	500	25	0	20	Grid
5	Lotus3	1.975	250	500	25	0	50	Grid
6	Grid1	3.945	500	500	40	0	20	Grid
7	Grid2	3.945	500	500	60	0	20	Grid
8	Grid3	3.945	500	500	80	0	20	Grid

6.2.2 Micro-injection moulding

Polypropylene (PP) is commonly used for injection moulding polymer parts for many application areas, e.g. in producing home appliances, automobile air ducting parts, wet-cell battery cases,

pipes and pipefittings, etc. Therefore, a polypropylene-homopolymer compound (Ineos PP 100-GA12) in the form of a translucent non-polar thermoplastic was selected to investigate the durability of different surface topographies.

The replication process was performed employing a state-of-the-art micro-injection moulding (micromoulding) machine (Wittmann Battenfeld MicroPower 15). A schematic of the micromoulding set-up is provided in Figure 57c. Based on the material manufacturer's datasheet and some initial trials, the heating profile was set to increase progressively along the four defined zones from the hopper to the nozzle with values of 200, 200, 215 and 230 °C, respectively. The temperatures of the moving and fixed halves of the mould were controlled using pairs of cartridge heaters and J-type thermocouples. The textured inserts were integrated into a modular tool and polypropylene parts with outer circular cavity of ∅17 mm and 0.5 mm thickness were produced. The textured area was located in the middle of the outer cavity of the polymer parts with a diameter of 10 mm as illustrated in Figure 57. Micromoulding was carried out using an injection pressure of 400 bar and an injection speed of 200 mm/s. After the filling stage a holding pressure of 450 bar was applied for 5 s. The micromoulding cycle time was 25 s and its four stages are shown in Figure 57d. Micromoulding studies reported in the literature (Huang, 2007; Sha et al., 2007; Vella et al., 2015) and the initial trials showed that mould temperature and holding pressure were the most important factors affecting the replication quality of micro/nano features. Therefore, two different levels for mould temperature (60 and 80 °C) and holding pressure (450 and 700 bar) were used. Further moulding trials were performed and micromoulded parts were visually inspected to avoid burrs and demoulding defects. The topographies achieved on textured surfaces were investigated to maximise their aspect ratio and replication quality. The replication process was stable after 20 micromoulding cycles and then

batches of 50 samples were produced using the eight textured inserts and one polished reference insert. The parts were produced without using any demoulding agent and thus to avoid potential contaminations of replicas and to ensure a good replication of textured surfaces.

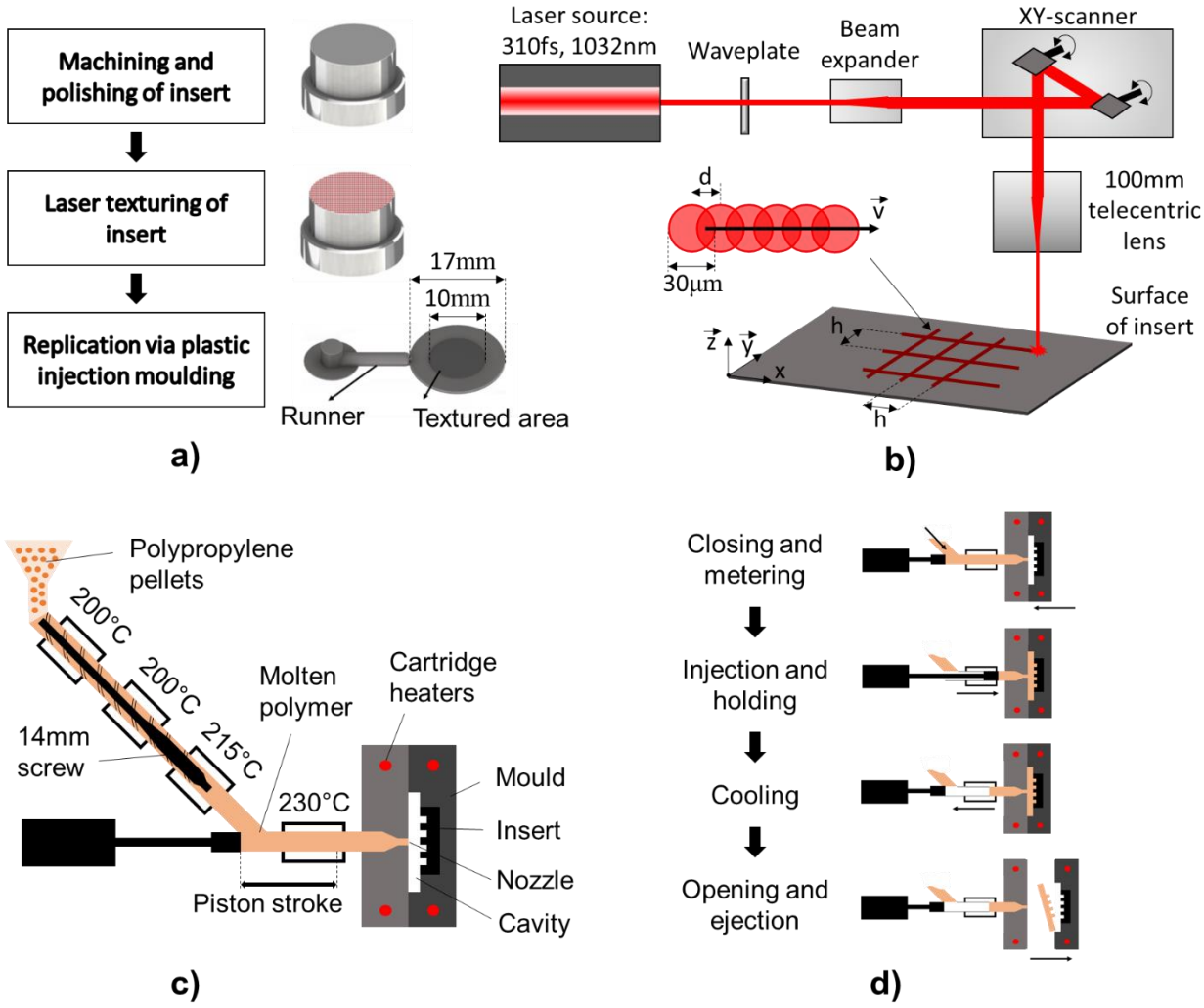

Figure 57. The process chain used to produce polypropylene samples; a) the process steps included in the chain; b) the laser processing employed to texture the inserts where d and h refer to the pulse-to-pulse and hatch distance, respectively; c) replication of textured surfaces via injection moulding; d) the stages in the 25 s injection moulding cycle.

6.2.3 Abrasion test

The mechanical durability of the textured polymer samples was assessed by adapting the ASTM D3450 standard that was originally developed for abrasion tests of coatings (ASTM D3450-15, 2015). In particular, the micromoulded discs were positioned in a washability tester (Elcometer 1720) and a multipurpose cloth (Ubesol, composition: 60 % Viscose, 25 % Polyester, 15 % Polypropylene) was used as counterpart in the cleaning cycles. The cloth fibres had a diameter of approximately 13 μm. The cycles were performed in reciprocating mode with a total dry load of 0.05 kgf/cm^2. The texture orientation in regard to the reciprocating movement was randomised. The 180-mm full stroke length was performed at 37 cycles/min. The cloth was renewed every 125 cycles. For the test in the wet conditions, 15 ml of detergent (Fairy original) dissolved at 3:100 into distilled water was poured into the tribological contact every 75 cycles. To remove any debris and detergent before analysing the surface topology evolution and functional response, the samples were rinsed 3 times with water and air dried.

6.2.4 Surface topography

The morphologies of textured thermoplastic samples were analysed using a focus variation microscope (Alicona G5) with 50x and 100x magnification objectives, in particular with lateral and vertical resolutions of up to 440 nm and 10 nm, respectively. The 3D areal parameters were acquired by the Alicona IF-MeasureSuite 4.1 software according to the ISO 25178-2:2012 standard (ISO 25178-2:2012, 2012). The statistical analysis of areal parameters for textured steel (n = 3) and polymer replicas (n = 9) was performed in Minitab 17.1.0. 3D topographical inspections were carried out employing a scanning electron microscope (Hitachi TEM3030Plus)

with a back-scattered secondary electron detector and low vacuum. The 2D Fast Fourier Transforms (FFT) of the SEM images were performed with Gwyddion 2.51 to characterize the periodic patterns.

6.2.5 Wettability and surface energy

Each of the surfaces' wetting properties were characterised under ambient conditions using an optical tensiometer (Attension Biolin Scientific Theta T2000-Basic+). Static contact angles (θ) were measured using the sessile drop technique, after stabilisation of a 6 µl sessile drop on the surface and by applying the Young-Laplace fitting method. Dynamic contact angles were studied by dispensing 30 µl of liquid at 0.5 µl/s with the needle-in-drop method and thus to measure the evolution of quasi-static contact angles. Cycles of volume increase and decrease were performed until the values had stabilised for determining advancing (θ_{adv}) and receding (θ_{rec}) angles, respectively. The contact angle hysteresis (θ_H) was defined as the maximum value obtained with the two methods, i.e. either the difference between the advancing and receding contact angles or using the inclined plate method up to 45°.

The surface energies were quantified using a simplified Fowkes' two-component model developed by Owens and Wendt (Owens and Wendt, 1969). The overall surface energy (σ) of a liquid or a solid is considered as the sum of two intramolecular components; a dispersive (σ^D) and a polar (σ^P) contributions that are assumed to equal:

$$\sigma = \sigma^D + \sigma^P \tag{6.4}$$

Static contact angles were measured with two liquids, purified milli-Q water and diiodomethane, which surface tension components are detailed in Table 5. Diiodomethane (CH_2I_2) is used as non-polar probe liquid ($\sigma^P = 0$) because of its relatively high overall surface tension, while having a molecular symmetry. The surface tension components of textured surfaces were approximated using a geometric mean approach (Owens and Wendt, 1969):

$$\sigma_{SL} = \sigma_S + \sigma_L - 2\,(\sigma^D_S + \sigma^D_L)^{1/2} - 2\,(\sigma^P_S + \sigma^P_L)^{1/2} \quad (6.5)$$

Table 5. Surface energy components of water and diiodomethane.

	Surface energy σ_L (mJ/m^2)	**Dispersive component** σ^D_L (mJ/m^2)	**Polar component** σ^P_L (mJ/m^2)
Water	72.8	21.8	51.0
Diiodomethane	50.8	50.8	0.0

Assuming complete wetting ($\theta = 0°$), the wetting envelopes of the solid surfaces were calculated with the following equation:

$$R = \{[(\sigma^D_S \cos\varphi)^{1/2} + (\sigma^P_S \sin\varphi)^{1/2}\,] / (\cos\varphi + \sin\varphi)\}^2 \quad (6.6)$$

where $0 \leq R$ and $0° \leq \varphi \leq 90°$ are the polar coordinates.

The work of adhesion (W_{SL}) refers to the force required to separate the solid-liquid interface and can be described with the free energy of adhesion (ΔG_{SL}) that is measured using the Young-Dupré equation (Van Oss et al., 1989):

$$W_{SL} = -\,\Delta G_{SL} = \sigma_L\,(1 + \cos\theta) \quad (6.7)$$

6.3 Results and discussion

6.3.1 Replication of laser-textured surfaces

Figure 58 shows the SEM micrographs of surface textures on the eight inserts processed with the laser texturing methods/strategies described in Table 4.

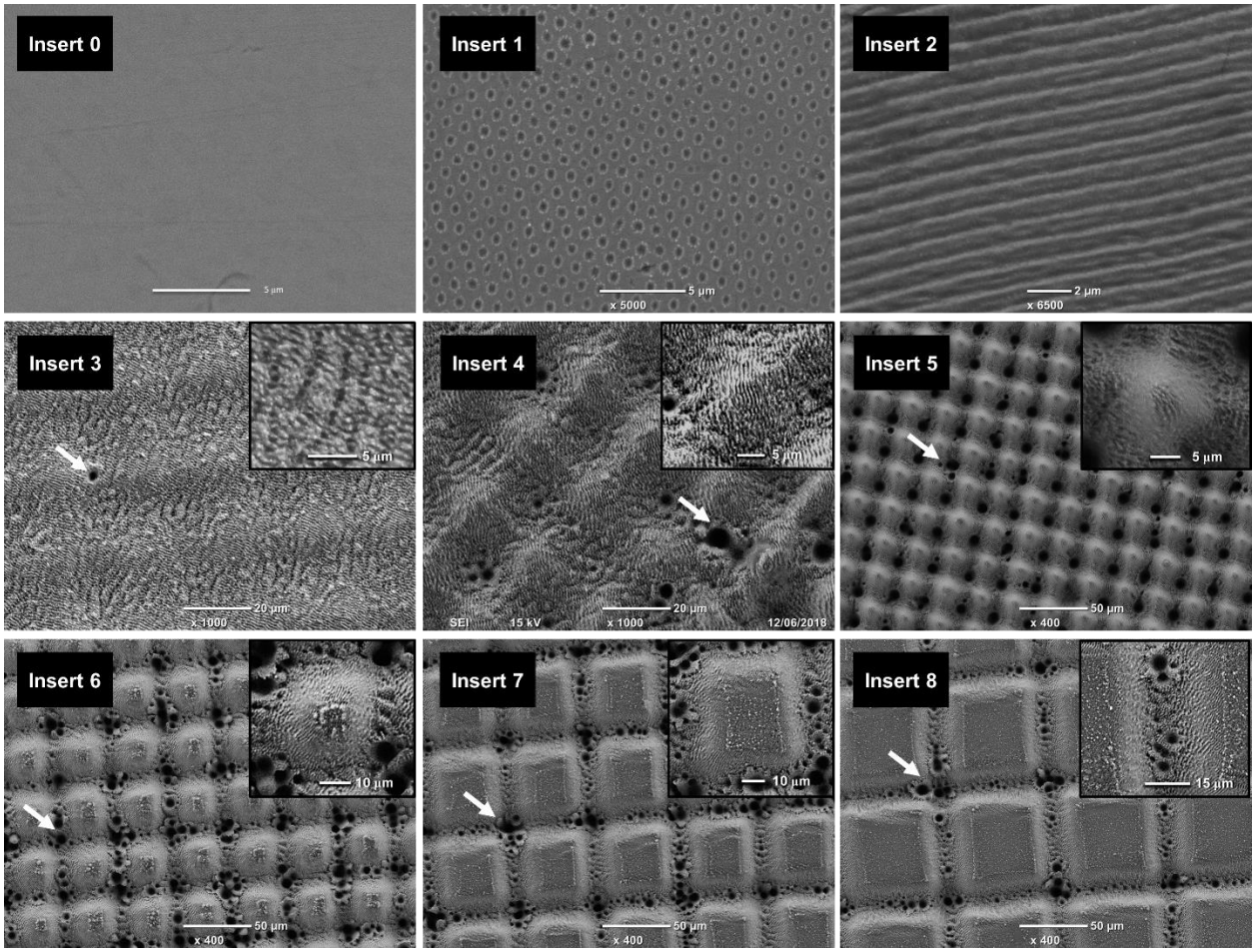

Figure 58. SEM images of laser-textured steel inserts where the white arrows point at sporadic holes. Topographical details are highlighted in close-up views. First row, from left to right: a polished surface, array of holes after 2.5-μJ laser irradiation, 1D grating generated with 90 0.7 μJ pulses. Middle row: laser processing with 7.9 μJ/pulse, 2 μm pulse-to-pulse distance, 25 μm pitch distance and 10, 20 and 50 pulses, respectively, from left to right. Bottom row: 20 scans at 7.9 μJ/pulse, 1 μm pulse-to-pulse distance and pitch distances of 40, 60 and 80 μm, respectively, from left to right.

An array of submicron holes was fabricated on Insert 1 using a microsphere-assisted near field focusing technique. As described in Section 6.2.1, a prerequisite to this laser texturing method is the deposition of a closely-packed microspheres' monolayer. The laser beam is focused beneath each microsphere by creating PJs. Upon the laser irradiation, the energy is sufficient to ablate material. Holes of $\varnothing$ 0.57 μm with standard deviation of 0.15 μm were generated. As a hexagonal closely-packed monolayer of microspheres was used, the periodicity of the resulting array of holes was equal to their diameter, i.e. 1 μm.

A submicron grating was generated on Insert 2. The self-organised LIPSS structures were created with fluence per pulse of 0.09 J/cm^2, close to the LIPSS generation threshold. The linear-like LIPSS are oriented perpendicular to the laser polarisation. The periodicity of the ripples is approximately 0.93 μm. The width of the ripples' ridges is approximately half of their periodicity.

By using a circular polarisation, the ripples' orientation was changed to 45° relatively to the scanning direction. By increasing the pulse fluence to 1.1 J/cm^2, the submicron ripples were maintained while another type of LIPSS were generated at the microscale that was perpendicular to the previous ones. At this pulse fluence, the high pulse overlap led to ablation of material and grooves were formed with a width equal to the beam spot diameter of 30 μm. Even though material was ablated, multi-scale LIPSS topographies covered the grooves as shown in Figure 58 (Inserts 3 and 4). The depth of the grooves could be increased with the number of scans.

By using these laser settings and by intersecting the laser scans, various surface topographies were fabricated on Inserts 3 to 8. In particular, multi-scale topographies were obtained on Insert 3 by scanning 10 times the surface. At the same time intersecting laser scans led to the

formation of microscale topographies consisting of peaks and valleys with aspect ratios 0.1, 0.3 and 0.9 for Inserts 3, 4 and 5, respectively. The processed areas were fully covered with LIPSS that had two distinguishable periodicities, one below the laser wavelength and the other above it. Sporadic holes were generated as a result of the increased number of scans. Especially, uncontrolled holes' formation was observed when the accumulated fluence reached the ablation threshold of the material. This physical effect was used to fabricate more complex surface geometries on Inserts 6 to 8, i.e. surface topographies with lower texturing density. The spatial distance between the intersecting scans was increased to exceed the laser spot diameter and thus to create more defined groove structures with larger untextured areas.

The textured surfaces of the steel inserts were replicated onto the polypropylene discs via micromoulding as shown in Figure 59. Even though no release agent was used in the process, no trace of polymer was observed on the cavity insert after demoulding. Insert 5 had the highest aspect ratio and was inspected closely but no noticeable polymeric debris were observed after 100 moulding cycles. Diffractive light scattering effects on the discs' textured surfaces obtained with Inserts 1 and 2 were observed as well, indicating a good qualitative replication of submicron patterns.

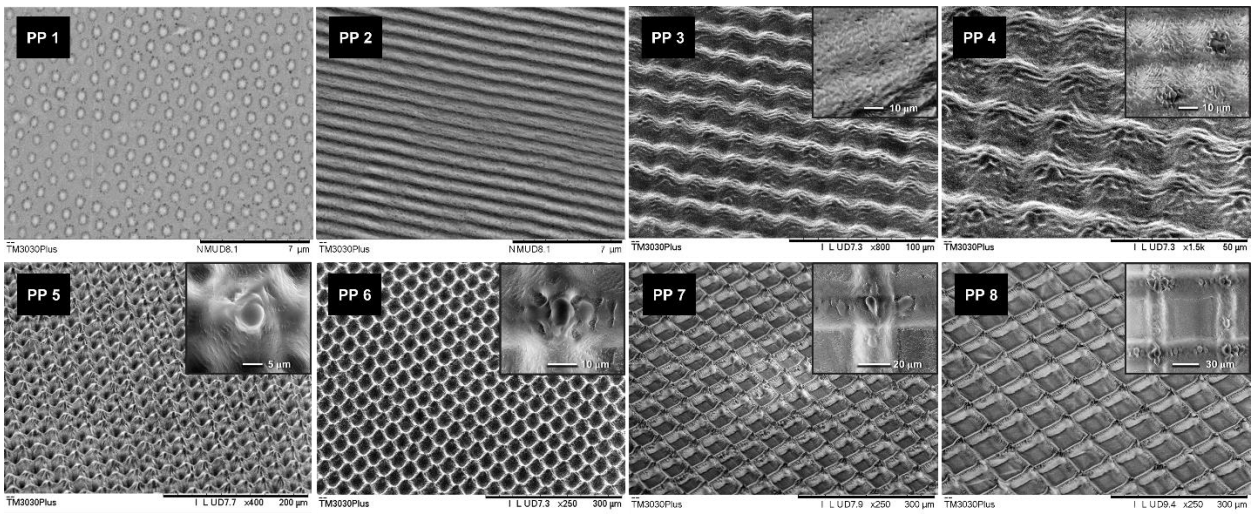

Figure 59. SEM images of micromoulded polypropylene surfaces. Topographical details are displayed in close-up views. PP1 to PP8 refer to the replica of laser-textured Inserts 1 to 8, micromoulded with 200 mm/s injection speed and 400 bars injection pressure. The mould temperature and holding pressure were 60°C and 450 bars for dual-scale topographies while 80°C and 700 bars for submicron topographies, respectively. Note: large views of PP3 to PP8 were viewed at 45°.

The previously discussed surface periodicities are depicted in Figure 60a. It appears that an increase of scanning repetitions led to a periodicity increase or decrease of the smaller and larger LIPSS, respectively. The FFT of the microscale topographies gave periodicities slightly larger than the laser pitch distance due to the cross-like texturing strategy.

Two representative areal parameters were used to assess the quality of replicated surface topographies. In particular, the arithmetical mean height (Sa) and the maximal height (Sz) were found to be consistent on as-fabricated and replicated topographies as shown in Figures 60b-c. In case of multi scale topographies, Sz values remained lower on replicas. Polypropylene exhibits a shrinkage up to 2 % (Jerry M. Fischer, 2003) that could affect the aspect ratio of replicated topographies but at the same time is beneficial during demoulding. Nevertheless, Sa values of replicated microstructures were within 90 to 105 % of those obtained on Inserts 3 to 8. The focus variation microscope did not acquire sufficient data points from the surfaces of the PP0, PP1 and PP2 samples, due to their nano scale texturing and the transparency of the material. In the case of

the untextured replica, no values were obtained. For PP1 and PP2, Sa and Sz values were larger than those on their respective inserts. This is potentially due to deformation during ejection caused by mould adhesion during the replication process. Sa remained below 0.15 µm while Sz reached 1.8 µm for submicron textures on the PP1 and PP2 samples. The peak to peak values of the PP5 samples were slightly higher than those on Insert 5, whereas Sz of the PP4 samples reached only 75 % of those obtained on Insert 4. Such variations may be explained with the low number of data points obtained at the bottom of valley's interstices and the sporadic holes.

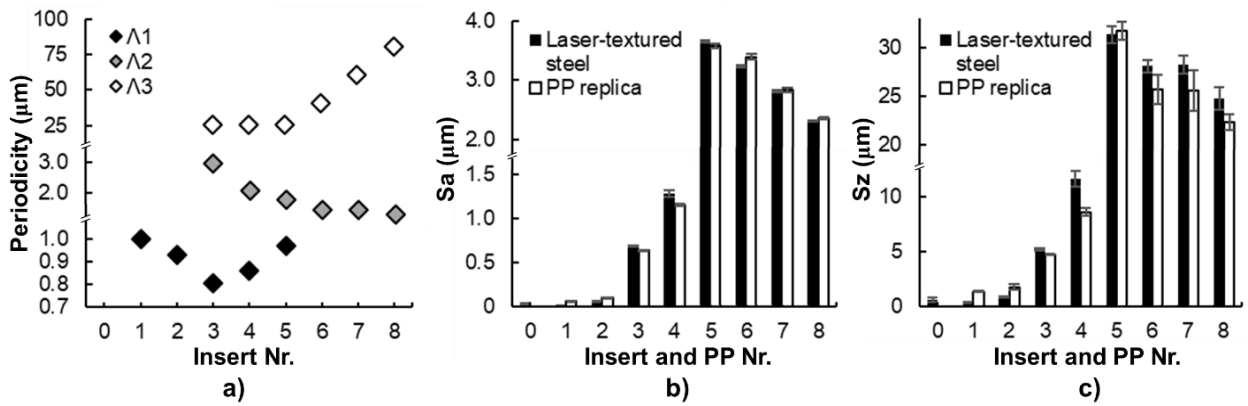

Figure 60. Comparison of topographies on inserts and replicas: a) multiple periodicities of laser-textured topographies on the steel inserts; b) Sa of replicas and their respective inserts; c) Sz of replicas and their respective inserts.

6.3.2 Wettability of laser-textured replicated surfaces

The wettability of different topographies micromoulded on PP1 to PP8 samples was assessed. The average results from 3 measurements are provided in Table 6. The physicochemistry of the polymer is considered not altered by the micromoulding process. The polymer parts are therefore assumed to remain inert and possess a stable surface chemistry over time. Indeed, no significant variations of water contact angles were observed after storing them for several weeks or after cleaning the surfaces. The homogeneous flat surfaces of the PP0 samples were taken as a

reference, i.e. with a water contact angle larger than 90° and a hysteresis larger than 10°. PP0 is slightly hydrophobic and water is "pinned" onto the surface. As predicted by the Wenzel equation, any increase in surface roughness led to a higher water contact angle (see Fig. 61a). Moreover, surface roughness had the tendency to increase the contact angle hysteresis, preventing the water drop from rolling off the surface. At the same time, submicron topographies, i.e. on the PP1 and PP2 samples, or low aspect ratio micro textures, i.e. on the PP3 and PP4 samples, did not significantly change the hysteresis but a further increase of Sa and Sz led to more than doubling of the θ_H value, i.e. on the PP6 and PP7 samples.

Table 6. Wettability analysis of polypropylene replicas, the average results from 3 measurements.

Nr.	**θ** (°)	**θ_H** (°)	**σ_S** (mJ/m^2)	**σ^P_S** (mJ/m^2)	**ΔG_{SL}** (mJ/m^2)	**r_W** (-)	**φ_{CB}** (-)
PP0	105.7	13.3	27.4	0.1	-53.1	1.00*	1.00
PP1	109.1	13.8	27.8	0.0	-48.9	1.21*	0.92
PP2	115.0	13.7	31.4	0.5	-42.1	1.56*	0.79
PP3	115.9	14.3	31.6	0.6	-41.0	1.62*	0.77
PP4	124.3	15.9	34.5	2.2	-31.8	2.08*	0.60
PP5	159.9	27.0*	36.2	9.4	-4.4	2.80*	0.08
PP6	142.5	33.9	17.6	2.3	-15.0	2.69*	0.28
PP7	142.3	34.2	15.6	1.8	-15.2	2.59*	0.29
PP8	133.0	23.3	16.6	0.9	-23.2	1.97*	0.44

Notes: θ - water contact angle; θ_H - contact angle hysteresis; σ_S - surface energy; σ^P_S – the polar component; ΔG_{SL} - surface free energy; r_W - calculated Wenzel roughness; φ_{CB} - calculated Cassie-Baxter factor (*Wenzel state).

Using Equations 6.4 and 6.5, the surface energies and polar components of micromoulded samples were calculated (see Table 6 and Fig. 61b). The surface energy remained similar between the PP0 and PP1 samples while it increased for LIPSS and Lotus textures (PP2 to PP5) and reduced for grid textures with the larger spacing (PP6 to PP8). The homopolymer chains $(C_3H_6)_n$ present in polypropylene are non-polar molecules. Accordingly, the polar component of surface energy remained close to 0 for the non-textured and most of low aspect ratio textured

replicas. The polar component was the highest for the PP5 samples and reached similar levels as corona-discharge-treated polypropylene (O'Hare et al., 2002), though remained stable over time. The replication of surface topography by micromoulding resulted in an increased surface roughness, too, and also appeared to create a polar state that might inhibit the necessary plasma activation if bonding is required. Therefore, the effects of the polar state on potential follow up plasma activation operations should be investigated further.

Equation 6.6 was used to plot the wetting envelopes of micromoulded surfaces as shown in Figure 61c. The plotted lines indicate the scale of adhesive forces at the liquid/solid interface that are necessary to overcome the cohesive forces within the liquid and would result in complete wetting of the surface ($\theta=0°$). The resulting graph shows the expected wettability of any liquids on the investigated textured polypropylene surfaces. No polar components were calculated with Equations 6.4 and 6.5 for the reference as shown in Figure 61b, but a polar component close to 7 mJ/m^2 was observed for the PP5 samples. Nanotextures on the PP1 samples did not affect the surface energy or the wetting envelope significantly. The LIPSS morphologies on the PP2 samples enlarged the area enclosed by the wetting envelope. In regard to the surface energy components, the dual scale topographies on the PP3 samples had the same effect as those on the PP2 ones. The PP4 envelope is enlarged slightly towards the dispersive component while the PP5 one has the largest overall enclosed area due to the bigger polar component. On the contrary, the areas enclosed by the PP6, 7 and 8 envelopes are significantly smaller despite their higher polar components compared with the reference. At the same time, their surfaces have the lower surface energy per unit area and the reasons for this should be investigated further. The graphs show that a good wetting can be expected if low polar and low surface tension liquids, such as oils and adhesives, are used.

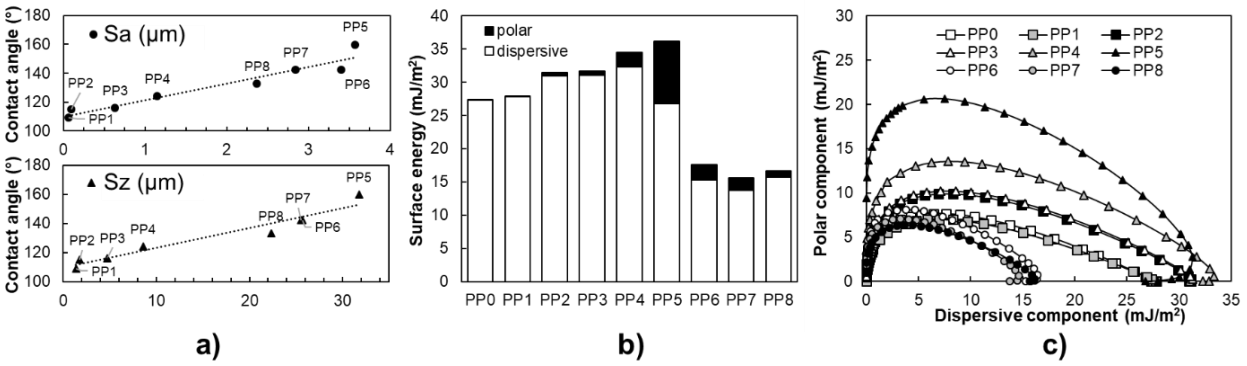

Figure 61. The wetting properties of textured surfaces on micromoulded polypropylene samples: a) the evolution of contact angle relative to Sa and Sz; b) surface energy and c) wetting envelopes.

The free surface energy was calculated using Equation 6.7. From the formula, it can be expected that a lower contact angle entails a higher work of adhesion W_{SL} and thus more energy would be required to separate the solid-liquid interface. Indeed, the absolute value of ΔG_{SL} was the highest for the PP0 samples and then dropped strongly with the increase of roughness and aspect ratios. In the superhydrophobic regime, the water contact angle needs to be larger than 150° and the rolling angle should be lower than 10°. In such case, the surface exhibits low contact angle hysteresis and little energy would be required to separate a liquid drop from the textured surface. However, the topologies with the high aspect ratio had a detrimental effect on θ_H and the values for all textured surfaces were higher than the reference of 13.3°, hence preventing water drops to roll out of the micromoulded surfaces. Only the textured surfaces on the PP5 samples were superhydrophobic with θ = 159.9° and a rolling angle estimated to be below 5°. The rolling was assessed by dropping a sufficient volume of water on a slightly tilted surface so that the gravity releases the water drop from the needle. PP5's rolling angle could not be measured accurately, as the water drop could only be deposited by applying a gentle pressure that resulted in wetting the surface and "pinning" the water drop onto the high aspect ratio surface topography as shown in Figure 62a.

Starting with a contact angle of 105.7° on the reference PP0 samples, the theoretical value of 3.20 for r_W is required to achieve a superhydrophobic regime, i.e. $\theta = 150°$. However, the maximum r_W value measured in this research was 2.80, confirming that the Wenzel regime didn't apply on all topographies. Also, based on the experiments carried out in this research it could be stated that it is more probable to reach a Cassie-Baxter state when r_W is higher, as expected. The Cassie-Baxter (φ_{CB}) and Wenzel (r_W) factors were calculated by using the apparent contact angle and the one after inducing micro vibration on the samples. In this way, it was possible to avoid metastable regimes and reach the most stable Wenzel state. The values are provided in Table 6. The Cassie-Baxter state is very pronounced on the textured surfaces of the PP5 samples ($\varphi_{CB} << 1$), however it is metastable as depicted in Figure 62b. Micro vibrations could reduce the contact angles from superhydrophobic to lower hydrophobic states. All other investigated surface topographies were either in full Wenzel or mixed Cassie-Baxter/Wenzel states (see Fig. 62c).

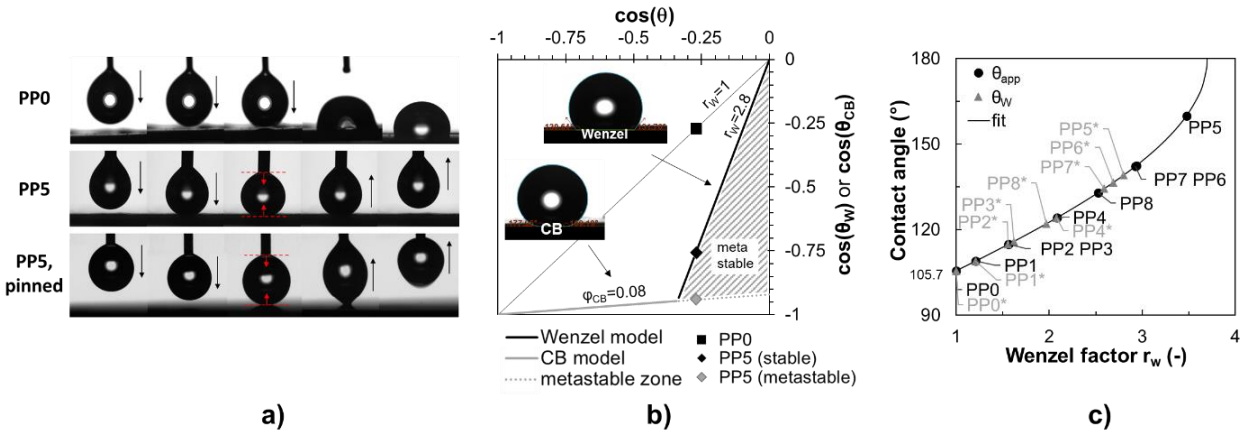

Figure 62. Wettability analysis: a) deposition of a 6 µl water drop on the untextured polymer compared to the PP5 one in Cassie-Baxter or Wenzel states, due to the exercised mechanical pressure; b) Wetting state transition for the PP5 sample; c) a comparison of apparent contact angle with the induced Wenzel state (*) for the investigated topographies on the micromoulded samples.

6.3.3 Effects of cleaning cycles on surface functionality

The robustness of textured polymeric surfaces was assessed by performing reciprocating abrasion cycles in both wet and dry environments. These specifically designed cleaning cycles were aimed to mimic real-life cleaning routines on surfaces (see Section 6.2.3). The number of cycles was varied to study the progressive damage imposed to the micromoulded surfaces. The asperities of the investigated topographies were the first entities to be in tribological contact with the cleaning cloths and this can explain why they were progressively abraded and worn, as shown in Figure 63 for the PP5 to PP7 samples. Wet cycles did not abrade the surfaces significantly when compared to the dry cycles. Especially, only the asperities of investigated PP microscale topographies were abraded after 1000 cycles in wet conditions. In dry conditions, the lotus-inspired topographies exhibited the highest sensitivity to wear and the surfaces were abraded, forming new structures with square-periodic micropatterns without dual-scale topographies.

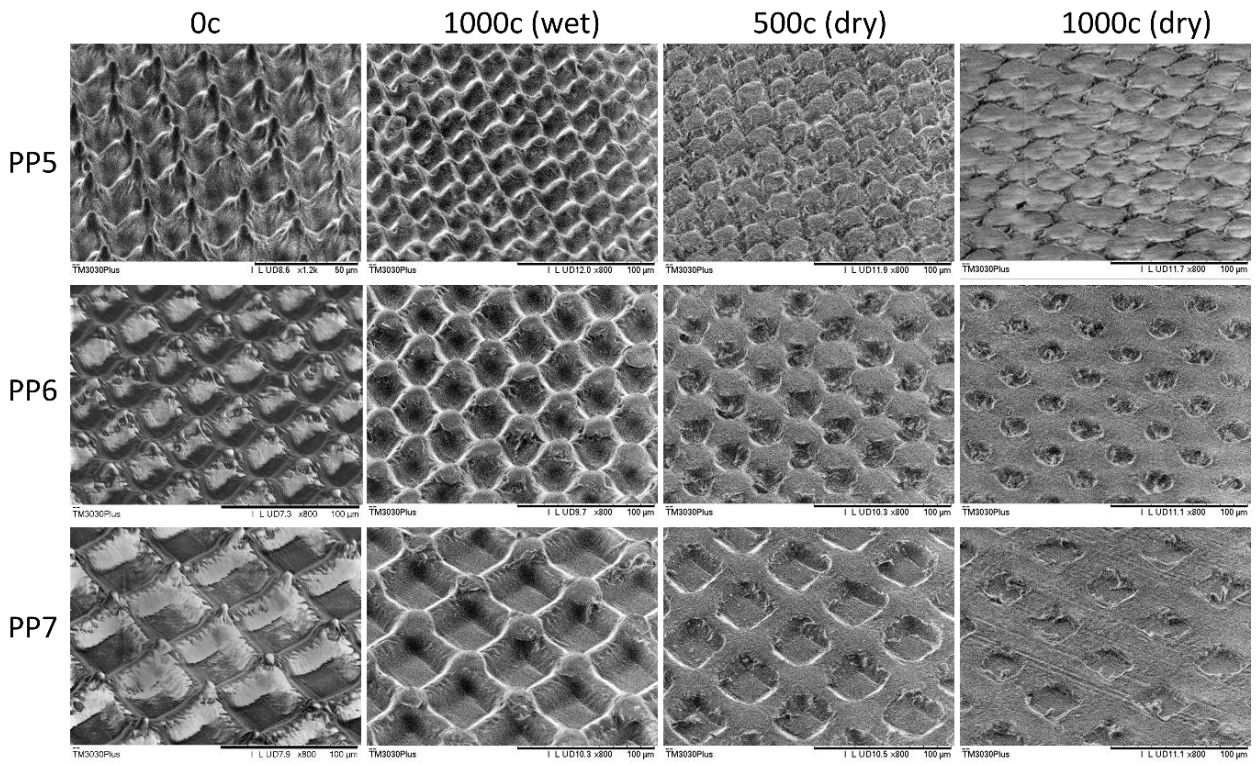

Figure 63. SEM images of textured surfaces on the PP5, PP6 and PP7 samples viewed at 45° after cleaning cycles in wet and dry conditions.

The evolution of surface topography was measured after 1000 wet and dry cleaning cycles of the textured polymer. Due to the broad variations of surface topographies and roughness scales, the absolute values are displayed in Table 7 and the relative evolution in percentage of Sa, Sz and F, normalized with the measurements before cleaning, are presented in Figure 64. There were relative increases of Sa and Sz values for the PP0 to PP2 samples, however in the PP2 case an increase was obtained only after the dry cleaning cycles. All micro-scale topographies, i.e. on PP3 to PP8 samples, exhibited a decrease of Sa and Sz by 25 % and 40 % in dry conditions, respectively, as shown in Figures 64a-b. The spread of the Sa values based on 9 measurements was within + 5 % and - 10 %, after the wet cycles while much bigger deviations were observed for Sz after the dry cycles. Moreover, the ratio (F) between measured and projected topographies, another standardised parameter, that again can be obtained directly with the

measurement systems, is displayed in Figure 64c. As the F ratio has the same definition as the Wenzel roughness (see Section 6.1), it is used to give further indication about the wetting properties of the polymer replicas. The overall evolution of F after the abrasive cleaning cycles was similar to that obtained for Sa and Sz on the samples with microscale topographies, i.e. PP3 to PP8. The maximum F value of 1.73 was measured on the initial PP5 surface but was not retained after the abrasive cycles. In particular, F decreased significantly after 1000 dry cycles to values below 1.10 for the PP6 to PP8 samples. At the same time, it should be noted that the resolution of the measurement devices did not allow a higher F to be obtained on submicron topographies, i.e. on the PP1 and PP2 samples. The low aspect ratio topographies on the PP3 and PP4 samples had also F values below 1.10 that decreased slightly after the abrasion cycles.

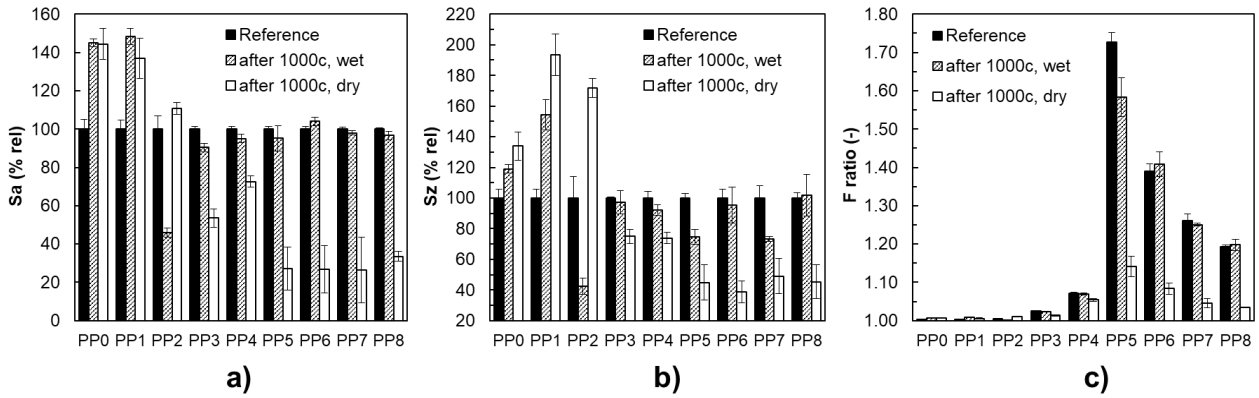

Figure 64. The evolution of surface topographies on micromoulded polypropylene samples after 1000 cleaning cycles for: a) Sa; b) Sz; and c) F.

As the topographical changes affected the surface functionality, the evolution of wettability was assessed after the abrasive cycles on micromoulded surfaces. The wetting properties were affected even after a low number of cycles, a minimum of 250 cycles being considered in this study. Overall, the wettability was retained within +/- 10 % of the reference values after 500 and 1000 cycles on all samples except PP1 and PP5. The water contact angle measurements after 1000 wet and dry cycles are provided in Figure 65a. The progressive decrease of θ was similar

for the PP6 to PP8 samples, signifying that a large spatial distance between intersecting grooves is non-significant for the mechanical robustness. For the reference PP0 sample and those with submicron roughness, such as the PP1 sample, a significant drop of θ was observed, especially below the reference value and in some cases, even below 90°. This could be explained with the increase of surface roughness, agglomeration of debris or re-entrant topographies with capillarity properties. The repeated reciprocating cycles in dry conditions could create wear tracks leading to a higher θ, as it was the case with the PP0 to PP4 samples and this is highlighted in Figure 65b. Regarding the PP5 samples, the Cassie-Baxter state seems to be lost after first contact with the surface. However, if it is compared with the Wenzel regime (θ_{PP5*} = 139.2°), the wetting properties could be retained within +/- 2 % and +/- 10 % after 1000 wet cycles and dry cycles, respectively. Dynamic contact angle measurements were performed on the cleaned PP5 surfaces, too, as shown in Figure 65c. The advancing and receding angles remained similar after 1000 wet cycles on the PP5 samples, however the same advancing angle was reached when the drop volume increased from 2 to 10 µl. The maximum advancing contact angle for the PP5 samples after 1000 wet cycles was found close to the values obtained on as-micromoulded surfaces (> 150°). The asperities of the lotus-liked valleys were certainly abraded and lost their as-micromoulded roughness. Nevertheless, the PP5 surfaces managed to retain to some extent part of their wetting properties. Topographies similar to those on the PP5 samples could be considered as a starting point for a further research into robust functional surfaces, potentially by increasing the aspect ratio of considered topographies in this research. Especially, such follow up research should provide an answer whether it would be possible to demould parts from inserts incorporating higher aspect ratio topographies.

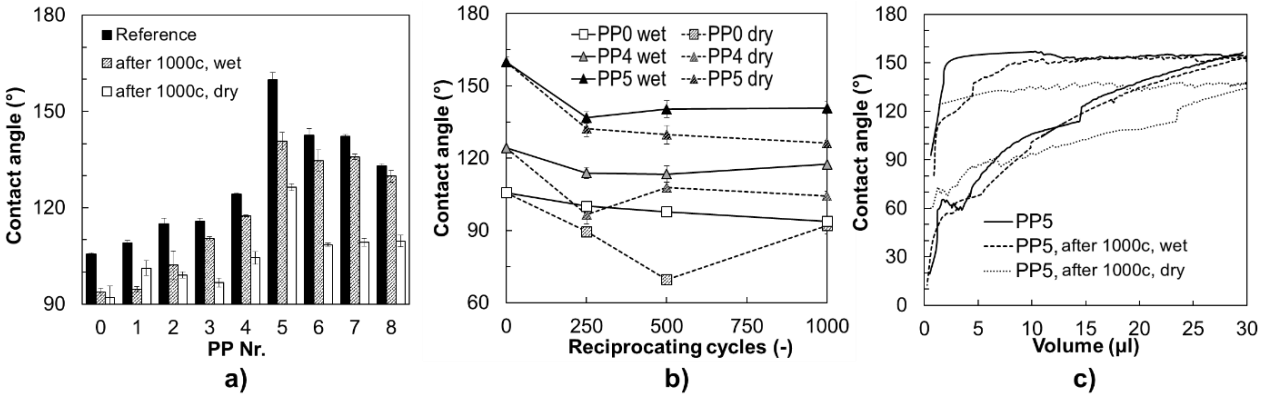

Figure 65. The wettability evolution on micromoulded polypropylene surfaces after the abrasive cycles: a) water contact angles after 1000 cycles in wet and dry conditions; b) the evolution of contact angles on the PP0, PP4 and PP5 samples after 250, 500, 750 and 1000 cleaning cycles; and c) the advancing and receding contact angles of PP5 surfaces before and after 1000 wet and dry abrasion cycles.

6.3.4 3D areal parameters vs. wettability

The 3D areal parameters measured on as-micromoulded surfaces are provided in Table 7. These parameters were analysed with the aim to identify interdependences between topographies and their resulting functional responses, i.e. wettability. In this section, the complete dataset acquired in this research (n = 62) is used. It should be noted that standardised 3D areal parameters were used to characterize the surface topographies and such data could be acquired with any state of the art surface characterisation systems, e.g. as Alicona G5 in this research. For wettability, a normalised value, i.e. $\cos(\theta) / \cos(\theta_Y)$, equivalent to the Wenzel roughness coefficient (r_{Weq}) is used. First, the evolution of r_{Weq} was compared to the F values in Figure 66a. While a general trend could be identified, the comparison did not suggest any clear linear regression and a significant deviation from the theoretical contact angles, calculated using Equation 6.2, was noticed.

Table 7. The 3D areal surface parameters and the respective Wenzel factor of the textured polypropylene samples.

Nr.	Sa (μm)	Sq (μm)	Sz (μm)	Sk (μm)	Sku (-)	Ssk (-)	Sdr (%)	F (-)	r_{weq} (-)
PP0	n.m.	n.m.	n.m.	n.m.	n.m.	n.m.	n.m.	n.m.	1.00
PP1	0.06	0.09	1.36	0.19	5.20	0.02	0.30	1.004	1.21
PP2	0.10	0.14	1.75	0.26	7.17	-1.15	0.51	1.005	1.56
PP3	0.63	0.78	4.71	2.12	2.52	-0.08	2.38	1.025	1.61
PP4	1.15	1.40	8.61	3.85	2.46	-0.19	7.12	1.071	2.08
PP5	3.57	4.95	31.81	8.57	3.68	-0.08	157.20	1.728	3.47
PP6	3.40	4.30	25.65	9.50	3.13	0.18	58.36	1.390	2.93
PP7	2.84	3.40	25.56	7.84	4.08	0.81	39.44	1.261	2.92
PP8	2.37	2.91	22.31	5.99	4.25	0.95	23.88	1.192	2.52

Notes: Sa - average height; Sq - root mean square height; Sz - maximum height; Sk - core roughness depth; Sku - kurtosis; Ssk - skewness; Sdr - developed interfacial area ratio; F - true to nominal area ratio; r_{weq} - equivalent Wenzel factor.

The F ratio seems to be strongly linked to Sa and Sz (see Fig. 66b). However, to have a better understanding of interdependences between wettability and surface topography, a correlation analysis was carried out between the obtained contact angles (normalised as r_{Weq}) and 3D areal parameters Sa, Sq, Sz, Sk, Sdr and F (see Fig. 66c). The highest Pearson correlation coefficient was obtained for the peak-to-peak height Sz ($r = 0.85$) followed closely by Sa and then Sq. The skewness Ssk could be considered non-correlated to wettability or the other 3D areal parameters (r between 0.02 and 0.2). The F factor evolved similarly to Sa and Sz, but its highest linear correlation was with the developed interfacial ratio, Sdr ($r = 0.97$), in particular F and Sdr increased for topographies with high density or aspect ratio. In addition, the effects of two positive factors, F and r_{Weq}, in regard to the true to nominal surface ratios were compared. There were differences in F and r_{Weq} effects but both showed a similar trend, i.e. wettability increased with F. Sa, Sq and Sz were strongly linearly correlated between each other ($r > 0.97$). The strongest correlation of Sk was with Sa ($r = 0.97$). A predicative analysis was performed to study the relationship between wettability and investigated topographies (see Fig. 66d). The 3D areal

parameters with high correlation to surface wettability were identified as Sa, Sq, Sz, Sk, Sdr and F. At the same time, Sku and Ssk were discarded as their relation to the surface functional response was below 20 %. Therefore, taking into account the correlations between considered areal parameters it could be sufficient to use Sa or Sz together with F to assess the wetting properties of surface topographies investigated in this research. Further research could be carried out in order to quantify the contribution of such 3D areal factors on the Cassie-Baxter state, especially regarding superhydrophobicity.

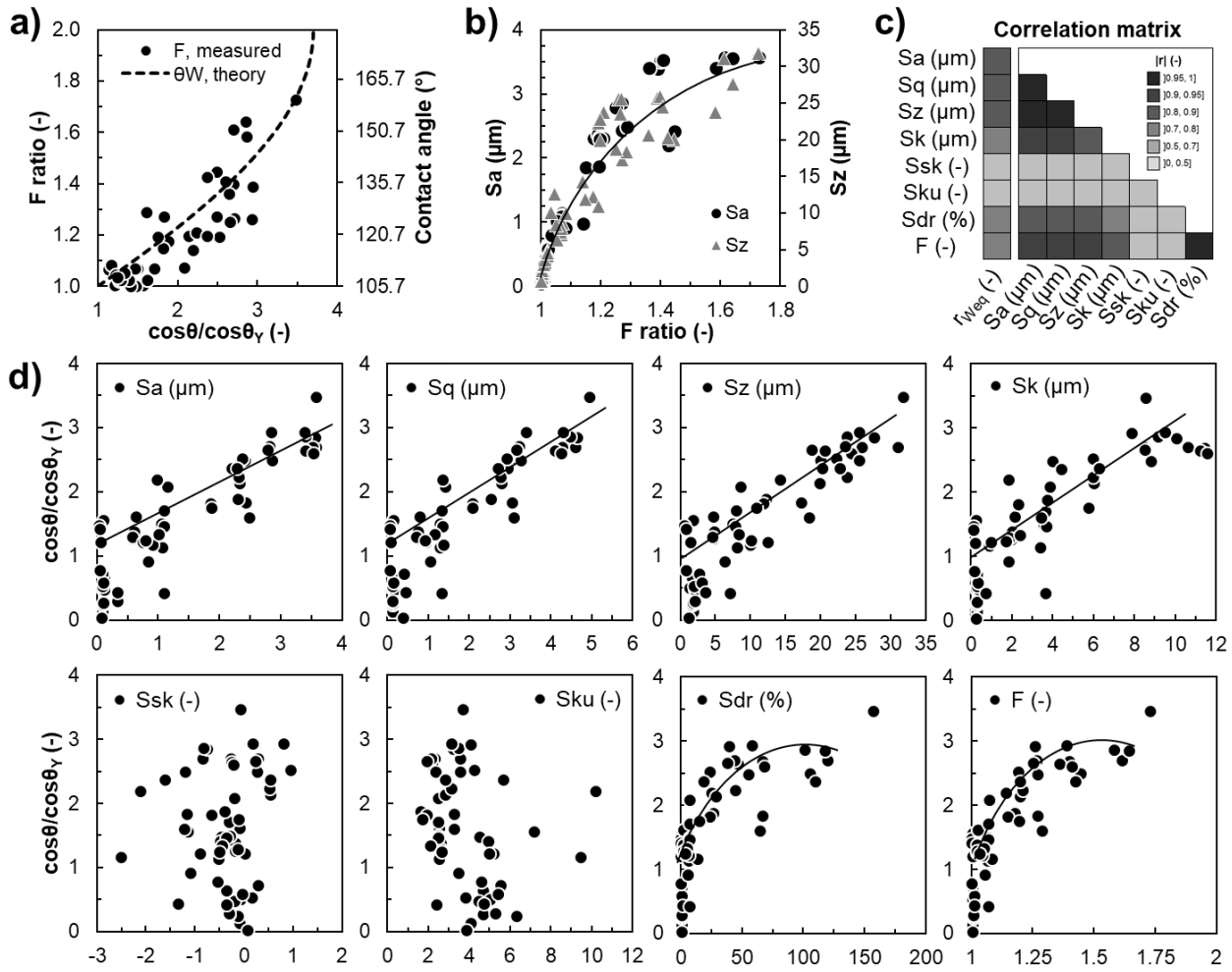

Figure 66. The interdependencies between 3D areal parameters and wettability: a) the interdependence between F and wettability; b) the relation between Sa, Sz and F; c) the matrix of Pearson correlation coefficients; d) the scatter plot screeners for the 3D areal parameters of every investigated polypropylene topography in regard to normalised wettability.

6.4 Conclusion

The durability of textured polymeric surfaces was investigated. A process chain combining ultrashort pulsed laser texturing of tool steel inserts with micromoulding of polypropylene parts was deployed. In that way, multi-scale laser-based topographies were fabricated on polypropylene surfaces. The textured samples exhibited different wetting states from hydrophobic to superhydrophobic that were quantified in terms of surface energy and surface free energy. Also, the wetting states were quantified by estimating their Wenzel and Cassie-Baxter factors.

Cleanability tests were performed with multipurpose cloths in reciprocating cycles. The mechanical abrasion of the textured surfaces led to a decrease of water contact angle. The topographies with a sole submicron roughness were not found sufficiently robust to withstand the cleaning cycles. On the contrary, the dual scale textures exhibited a minimal wear and thus to some extend were able to retain the surface topographies together their respective wetting properties. The wet cleaning cycles were found to be much less harsh to the surface textures and surface functionalities. Thus, it would be possible to define wet cleaning procedures that textured polymer surfaces could withstand with minimal deterioration of their wetting properties. In this way, the subtle metastable Cassie-Baxter state could be maintained and hence the desired superhydrophobic properties.

The empirical data gathered in the experiments suggest that the 3D areal parameters with a high correlation to surface wettability are Sa, Sq, Sz, Sk, Sdr and F. At the same time, it was found that Sku and Ssk had very low correlation, i.e. below 20 %, to the surface wetting properties. Therefore, taking into account the identified correlations between 3D areal parameters, a small

number of 3D areal parameters, e.g. Sa or Sz together with F in this research, could be considered to judge about the wetting properties of surface topographies on polypropylene parts. Such standardised areal parameters can be obtained readily using any state-of-the-art surface characterisation system and could be used to define inspection routines and also to estimate indirectly the current state of surfaces' functional response.

Acknowledgment

The research reported in this paper was carried out within the framework of European Commission H2020 ITN programme "European ESRs Network on Short Pulsed Laser Micro/Nanostructuring of Surfaces for Improved Functional Applications" (Laser4Fun) under the Marie Skłodowska-Curie grant agreement No. 675063 (www.laser4fun.eu) and the UKIERI DST programme "Surface functionalisation for food, packaging, and healthcare applications". In addition, the work was supported by three other H2020 programmes, i.e. the projects on "Modular laser based additive manufacturing platform for large scale industrial applications" (MAESTRO), "High-Impact Injection Moulding Platform for mass-production of 3D and/or large micro-structured surfaces with Antimicrobial, Self-cleaning, Anti-scratch, Anti-squeak and Aesthetic functionalities" (HIMALAIA) and "Process Fingerprint for Zero-defect Net-shape Micromanufacturing" (MICROMAN). The authors would like also to acknowledge the support and assistance of Bosch Siemens Home Appliances (B/S/H/ Spain) in conducting this research.

Chapter 7

Effects of tool wear on hydrophobic polymer surfaces replicated using plasma treated and laser-textured stainless steel inserts

Journal article, submitted

Romano J.-M. [(1)], Fantova Sarasa J. [(2)], Concheso C. [(2)], Gulcur M. [(3)], Dashtbozorg B. [(4)], Garcia-Giron A. [(1)], Penchev P. [(1)], Dong H. [(4)], Whiteside B.R. [(3)], Dimov S.S. [(1)]: Effects of tool wear on hydrophobic polymer surfaces replicated using plasma treated and laser-textured stainless steel inserts. *(Tribology – Materials, Surfaces & Interfaces, Submitted on 23/04/2019, Manuscript Number TRB685)*.

[(1)] Department of Mechanical Engineering, School of Engineering, University of Birmingham, B15 2TT Birmingham, United Kingdom
[(2)] Center for Corporate Technology and Innovation Spain, BSH Electrodomésticos España, S.A., 50016 Zaragoza, Spain
[(3)] Centre for Polymer Micro & Nano Technology, Faculty of Engineering and Informatics, School of Engineering, University of Bradford, Bradford BD7 1DJ, United Kingdom
[(4)] School of Metallurgy and Materials, University of Birmingham, Edgbaston, Birmingham B15 2TT, United Kingdom

Authors' contributions: J.-M. Romano is the first and main author of this publication. He conceived the idea of investigating the effects of tool wear on the wetting properties of textured replicas. He performed the laser-texturing of the inserts. M. Gulcur participated in conducting preliminary trials, up to 350 injection cycles. J. Fantova Sarasa performed the 5000 injections under supervision of C. Concheso. B. Dashtbozorg contributed with the GDOES measurements, sample preparation and imaging. J.-M. Romano characterised the replicas' topographies and wetting properties; and wrote the manuscript that was reviewed by B. Dashtbozorg, M. Gulcur, J. Fantova Sarasa, C. Concheso, A. Garcia-Giron, Dr. P. Penchev, under supervision of Prof. H. Dong, Prof. B.R. Whiteside and Prof. S.S. Dimov.

Highlights

- Hierarchical micro- and submicron-scale topographies were laser fabricated on plasma carburised stainless steel inserts.
- Durability of inserts after injection moulding 5000 talc-reinforced PP parts was investigated.
- Wear damages were observed on both untreated and treated inserts.
- Superhydrophobicity was retained for longer on plasma treated inserts.

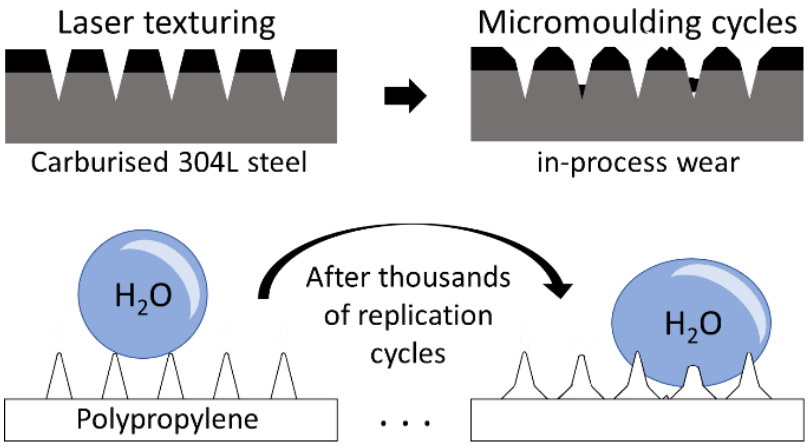

Figure 67. Graphical abstract.

Keywords: wear, injection moulding, plasma surface alloying, laser texturing, wettability.

Abstract

The mass production of polymeric parts with functional surfaces requires economically viable manufacturing routes. Injection moulding is a very attractive option however wear and surface damages can be detrimental to the lifespan of replication masters. In this research, the replication of superhydrophobic surfaces is investigated by employing a process chain that integrates surface hardening, laser texturing and injection moulding. Austenitic stainless steel inserts were hardened by low temperature plasma carburising and three different micro and nano scale surface textures were laser fabricated, i.e. submicron triangular Laser-Induced Periodic Surface Structures (LIPSS), micro grooves and Lotus-leaf like topographies. Then, a commonly available talc-reinforced polypropylene was used to produce 5000 replicas to investigate the evolution of surface textures on both inserts and replicas together with their functional response. Any wear or surface damage progressively built up on the inserts during the injection moulding process had a clear impact on surface roughness and peak-to-peak topographies of the replicas. In general, the polymer replicas produced with the carburised inserts retained the wetting properties of their textured surfaces for longer periods compared with those produced with untreated replication masters.

7.1 Introduction

The fabrication of products that incorporate surfaces with tailored wetting properties has attracted significant interest recently (Liu et al., 2010). Inspired by water-repellent surfaces observed in nature, surface structures mimicking the Lotus leaf (Zorba et al., 2008), Rose petal (Long et al., 2015a) or Springtail cuticle (Helbig et al., 2011) effects, among others, have been

studied. An analytical description of wetting regimes was originally proposed by Wenzel (Wenzel, 1936) and Cassie-Baxter (Cassie and Baxter, 1944) and then used by many researchers to explain the response of various micro and nano scale structured/textured surfaces (Koch et al., 2009; Kietzig et al., 2011a). One of the technologies widely used to fabricate multi scale surface structures is ultra-short pulsed laser processing. In particular, the technology can be applied to produce Laser-Induced Periodic Surface Structures (LIPSS) (Fraggelakis et al., 2017; Kietzig et al., 2009) with superhydrophobic properties on metals (Zorba et al., 2008; Long et al., 2015a; Wu et al., 2009; Martínez-Calderon et al., 2016; Vorobyev and Guo, 2013; Huerta-Murillo et al., 2019) or polymers by direct laser writing (Rebollar et al., 2013; Mezera et al., 2018) or by replication (Noh et al., 2010; Cardoso et al., 2015; Chun et al., 2014; Jiang et al., 2016; Falah Toosi et al., 2016).

As a result of its cost-effectiveness, injection moulding has become a very attractive replication technology for the mass production of polymer components (Brezinová and Guzanová, 2010). One of the polymers widely used to produce engineering parts is polypropylene, which has found industrial applications in automotive, aerospace and home appliances products as a result of its desirable mechanical and thermal properties (Lapcik et al., 2008). The tensile strength of polypropylene parts can be further improved through the use of talc fillers (Lapcik et al., 2008), however, this comes in expense of increased mould wear and a reduced tool lifespan (Brezinová and Guzanová, 2010). The surface functionality of replicas can be directly impacted as a result of any damage on injection moulds (Han et al., 2018; Romano et al., 2019b; Garcia-Giron et al., 2018a). Therefore, material properties of replication masters, e.g. wear and corrosion resistance, become critical considerations (Brezinová and Guzanová, 2010; Bienk and Mikkelsen, 1997). Surface treatments, such as DLC coatings (Crema and Lucchetta, 2014) or low temperature

plasma treatments (Dong, 2010) can be used to extend the lifespan of tools by improving their wear, damage and corrosion resistance.

This research investigates the durability of stainless steel mould inserts that were both plasma treated and laser-textured before being used to produce talc-reinforced polypropylene parts. The evolution of tool wear and damage with the increase of moulding cycles have been studied and discussed together with the respective wetting properties of the replicas.

7.2 Materials and methods

The process chain used in this research to produce polymeric parts with textured surfaces is presented in Fig. 68. The manufacturing route employed includes:

i) machining of metallic inserts to the dimensions of the moulding cavity;
ii) surface hardening through plasma carburisation;
iii) fabrication of micro and nano scale surface structures using an ultra short pulsed laser; and finally,
iv) the replication of the surface textures by injection moulding. In this section, these process stages together with the used characterisation techniques are described.

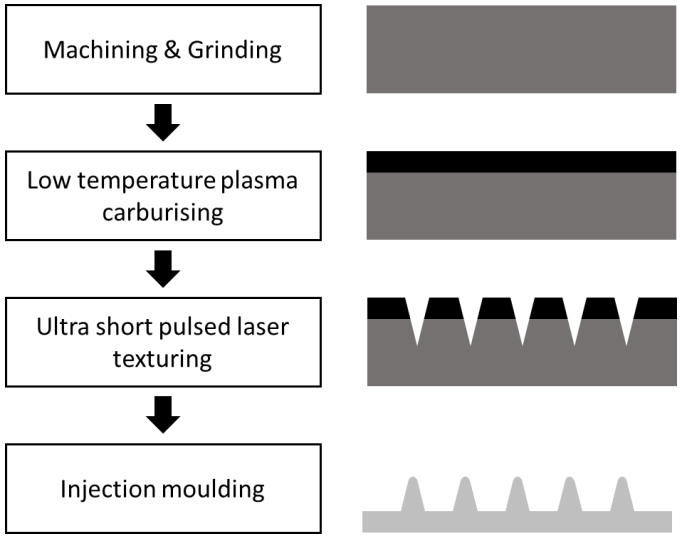

Figure 68. The process chain used in this research to produce polymer parts with textured surfaces.

7.2.1 Low temperature plasma carburising

The inserts were machined from 304L grade austenitic stainless steel to the dimensions of the moulding cavity, in particular a rectangular plate with dimensions of 60 mm x 40 mm. To enhance the wear resistance, a surface alloying treatment was utilised to diffuse carbon into the surfaces of the inserts. At low temperatures (<500°C) this results in the formation of an expanded austenite surface layer, otherwise known as S phase, that possesses significantly enhanced hardness and wear resistance. Moreover, the S phase has also been shown to retain and somewhat improve the corrosion resistance of 316L austenitic stainless steel surface even further (Dong, 2010).

Since surface oxides can act as a dense barrier to plasma treatment, samples were freshly grounded down to #1200 grit size prior to plasma treatments. Additionally, samples were also ultrasonically cleaned using Teepol and acetone in order to remove any dust, grease or contaminants on surfaces.

The inserts were then DC plasma carburised (DC Klockner Ionon 40 kVA plasma furnace) in a working gas mixture of 98.5% H_2 : 1.5% CH_4 at a pressure of 3 mbars (see Fig. 69a). The samples were treated at 400°C for 30 h. Following this treatment, the inserts were gently polished using 1 μm diamond suspension in order to remove any loose sputtered material left over from the treatment.

The resulting carburised layer was characterised by employing destructive techniques. Composition-depth profiles were obtained using a glow-discharge optical emission spectrometer (Spectruma GDA 650HR). Microhardness was measured using a Mitutoyo MVK-H1 equipped with a Vickers indenter. Also, cross section characterisation was performed on the inserts following mirror-finish polishing and chemical etching (50% HCl : 25% HNO_3 : 25% H_20) to reveal the microstructure.

7.2.2 Laser texturing

The treated stainless steel inserts were laser textured using a circular-polarised ultra-short pulsed laser (Amplitude Systemes Satsuma) with a wavelength of 1032 nm, 310 fs pulse duration and a repetition rate of 250 kHz. The beam delivery system used in this research is illustrated in Fig. 69b. In particular, a 100 mm focal length telecentric lens (QiOptiq LINOS) is integrated to focus the beam to a spot size of ~ 35 μm diameter at $1/e^2$ while a scan head (Newson RTA A2G) was utilised to steer the beam over the insert surface.

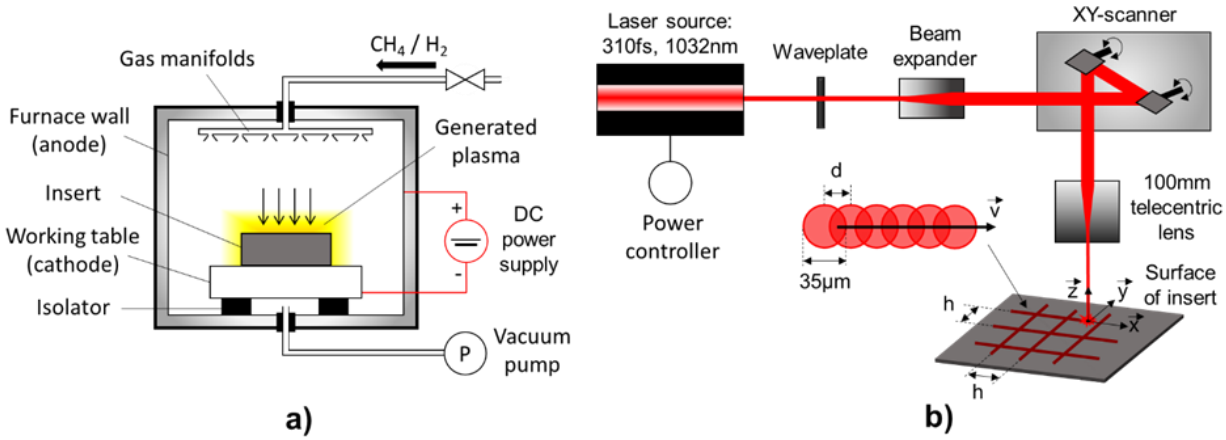

Figure 69. Diagrams depicting the plasma carburising and laser texturing setups used in the research, i.e. a) DC plasma carburising at 400°C in a gas pressure of 3 mbars; b) ultra-short laser processing in the near-infrared regime with beam spot of ~ 35 µm and surface scanning with a pulse-to-pulse distance d and hatch distance h.

Laser settings, i.e. the number of scans, fluence per pulse and hatch distance, were adjusted for producing three different surface textures and they are shown in Table 8. For each texture, the same process settings were used both on as-received stainless steel (S) and plasma carburised plates (C). The first topography was produced by parallel scan lines with a spatial displacement of 100 µm. The second one, with Lotus-leaf like structures was made by intersecting perpendicular scan lines with spatial displacement equal to the laser spot size, i.e. 35 µm. The third texture was generated using a single scan of close parallel lines at low fluence per pulse, enabling the LIPSS formation.

Table 8. List of laser processing parameters.

Topography Nr.	**Description**	**Number of scans** (-)	**Fluence per pulse** (mJ/cm^2)	**Hatch distance** h (µm)	**Pulse-to-pulse distance** d (µm)
S0 and C0	Untextured	-	-	-	-
S1 and C1	Grooves	100	950	100	2
S2 and C2	Lotus	1250	950	35	35
S3 and C3	LIPSS	1	92	2	2

Notes: S0 to S3 and C0 to C3 denote as received and plasma carburised inserts, respectively.

After the laser processing, the inserts were ultrasonically cleaned in ethanol for 15 min, rinsed and dried with compressed air.

7.2.3 Injection moulding of polymeric parts

The untextured and textured inserts were integrated into an injection moulding machine (Arburg Allrounder 170) which is schematically depicted in Fig. 70a. A polypropylene (PP) homopolymer compound containing 30 wt% talc-based mineral fillers (LyondellBasell Hostacom HKC 182L W92607) was selected due to its common use in producing polymer parts of home appliances and other engineering applications. The temperatures of the 3-zone extrusion screw and nozzle were set at 225, 230, 230 and 235°C from the hopper to the nozzle respectively while the mould temperature was set at 80°C. The heating profile was chosen based on the material datasheets and preliminary trials. The ranges of other important process variables, i.e. the flow rate from 20 to 45 cm^3/s, injection pressure from 350 to 650 bar and holding pressure from 350 to 750 bar were identified by conducting moulding trials using the laser-textured insert S1. The demoulding and ejection conditions together with the presence of flashes on the parts were monitored. The height of surface structures on the PP samples were optimised to achieve less peak-to-peak disparities. The duration of one injection moulding cycle was ~ 30 s and its stages i.e. mould closure, injection (42 cm3/s volume 10 cm^3 with 3 cm^3 cushion, 450 bar injection pressure and 80 bar back pressure), holding (550, 500, 450 bar for 1, 3, 2 s respectively), cooling (15 s), mould opening and ejection of the plastic part, are depicted in Fig. 70b. No demoulding agents were used to preserve the surface chemistry and also to prevent altering the tribological contact.

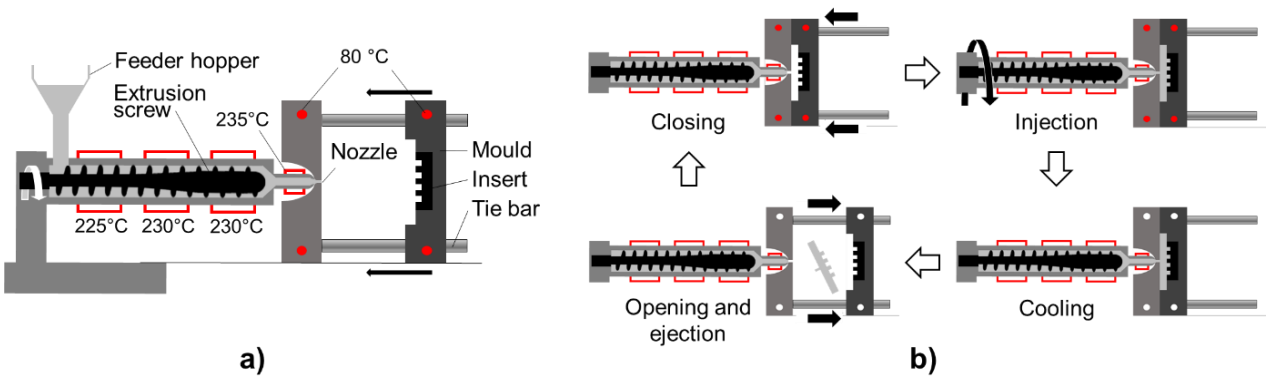

Figure 70. Schematic representations of injection moulding machine and moulding stages: a) the injection moulding setup used to fabricate the polypropylene parts; b) the stages of the injection moulding cycle.

7.2.4 Surface characterisation

A focus variation microscope (Alicona G5, objective 50x) was used to measure the arithmetical mean (Sa) and maximum peak-to-valley (Δz) heights of the structured surfaces. The average values of nine measurements were used. Topographical datasets were acquired for areas of 800x800 μm^2 with vertical and lateral resolutions of 100 nm and 1.00 µm, respectively. Also, the surfaces were inspected with a field emission gun scanning electron microscope (JEOL 7000F FEG-SEM). The polymer replicas were examined following a sputter coating of a thin gold layer and 10keV accelerating voltage was used to minimise any damage from the electron beam. The spatial periodicity of LIPSS were analysed using 2D Fast Fourier Transform (FFT) tools of the Gwyddion 2.51 software. The height of the LIPSS was measured using an atomic force microscope (Bruker Dimension 3100) equipped with tapping-mode probes (Nanosensors, PPP-Rt-NCHR). Finally, the average values of static contact angles were obtained from nine measurements with an optical tensiometer (Biolin Scientific Attension Theta T2000-Basic+) by dispensing 6 µl of milli Q water in ambient conditions.

7.3 Results and discussion

7.3.1 Carburising and laser texturing of stainless steel inserts

The first step in producing the injection moulding inserts was the surface hardening of the 304L stainless steel workpieces. The composition-depth profiles of untreated and treated workpieces are provided in Fig. 71a-b. The profiles confirmed the oxygen content at the surface of untreated stainless steel samples, i.e. 9.0 wt%, while there were no traces of oxidation in the carburised ones. As a result of the plasma carburising treatment, the carbon content at the surface increased to 9.8 wt% compared with the 1.3 wt% of the untreated samples. The surface carbon content on untreated samples exhibits a sudden drop in concentrations, showing that they are very likely as a result of surface contaminations rather than carbon diffusion (see Fig. 71a). On the other hand, significant carbon content could still be seen in the composition profiles up to a depth of approximately 15 μm (see Fig. 71b). After the chemical etching of the cross section, a homogeneous layer could be clearly seen at the surface of the treated samples on top of underlying bulk filled with some inclusion holes (see Fig. 71c). Intrinsically, the dissolution of carbon atoms within the surface led to the expansion of the austenitic lattice (Dong, 2010). This interstitial intercalation was associated with high compressive residual stresses (Dong, 2010), confirmed by an increase of the microhardness from 184 to 495 $HV_{0.05}$, i.e. for a load of 50 gf (see Fig. 71d). The load bearing capacity was examined, too, by increasing further the indentation load and it was found that there was still a 40% hardness enhancement even under a load of 500 gf.

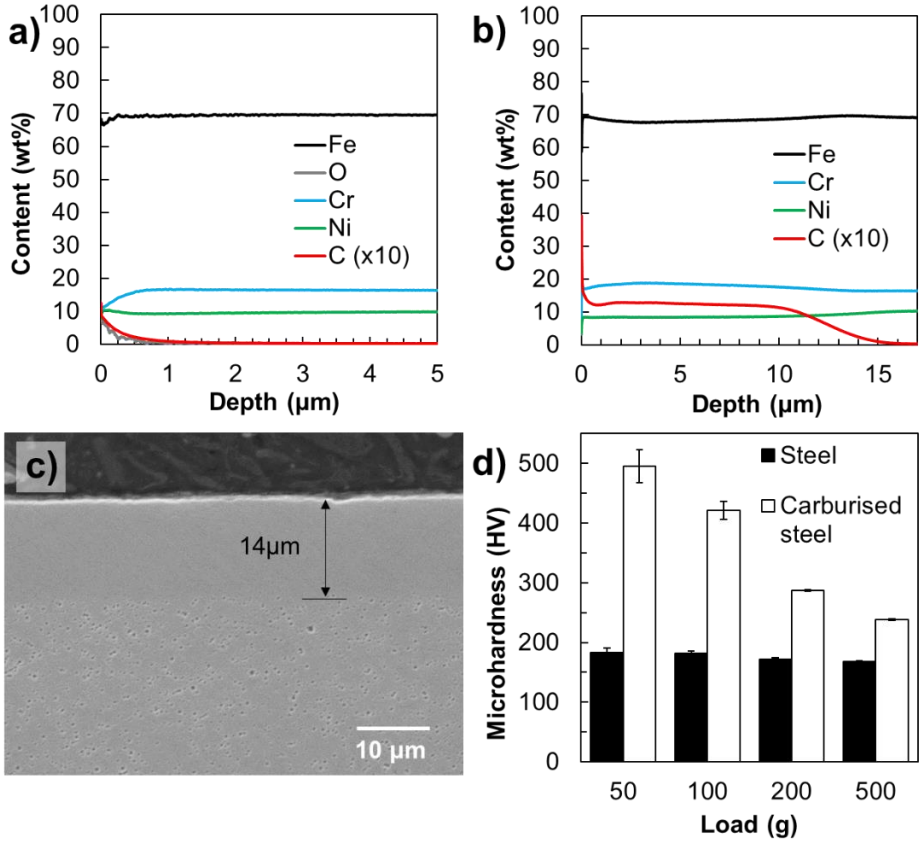

Figure 71. Composition-depth profiles of a) untreated (S0) and b) carburised (C0) inserts, c) a micrograph of the carbon expanded austenite layer and d) Vickers microhardness of untreated and carburised inserts.

The carburised layer is inherently a metastable phase (Dong, 2010), i.e. an exposure to high temperatures could trigger the precipitation of carbides, and thus to alter dramatically the corrosion resistance. Laser texturing typically leads to a thermal load on the surface with some associated negative side effects, i.e. melting, heat affected zones and topographical alterations. For example, the side effects of processing carburised (Garcia-Giron et al., 2018a) and nitrided (Garcia-Giron et al., 2018a; Gualtieri et al., 2009) stainless steels with nanosecond laser pulses have been investigated. A heat affected zone around the laser processed area was observed, resulting in the melting and oxidation of the expanded layer, and as a result its morphology, structure and mechanical properties were modified. By using ultrashort pulses in the femtosecond range in this research, the laser-material interaction time is drastically shortened to

a few picoseconds (Byskov-Nielsen et al., 2011), and therefore the laser processing could be considered athermal and this could be beneficial when texturing metastable materials. However, ultrashort laser processing with multiple pulses with high repetition rate in the MHz range has been proven to lead to incubation effects and thus to alter the morphology of laser textured surfaces (Fraggelakis et al., 2017). In this research, the repetition rate used was 250 kHz and no thermal damage, such as cracking or subsurface precipitation was observed after processing the carburised layer with femtosecond pulses.

The next step in producing the injection moulding inserts was surface texturing employing an ultrashort laser source. The three topographies that were investigated in this research are shown in Fig. 72. The laser processing parameters used to produce them are provided in Section 7.2.2. The first topography was parallel grooves with a 100 μm spacing that had a Gaussian-shaped profile with width and depth of approximately 39 and 65 μm, respectively (see Fig. 72a-b). The Lotus-leaf like structure included an array of holes with 37 μm diameter and approximately 60 μm depth (see Fig. 72c-d). The third topography consisted of Laser-Induced Periodic Surface Structures (LIPSS) (Bonse et al., 2009; Huang et al., 2009) that covered homogeneously a 6 x 12 mm^2 area. An example of the submicron surface structures is provided in Fig. 72e-f.

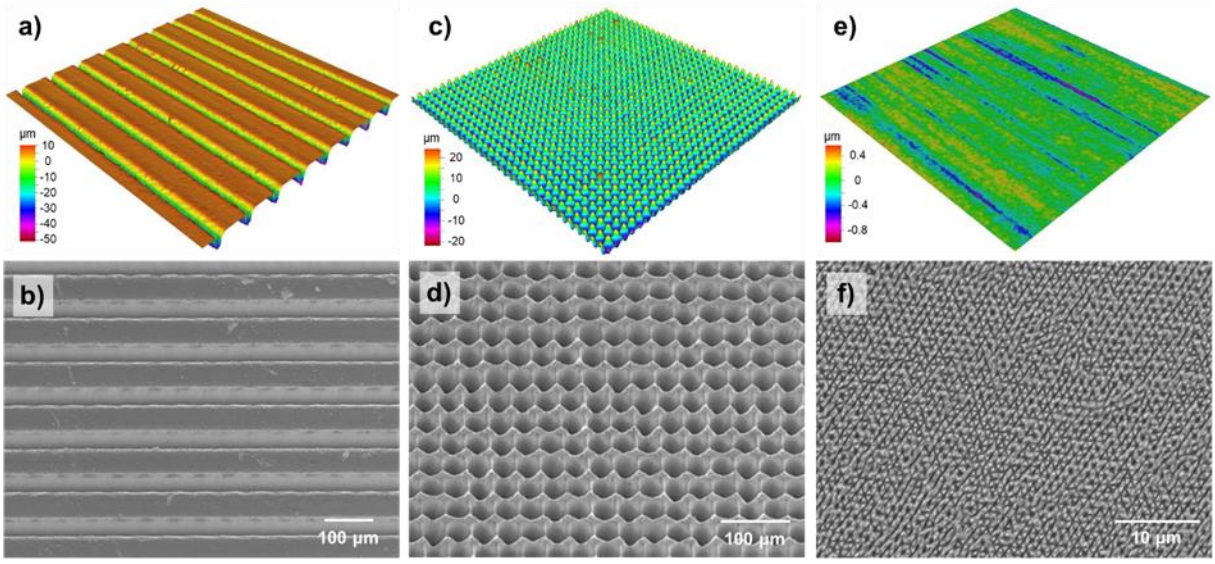

Figure 72. 3D views and SEM micrographs of the three investigated surface textures in this research, i.e. a-b) Grooves (S1), c-d) Lotus-leaf like (S2) and e-f) LIPSS (S3).
Note: The images in b) and d) are viewed at 45° angle.

The same process settings were used to texture both untreated and carburised stainless steel inserts and there were no significant differences in resulting topographies (see Fig. 73). In particular, the fabricated grooves (see Fig. 73a-b) and holes (see Fig. 73c-d) of the first two textures had similar depths and widths/diameters. Ultrashort laser processing with a polarised beam can simultaneously result in the creation of micro-scale features covered with LIPSS or some roughness (Long et al., 2015a). In this research, submicron ripples covered the grooves and Lotus-leaf like textures and thus dual-scale surface structures were produced while the ablated material and nanoparticles were deposited around the processed areas (Vorobyev and Guo, 2013). A follow up ultrasonic cleaning did not allow the redeposited material and particles to be detached and removed and they could be clearly seen along the grooves (see Fig. 73a-b) and around the holes on unprocessed areas (see Fig. 73c-d). LIPSS textures both on treated and untreated inserts were triangular in shape and the FFTs indicated a clear hexagonal arrangement (see Fig. 73e-f). Ripple-like LIPSS fabricated on nitrided stainless steel by using femtosecond

pulses was already reported (Yasumaru et al., 2013) together with complex triangular LIPSS on stainless steel (Romano et al., 2018a). The spatial distance between the ripples was 10 to 20 % smaller into the nitrided layer compared with that on untreated samples and this was attributed to the compressive residual stresses in the plasma treated layer (Yasumaru et al., 2013).In this research, the LIPSS generation on carburised stainless steel is demonstrated and the results have shown that this surface treatment made little difference on the LIPSS morphology (see Fig. 73e-f). In particular, the generated LIPSS on treated and untreated inserts had an average spatial periodicity of approximately 900 nm while the peak-to-valley distance varied between 80 and 200 nm.

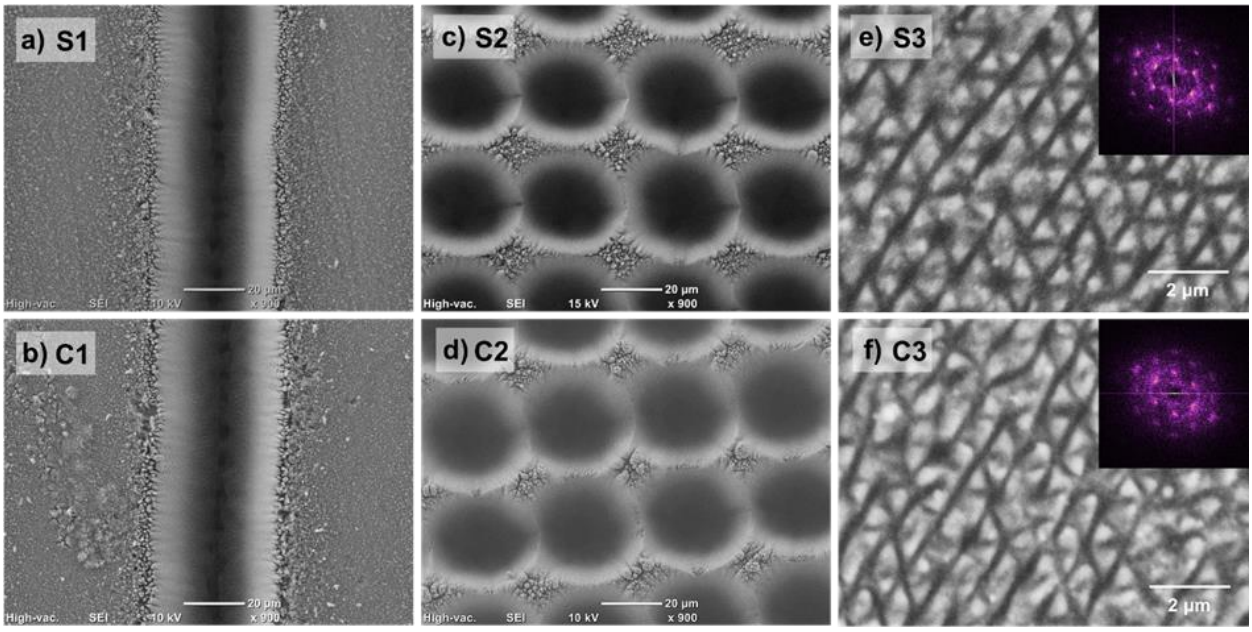

Figure 73. SEM micrographs of resulting topographies on untreated and carburised inserts, i.e.: a) S1, b) C1, c) S2, d) C2, e) S3, f) C3.
Notes: 1) the textures on untreated and carburised stainless steel are shown on top and bottom rows, respectively; 2) Grooves, Lotus-leaf like and LIPSS textures are shown from left to right; 3) the insets in e) and f) depict the respective 2D-FFTs of the S3 and C3 inserts.

7.3.2 Injection moulding of polymer replicas

The laser-textured inserts were mounted into the injection moulding modular tool and polymer replicas were produced with the process settings described in Section 7.2.3. The replicas of grooves and Lotus-leaf like textures were protruding structures with height of approximately 35 μm as shown in Figs. 74a and 74b. The generation of textures with higher aspect ratios were attempted, too, and heights up to 48 μm were achieved, however, the demoulding performance was drastically reduced, i.e. the replicas could not be readily released from the inserts. Therefore, it was more appropriate in the context of this research to use textures with a lower aspect ratios and thus to achieve a replication efficiency of at least 55%.

Both micro- and submicron textures were replicated simultaneously. For instance, the base and the walls of the features replicated from the grooves' textures were covered with LIPSS, while their tops were flat (see Fig. 74a). Similarly, denser surface topographies were produced with the Lotus-leaf like textured inserts and again LIPSS were observed around the resulting protrusions (see Fig. 74b). The triangular LIPSS were also successfully replicated, with the resulting textures being negative copies in a clear hexagonal arrangement (see Fig. 74c). The peak-to-valley heights of the replicated submicron features were in the range of 40 to 140 nm while the replication efficiency was higher (up to 70-80%).

The mineral fillers are visible on the planar surface of the moulded parts and also on the replicated surface structures. The filler-matrix interface was analysed by cryogenically fracturing the PP parts in liquid nitrogen. The layers of fillers and platelet talc particles with sizes from half a micron up to dozens of microns could be seen in the polymer matrix. The fillers had a random-in-plane alignment in the polymer bulk and an orientation parallel to the flow direction in the

replicas' skin layers due to combination of elongation forces and shear flow around the melt front (Patcharaphun and Mennig, 2007; Bay and Tucker, 1992), as shown in Fig. 74d. Also, the replicated groove-structures, depicted in Fig. 74e, illustrate how the polymer fills the cavities. The talc platelets inside the surface structures follow the cavity profile and thus a more complex alignment is formed (see Fig. 74e).

At the same time, the laser processing debris that remained after ultrasonic cleaning were transferred to the replicas during the initial injection moulding cycles (see Fig. 74f). Therefore, it is a common practice to discard the initial moulded parts (Baruffi et al., 2018), and instead begin analysing the replicas when the injection moulding process can be considered stable and performing as intended. In this research, the replicated topographies and their functional characteristics were studied after the first 50 injection moulding shots.

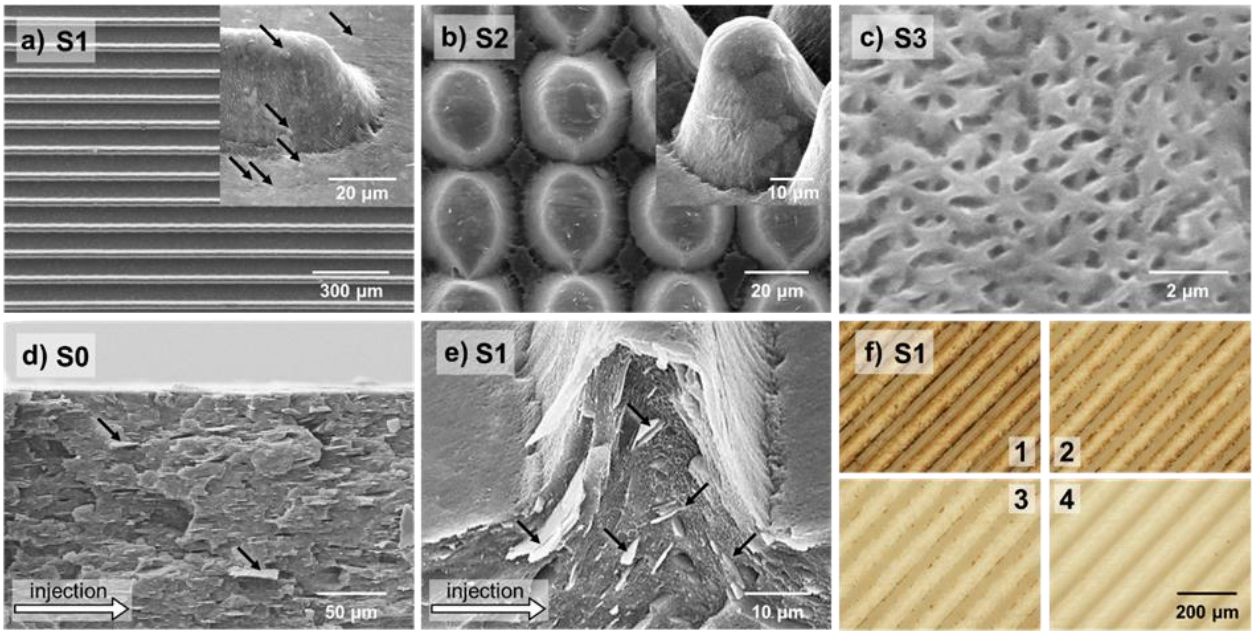

Figure 74. Top view SEM micrographs of the textured PP replicas: a) Grooves (S1), b) Lotus-leaf like (S2) and c) LIPSS (S3). SEM views of fractured PP replicas along the flow direction of injection moulded samples with d) untextured (S0) and e) Grooves (S1) inserts. Finally, the captured images of the first four replicas produced with the S1 insert are shown in f).
Note: The images in e) and in the insets a) and b) were viewed at 45° angle and the black arrows point out some mineral fillers.

7.3.3 Effects of in-process tool wear on surface topographies

5000 replicas were produced using the 30 wt% talc reinforced polypropylene from each insert. The surfaces of the inserts were analysed before and after the injection moulding cycles. Inspections following the first few cycles revealed that the laser processing debris were removed and some pits and scratches were formed, despite the fact that the insert surface was hardened (see Fig. 75a). Such surface damage could be attributed to tool wear arising from shear and frictional forces occurring between the melt flow and the insert surface during the injection stage and also during the demoulding stage (Brezinová and Guzanová, 2010; Bienk and Mikkelsen, 1997; Crema and Lucchetta, 2014). In particular, the flow of the highly viscous molten polymer induced adhesive-abrasive wear on inserts' surfaces. The formation of pits, of various sizes (see Fig. 75b-c), can be explained as a combined effect of adhesive and corrosion wear, together with abrasion wear due to the presence of talc platelets in the melt flow. An example of underling mechanism of pits' formation, as shown in Fig. 75c, is the abrasive tearing (i.e. removal) of any inclusions present on the surface of the inserts, followed by a corrosive damage of the exposed rough bulk. Traces of polypropylene could be found entrapped in the formed pits (see Fig. 75d). Such wear damage can have detrimental effects on the functional response of replicated surfaces, and therefore should be minimised by optimising the injection moulding process.

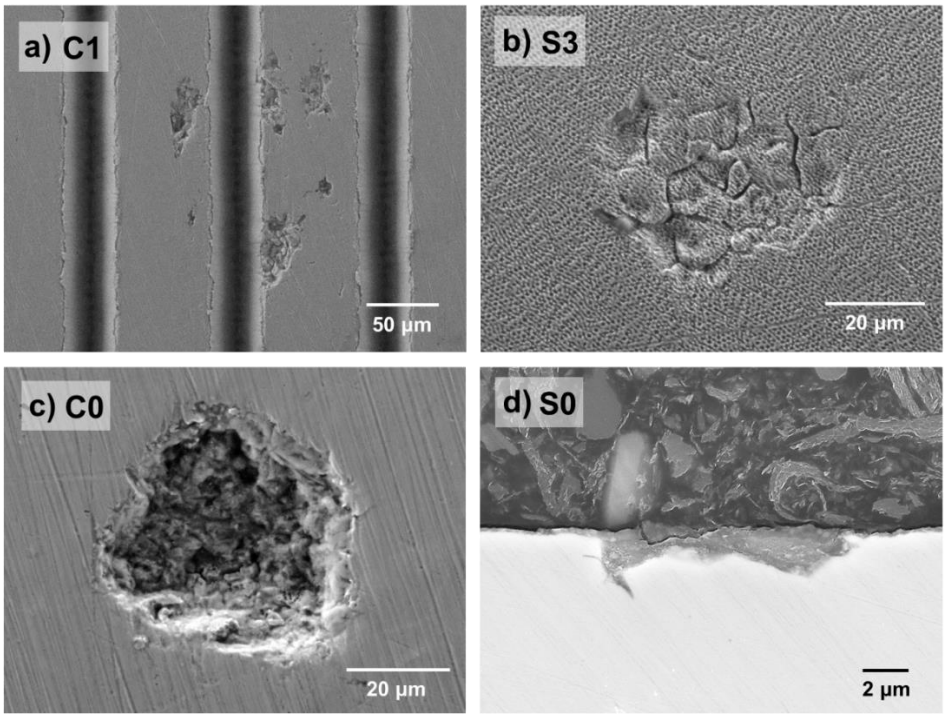

Figure 75. SEM micrographs of untreated and carburised inserts after 5000 injection cycles: a) C1 b) S3 c) C0. d) cross section of a representative surface damage/wear on S0, exhibiting traces of PP.

Further inspections of the inserts revealed the presence of redeposited material along the grooves, on both carburised and untreated stainless steel as shown in Fig. 76a-b. Through a closer look at the side walls it is possible to distinguish LIPSS inside the grooves (see Fig. 76b). Therefore, following the injection cycles, the redeposited material found at the edge of the grooves was removed due to physical delamination and wear (see Fig. 76c-d). At the same time some micro cracks into the carburised layer had been initiated near the interface with the bulk material (see Fig. 76d). Such failure mode has been previously reported for laser-textured nitrided stainless steel (Garcia-Giron et al., 2018a) or plastic injection moulding (Crema and Lucchetta, 2014), however, it is unlikely for carburised samples where the treated layer is usually much thicker and with a superior load bearing capacity.

Regarding the Lotus-leaf like structures, the redeposited material formed bulges around the holes, with no signs of any delamination (see Fig. 76e). The observed differences in comparison to the groove structures, can be attributed to the different laser processing conditions or wear mechanisms present during the injection moulding cycles. Lastly, the submicron textures, especially LIPSS, were still visible after the 5000 injections, with approximate aspect ratios between 1:5 and 1:10 on both untreated and carburised stainless steel as shown in Fig. 76h-i.

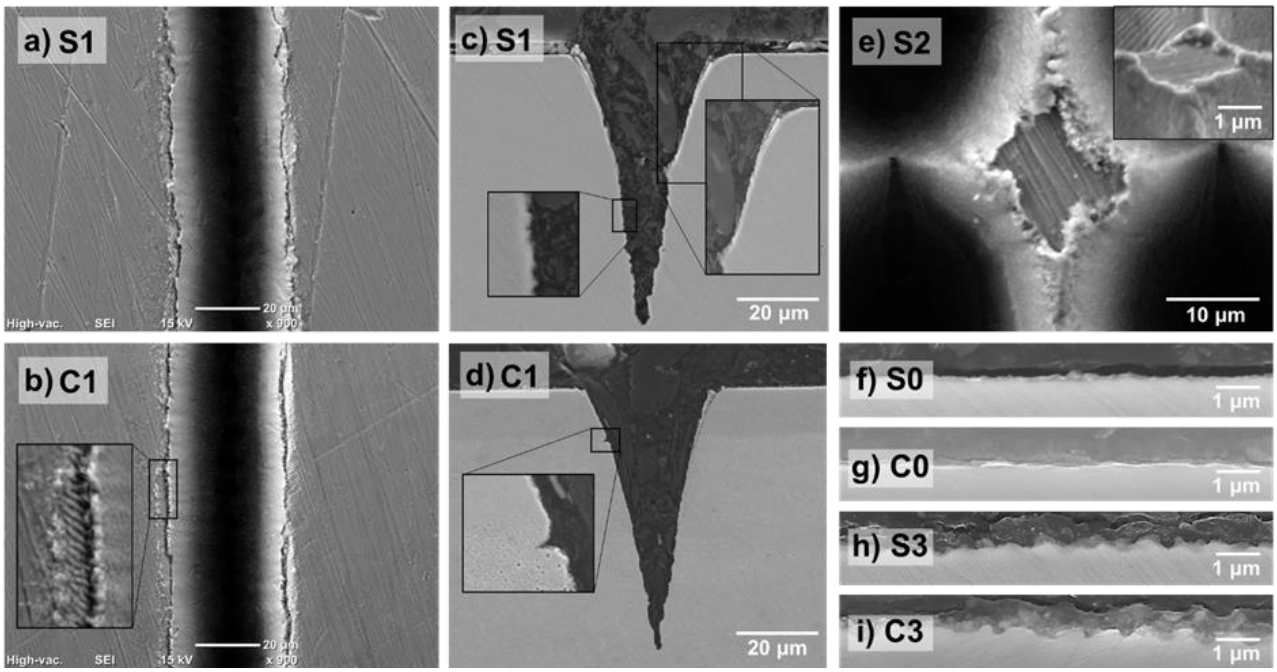

Figure 76. SEM top views and cross sections of the laser-textured inserts after 5000 injection moulding cycles: a,c) S1, b,d) C1, e) S2, f) S0, g) C0, h) S3, i) C3.
Note: the inset in e) was viewed at 45° angle.

As a result of abrasion and friction phenomena, the surface finish of the inserts was only slightly altered. Notably, the roughness of untreated inserts increased marginally after 5000 injection moulding cycles while it decreased slightly on the carburised ones. However, the Sa values remained of a similar magnitude, from 60 to 100 nm, with a maximum variation of + 3 % and - 10 % (see Fig. 77a). In comparison with other inserts a lower roughness variation was observed on the LIPSS surfaces. On the other two textured inserts, the depth of the grooves and the holes

was almost the same after the 5000 moulding cycles while the peak-to-valley height of the laser textures varied up to - 12 % (see Fig. 77b) due to the removal of debris from the surface and, eventually, the general wear of the top surface.

The topography evolution of the PP replicas with the increase of injection moulding cycles was also analysed. Arithmetical mean roughness (Sa) and maximum peak-to-valley heights (Δz) were measured on LIPSS (see Fig. 77c,e) and groove (see Fig. 77d,f) structures after 50, 200, 500, 1000, 2000, 3000, 4000 and 5000 cycles. On LIPSS replicas the roughness varied in the range from 184 to 272 nm without any specific trends. However, the height of the grooves decreased after the first 100 cycles and then increased marginally from 31 to 34 μm on replicas from both untreated and carburised inserts. Overall, the standard deviations of roughness measurements were smaller on replicas produced with the carburised inserts and this can be attributed to their higher hardness and wear resistance.

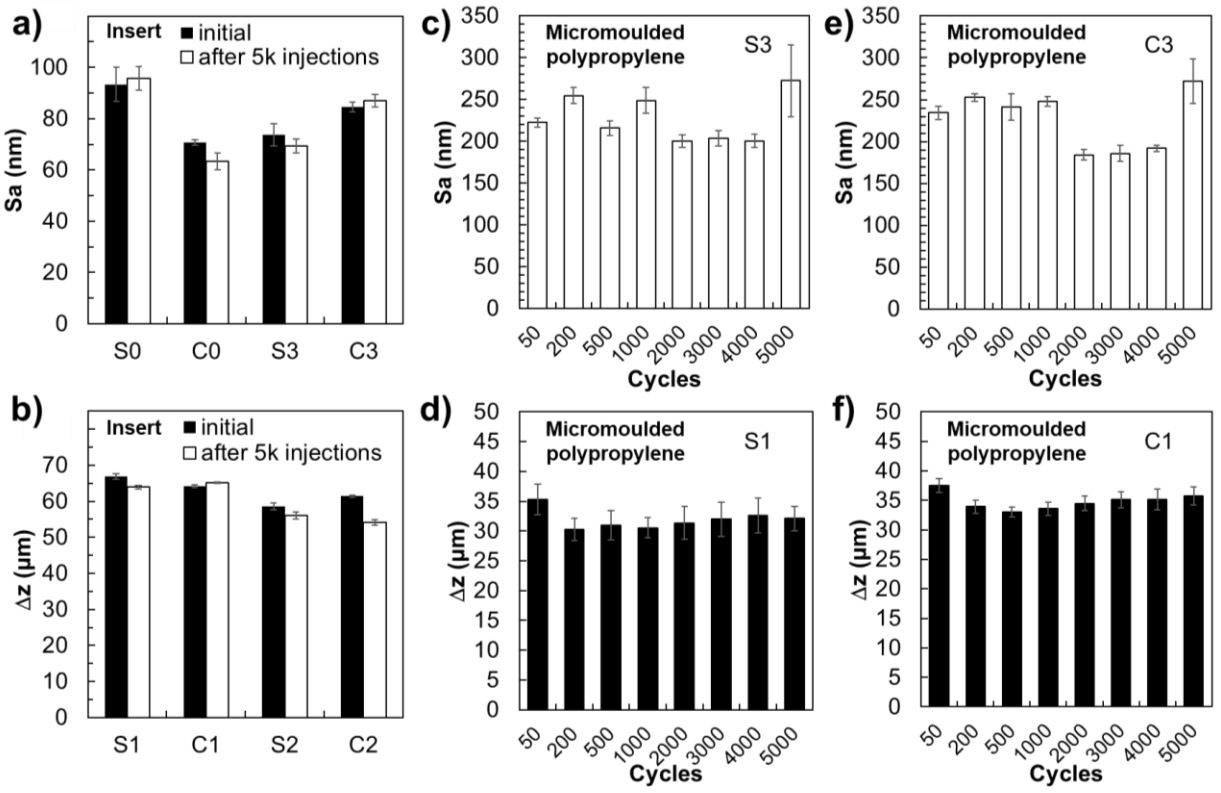

Figure 77. The evolution of surface roughness on inserts and replicas with the increase of injection moulding cycles. Arithmetical mean height measurements (top row) and maximum peak-to-valley heights (bottom row) obtained on inserts, i.e. a) S0, C0, S3, C3 and b) S1, C1, S2, C2; and PP replicas, i.e. c) S3, d) S1, e) C3 and f) C1.

The topographies of replicated grooves from both treated and untreated inserts were similar (see Fig. 78a-d). After 5000 injection moulding cycles, the walls were still covered with a submicron roughness and the top of the groove remained smooth, with sporadic talc platelets visible. However, micro-scale defects were apparent on replicated topographies, e.g. some portions of the grooves or the holes were missing, as shown in Fig. 78e-f. This can be explained with polymer or wear debris clogging the insert topographies. Regarding the LIPSS inserts, the submicron features seemed to have been damaged after the first 200 mouldings as shown in Fig. 78g. Such small replication defects can appear following wear damage on the inserts. After 5000 mouldings, damages such as scratches and wear tracks were much more apparent across the

surfaces (see Fig. 78h). Additionally, the wear pits were replicated forming micro-scale bumps on the PP surfaces.

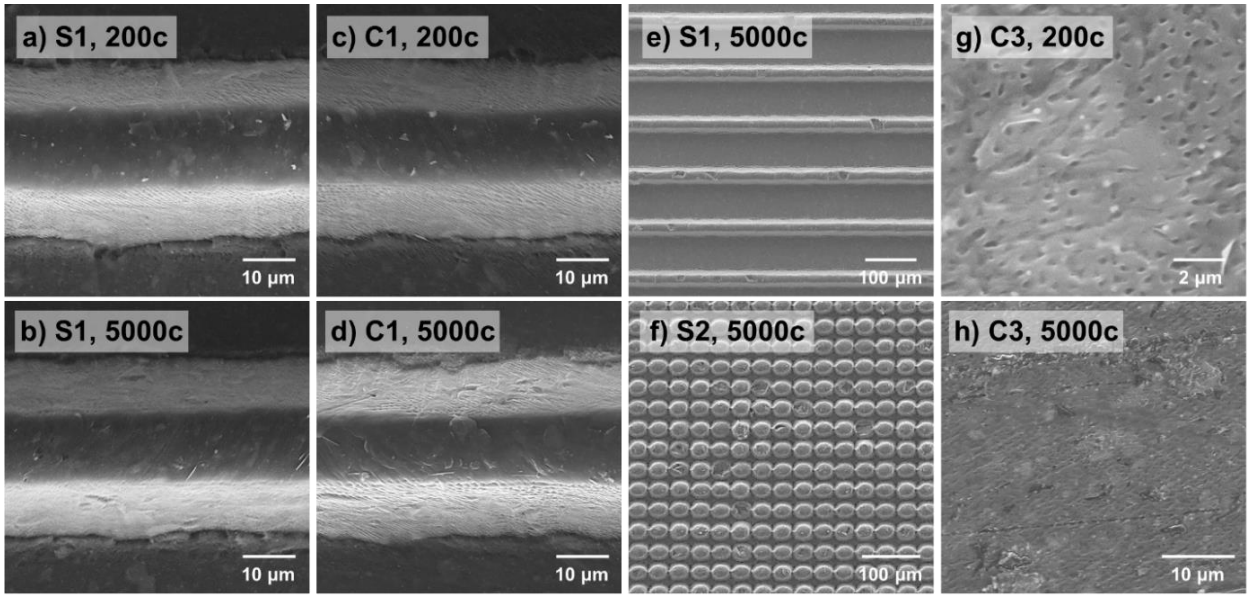

Figure 78. SEM top views of replicated S1 and C1 surfaces on PP samples, i.e. after 200 mouldings a) and c), and after 5000 mouldings b) and d), respectively. Magnified views of replicated S1 and S2 surfaces after 5000 injections in e) and f), correspondingly. Defects on C3 after 200 and 5000 mouldings in g) and h), respectively.

7.3.4 Effects of in-process wear on surface functionality

The replicated PP surfaces exhibited different wetting properties, ranging from hydrophobic to superhydrophobic as shown in Fig. 79a. The water contact angles measured on untextured PP samples were between 105° and 110° and relatively stable even after 5000 cycles. A lower contact angle was measured on the worn carburised layer (C0 after 5000 mouldings), while LIPSS increased the contact angle to approximately 130°. In particular, the PP replicas with grooves and Lotus-leaf like textures were superhydrophobic, initially, with contact angles of approximately 155° and low rolling-off angles. With the increase of moulding cycles, the hydrophobicity of the micro-scale textures decreased, in particular the contact angles decreased

to approximately 125°, 140°, 135° and 140° on PP replicas produced with the S1, C1, S2 and C2 inserts respectively, as shown in Fig. 79b.

In overall, the PP replicas produced with the carburised inserts (C1 and C2) retained higher contact angles after 5000 mouldings (see Fig. 79b) and this can be attributed to their higher hardness and wear resistance. It should also be noted that an average contact angle above 150° was maintained after 1000 and 3000 mouldings produced with S1 and C1 inserts, respectively (see Fig. 79d,f). This clearly demonstrated a three-fold increase in durability of the grooves' functional properties on plasma carburised inserts in comparisons to as-received steel inserts. For the replicas with LIPSS textures, the decrease of contact angle was progressive from 132° to 114° with the increase of the moulding cycles and the spread of the measurements remained low, approximately +/- 4° (see Fig. 79c). Marginal changes were observed when using the carburised insert (see Fig. 79e). However, in some cases, sharp variations in contact angle were observed, presumably due to the presence of wear defects where the water drops would pin and spread.

As reported by Wenzel, for a hydrophobic flat substrate, an increase of surface roughness leads to a higher hydrophobicity (Wenzel, 1936). A further increase of surface roughness and area ratio could lead to even higher contact angles, sometimes above 150°, due to trapped air (Cassie and Baxter, 1944). However, there was no apparent correlation between the roughness variations and the contact angles in this research. For untextured or submicron topographies, the roughness of LIPSS samples did not significantly varied before and after the injection moulding cycles, however, the contact angles decreased progressively. It is worth noting that the areal parameters, Sa or Δz used in this research to study the surface topography evolution on replicas, were not affected by any localised damage on injection mouldings. Therefore, these areal parameters were

selected to analyse the surface topography and not Sa and Sz that were used in another research to investigate dependences between surface roughness and superhydrophobicity on injection moulded parts (Romano et al., 2019b), Thus, the use of Sa or Δz could explain the reduction of hydrophobicity with the development of surface defects and the increase of roughness values, as discussed in Section 7.3.2. Especially, any localised defects as a result of the tool wear may breach the quasi-static equilibrium of the droplet, spreading the liquid drop and thus decreasing the contact angle. Further research is necessary to determine the specific effects of tool wear on replicas with the increase of moulding cycles and also what areal parameters could be used to judge indirectly about the wetting properties of injection moulded parts.

In industrial conditions, the use of demoulding agents and less abrasive polymers and/or optimised injection moulding settings can improve the lifespan of replication masters that incorporate textured functional surfaces. Moreover, in spite of using an abrasive polymer compound (30 wt% talc loaded PP) to accelerate tool wear and surface damage, the plasma treatment of 304L stainless steel inserts allowed the wetting properties of replicated micro-scale textures to be retained for much longer, i.e. to withstand 3 times more injection moulding cycles. Overall, the highest contact angle of almost 140° after 5000 moulding cycles was obtained on groove-textured PP replicas produced with the carburised (C1) insert in comparison to the other two surface topographies investigated in this research.

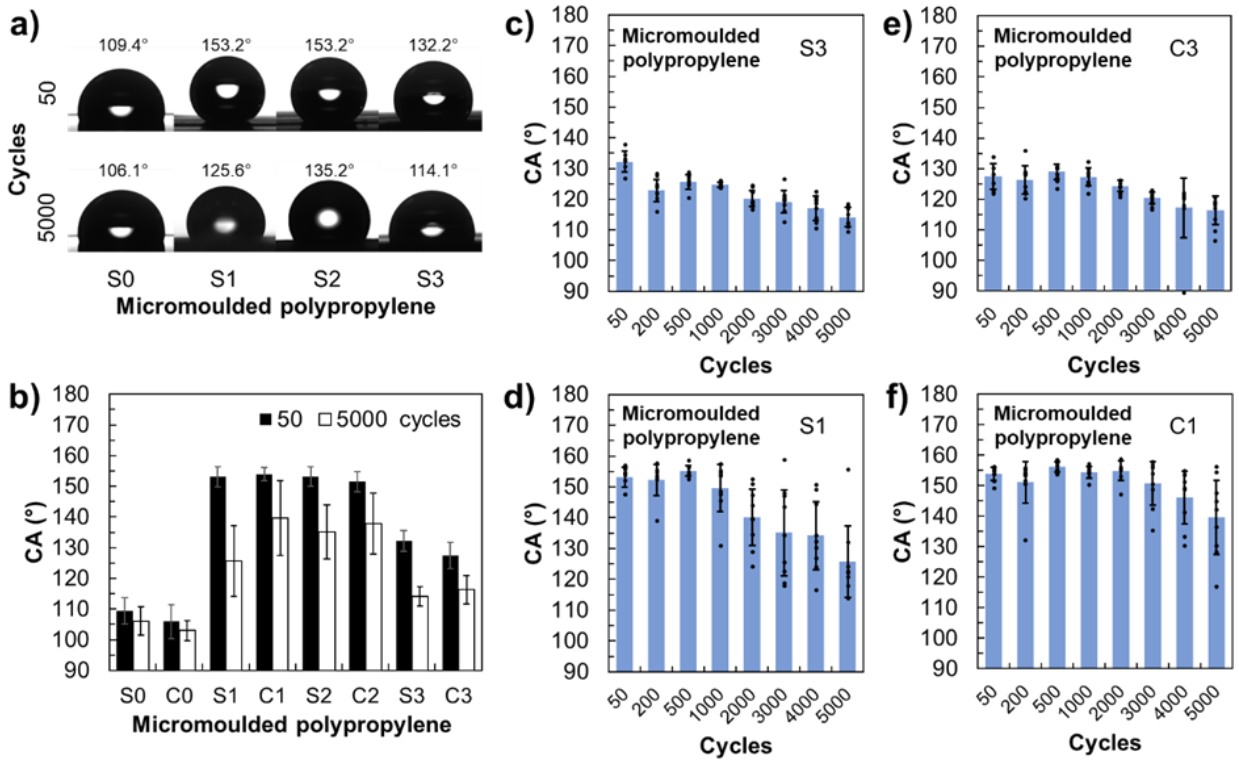

Figure 79. Wetting properties of textured PP replicas: a) 6 µl water drops on surfaces replicated using untreated stainless steel inserts after 50 and 5000 mouldings; b) comparison of contact angles obtained on all 8 inserts, after 50 and 5000 injection moulding cycles; and the evolution of contact angles on replicated surfaces with c) S3, d) S1, e) C3 and f) C1 inserts, after 50, 200, 500, 1000, 2000, 3000, 4000 and 5000 mouldings.

7.4 Conclusion

In this research, a process chain for replicating superhydrophobic thermoplastic surfaces was investigated. The process chain included, firstly low temperature plasma carburising of austenitic stainless steel to increase its hardness, followed by laser texturing to produce replication masters for injection moulding. Ultrashort laser pulses were used to texture the surface of the inserts, by producing three different functional topographies: microscale grooves, holes and sub-microscale LIPSS. Then, a commercially available talc-reinforced PP was used to investigate the evolution of surface textures on both inserts and replicas together with their functional response with

increasing injection moulding cycles. The surface structures on inserts were reproduced on PP parts with a replication efficiency of approximately 55% and 70-80% for microscale and submicron textures, respectively. Dual-scale topographies were present on microscale textures, in particular LIPSS on top of micro structures, and they exhibited superhydrophobic properties, with water contact angles higher than 150° and low rolling-off angles.

The inspection of the inserts after 5000 injection moulding cycles revealed that debris from the laser processing were removed while there were clear signs of wear and surface damages, such as pits and scratches. At the same time, the carburised layer on plasma treated inserts exhibited signs of delamination. The evolution of surface topographies with the increase of injection moulding cycles were analysed together with their wettability, both on inserts and replicas. Any wear or damage on inserts as a result of the increasing moulding cycles, were replicated onto the PP surfaces and had a clear impact on their surface roughness and peak-to-valley topographies. Superhydrophobicity was retained on PP replicas for longer, approximately 3000 cycles, when the groove-structured carburised insert was used, whereas, only 1000 parts with similar wetting properties were produced with its respective untreated counterpart. Regarding the submicron LIPSS textures, the contact angles of replicas decreased after 5000 injections from 132° to 114°, close to the values obtained on untextured PP replica. In general, the PP replicas produced with the carburised inserts retained higher contact angles after 5000 cycles. This could be considered as a clear evidence of the impact that their higher hardness and wear resistance had on retaining the wetting properties of textured PP replicas.

Acknowledgment

The research was carried out in the framework of the Laser4Fun project on “Short Pulsed Laser Micro/Nanostructuring of Surfaces for Improved Functional Applications” (Laser4Fun), which has received funding from the European Union’s H2020 research and innovation programme under the Marie Skłodowska-Curie grant agreement No. 675063 (www.laser4fun.eu). The work was also supported by three other H2020 projects, i.e. “High-Impact Injection Moulding Platform for mass-production of 3D and/or large micro-structured surfaces with Antimicrobial, Self-cleaning, Anti-scratch, Anti-squeak and Aesthetic functionalities” (HIMALAIA, No. 766871), “Process Fingerprint for Zero-defect Net-shape Micromanufacturing” (MICROMAN, No. 674801) and “Modular laser based additive manufacturing platform for large scale industrial applications” (MAESTRO, No. 723826). Further support was provided by the UKIERI DST programme “Surface functionalisation for food, packaging, and healthcare applications”. Finally, the authors would like to acknowledge the support and assistance of the University of Bradford and BSH Electrodomésticos España, S.A. in conducting this research.

Chapter 8

Contribution to knowledge and future research

This chapter reviews the main contributions to knowledge resulting from the carried out research and summarizes the main conclusions made in achieving the aims and objectives stated in **Chapter 1**. Finally, an outlook for future research directions is presented.

8.1 Contributions

The overall aim of this research was to develop laser-based technologies for functionalizing relatively large surfaces by tailoring their topographies. Several functional properties were considered, including optical and non-fouling, but with a special emphasis on superhydrophobicity. Examples of functional surfaces found in nature were presented (**Chapter 2**). Employing a near-infrared ultra-short laser, micro/nano-scale topographies inspired by nature were fabricated onto stainless steel and titanium substrates (**Chapters 3 to 5**). The functional durability of replicated polypropylene surfaces was assessed by using reciprocating abrasion tests (**Chapter 6**). A process chain was demonstrated that integrates laser-texturing of plasma carburised stainless steel inserts with injection moulding for producing polymer replicas with functional surfaces. Injection moulding trials with abrasive polymer were conducted to investigate the effect of tool wear on the wetting properties of replicas (**Chapter 7**). In particular, the following findings against the research objectives of this PhD thesis underpin the claimed contributions to knowledge:

i) *To develop laser-based surface texturing technologies for creating bio-inspired micro/nano scale topographies on masters for polymer replication:*

Different approaches for laser texturing stainless steel were investigated by employing femtosecond near infrared laser source:

- Uniform low spatial frequency LIPSS were demonstrated over relatively large areas. A one-step processing was developed using a circular-polarized laser beam. Parallel lines and hexagonally-aligned triangles with heights between 80 and 200 nm and approximatively 900 nm spatial periodicity, i.e. close to the laser wavelength, were fabricated. The LIPSS resembled the surface textures present on Springtail cuticles, i.e. similar in shape and around twice larger in size and spacing. The created triangular LIPSS were not limited to one material and it was demonstrated that surfaces can be textured with processing speed of 10 mm^2/s. A processing window for the generation of triangular LIPSS was identified. (**Chapters 3, 4 and 7**).

- The large area fabrication of close-packed submicron features was investigated, employing a microlens-assisted laser texturing approach. A silica sphere of 1 µm-diameter to deliver PJ with a calculated spot size of 470 nm enabled the fabrication of bumps and holes, with sizes from 120 nm to 1.23 µm in diameter and 30 to 100 nm in height/depth. 46 % density of these submicron features on relatively large areas was achieved by minimizing the cleaning of microspheres. Multiple pulses generated rhombic and triangular LIPSS with spatial periodicity of 1 µm, i.e. the spacing of pre-fabricated array of holes (**Chapters 5 and 6**).

- Employing a Direct Laser Writing (DLW) approach, different Lotus-leaf inspired hierarchical topographies were fabricated on stainless steel and carburised steel. Microscale textures in the form of peaks and valleys in the range of the laser spot size were covered with sporadic holes of various diameters down to one micron and a composed mix of LIPSS, from

submicron ripples with periodicities in the range from 800 nm to 1 µm to perpendicular microgrooves with periodicities from 1.7 to 3 µm (**Chapters 6 and 7**).

- A laser-based process chain enabled the production of polymer part with textured surfaces. Various surface structures were laser-fabricated on tool steel and carburised steel inserts and then they were successfully replicated on polymer parts by employing injection moulding technology. In particular, microscale topographies were replicated with 55-80 % and 90-101 % efficiency, in term of heights, using standard and micro injection moulding machines, respectively. Replicated LIPSS had heights in the range of 40 to 140 nm that were approximatively 70 to 80 % of their heights on the replication masters (**Chapters 6 and 7**).

ii) To investigate the functional properties of laser-textured surfaces:

- The wetting properties of laser-textured steel surfaces and polypropylene replicas were assessed. An ageing process was observed on all laser-textured steel substrates, with a constant CA increase and a hydrophilic-hydrophobic transition. A superhydrophobic behaviour ($CA \geq 150°$ and roll-off angles $\leq 10°$) was observed on LIPSS after 7 days stored in ambient air or in plastic bags (**Chapters 3 and 4**). After cleaning of the laser-textured steel surfaces, no superhydrophobic behaviour was observed (**Chapter 5**). Only surface structures affected the wetting properties of replicas; submicron topographies increased the hydrophobic behaviour of the surfaces (Wenzel regime) and superhydrophobicity was reached on hierarchical structures (Wenzel to Cassie-Baxter regimes). The correlation between standardized 3D areal parameters (Sa, Sz and true-to-projected area ratio) of laser-textured surfaces and their wetting properties was investigated (**Chapters 6 and 7**).

- Light scattering was observed on steel substrates and polymer replicas, textured with LIPSS and array of submicron holes. The hexagonally aligned surface structures exhibited

structural colorization in multiple directions and planes. During the fabrication of triangular LIPSS, increasing the pulse repetition rate was detrimental to the alignments of LIPSS and also to the uniformity of the light scattering properties (**Chapter 3**). A focal offset up to 550 μm did not lead to noticeable changes in the light scattering properties (**Chapter 4**). Surfaces with LIPSS exhibited low optical reflection, below 10 %. By varying the submicron dimensions of the holes' arrays, the reflection properties could be tailored for selected wavelength. (**Chapter 5**).

- Microbial adhesion tests were performed on replicas by incubating a strain of *E. coli* for 4h. The periodicity of the pattern, in the range of the bacteria size, was expected to increase the bacterial adhesion and this was verified on ripple-like LIPSS structures. However, the arrays of holes did not show a significant change in bacterial adhesion. In addition, in one specific case, a transition between holes and LIPSS, a significant decrease in bacterial colonization was observed (**Chapter 5**).

iii) *To evaluate the durability of wetting behaviour of laser textured surfaces:*

- The deterioration of superhydrophobic properties of textured polymer surfaces was investigated by conducting reciprocating cleaning tests that comply with the standardized procedure for assessing the durability of coatings. The single-scale submicron topographies were not robust enough to withstand the cleaning cycles. Overall, the dual-scale topographies retained their wetting properties after a higher number of cycles. Some Lotus-leaf inspired topographies exhibited an advancing CA still higher than 150° after 1000 wet cleaning cycles (**Chapter 6**).

- Tool wear and surface damages occurring during 5000 abrasive injection moulding cycles were analysed and had clear detrimental effects on the wetting properties of the textured replicas. The occurrence of surface damages resulted in progressive statistical loss of Cassie-Baxter state. Carburised steel surfaces, due to their enhanced wear resistance, could retain

superhydrophobic properties for 3 times longer than without this plasma carburising treatment to extend the life span of textured moulding inserts (**Chapter 7**).

8.2 Conclusions

i) *Laser-based surface texturing*: A process chain combining low temperature plasma carburising, laser texturing and injection moulding was proposed. Near-infrared femtosecond laser was shown to be a promising tool for the surface texturing of tool steels and other metals. One-step processes using a circular-polarized laser beam was used to fabricate surface structures mimicking the Springtail cuticles and the Lotus leaves. Laser processing parameters were optimized to obtain large-area uniformity of hexagonal-aligned submicron features using LIPSS and microlens-assisted PJ approaches. In particular, a narrow but reproducible processing window was identified for generating self-organized triangles. The achievable processing efficiency by increasing the pulse repetition rates up to MHz regimes were analysed. Moreover, close-packed microlenses with diameters close to the laser wavelength enabled the generation of nanobumps, arrays of holes and honeycomb structures. Tailoring the Gaussian spatial intensity was crucial for achieving a higher uniformity over bigger surface areas, especially by avoiding the cleaning effect on microlenses. Rhombic and triangular LIPSS with tailored periodicity could be fabricated on top of pre-textured arrays of holes. Furthermore, different hierarchical topographies, made of micro-scale peaks and valleys and covered with LIPSS and sporadic holes, were also fabricated successfully. Similar surface structures were fabricated on stainless steel and carburised steel and were integrated as replication masters for injection moulding. All surface structures were successfully reproduced onto the polymer replicas.

ii) *Surface functionalities*: The investigated laser-textured surfaces exhibited multiple functional properties, i.e. wetting, optical and non-fouling. The textured metallic surfaces underwent a hydrophilic-superhydrophobic transition in a week time, independently from the fabricated surface structures (combination of micro and nano-scale features or solely submicron ones). The same ageing process was observed when the functionalised metallic samples were stored in plastic bags. Replicated surface structures had more stable wetting properties over time and this was attributed to the absence of laser irradiation. In term of surface structures, there was some correlation between the increase of static contact angles with some standardized 3D areal parameters, in particular Sa, Sz and the true-to-projected area ratio. In cases of hierarchical structures with significant microscale features, superhydrophobic behaviours with metastable Cassie-Baxter states were reached. Moreover, the optical and non-fouling properties could be tailored by fabricating different surface features at the submicron scale. In particular, specific wavelength ranges could be absorbed depending on the structured surfaces. Tailoring LIPSS hexagonal alignments enabled light scattering in various orthogonal planes. Similarly, submicron features delivered different non-fouling responses. However, 4h incubation of *E.coli* did not show a clear correlation between the bacterial adhesion or repulsion and the periodicity of surface structures.

iii) *Durability of textured replicas in terms of wetting response*: In this research, the wetting properties of textured replicas were correlated to their topographies. It was shown that any surface damage was detrimental to the wetting response. Two types of abrasion cycles were conducted to investigate the functional durability, i.e. direct mechanical abrasion of textured polymer surfaces using a multipurpose cloth as counterpart and indirectly by analysing the tool wear induced by abrasive polymer during injection moulding cycles. In both cases, dual-scale

topographies were more robust to any surface damage and could retain the wetting properties for longer. Some textured replicas successfully withstand tests developed for analysing the durability of coatings. Wet cleaning procedures could be defined to limit the degradation of surface properties. Lastly, injection moulding trials with an abrasive polymer compound showed clearly the detrimental effects of tool wear and damage on functional response of replicas. Surface engineering of the replication masters prior to laser texturing operations could enhance their life span without any significant side effects on fabricated surface structures.

8.3 Future work

In the framework of this research, further research directions have been identified:

- *Laser structuring*. A better understanding of the laser-material interactions and the LIPSS could underpin the development of laser-based technologies for fabricating self-organized submicron features, especially in term of large area texturing and uniformity. Triangular submicron structures were demonstrated when near-infrared laser beams were deployed but the use of green or UV lasers to fabricate similar LIPSS pattern with a smaller periodicity should be investigated, too. The use of higher pulse repetition rates affected the LIPSS uniformity and therefore further investigations are required for increasing the process efficiency. In addition, fabrication of LIPSS or PJ-assisted arrays of holes was demonstrated on planar surfaces but should be investigated for creating hierarchical structures, too, e.g. triangular LIPSS or arrays of holes on top of microscale peaks and valleys. In general, a better understanding of LIPSS morphology evolution with the increase of beam intensity could enable the fabrication of tailored hierarchical surface structures. The influence of incident angle and other laser-based approaches

could be investigated to fabricate re-entrant or mushroom-shaped topographies that could improve surface functionalities, in particular, oleophobicity. Finally, research is needed to enable the fabrication of such surface structures on 3D surfaces.

- *Injection moulding*. In this research, the empirical studies were conducted with process settings that were not properly optimised and only for one polymer material. Therefore, further research is required to improve the replication efficiency and also to employ the same laser texturing approaches for producing textured replicas with other polymers. Potential entrapment of polymer and material debris onto the mould topographies could also be investigated. The role of demoulding agents and periodic cleaning of the tool could be assessed, too.

- *Non-fouling applications.* Examples of submicron surface textures with tailored fouling properties were presented in this research, however no clear correlation was identified between topographies and surface responses. Further studies could investigate the links between bacterial attachments and surface topographies and/or wetting properties, for example.

- *Storage of superhydrophobic laser-treated surfaces*. On laser-textured metals, the wetting properties evolved over time until reaching a steady state in regard to contact angles. Further research on effects of surface chemistry could be conducted, especially on controlling or accelerating the ageing process after laser-processing in different storage conditions.

- *Mechanical durability of functional surfaces*. The conducted research has shown that the replication process and direct mechanical contacts with textured polymer replicas can lead to surface damage and topographical defects. However, the effects of such surface damage and topographical changes on replicas' functionality should be quantified. Durability tests that are more industrially relevant and closer to real life applications could be developed.

- *Process and durability monitoring*. The processing domains reported for laser-texturing are relatively narrow in term of investigated focal offsets, number of pulses and fluence levels. Submicron topographies achieved in this research required off-line time-consuming characterisation. In-line inspection solutions could be deployed for monitoring laser-texturing and/or replication processes. Some potential approaches to achieve this were highlighted in this research, such as light scattering or the use of standardized 3D areal parameters. Nevertheless, monitoring the laser texturing of areas significantly larger than the feature sizes, feature defects or surface damages, would require further investigations.

- *Design of functional surfaces*. In nature, functional surfaces often use a combination of multi-scale features and surface chemistries. Laser-based surface treatments/texturing approaches are limited in terms of surface features that can be fabricated. Overall, a deeper understanding of functional responses of specific surface topographies could be used to inform the design of such engineered surfaces. In term of durability, dual-scale topographies retained superhydrophobicity for longer and performed consistently better, even though the subtle Cassie-Baxter state could have been lost in early stage of durability tests. Therefore, surface structures with increased aspect ratios should be tested while taking into account the constraints of replication processes. Ultimately, combinations of surface topographies with hydrophobic coatings could be investigated, as the coatings could be protected inside the surface structures.

List of References

Abbe E (1873) Beiträge zur Theorie des Mikroskops und der mikroskopischen Wahrnehmung. *Arch. Für Mikrosk. Anat.* 9:413–468.

Abdulhussein AT, Kannarpady GK, Wright AB, Ghosh A, Biris AS (2016) Current trend in fabrication of complex morphologically tunable superhydrophobic nano scale surfaces. *Appl. Surf. Sci.* 384:311–332.

Abdurrochman A, Lecler S, Mermet F, Tumbelaka BY, Serio B, Fontaine J (2014) Photonic jet breakthrough for direct laser microetching using nanosecond near-infrared laser. *Appl. Opt.* 53(31):7202–7207.

Afanasiev A, Bredikhin V, Pikulin A, Ilyakov I, Shishkin B, Akhmedzhanov R, Bityurin N (2015) Two-color beam improvement of the colloidal particle lens array assisted surface nanostructuring. *Appl. Phys. Lett.* 106(18):183102.

Afferrante L, Carbone G (2010) Microstructured superhydrorepellent surfaces: effect of drop pressure on fakir-state stability and apparent contact angles. *J. Phys. Condens. Matter* 22(32):325107.

Aguilar-Morales AI, Alamri S, Lasagni AF (2018) Micro-fabrication of high aspect ratio periodic structures on stainless steel by picosecond direct laser interference patterning. *J. Mater. Process. Technol.* 252:313–321.

Ahmed R, Rifat AA, Hassan MU, Yetisen AK, Butt H (2017d) Phase-conjugated directional diffraction from a retroreflector array hologram. *RSC Adv.* 7(41):25657–25664.

Ahmed R, Yetisen AK, Butt H (2017c) High Numerical Aperture Hexagonal Stacked Ring-Based Bidirectional Flexible Polymer Microlens Array. *ACS Nano* 11(3):3155–3165.

Ahmed R, Yetisen AK, Khoury AE, Butt H (2017a) Printable ink lenses, diffusers, and 2D gratings. *Nanoscale* 9(1):266–276.

Ahmed R, Yetisen AK, Yun SH, Butt H (2017b) Color-selective holographic retroreflector array for sensing applications. *Light Sci. Appl.* 6(2):e16214.

Ahmmed KMT, Ling EJY, Servio P, Kietzig AM (2015) Introducing a new optimization tool for femtosecond laser-induced surface texturing on titanium, stainless steel, aluminum and copper. *Opt. Lasers Eng.* 66:258–268.

Aizawa T (2013) Micro-Texturing onto Amorphous Carbon Materials as a Mold-Die for Micro-Forming. *Appl. Mech. Mater.* 289:23.

Alamri S, El-Khoury M, Aguilar-Morales AI, Storm S, Kunze T, Lasagni AF (2019b) Fabrication of inclined non-symmetrical periodic micro-structures using Direct Laser Interference Patterning. *Sci. Rep.* 9(1):5455.

Alamri S, Fraggelakis F, Kunze T, Krupop B, Mincuzzi G, Kling R, Lasagni AF (2019a) On the Interplay of DLIP and LIPSS Upon Ultra-Short Laser Pulse Irradiation. *Materials* 12(7):1018.

Anisimov SI, Kapeliovich BL, Perel'man TL (1974) Electron emission from metal surfaces exposed to ultrashort laser pulses. *Sov. Phys. JETP* 39(2):375–377.

Anselme K, Davidson P, Popa AM, Giazzon M, Liley M, Ploux L (2010) The interaction of cells and bacteria with surfaces structured at the nanometre scale. *Acta Biomater.* 6(10):3824–3846.

Ardron M, Weston N, Hand D (2014) A practical technique for the generation of highly uniform LIPSS. *Appl. Surf. Sci.* 313:123–131.

Arnaldo del Cerro D (2014) *Picosecond pulsed laser microstructuring of metals for microfluidics*. (PhD Thesis, University of Twente, Enschede).

Arnold N (2003) Theoretical description of dry laser cleaning. *Appl. Surf. Sci.* 208–209:15–22.

Asthana R, Sobczak N (2000) Wettability, spreading, and interfacial phenomena in high-temperature coatings. *JOM USA* 52(1):18.

ASTM D3450-15 (2015) Standard Test Method for Washability Properties of Interior Architectural Coatings, ASTM International, West Conshohocken, PA. (June) doi:10.1520/D3450-15.

Autumn K, Sitti M, Liang YA, Peattie AM, Hansen WR, Sponberg S, Kenny TW, Fearing R, Israelachvili JN, Full RJ (2002) Evidence for van der Waals adhesion in gecko setae. *Proc. Natl. Acad. Sci.* 99(19):12252–12256.

Ayrton H (1910) The Origin and Growth of Ripple-mark. *Proc. R. Soc. Lond.* 84(285).

Azuma D (2012) Wikimedia Commons: Carcharhinus brachyurus in Okinawa Churaumi Aquarium, Japan. Retrieved (March 11, 2019), https://commons.wikimedia.org/wiki/File:Carcharhinus_brachyurus_by_OpenCage.jpg.

Bahadur V, Mishchenko L, Hatton B, Taylor JA, Aizenberg J, Krupenkin T (2011) Predictive Model for Ice Formation on Superhydrophobic Surfaces. *Langmuir* 27(23):14143–14150.

Bai X, Xue CH, Jia ST (2016) Surfaces with Sustainable Superhydrophobicity upon Mechanical Abrasion. *ACS Appl. Mater. Interfaces* 8(41):28171–28179.

Ball P (1999) Engineering Shark skin and other solutions. *Nature* 400(6744):507–509.

Baraldi G, Bakhti S, Liu Z, Reynaud S, Lefkir Y, Vocanson F, Destouches N (2017) Polarization-driven self-organization of silver nanoparticles in 1D and 2D subwavelength gratings for plasmonic photocatalysis. *Nanotechnology* 28(3):035302.

Barberoglou M, Gray D, Magoulakis E, Fotakis C, Loukakos PA, Stratakis E (2013) Controlling ripples' periodicity using temporally delayed femtosecond laser double pulses. *Opt. Express* 21(15):18501–18508.

Barberoglou M, Zorba V, Stratakis E, Spanakis E, Tzanetakis P, Anastasiadis SH, Fotakis C (2009) Bio-inspired water repellent surfaces produced by ultrafast laser structuring of silicon. *Appl. Surf. Sci.* 255(10):5425–5429.

Barthlott W, Neinhuis C (1997) Purity of the sacred lotus, or escape from contamination in biological surfaces. *Planta* 202(1):1–8.

Barthlott W, Neinbuis C (1998) Lotus-Effekt und Autolack: Die Selbstreinigungsfähigkeit mikrostrukturierter Oberflächen. Biol. Unserer Zeit 28(5):314–321.

Barthlott W, Schimmel T, Wiersch S, Koch K, Brede M, Barczewski M, Walheim S, Weis A, Kaltenmaier A, Leder A, Bohn HF (2010) The Salvinia Paradox: Superhydrophobic Surfaces with Hydrophilic Pins for Air Retention Under Water. *Adv. Mater.* 22(21):2325–2328.

Baruffi F, Calaon M, Tosello G (2018) Micro-Injection Moulding In-Line Quality Assurance Based on Product and Process Fingerprints. *Micromachines* 9(6):293.

Bashir S, Shahid Rafique M, Husinsky W (2012) Femtosecond laser-induced subwavelength ripples on Al, Si, CaF2 and CR-39. *Nucl. Instrum. Methods Phys. Res. Sect. B Beam Interact. Mater. At.* 275:1–6.

Bauer F, Michalowski A, Kiedrowski T, Nolte S (2015) Heat accumulation in ultra-short pulsed scanning laser ablation of metals. *Opt. Express* 23(2):1035–1043.

Bauer U, Bohn HF, Federle W (2008) Harmless nectar source or deadly trap: Nepenthes pitchers are activated by rain, condensation and nectar. *Proc. R. Soc. B Biol. Sci.* 275(1632):259–265.

Bauer U, Federle W (2009) The insect-trapping rim of Nepenthes pitchers: surface structure and function. *Plant Signal. Behav.* 4(11):1019–1023.

Bäuerle DW (2011) *Laser Processing and Chemistry* 4th ed. (Springer-Verlag, Berlin Heidelberg).

Bay RS, Tucker CL (1992) Fiber orientation in simple injection moldings. Part I: Theory and numerical methods. *Polym. Compos.* 13(4):317–331.

Bekesi J, Kaakkunen JJJ, Michaeli W, Klaiber F, Schoengart M, Ihlemann J, Simon P (2010) Fast fabrication of super-hydrophobic surfaces on polypropylene by replication of short-pulse laser structured molds. *Appl. Phys. A* 99(4):691–695.

Belhadjamor M, Mansori ME, Belghith S, Mezlini S (2018) Anti-fingerprint properties of engineering surfaces: a review. *Surf. Eng.* 34(2):85–120.

Berthod L, Shavdina O, Verrier I, Kämpfe T, Dellea O, Vocanson F, Bichotte M, Jamon D, Jourlin Y (2017) Periodic TiO2 Nanostructures with Improved Aspect and Line/Space Ratio Realized by Colloidal Photolithography Technique. *Nanomaterials* 7(10):316.

Bhushan B (2007) Adhesion of multi-level hierarchical attachment systems in gecko feet. *J. Adhes. Sci. Technol.* 21(12–13):1213–1258.

Bhushan B, Her EK (2010) Fabrication of Superhydrophobic Surfaces with High and Low Adhesion Inspired from Rose Petal. *Langmuir* 26(11):8207–8217.

Bhushan B, Jung YC, Koch K (2009) Micro-, nano- and hierarchical structures for superhydrophobicity, self-cleaning and low adhesion. *Philos. Trans. R. Soc. Math. Phys. Eng. Sci.* 367(1894):1631–1672.

Bhushan B, Jung YC (2008) Wetting, adhesion and friction of superhydrophobic and hydrophilic leaves and fabricated micro/nanopatterned surfaces. *J. Phys. Condens. Matter* 20(22):225010.

Bieda M, Siebold M, Lasagni AF (2016) Fabrication of sub-micron surface structures on copper, stainless steel and titanium using picosecond laser interference patterning. *Appl. Surf. Sci.* 387:175–182.

Bienk EJ, Mikkelsen NJ (1997) Application of advanced surface treatment technologies in the modern plastics moulding industry. *Wear* 207(1):6–9.

Binetti VR, Schiffman JD, Leaffer OD, Spanier JE, Schauer CL (2009) The natural transparency and piezoelectric response of the Greta oto butterfly wing. *Integr. Biol.* 1(4):324–329.

Birnbaum M (1965) Semiconductor Surface Damage Produced by Ruby Lasers. *J. Appl. Phys.* 36(11):3688–3689.

Bittoun E, Marmur A (2012) The Role of Multiscale Roughness in the Lotus Effect: Is It Essential for Super-Hydrophobicity? *Langmuir* 28(39):13933–13942.

Bohn HF, Federle W (2004) Insect aquaplaning: Nepenthes pitcher plants capture prey with the peristome, a fully wettable water-lubricated anisotropic surface. *Proc. Natl. Acad. Sci.* 101(39):14138–14143.

Boinovich LB, Emelyanenko AM, Emelyanenko KA, Domantovsky AG, Shiryaev AA (2016) Comment on “Nanosecond laser textured superhydrophobic metallic surfaces and their chemical sensing applications” by Duong V. Ta, Andrew Dunn, Thomas J. Wasley, Robert W. Kay, Jonathan Stringer, Patrick J. Smith, Colm Connaughton, Jonathan D. Shephard (Appl. Surf. Sci. 357 (2015) 248–254). *Appl. Surf. Sci.* 379:111–113.

Boinovich LB, Emelyanenko KA, Domantovsky AG, Emelyanenko AM (2018) Laser Tailoring the Surface Chemistry and Morphology for Wear, Scale and Corrosion Resistant Superhydrophobic Coatings. *Langmuir* 34(24):7059–7066.

Boinovich LB, Modin EB, Sayfutdinova AR, Emelyanenko KA, Vasiliev AL, Emelyanenko AM (2017) Combination of Functional Nanoengineering and Nanosecond Laser Texturing for Design of Superhydrophobic Aluminum Alloy with Exceptional Mechanical and Chemical Properties. *ACS Nano* 11(10):10113–10123.

Bonse J, Kirner SV, Griepentrog M, Spaltmann D, Krüger J (2018) Femtosecond Laser Texturing of Surfaces for Tribological Applications. *Materials* 11(5).

Bonse J, Kirner SV, Koter R, Pentzien S, Spaltmann D, Krüger J (2017) Femtosecond laser-induced periodic surface structures on titanium nitride coatings for tribological applications. *Appl. Surf. Sci.* 418, Part B:572–579.

Bonse J, Krüger J, Höhm S, Rosenfeld A (2012) Femtosecond laser-induced periodic surface structures. *J. Laser Appl.* 24(4):042006.

Bonse J, Rosenfeld A, Krüger J (2009) On the role of surface plasmon polaritons in the formation of laser-induced periodic surface structures upon irradiation of silicon by femtosecond-laser pulses. *J. Appl. Phys.* 106(10):104910.

BotBln (2006) Wikimedia Commons: Stapelia gigantea, Habitus and Flower, location: Botanical Gardens Berlin. Retrieved (September 05, 2019), https://commons.wikimedia.org/wiki/File:Stapelia_gigantea_HabitusFlower_BotGardBln0806b.jpg.

Brezinová J, Guzanová A (2010) Friction Conditions during the Wear of Injection Mold Functional Parts in Contact with Polymer Composites. *J. Reinf. Plast. Compos.* 29(11):1712–1726.

Byskov-Nielsen J, Savolainen JM, Christensen MS, Balling P (2011) Ultra-short pulse laser ablation of copper, silver and tungsten: experimental data and two-temperature model simulations. *Appl. Phys. A* 103(2):447–453.

Caffrey PO, Nayak BK, Gupta MC (2012) Ultrafast laser-induced microstructure/nanostructure replication and optical properties. *Appl. Opt.* 51(5):604–609.

Cai W, Piestun R (2006) Patterning of silica microsphere monolayers with focused femtosecond laser pulses. *Appl. Phys. Lett.* 88(11):111112.

Cai Y, Chang W, Luo X, Sousa AML, Lau KHA, Qin Y (2018) Superhydrophobic structures on 316L stainless steel surfaces machined by nanosecond pulsed laser. *Precis. Eng.* 52:266–275.

Cardoso JT, Aguilar-Morales AI, Alamri S, Huerta-Murillo D, Cordovilla F, Lasagni AF, Ocaña JL (2018) Superhydrophobicity on hierarchical periodic surface structures fabricated via direct laser writing and direct laser interference patterning on an aluminium alloy. *Opt. Lasers Eng.* 111:193–200.

Cardoso JT, Garcia-Girón A, Romano JM, Huerta-Murillo D, Jagdheesh R, Walker M, Dimov SS, Ocaña JL (2017) Influence of ambient conditions on the evolution of wettability properties of an IR-, ns-laser textured aluminium alloy. *RSC Adv.* 7(63):39617–39627.

Cardoso MR, Martins RJ, Dev A, Voss T, Mendonca CR (2015) Highly hydrophobic hierarchical nanomicro roughness polymer surface created by stamping and laser micromachining. *J. Appl. Polym. Sci.* 132(24):n/a-n/a.

Cassie ABD, Baxter S (1944) Wettability of porous surfaces. *Trans. Faraday Soc.* 40(0):546–551.

Cassie ABD, Baxter S (1945) Large Contact Angles of Plant and Animal Surfaces. *Nature* 155(3923):21–22.

Chen H, Zhang P, Zhang L, Liu H, Jiang Y, Zhang D, Han Z, Jiang L (2016) Continuous directional water transport on the peristome surface of Nepenthes alata. *Nature* 532(7597):85–89.

Chen Z, Taflove A, Backman V (2004) Photonic nanojet enhancement of backscattering of light by nanoparticles: a potential novel visible-light ultramicroscopy technique. *Opt. Express* 12(7):1214–1220.

Cheng Q, Li M, Zheng Y, Su B, Wang S, Jiang L (2011) Janus interface materials: superhydrophobic air/solid interface and superoleophobic water/solid interface inspired by a lotus leaf. *Soft Matter* 7(13):5948–5951.

Chereshen'ka P (2016) Wikimedia Commons: Tetrodontophora bielanensis. Retrieved (March 12, 2019), https://commons.wikimedia.org/wiki/File:Tetrodontophora_bielanensis.jpg.

Chichkov BN, Momma C, Nolte S, von Alvensleben F, Tünnermann A (1996) Femtosecond, picosecond and nanosecond laser ablation of solids. *Appl. Phys. A* 63(2):109–115.

Chun DM, Davaasuren G, Ngo CV, Kim CS, Lee GY, Ahn SH (2014) Fabrication of transparent superhydrophobic surface on thermoplastic polymer using laser beam machining and compression molding for mass production. *CIRP Ann. - Manuf. Technol.* 63(1):525–528.

Chun DM, Ngo CV, Lee KM (2016) Fast fabrication of superhydrophobic metallic surface using nanosecond laser texturing and low-temperature annealing. *CIRP Ann. - Manuf. Technol.* 65(1):519–522.

Clark SE, Kerr NC, Emmony DC (1989) Anomalous laser-induced periodic surface structures. *J. Phys. Appl. Phys.* 22(4):527–534.

Cong H, Yu B, Zhao XS (2011) Imitation of variable structural color in paracheirodon innesi using colloidal crystal films. *Opt. Express* 19(13):12799–12808.

Crema L, Lucchetta G (2014) A Study of Mold Friction and Wear in Injection Molding of Plastic-Bonded Hard Ferrite. *Key Eng. Mater.* 611–612:460–472.

Cruz AR de la, Lahoz R, Siegel J, Fuente GF de la, Solis J (2014) High speed inscription of uniform, large-area laser-induced periodic surface structures in Cr films using a high repetition rate fs laser. *Opt. Lett.* 39(8):2491–2494.

Cunha A, Elie AM, Plawinski L, Serro AP, Botelho do Rego AM, Almeida A, Urdaci MC, Durrieu MC, Vilar R (2016) Femtosecond laser surface texturing of titanium as a method to reduce the adhesion of Staphylococcus aureus and biofilm formation. *Appl. Surf. Sci.* 360, Part B:485–493.

Cunha A, Serro AP, Oliveira V, Almeida A, Vilar R, Durrieu MC (2013) Wetting behaviour of femtosecond laser textured Ti–6Al–4V surfaces. *Appl. Surf. Sci.* 265:688–696.

Cyrillic (2006) Wikimedia Commons: Fingerprint for criminology stubs2. Retrieved (September 05, 2019), https://en.wikipedia.org/wiki/File:Fingerprintforcriminologystubs2.png.

Daglar B, Birlik Demirel G, Khudiyev T, Dogan T, Tobail O, Altuntas S, Buyukserin F, Bayindir M (2014) Anemone-like nanostructures for non-lithographic, reproducible, large-area, and ultra-sensitive SERS substrates. *Nanoscale* 6(21):12710–12717.

Dar MH, Saad NA, Sahoo C, Naraharisetty SRG, Desai NR (2017) Ultrafast laser-induced reproducible nano-gratings on a molybdenum surface. *Laser Phys. Lett.* 14(2):026101.

Dean B, Bhushan B (2010) Shark-skin surfaces for fluid-drag reduction in turbulent flow: a review. *Philos. Trans. R. Soc. Math. Phys. Eng. Sci.* 368(1929):4775–4806.

Delléa O, Shavdina O, Fugier P, Coronel P, Ollier E, Désage SF (2014) Control Methods in Microspheres Precision Assembly for Colloidal Lithography. *Precis. Assem. Technol. Syst.* IFIP Advances in Information and Communication Technology. (Springer, Berlin, Heidelberg), 107–117.

Dettre RH, Johnson RE (1964) Contact Angle Hysteresis. *Contact Angle Wettability Adhes*. Advances in Chemistry. (American Chemical Society), 136–144.

Dewan R, Fischer S, Meyer-Rochow VB, Özdemir Y, Hamraz S, Knipp D (2011) Studying nanostructured nipple arrays of moth eye facets helps to design better thin film solar cells. *Bioinspir. Biomim.* 7(1):016003.

Dong H (2010) S-phase surface engineering of Fe-Cr, Co-Cr and Ni-Cr alloys. *Int. Mater. Rev.* 55(2):65–98.

Drzymala J (1994) Hydrophobicityand collectorless flotation of inorganic materials. *Adv. Colloid Interface Sci.* 50:143–185.

Dufft D, Rosenfeld A, Das SK, Grunwald R, Bonse J (2009) Femtosecond laser-induced periodic surface structures revisited: A comparative study on ZnO. *J. Appl. Phys.* 105(3):034908.

Dufour R, Harnois M, Thomy V, Boukherroub R, Senez V (2011) Contact angle hysteresis origins: Investigation on super-omniphobic surfaces. *Soft Matter* 7(19):9380.

Dusser B, Sagan Z, Soder H, Faure N, Colombier JP, Jourlin M, Audouard E (2010) Controlled nanostructrures formation by ultra fast laser pulses for color marking. *Opt. Express* 18(3):2913–2924.

Dyne Technology Ltd. (n.d.) Surface Energy Testing. Retrieved (March 22, 2019), http://www.dynetechnology.co.uk/ebooks/surfaceenergytesting/files/assets/downloads/publication.pdf.

Elliott PR, Stagon SP, Huang H, Furrer DU, Burlatsky SF, Filburn TP (2015) Combined Hydrophobicity and Mechanical Durability through Surface Nanoengineering. *Sci. Rep.* 5:9260.

Emelyanenko AM, Shagieva FM, Domantovsky AG, Boinovich LB (2015) Nanosecond laser micro- and nanotexturing for the design of a superhydrophobic coating robust against long-term contact with water, cavitation, and abrasion. *Appl. Surf. Sci.* 332:513–517.

Emmony DC, Howson RP, Willis LJ (1973) Laser mirror damage in germanium at 10.6 μm. *Appl. Phys. Lett.* 23(11):598–600.

Etoombs (2011) Wikimedia Commons: Plot of instantaneous intensity of a Gaussian beam as a function of r and x. Retrieved (September 12, 2019), https://commons.wikimedia.org/wiki/File:Gaussian_beam_w40mm_lambda30mm.png#mw-jump-to-license

Etsion I (2004) Improving Tribological Performance of Mechanical Components by Laser Surface Texturing. *Tribol. Lett.* 17(4):733–737.

Etsion I (2005) State of the Art in Laser Surface Texturing. *J. Tribol.* 127(1):248.

Evans E (2007) Wikimedia Commons: Ripples on the beach Looking southwards along the beach at West Shore, Llandudno. Retrieved (March 10, 2019), https://commons.wikimedia.org/wiki/File:Ripples_on_the_beach_-_geograph.org.uk_-_575599.jpg.

Extrand CW, Kumagai Y (1995) Liquid Drops on an Inclined Plane: The Relation between Contact Angles, Drop Shape, and Retentive Force. *J. Colloid Interface Sci.* 170(2):515–521.

Fadeeva E, Schlie S, Koch J, Chichkov BN (2010) Selective Cell Control by Surface Structuring for Orthopedic Applications. *J. Adhes. Sci. Technol.* 24(13–14):2257–2270.

Fadeeva E, Truong VK, Stiesch M, Chichkov BN, Crawford RJ, Wang J, Ivanova EP (2011) Bacterial Retention on Superhydrophobic Titanium Surfaces Fabricated by Femtosecond Laser Ablation. *Langmuir* 27(6):3012–3019.

Falah Toosi S, Moradi S, Ebrahimi M, Hatzikiriakos SG (2016) Microfabrication of polymeric surfaces with extreme wettability using hot embossing. *Appl. Surf. Sci.* 378:426–434.

Faucon M, Laffitte A, Lopez J, Kling R (2014) Surface blackening by laser texturing with high repetition rate femtosecond laser up to 1MHz. 89721M-89721M–8.

Feng L, Li S, Li Y, Li H, Zhang L, Zhai J, Song Y, Liu B, Jiang L, Zhu D (2002) Super-Hydrophobic Surfaces: From Natural to Artificial. *Adv. Mater.* 14(24):1857–1860.

Feng L, Zhang Y, Li M, Zheng Y, Shen W, Jiang L (2010) The Structural Color of Red Rose Petals and Their Duplicates. *Langmuir* 26(18):14885–14888.

Feng L, Zhang Y, Xi J, Zhu Y, Wang N, Xia F, Jiang L (2008) Petal Effect: A Superhydrophobic State with High Adhesive Force. *Langmuir* 24(8):4114–4119.

Ferrand P, Wenger J, Devilez A, Pianta M, Stout B, Bonod N, Popov E, Rigneault H (2008) Direct imaging of photonic nanojets. *Opt. Express* 16(10):6930–6940.

Ferrón HG, Botella H (2017) Squamation and ecology of thelodonts Friedman M, ed. *PLOS ONE* 12(2):e0172781.

Fowkes FM (1964) Attractive forces at interfaces. *Ind. Eng. Chem.* 56(12):40–52.

Fraggelakis F, Mincuzzi G, Lopez J, Manek-Hönninger I, Kling R (2017) Texturing metal surface with MHz ultra-short laser pulses. *Opt. Express* 25(15):18131–18139.

Fraggelakis F, Mincuzzi G, Lopez J, Manek-Hönninger I, Kling R (2019) Controlling 2D laser nano structuring over large area with double femtosecond pulses. *Appl. Surf. Sci.* 470:677–686.

Fraggelakis F, Stratakis E, Loukakos PA (2018) Control of periodic surface structures on silicon by combined temporal and polarization shaping of femtosecond laser pulses. *Appl. Surf. Sci.* 444:154–160.

Galusha JW, Richey LR, Gardner JS, Cha JN, Bartl MH (2008) Discovery of a diamond-based photonic crystal structure in beetle scales. *Phys. Rev. E* 77(5):050904.

Gao H, Wang X, Yao H, Gorb S, Arzt E (2005) Mechanics of hierarchical adhesion structures of geckos. *Mech. Mater.* 37(2–3):275–285.

Gao X, Jiang L (2004) Biophysics: Water-repellent legs of water striders. *Nature* 432(7013):36.

Gao X, Yan X, Yao X, Xu L, Zhang K, Zhang J, Yang B, Jiang L (2007) The Dry-Style Antifogging Properties of Mosquito Compound Eyes and Artificial Analogues Prepared by Soft Lithography. *Adv. Mater.* 19(17):2213–2217.

Garcia-Giron A, Romano JM, Batal A, Dashtbozorg B, Dong H, Solanas EM, Angos DU, Walker M, Penchev P, Dimov SS (2019) Durability and Wear Resistance of Laser-Textured Hardened Stainless Steel Surfaces with Hydrophobic Properties. *Langmuir* 35(15):5353–5363.

Garcia-Giron A, Romano JM, Liang Y, Dashtbozorg B, Dong H, Penchev P, Dimov SS (2018a) Combined surface hardening and laser patterning approach for functionalising stainless steel surfaces. *Appl. Surf. Sci.* 439:516–524.

Garcia-Giron A, Romano JM, Liang Y, Dashtbozorg B, Dong H, Penchev P, Dimov S (2018b) Combined Surface Hardening and Laser Patterning for Producing Wear Resistant Hydrophobic Surfaces. *Proc. of 2nd World Congr. Micro Nano Manuf. (WCMNM2018, Portorož, Slovenia)*, 75–78.

Gemini L, Faucon M, Romoli L, Kling R (2017) High throughput laser texturing of super-hydrophobic surfaces on steel. *Proc SPIE 10092*. 100921G-100921G–6.

Glover BJ, Whitney HM (2010) Structural colour and iridescence in plants: the poorly studied relations of pigment colour. *Ann. Bot.* 105(4):505–511.

Gnilitskyi I, Orazi L, Bulgakova NM, Derrien TJY, Mocek T, Levy Y (2017) High-speed manufacturing of highly regular femtosecond laser-induced periodic surface structures: physical origin of regularity. *Sci. Rep.* 7(1):8485.

Golosov EV, Ionin AA, Kolobov YuR, Kudryashov SI, Ligachev AE, Novoselov YuN, Seleznev LV, Sinitsyn DV (2011) Ultrafast changes in the optical properties of a titanium surface and femtosecond laser writing of one-dimensional quasi-periodic nanogratings of its relief. *J. Exp. Theor. Phys.* 113(1):14.

Gong D, Long J, Jiang D, Fan P, Zhang H, Li L, Zhong M (2016) Robust and Stable Transparent Superhydrophobic Polydimethylsiloxane Films by Duplicating via a Femtosecond Laser-Ablated Template. *ACS Appl. Mater. Interfaces* 8(27):17511–17518.

Gonzalez FL, Gordon MJ (2014) Bio-inspired, sub-wavelength surface structures for ultra-broadband, omni-directional anti-reflection in the mid and far IR. *Opt. Express* 22(11):12808–12816.

Good RJ, Van Oss CJ (2013) The Modern Theory of Contact Angles and the Hydrogen Bond Components of Surface Energies. *Mod. Approaches Wettability Theory Appl. Ed GI Loeb ME Schrader*. (Springer Science & Business Media).

Gorb EV, Gorb SN (2006) Physicochemical Properties of Functional Surfaces in Pitchers of the Carnivorous Plant Nepenthes alata Blanco (Nepenthaceae). *Plant Biol.* 8(6):841–848.

Graf S, Muller FA (2015) Polarisation-dependent generation of fs-laser induced periodic surface structures. *Appl. Surf. Sci.* 331:150–155.

Gregorčič P, Conradi M, Hribar L, Hočevar M (2018) Long-Term Influence of Laser-Processing Parameters on (Super)hydrophobicity Development and Stability of Stainless-Steel Surfaces. *Materials* 11(11):2240.

Gregorčič P, Sedlaček M, Podgornik B, Reif J (2016) Formation of laser-induced periodic surface structures (LIPSS) on tool steel by multiple picosecond laser pulses of different polarizations. *Appl. Surf. Sci.* 387:698–706.

Greiner C, Schäfer M (2015) Bio-inspired scale-like surface textures and their tribological properties. *Bioinspir. Biomim.* 10(4):044001.

Grojo D, Cros A, Delaporte P, Sentis M (2006) Time-of-flight measurements of ejected particles during dry laser cleaning. *Appl. Phys. B* 84(3):517–521.

Grojo D, Sandeau N, Boarino L, Constantinescu C, Leo ND, Laus M, Sparnacci K (2014) Bessel-like photonic nanojets from core-shell sub-wavelength spheres. *Opt. Lett.* 39(13):3989–3992.

Gualtieri E, Borghi A, Calabri L, Pugno N, Valeri S (2009) Increasing nanohardness and reducing friction of nitride steel by laser surface texturing. *Tribol. Int.* 42(5):699–705.

Guan YC, Luo FF, Lim GC, Hong MH, Zheng HY, Qi B (2015) Fabrication of metallic surfaces with long-term superhydrophilic property using one-stop laser method. *Mater. Des.* 78:19–24.

Guenther D, Valle J, Burgui S, Gil C, Solano C, Toledo-Arana A, Helbig R, Werner C, Lasa I, Lasagni AF (2016) Direct laser interference patterning for decreased bacterial attachment. *Laser-Based Micro- Nanoprocessing X*. 973611-973611–9.

Guo W, Wang ZB, Li L, Liu Z, Luk'yanchuk B, Whitehead DJ (2008) Chemical-assisted laser parallel nanostructuring of silicon in optical near fields. *Nanotechnology* 19(45):455302.

Guo W, Wang ZB, Li L, Whitehead DJ, Luk'yanchuk BS, Liu Z (2007) Near-field laser parallel nanofabrication of arbitrary-shaped patterns. *Appl. Phys. Lett.* 90(24):243101.

Hamad AH (2016) Effects of Different Laser Pulse Regimes (Nanosecond, Picosecond and Femtosecond) on the Ablation of Materials for Production of Nanoparticles in Liquid Solution. Viskup R, ed. *High Energy Short Pulse Lasers*. (InTech).

Han J, Cai M, Lin Y, Liu W, Luo X, Zhang H, Wang K, Zhong M (2018) Comprehensively durable superhydrophobic metallic hierarchical surfaces via tunable micro-cone design to protect functional nanostructures. *RSC Adv.* 8(12):6733–6744.

Han L, Han Y, Gouesbet G, Wang J, Gréhan G (2014) Photonic jet generated by spheroidal particle with Gaussian-beam illumination. *JOSA B* 31(7):1476–1483.

Hasan J, Webb HK, Truong VK, Pogodin S, Baulin VA, Watson GS, Watson JA, Crawford RJ, Ivanova EP (2013) Selective bactericidal activity of nanopatterned superhydrophobic cicada Psaltoda claripennis wing surfaces. *Appl. Microbiol. Biotechnol.* 97(20):9257–9262.

Heifetz A, Kong SC, Sahakian AV, Taflove A, Backman V (2009) Photonic Nanojets. *J. Comput. Theor. Nanosci.* 6(9):1979–1992.

Helbig R, Günther D, Friedrichs J, Rößler F, Lasagni A, Werner C (2016) The impact of structure dimensions on initial bacterial adhesion. *Biomater Sci* 4(7):1074–1078.

Helbig R, Nickerl J, Neinhuis C, Werner C (2011) Smart Skin Patterns Protect Springtails. *PLOS ONE* 6(9):e25105.

Hensel R, Helbig R, Aland S, Braun HG, Voigt A, Neinhuis C, Werner C (2013a) Wetting Resistance at Its Topographical Limit: The Benefit of Mushroom and Serif T Structures. *Langmuir* 29(4):1100–1112.

Hensel R, Helbig R, Aland S, Voigt A, Neinhuis C, Werner C (2013b) Tunable nano-replication to explore the omniphobic characteristics of springtail skin. *NPG Asia Mater.* 5(2):e37–e37.

Hensel R, Neinhuis C, Werner C (2016) The springtail cuticle as a blueprint for omniphobic surfaces. *Chem. Soc. Rev.* 45(2):323–341.

Hermans R (2009) Wikimedia Commons: Gaussian Beam Waist. Retrieved (March 23, 2019), https://commons.wikimedia.org/wiki/File:GaussianBeamWaist.svg.

Hermens U, Kirner SV, Emonts C, Comanns P, Skoulas E, Mimidis A, Mescheder H, Winands K, Krüger J, Stratakis E, Bonse J (2017) Mimicking lizard-like surface structures upon ultrashort laser pulse irradiation of inorganic materials. *Appl. Surf. Sci.* 418:499–507.

Hintze C (2006) Gordon Gould: The Long Battle For The Laser Patent. *Electron. Des.* 54(23):72–72.

Hong L, Rusli, Wang XC, Zheng HY, Wang H, Yu HY (2014) Femtosecond laser fabrication of large-area periodic surface ripple structure on Si substrate. *Appl. Surf. Sci.* 297:134–138.

Hong SH, Hwang J, Lee H (2009) Replication of cicada wing's nano-patterns by hot embossing and UV nanoimprinting. *Nanotechnology* 20(38):385303.

Hou S, Huo Y, Xiong P, Zhang Y, Zhang S, Jia T, Sun Z, Qiu J, Xu Z (2011) Formation of long- and short-periodic nanoripples on stainless steel irradiated by femtosecond laser pulses. *J. Phys. Appl. Phys.* 44(50):505401.

Hoyle R (2006) *Pattern Formation: An Introduction to Methods.* (Cambridge University Press, Cambridge).

Hu S, Lopez S, Niewiarowski PH, Xia Z (2012) Dynamic self-cleaning in gecko setae via digital hyperextension. *J. R. Soc. Interface* 9(76):2781–2790.

Huang CK (2007) Polymeric nanofeatures of 100 nm using injection moulding for replication. *J. Micromechanics Microengineering* 17(8):1518.

Huang M, Zhao F, Cheng Y, Xu N, Xu Z (2009) Origin of Laser-Induced Near-Subwavelength Ripples: Interference between Surface Plasmons and Incident Laser. *ACS Nano* 3(12):4062–4070.

Huang SM, Hong MH, Lukiyanchuk B, Chong TC (2003) Nanostructures fabricated on metal surfaces assisted by laser with optical near-field effects. *Appl. Phys. A* 77(2):293–296.

Huang SM, Hong MH, Luk'yanchuk BS, Zheng YW, Song WD, Lu YF, Chong TC (2002) Pulsed laser-assisted surface structuring with optical near-field enhanced effects. *J. Appl. Phys.* 92(5):2495–2500.

Huang SM, Sun Z, Luk'yanchuk BS, Hong MH, Shi LP (2005) Nanobump arrays fabricated by laser irradiation of polystyrene particle layers on silicon. *Appl. Phys. Lett.* 86(16):161911.

Huerta-Murillo D, Aguilar-Morales AI, Alamri S, Cardoso JT, Jagdheesh R, Lasagni AF, Ocaña JL (2017) Fabrication of multi-scale periodic surface structures on Ti-6Al-4V by direct laser writing and direct laser interference patterning for modified wettability applications. *Opt. Lasers Eng.* 98:134–142.

Huerta-Murillo D, García-Girón A, Romano JM, Cardoso JT, Cordovilla F, Walker M, Dimov SS, Ocaña JL (2019) Wettability modification of laser-fabricated hierarchical surface structures in Ti-6Al-4V titanium alloy. *Appl. Surf. Sci.* 463:838–846.

Inchaussandague M, Skigin D, Carmaran C, Rosenfeldt S (2010) Structural color in Myxomycetes. *Opt. Express* 18(15):16055–16063.

ISO 25178-2:2012 (2012) Geometrical product specifications (GPS); Surface texture: Areal; Part 2: Terms, definitions and surface texture parameters. (April) www.iso.org/standard/42785.html.

Itagi AV, Challener WA (2005) Optics of photonic nanojets. *JOSA A* 22(12):2847–2858.

Ivanova EP, Hasan J, Webb HK, Truong VK, Watson GS, Watson JA, Baulin VA, Pogodin S, Wag JY, Tobin MJ, Löbbe C, Crawford RJ (2012) Natural Bactericidal Surfaces: Mechanical Rupture of Pseudomonas aeruginosa Cells by Cicada Wings. *Small* 8(16):2489–2494.

Ivanović L, Vencl A, Stojanović B, Marković B (2018) Biomimetics Design for Tribological Applications. *Tribol. Ind.* 40(3):448–456.

Jagdheesh R, Diaz M, Marimuthu S, L. Ocana J (2017) Robust fabrication of μ-patterns with tunable and durable wetting properties: hydrophilic to ultrahydrophobic via a vacuum process. *J. Mater. Chem. A* 5(15):7125–7136.

Jagdheesh R, Diaz M, Ocaña JL (2016) Bio inspired self-cleaning ultrahydrophobic aluminium surface by laser processing. *RSC Adv.* 6(77):72933–72941.

Jang H, Lee HS, Lee KS, Kim DR (2017) Facile Fabrication of Superomniphobic Polymer Hierarchical Structures for Directional Droplet Movement. *ACS Appl. Mater. Interfaces* 9(11):9213–9220.

Jeong HE, Suh KY (2009) Nanohairs and nanotubes: Efficient structural elements for gecko-inspired artificial dry adhesives. *Nano Today* 4(4):335–346.

Jerry M. Fischer (2003) *Handbook of Molded Part Shrinkage and Warpage* (William Andrew).

Ji X, Jiang L, Li X, Han W, Liu Y, Wang A, Lu Y (2015) Femtosecond laser-induced cross-periodic structures on a crystalline silicon surface under low pulse number irradiation. *Appl. Surf. Sci.* 326:216–221.

Jiang D, Fan P, Gong D, Long J, Zhang H, Zhong M (2016) High-temperature imprinting and superhydrophobicity of micro/nano surface structures on metals using molds fabricated by ultrafast laser ablation. *J. Mater. Process. Technol.* 236:56–63.

Jiang L, Shi X, Li X, Yuan Y, Wang C, Lu Y (2012) Subwavelength ripples adjustment based on electron dynamics control by using shaped ultrafast laser pulse trains. *Opt. Express* 20(19):21505–21511.

Jiang T, Koch J, Unger C, Fadeeva E, Koroleva A, Zhao Q, Chichkov BN (2012) Ultrashort picosecond laser processing of micro-molds for fabricating plastic parts with superhydrophobic surfaces. *Appl. Phys. A* 108(4):863–869.

Jiao LS, Ng EYK, Zheng HY (2013) Refining femtosecond laser induced periodical surface structures with liquid assist. *Appl. Surf. Sci.* 264:52–55.

Jie-Rong C, Wakida T (1997) Studies on the surface free energy and surface structure of PTFE film treated with low temperature plasma. *J. Appl. Polym. Sci.* 63(13):1733–1739.

Jin H, Tian X, Ikkala O, Ras RHA (2013) Preservation of Superhydrophobic and Superoleophobic Properties upon Wear Damage. *ACS Appl. Mater. Interfaces* 5(3):485–488.

Joshi GS, Dashtbozorg B, Romano JM, Garcia-Giron A, Gaudiuso C, Dong H, Dimov SS, Ancona A, Carbone G (2018) Experimental investigation of the tribological and wettability properties of laser-textured martensitic steel surfaces. *19th Int. Symp. Laser Precis. Microfabr. (LPM2018, Edinburgh, UK)*. JLMN-18-049, 1–5.

Jung YC, Bhushan B (2008) Dynamic Effects of Bouncing Water Droplets on Superhydrophobic Surfaces. *Langmuir* 24(12):6262–6269.

Jung YC, Bhushan B (2009) Biomimetic structures for fluid drag reduction in laminar and turbulent flows. *J. Phys. Condens. Matter* 22(3):035104.

Jwad T, Penchev P, Nasrollahi V, Dimov S (2018) Laser induced ripples' gratings with angular periodicity for fabrication of diffraction holograms. *Appl. Surf. Sci.* 453:449–456.

Kalin M, Polajnar M (2013) The Effect of Wetting and Surface Energy on the Friction and Slip in Oil-Lubricated Contacts. *Tribol. Lett.* 52(2):185–194.

Kallepalli LND, Grojo D, Charmasson L, Delaporte P, Utéza O, Merlen A, Sangar A, Torchio P (2013) Long range nanostructuring of silicon surfaces by photonic nanojets from microsphere Langmuir films. *J. Phys. Appl. Phys.* 46(14):145102.

Keilmann F, Bai YH (1982) Periodic surface structures frozen into CO2 laser-melted quartz. *Appl. Phys. A* 29(1):9–18.

Kelleher SM, Habimana O, Lawler J, O' Reilly B, Daniels S, Casey E, Cowley A (2016) Cicada Wing Surface Topography: An Investigation into the Bactericidal Properties of Nanostructural Features. *ACS Appl. Mater. Interfaces* 8(24):14966–14974.

Khan A, Wang Z, Sheikh MA, Whitehead DJ, Li L (2010) Parallel near-field optical micro/nanopatterning on curved surfaces by transported micro-particle lens arrays. *J. Phys. Appl. Phys.* 43(30):305302.

Khan A, Wang Z, Sheikh MA, Whitehead DJ, Li L (2011) Laser micro/nano patterning of hydrophobic surface by contact particle lens array. *Appl. Surf. Sci.* 258(2):774–779.

Kieffer M, Fuller MP, Jellings AJ (1998) Explaining curd and spear geometry in broccoli, cauliflower and `romanesco': quantitative variation in activity of primary meristems. *Planta* 206(1):34–43.

Kietzig AM, Hatzikiriakos SG, Englezos P (2009) Patterned Superhydrophobic Metallic Surfaces. *Langmuir* 25(8):4821–4827.

Kietzig AM, Mirvakili MN, Kamal S, Englezos P, Hatzikiriakos SG (2011a) Laser-Patterned Super-Hydrophobic Pure Metallic Substrates: Cassie to Wenzel Wetting Transitions. *J. Adhes. Sci. Technol.* 25(20):2789–2809.

Kietzig AM, Mirvakili MN, Kamalb S, Englezos P, Hatzikiriakos SG (2011b) Nanopatterned Metallic Surfaces: Their Wettability and Impact on Ice Friction. *J. Adhes. Sci. Technol.* 25(12):1293–1303.

Kim Doogon, Kim JG, Chu CN (2016b) Aging effect on the wettability of stainless steel. *Mater. Lett.* 170:18–20.

Kim Donggyu, Pugno NM, Ryu S (2016a) Wetting theory for small droplets on textured solid surfaces. *Sci. Rep.* 6:37813.

Kim S, Polycarpou AA, Liang H (2015) Electrical-potential induced surface wettability of porous metallic nanostructures. *Appl. Surf. Sci.* 351(Supplement C):460–465.

Kinoshita S, Yoshioka S, Fujii Y, Okamoto N (2002) Photophysics of Structural Color in the Morpho Butterflies. *Forma* 17:103–121.

Kirichenko NA (2009) Large-scale structures produced on metal surfaces by multiple laser pulses. *Quantum Electron.* 39(5):442.

Koch K, Bhushan B, Jung YC, Barthlott W (2009) Fabrication of artificial Lotus leaves and significance of hierarchical structure for superhydrophobicity and low adhesion. *Soft Matter* 5(7):1386–1393.

Korhonen JT, Huhtamäki T, Ikkala O, Ras RHA (2013) Reliable Measurement of the Receding Contact Angle. *Langmuir* 29(12):3858–3863.

Kozlov A, Chowdhury H, Mustary I, Loganathan B, Alam F (2015) Bio-Inspired Design: Aerodynamics of Boxfish. *Procedia Eng.* 105:323–328.

Krüss GmbH (1999) Models for Surface Free Energy Calculation. Technical note TN306e. https://www.kruss-scientific.com/fileadmin/user_upload/website/literature/kruss-tn306-en.pdf.

Krüss GmbH (n.d.) Glossary: Young-Laplace fit. Retrieved (March 5, 2019), https://www.kruss-scientific.com/services/education-theory/glossary/young-laplace-fit/.

Kubiak KJ, Mathia TG (2014) Anisotropic Wetting of Hydrophobic and Hydrophilic Surfaces–Modelling by Lattice Boltzmann Method. *Procedia Eng.* 79:45–48.

Kulinich SA, Farhadi S, Nose K, Du XW (2011) Superhydrophobic Surfaces: Are They Really Ice-Repellent? *Langmuir* 27(1):25–29.

Lafuma A, Quere D (2003) Superhydrophobic states. *Nat. Mater.* 2(7):457–460.

Lapcik L, Jindrova P, Lapcikova B, Tamblyn R, Greenwood R, Rowson N (2008) Effect of the talc filler content on the mechanical properties of polypropylene composites. *J. Appl. Polym. Sci.* 110(5):2742–2747.

Larison B, Harrigan RJ, Thomassen HA, Rubenstein DI, Chan-Golston AM, Li E, Smith TB (2015) How the zebra got its stripes: a problem with too many solutions. *R. Soc. Open Sci.* 2(140452).

Lasagni AF, Roch T, Langheinrich D, Bieda M, Wetzig A (2011) Large Area Direct Fabrication of periodic Arrays using Interference Patterning. *Phys. Procedia* 12:214–220.

Lasagni AF, Shao P, Hendricks JL, Shaw CM, Martin DC, Das S (2010) Direct fabrication of periodic patterns with hierarchical sub-wavelength structures on poly(3,4-ethylene dioxythiophene)–poly(styrene sulfonate) thin films using femtosecond laser interference patterning. *Appl. Surf. Sci.* 256(6):1708–1713.

Lecler S, Takakura Y, Meyrueis P (2005) Properties of a three-dimensional photonic jet. *Opt. Lett.* 30(19):2641–2643.

Lee Y, Park SH, Kim KB, Lee JK (2007) Fabrication of Hierarchical Structures on a Polymer Surface to Mimic Natural Superhydrophobic Surfaces. *Adv. Mater.* 19(17):2330–2335.

Lehr J, Kietzig AM (2014) Production of homogenous micro-structures by femtosecond laser micro-machining. *Opt. Lasers Eng.* 57:121–129.

Leitz KH, Quentin U, Hornung B, Otto A, Alexeev I, Schmidt M (2010) Microsphere near-field nanostructuring using picosecond pulses. *Phys. Procedia* 5:237–244.

Leitz KH, Redlingshöfer B, Reg Y, Otto A, Schmidt M (2011) Metal Ablation with Short and Ultrashort Laser Pulses. *Phys. Procedia* 12:230–238.

Leone C, Papa I, Tagliaferri F, Lopresto V (2013) Investigation of CFRP laser milling using a 30W Q-switched Yb:YAG fiber laser: Effect of process parameters on removal mechanisms and HAZ formation. *Compos. Part Appl. Sci. Manuf.* 55:129–142.

Li C, Kattawar GW, Zhai PW, Yang P (2005) Electric and magnetic energy density distributions inside and outside dielectric particles illuminated by a plane electromagnetic wave. *Opt. Express* 13(12):4554–4559.

Li L, Guo W, Wang ZB, Liu Z, Whitehead D, Luk'yanchuk B (2009) Large-area laser nano-texturing with user-defined patterns. *J. Micromechanics Microengineering* 19(5):054002.

Li S, Yang Z, Zhang Z, Gao F, Du J, Zhang S (2013) Study of nanospheres lithography technology with super-lens for fabricating nano holes. *J. Appl. Phys.* 113(18):183102.

Li X, Chen Z, Taflove A, Backman V (2005) Optical analysis of nanoparticles via enhanced backscattering facilitated by 3-D photonic nanojets. *Opt. Express* 13(2):526–533.

Li XM, Reinhoudt D, Crego-Calama M (2007) What do we need for a superhydrophobic surface? A review on the recent progress in the preparation of superhydrophobic surfaces. *Chem. Soc. Rev.* 36(8):1350–1368.

Li Y, Li L, Sun J (2010) Bioinspired Self-Healing Superhydrophobic Coatings. *Angew. Chem. Int. Ed.* 49(35):6129–6133.

Liang C, Wang H, Yang J, Li B, Yang Y, Li H (2012) Biocompatibility of the micro-patterned NiTi surface produced by femtosecond laser. *Appl. Surf. Sci.* 261:337–342.

Lightmotif (2019) Lightmotif — Ultrashort pulse laser machining. *Lightmotif*. Retrieved (May 2, 2019), https://www.lightmotif.nl/ultrashort.

Lin Y, Hong MH, Chong TC, Lim CS, Chen GX, Tan LS, Wang ZB, Shi LP (2006) Ultrafast-laser-induced parallel phase-change nanolithography. *Appl. Phys. Lett.* 89(4):041108.

von der Linde D, Sokolowski-Tinten K, Bialkowski J (1997) Laser–solid interaction in the femtosecond time regime. *Appl. Surf. Sci.* 109–110:1–10.

Liu B, Wang W, Jiang G, Mei X, Wang Z, Wang K, Cui J (2016) Study on hierarchical structured PDMS for surface super-hydrophobicity using imprinting with ultrafast laser structured models. *Appl. Surf. Sci.* 364:528–538.

Liu F, Dong BQ, Liu XH, Zheng YM, Zi J (2009) Structural color change in longhorn beetles Tmesisternus isabellae. *Opt. Express* 17(18):16183–16191.

Liu JM (1982) Simple technique for measurements of pulsed Gaussian-beam spot sizes. *Opt. Lett.* 7(5):196–198.

Liu K, Du J, Wu J, Jiang L (2012) Superhydrophobic gecko feet with high adhesive forces towards water and their bio-inspired materials. *Nanoscale* 4(3):768–772.

Liu K, Yao X, Jiang L (2010) Recent developments in bio-inspired special wettability. *Chem. Soc. Rev.* 39(8):3240.

Liu M, Wang S, Wei Z, Song Y, Jiang L (2009) Bioinspired Design of a Superoleophobic and Low Adhesive Water/Solid Interface. *Adv. Mater.* 21(6):665–669.

Liu Q, Zhang N, Yang J, Qiao H, Guo C (2018) Direct fabricating large-area nanotriangle structure arrays on tungsten surface by nonlinear lithography of two femtosecond laser beams. *Opt. Express* 26(9):11718–11727.

Liu X, Zhou J, Xue Z, Gao J, Meng J, Wang S, Jiang L (2012) Clam's Shell Inspired High-Energy Inorganic Coatings with Underwater Low Adhesive Superoleophobicity. *Adv. Mater.* 24(25):3401–3405.

Liu Y, Li L, Li H, Hu H (2018) An experimental study of surface wettability effects on dynamic ice accretion process over an UAS propeller model. *Aerosp. Sci. Technol.* 73:164–172.

Long J, Fan P, Gong D, Jiang D, Zhang H, Li L, Zhong M (2015a) Superhydrophobic Surfaces Fabricated by Femtosecond Laser with Tunable Water Adhesion: From Lotus Leaf to Rose Petal. *ACS Appl. Mater. Interfaces* 7(18):9858–9865.

Long J, Zhong M, Zhang H, Fan P (2015b) Superhydrophilicity to superhydrophobicity transition of picosecond laser microstructured aluminum in ambient air. *J. Colloid Interface Sci.* 441(Supplement C):1–9.

Lu Y, Shi X, Huang Z, Li T, Zhang M, Czajkowski J, Fabritius T, Huttula M, Cao W (2017) Nanosecond laser coloration on stainless steel surface. *Sci. Rep.* 7(1):7092.

Lu Y, Theppakuttai S, Chen SC (2003) Marangoni effect in nanosphere-enhanced laser nanopatterning of silicon. *Appl. Phys. Lett.* 82(23):4143–4145.

Lu YF, Zhang L, Song WD, Zheng YW, Luk'yanchuk BS (2000) Laser writing of a subwavelength structure on silicon (100) surfaces with particle-enhanced optical irradiation. *J. Exp. Theor. Phys. Lett.* 72(9):457–459.

Luna A, Macías D, Skigin D, Inchaussandague M, Schinca D, Gigli M, Vial A (2013) Characterization of the iridescence-causing multilayer structure of the Ceroglossus suturalis beetle using bio-inspired optimization strategies. *Opt. Express* 21(16):19189–19201.

Macdougall G, Ockrent C (1942) Surface Energy Relations in Liquid/Solid Systems. I. The Adhesion of Liquids to Solids and a New Method of Determining the Surface Tension of Liquids. *Proc. R. Soc. Math. Phys. Eng. Sci.* 180(981):151–173.

Magono C, Lee CW (1966) Meteorological Classification of Natural Snow Crystals. *J. Fac. Sci. Hokkaido Univ. Ser. 7 Geophys.* 2(4):321–335.

Maiman TH (1960) Stimulated Optical Radiation in Ruby. *Nature* 187(4736):493.

Mandelbrot BB (1982) *The fractal geometry of nature* Updated and augmented. (Freeman, New York ; (Oxford)).

Mann EE, Magin CM, Mettetal MR, May RM, Henry MM, DeLoid H, Prater J, Sullivan L, Thomas JG, Twite MD, Parker AE, Brennan AB, Reddy ST (2016) Micropatterned Endotracheal Tubes Reduce Secretion-Related Lumen Occlusion. *Ann. Biomed. Eng.* 44(12):3645–3654.

Mann EE, Manna D, Mettetal MR, May RM, Dannemiller EM, Chung KK, Brennan AB, Reddy ST (2014) Surface micropattern limits bacterial contamination. *Antimicrob. Resist. Infect. Control* 3:28.

Mannion PT, Magee J, Coyne E, O'Connor GM, Glynn TJ (2004) The effect of damage accumulation behaviour on ablation thresholds and damage morphology in ultrafast laser micro-machining of common metals in air. *Appl. Surf. Sci.* 233(1):275–287.

Marmur A (2003) Wetting on Hydrophobic Rough Surfaces: To Be Heterogeneous or Not To Be? *Langmuir* 19(20):8343–8348.

Marmur A (2006) Soft contact: measurement and interpretation of contact angles. *Soft Matter* 2(1):12–17.

Marmur A, Valal D (2010) Correlating Interfacial Tensions with Surface Tensions: A Gibbsian Approach. *Langmuir* 26(8):5568–5575.

Martínez-Calderon M, Rodríguez A, Dias-Ponte A, Morant-Miñana MC, Gómez-Aranzadi M, Olaizola SM (2016) Femtosecond laser fabrication of highly hydrophobic stainless steel surface with hierarchical structures fabricated by combining ordered microstructures and LIPSS. *Appl. Surf. Sci.* 374:81–89.

Mattheck C, Tesari I (2004) The mechanical self-optimisation of trees. *Des. Nat. II MW Collins CA Brebbia*. (WIT Press), 197–206.

McCloskey D, Rakovich YP, Donegan JF (2010) Controlling the properties of Photonic Jets. *2010 12th Int. Conf. Transparent Opt. Netw.* 1–3.

McLeod E, Arnold CB (2008) Subwavelength direct-write nanopatterning using optically trapped microspheres. *Nat. Nanotechnol.* 3(7):413–417.

Mengüç Y, Röhrig M, Abusomwan U, Hölscher H, Sitti M (2014) Staying sticky: contact self-cleaning of gecko-inspired adhesives. *J. R. Soc. Interface* 11(94):20131205.

Mezera M, van Drongelen M, Römer GRBE (2018) Laser-Induced Periodic Surface Structures (LIPSS) on Polymers Processed with Picosecond Laser Pulses. *J. Laser Micro Nanoeng.* 13(2):105–116.

Milionis A, Loth E, Bayer IS (2016) Recent advances in the mechanical durability of superhydrophobic materials. *Adv. Colloid Interface Sci.* 229:57–79.

Miljkovic N, Wang EN (2013) Condensation heat transfer on superhydrophobic surfaces. *MRS Bull.* 38(5):397–406.

Mincuzzi G, Gemini L, Faucon M, Kling R (2016) Extending ultra-short pulse laser texturing over large area. *Appl. Surf. Sci.* 386:65–71.

Mishchenko L, Hatton B, Bahadur V, Taylor JA, Krupenkin T, Aizenberg J (2010) Design of Ice-free Nanostructured Surfaces Based on Repulsion of Impacting Water Droplets. *ACS Nano* 4(12):7699–7707.

Mishchenko L, Khan M, Aizenberg J, Hatton BD (2013) Spatial Control of Condensation and Freezing on Superhydrophobic Surfaces with Hydrophilic Patches. *Adv. Funct. Mater.* 23(36):4577–4584.

Mishra SP, Polycarpou AA (2011) Tribological studies of unpolished laser surface textures under starved lubrication conditions for use in air-conditioning and refrigeration compressors. *Tribol. Int.* 44(12):1890–1901.

Mittal KL ed. (1994) *Particles on Surfaces: Detection, Adhesion and Removal* (Marcel Dekker, Inc.).

Moradi S, Kamal S, Englezos P, Hatzikiriakos SG (2013) Femtosecond laser irradiation of metallic surfaces: effects of laser parameters on superhydrophobicity. *Nanotechnology* 24(41):415302.

Mosbacher M, Dobler V, Boneberg J, Leiderer P (2000) Universal threshold for the steam laser cleaning of submicron spherical particles from silicon. *Appl. Phys. A* 70(6):669–672.

Mosbacher M, Münzer HJ, Zimmermann J, Solis J, Boneberg J, Leiderer P (2001) Optical field enhancement effects in laser-assisted particle removal. *Appl. Phys. A* 72(1):41–44.

Müller FA, Kunz C, Gräf S (2016) Bio-Inspired Functional Surfaces Based on Laser-Induced Periodic Surface Structures. *Materials* 9(6):476.

Müller-Meskamp L, Kim YH, Roch T, Hofmann S, Scholz R, Eckardt S, Leo K, Lasagni AF (2012) Efficiency Enhancement of Organic Solar Cells by Fabricating Periodic Surface Textures using Direct Laser Interference Patterning. *Adv. Mater.* 24(7):906–910.

Münzer HJ, Mosbacher M, Bertsch M, Zimmermann J, Leiderer P, Boneberg J (2001) Local field enhancement effects for nanostructuring of surfaces. *J. Microsc.* 202(1):129–135.

Murphy EB, Wudl F (2010) The world of smart healable materials. *Prog. Polym. Sci.* 35(1):223–251.

Nakashima S, Sugioka K, Ito T, Takai H, Midorikawa K (2011) Fabrication of High-aspect-ratio Nanohole Arrays on GaN Surface by Using Wet-chemical-assisted Femtosecond Laser Ablation. *J. Laser Micro Nanoeng. Ibaraki* 6(1):15–19.

Nayak BK, Caffrey PO, Speck CR, Gupta MC (2013) Superhydrophobic surfaces by replication of micro/nano-structures fabricated by ultrafast-laser-microtexturing. *Appl. Surf. Sci.* 266:27–32.

Nayak BK, Gupta MC (2010) Ultrafast laser-induced self-organized conical micro/nano surface structures and their origin. *Opt. Lasers Eng.* 48(10):966–973.

Nayak BK, Iyengar VV, Gupta MC (2011) Efficient light trapping in silicon solar cells by ultrafast-laser-induced self-assembled micro/nano structures. *Prog. Photovolt. Res. Appl.* 19(6):631–639.

Nedyalkov NN, Atanasov PA, Obara M (2007) Near-field properties of a gold nanoparticle array on different substrates excited by a femtosecond laser. *Nanotechnology* 18(30):305703.

Neinhuis C, Barthlott W (1997) Characterization and Distribution of Water-repellent, Self-cleaning Plant Surfaces. *Ann. Bot.* 79(6):667–677.

Ng MK, Saxena I, Ehmann KF, Cao J (2016) Improving Surface Hydrophobicity by Microrolling-Based Texturing. *J. Micro Nano-Manuf.* 4(3):031001-031001–8.

Ngo CV, Chun DM (2017) Fast wettability transition from hydrophilic to superhydrophobic laser-textured stainless steel surfaces under low-temperature annealing. *Appl. Surf. Sci.* 409:232–240.

Ngo CV, Chun DM (2018) Control of laser-ablated aluminum surface wettability to superhydrophobic or superhydrophilic through simple heat treatment or water boiling post-processing. *Appl. Surf. Sci.* 435:974–982.

Nickerl J, Helbig R, Schulz HJ, Werner C, Neinhuis C (2013) Diversity and potential correlations to the function of Collembola cuticle structures. *Zoomorphology* 132(2):183–195.

Noh J, Lee JH, Na S, Lim H, Jung DH (2010) Fabrication of Hierarchically Micro- and Nano-structured Mold Surfaces Using Laser Ablation for Mass Production of Superhydrophobic Surfaces. *Jpn. J. Appl. Phys.* 49(10R):106502.

Nolte S, Momma C, Jacobs H, Tünnermann A, Chichkov BN, Wellegehausen B, Welling H (1997) Ablation of metals by ultrashort laser pulses. *JOSA B* 14(10):2716–2722.

Noordmans J, Busscher HJ (1991) The influence of droplet volume and contact angle on liquid surface tension measurements by axisymmetric drop shape analysis-profile (ADSA-P). *Colloids Surf.* 58(3):239–249.

Nosonovsky M, Bhushan B (2005) Roughness optimization for biomimetic superhydrophobic surfaces. *Microsyst. Technol.* 11(7):535–549.

Nosonovsky M, Hejazi V (2012) Why Superhydrophobic Surfaces Are Not Always Icephobic. *ACS Nano* 6(10):8488–8491.

O’Beirne G (2009) Wikimedia Commons: Altostratus undulatus cloud. Retrieved (March 10, 2019), https://commons.wikimedia.org/wiki/File:CloudRipples_gobeirne.jpg.

O’Connell C, Sherlock RJ, Glynn TJ (2010) Fabrication of a reusable microlens array for laser-based structuring. *Opt. Eng.* 49(1):014201.

O’Hare LA, Leadley S, Parbhoo B (2002) Surface physicochemistry of corona-discharge-treated polypropylene film. *Surf. Interface Anal.* 33(4):335–342.

Ou Z, Huang M, Zhao F (2016) The fluence threshold of femtosecond laser blackening of metals: The effect of laser-induced ripples. *Opt. Laser Technol.* 79:79–87.

Ouyang J, Perrie W, Allegre OJ, Heil T, Jin Y, Fearon E, Eckford D, Edwardson SP, Dearden G (2015) Tailored optical vector fields for ultrashort-pulse laser induced complex surface plasmon structuring. *Opt. Express* 23(10):12562–12572.

Owens DK, Wendt RC (1969) Estimation of the surface free energy of polymers. *J. Appl. Polym. Sci.* 13(8):1741–1747.

Palneedi H, Park JH, Maurya D, Peddigari M, Hwang GT, Annapureddy V, Kim JW, Choi JJ, Hahn BD, Priya S, Lee KJ, Ryu J (2018) Laser Irradiation of Metal Oxide Films and Nanostructures: Applications and Advances. *Adv. Mater.* 30(14).

Papadopoulos P, Mammen L, Deng X, Vollmer D, Butt HJ (2013) How superhydrophobicity breaks down. *Proc. Natl. Acad. Sci.* 110(9):3254–3258.

Park KS, Cha KJ, Han IB, Shin DA, Cho DW, Lee SH, Kim DS (2012) Mass-producible Nano-featured Polystyrene Surfaces for Regulating the Differentiation of Human Adipose-derived Stem Cells. *Macromol. Biosci.* 12(11):1480–1489.

Parker AR, Lawrence CR (2001) Water capture by a desert beetle. *Nature* 414(6859):33–34.

Parker AR, Welch VL, Driver D, Martini N (2003) Structural colour: Opal analogue discovered in a weevil. *Nature* 426(6968):786–787.

Patankar NA (2004) Mimicking the Lotus Effect: Influence of Double Roughness Structures and Slender Pillars. *Langmuir* 20(19):8209–8213.

Patcharaphun S, Mennig G (2007) Prediction of tensile strength for sandwich injection molded short-glass-fiber reinforced thermoplastics. *J. Met. Mater. Miner.* 17(2):9–16.

Pereira A, Grojo D, Chaker M, Delaporte P, Guay D, Sentis M (2008) Laser-Fabricated Porous Alumina Membranes for the Preparation of Metal Nanodot Arrays. *Small* 4(5):572–576.

Perkowitz S (2010) From ray-gun to Blu-ray. *Phys. World* 23(05):16–20.

Piglmayer K, Denk R, Bäuerle D (2002) Laser-induced surface patterning by means of microspheres. *Appl. Phys. Lett.* 80(25):4693–4695.

Pina-Estany J, García-Granada AA, Corull-Massana E (2018) Injection moulding of plastic parts with laser textured surfaces with optical applications. *Opt. Mater.* 79:372–380.

Piparia R, Rothe EW, Baird RJ (2006) Nanobumps on silicon created with polystyrene spheres and 248 or 308nm laser pulses. *Appl. Phys. Lett.* 89(22):223113.

Pogodin S, Hasan J, Baulin VA, Webb HK, Truong VK, Phong Nguyen TH, Boshkovikj V, Fluke CJ, Watson GS, Watson JA, Crawford RJ, Ivanova EP (2013) Biophysical Model of Bacterial Cell Interactions with Nanopatterned Cicada Wing Surfaces. *Biophys. J.* 104(4):835–840.

Preusch F, Rung S, Hellmann R (2016) Influence of Polishing Orientation on the Generation of LIPSS on Stainless Steel. *J. Laser Micro Nanoeng.* 11(1):137–142.

Qi L, Nishii K, Namba Y (2009) Regular subwavelength surface structures induced by femtosecond laser pulses on stainless steel. *Opt. Lett.* 34(12):1846–1848.

Quéré D (2002) Surface chemistry: Fakir droplets. *Nat. Mater.* 1(1):14–15.

Quéré D (2008) Wetting and Roughness. *Annu. Rev. Mater. Res.* 38(1):71–99.

Radhakrishnan T (1951) Refractive index of SiO2. Retrieved (June 28, 2018), https://refractiveindex.info/?shelf=main&book=SiO2&page=Radhakrishnan-o.

Rajab FH, Liauw CM, Benson PS, Li L, Whitehead KA (2017) Production of hybrid macro/micro/nano surface structures on Ti6Al4V surfaces by picosecond laser surface texturing and their antifouling characteristics. *Colloids Surf. B Biointerfaces* 160:688–696.

Rajab FH, Liauw CM, Benson PS, Li L, Whitehead KA (2018) Picosecond laser treatment production of hierarchical structured stainless steel to reduce bacterial fouling. *Food Bioprod. Process.* 109:29–40.

Rajab FH, Liu Z, Wang T, Li L (2019) Controlling bacteria retention on polymer via replication of laser micro/nano textured metal mould. *Opt. Laser Technol.* 111:530–536.

Rank A, Kunze T, Hoffmann T, Lasagni AF (2016) Direct Laser Interference Patterning of Nickel Molds for Hot Embossing of Polymers. *Adv. Eng. Mater.* 18(7):1280–1288.

Rank A, Lang V, Voisiat B, Lasagni AF (2019) Roll-to-roll hot embossing process: A way to scale up the fabrication speed of micro-nano structures formed by direct laser interference patterning (Conference Presentation). *Laser-Based Micro- Nanoprocessing XIII*. (International Society for Optics and Photonics), 109060V.

Rebollar E, Aldana JRV de, Martín-Fabiani I, Hernández M, Rueda DR, Ezquerra TA, Domingo C, Moreno P, Castillejo M (2013) Assessment of femtosecond laser induced periodic surface structures on polymer films. *Phys. Chem. Chem. Phys.* 15(27):11287–11298.

Reif J, Martens C, Uhlig S, Ratzke M, Varlamova O, Valette S, Benayoun S (2015) On large area LIPSS coverage by multiple pulses. *Appl. Surf. Sci.* 336:249–254.

Reif WE (1985) *Squamation and Ecology of Sharks* (Schweizerbart Science Publishers, Stuttgart, Germany).

Roessler F, Lasagni AF (2018) Protecting Sub-Micrometer Surface Features in Polymers from Mechanical Damage Using Hierarchical Patterns. *J. Laser MicroNanoengineering* 13(2).

Romano JM, Ahmed R, Garcia-Giron A, Penchev P, Butt H, Delléa O, Sikosana M, Helbig R, Werner C, Dimov S (2019a) Subwavelength Direct Laser Nanopatterning via Microparticle Arrays for Functionalizing Metallic Surfaces. *J. Micro Nano-Manuf.* 7(1):010901.

Romano JM, Ahmed R, Garcia-Giron A, Penchev P, Delléa O, Dimov S (2018b) Towards Large area Submicron Surface Texturing by Femtosecond Laser Irradiation of Microparticle Arrays. *Proc. of 2nd World Congr. Micro Nano Manuf. (WCMNM2018, Portorož, Slovenia)*, 309–312.

Romano JM, Garcia-Giron A, Penchev P, Dimov S (2018a) Triangular laser-induced submicron textures for functionalising stainless steel surfaces. *Appl. Surf. Sci.* 440:162–169.

Romano JM, Garcia-Giron A, Penchev P, Dimov SS (2018c) Triangular self-organized surface textures produced by femtosecond laser irradiation on stainless steel and titanium alloy. *Proc. of 2nd World Congr. Micro Nano Manuf. (WCMNM2018, Portorož, Slovenia)*, 103–106.

Romano JM, Gulcur M, Garcia-Giron A, Martinez-Solanas E, Whiteside BR, Dimov SS (2019b) Mechanical durability of hydrophobic surfaces fabricated by injection moulding of laser-induced textures. *Appl. Surf. Sci.* 476:850–860.

Romano JM, Helbig R, Fraggelakis F, Garcia-Giron A, Werner C, Kling R, Dimov S (2019c) Springtail-inspired triangular laser-induced surface textures on metals using MHz ultrashort pulses. *J. Micro Nano-Manuf.* 7(2):024504.

Römer GRBE, Arnaldo del Cerro D, Sipkema RCJ, Groenendijk MNW, Huis in't Veld AJ (2009a) Ultra Short Pulse Laser Generated Surface Textures For Anti-Ice Applications in Aviation. *Proc. ICALEO 2009*. (Laser Institute of America, Orlando, United States), 30–37.

Römer GRBE, Huis in't Veld AJ, Meijer J, Groenendijk MNW (2009b) On the formation of laser induced self-organizing nanostructures. *CIRP Ann. - Manuf. Technol.* 58(1):201–204.

Rosenfeld A, Lorenz M, Stoian R, Ashkenasi D (1999) Ultrashort-laser-pulse damage threshold of transparent materials and the role of incubation. *Appl. Phys. A* 69(1):S373–S376.

Rosenkranz A, Hans M, Gachot C, Thome A, Bonk S, Mücklich F (2016) Direct Laser Interference Patterning: Tailoring of Contact Area for Frictional and Antibacterial Properties. *Lubricants* 4(1):2.

RP Photonics Consulting GmbH Encyclopedia of Laser Physics and Technology: Fluence. Retrieved (March 23, 2019b), https://www.rp-photonics.com/fluence.html.

RP Photonics Consulting GmbH Encyclopedia of Laser Physics and Technology: Peak Power. Retrieved (March 23, 2019a), https://www.rp-photonics.com/peak_power.html.

Ryazanov M (2015) Wikimedia Commons: Circular Polarization. Retrieved (September 10, 2019), https://upload.wikimedia.org/wikipedia/commons/8/84/Circular.Polarization.Circularly.Polarized.Light_Circular.Polarizer_Creating.Left.Handed.Helix.View.svg

Scarratt LRJ, Steiner U, Neto C (2017) A review on the mechanical and thermodynamic robustness of superhydrophobic surfaces. *Adv. Colloid Interface Sci.* 246:133–152.

Schille J, Schneider L, Loeschner U, Ebert R, Scully P, Goddard N, Steiger B, Exner H (2011) Micro processing of metals using a high repetition rate femtosecond laser: from laser process parameter study to machining examples. *Int. Congr. Appl. Lasers Electro-Opt.* 2011(1):773–782.

Schille J, Schneider L, Mueller M, Loeschner U, Goddard N, Scully P, Exner H (2014) Highspeed Laser Micro Processing using Ultrashort Laser Pulses. *J. Laser MicroNanoengineering* 9(2):161–168.

Schlie S, Fadeeva E, Koroleva A, Chichkov BN (2012) Laser-engineered topography: correlation between structure dimensions and cell control. *J. Mater. Sci. Mater. Med. Lond.* 23(11):2813–9.

Sedao X, Derrien TJY, Romer G willem RBE, Pathiraj B, Huis in ‘t Veld AJ (2012) Laser surface micro-/nano-structuring by a simple transportable micro-sphere lens array. *J. Appl. Phys.* 112(10):103111.

Senior A (1989) Symmetry and wayward nature. *Comput. Math. Appl.* 17(4):913–919.

Sha B, Dimov S, Griffiths C, Packianather MS (2007) Micro-injection moulding: Factors affecting the achievable aspect ratios. *Int. J. Adv. Manuf. Technol.* 33(1–2):147–156.

She Z, Li Q, Wang Z, Li L, Chen F, Zhou J (2013) Researching the fabrication of anticorrosion superhydrophobic surface on magnesium alloy and its mechanical stability and durability. *Chem. Eng. J.* 228:415–424.

Shinoda M, Gattass RR, Mazur E (2009) Femtosecond laser-induced formation of nanometer-width grooves on synthetic single-crystal diamond surfaces. *J. Appl. Phys.* 105(5):053102.

Shome A, Rather AM, Manna U (2018) Aloe vera mucilage derived highly tolerant underwater superoleophobic coatings. *J. Mater. Chem. A* 6(45):22465–22471.

Siddique RH, Gomard G, Hölscher H (2015) The role of random nanostructures for the omnidirectional anti-reflection properties of the glasswing butterfly. *Nat. Commun.* 6:6909.

Simões JGAB, Riva R, Miyakawa W (2018) High-speed Laser-Induced Periodic Surface Structures (LIPSS) generation on stainless steel surface using a nanosecond pulsed laser. *Surf. Coat. Technol.* 344:423–432.

Sipe JE, Young JF, Preston JS, van Driel HM (1983) Laser-induced periodic surface structure. I. Theory. *Phys. Rev. B* 27(2):1141–1154.

Sivasubramaniam S, Alkaisi MM (2014) Inverted nanopyramid texturing for silicon solar cells using interference lithography. *Microelectron. Eng.* 119:146–150.

Skoulas E, Manousaki A, Fotakis C, Stratakis E (2017) Biomimetic surface structuring using cylindrical vector femtosecond laser beams. *Sci. Rep.* 7:srep45114.

Sohn IB, Noh YC, Kim YS, Ko DK, Lee JM, Choi YJ (2008) Laser Ablation of Polypropylene Films using Nanosecond, Picosecond, and Femtosecond Laser. *J. Opt. Soc. Korea* 12(1):38–41.

Sola D, Escartín A, Cases R, Peña JI (2011) Laser ablation of advanced ceramics and glass-ceramic materials: Reference position dependence. *Appl. Surf. Sci.* 257(12):5413–5419.

Song F, Xiao KW, Bai K, Bai YL (2007) Microstructure and nanomechanical properties of the wing membrane of dragonfly. *Mater. Sci. Eng. A* 457(1):254–260.

Spencer M (1982) *Fundamentals of Light Microscopy* (Cambridge University Press).

Stark T, Alamri S, Aguilar-Morales AI, Kiedrowski T, Lasagni AF (2019) Positive Effect of Laser Structured Surfaces on Tribological Performance. *J. Laser MicroNanoengineering* 14(1):13–18.

Stavenga DG, Tinbergen J, Leertouwer HL, Wilts BD (2011) Kingfisher feathers – colouration by pigments, spongy nanostructures and thin films. *J. Exp. Biol.* 214(23):3960–3967.

Stoehr B, Hall C, Evans D, Murphy P (2016) Cleaning Dirty Surfaces: A Three-Body Problem. *ACS Appl. Mater. Interfaces* 8(28):18534–18539.

Stormonth-Darling JM, Pedersen RH, How C, Gadegaard N (2014) Injection moulding of ultra high aspect ratio nanostructures using coated polymer tooling. *J. Micromechanics Microengineering* 24(7):075019.

Su F, Yao K (2014) Facile Fabrication of Superhydrophobic Surface with Excellent Mechanical Abrasion and Corrosion Resistance on Copper Substrate by a Novel Method. *ACS Appl. Mater. Interfaces* 6(11):8762–8770.

Subramanian S (2009) Wikimedia Commons: Sand dunes of Thar Desert, Rajasthan. Retrieved (March 10, 2019), https://commons.wikimedia.org/wiki/File:A_sunset_on_the_dunes_of_the_Great_Indian_Thar_Desert_Rajasthan_India.jpg.

Sun G, Fang Y, Cong Q, Ren L quan (2009) Anisotropism of the Non-Smooth Surface of Butterfly Wing. *J. Bionic Eng.* 6(1):71–76.

Sun J, Bhushan B, Tong J (2013) Structural coloration in nature. *RSC Adv.* 3(35):14862–14889.

Sun M, Watson GS, Zheng Y, Watson JA, Liang A (2009) Wetting properties on nanostructured surfaces of cicada wings. *J. Exp. Biol.* 212(19):3148–3155.

Swiegers G, Lehn JM, Benyus J (2012) *Bioinspiration and Biomimicry in Chemistry : Reverse-Engineering Nature* (Wiley, Somerset, US).

Ta DV, Dunn A, Wasley TJ, Kay RW, Stringer J, Smith PJ, Connaughton C, Shephard JD (2015) Nanosecond laser textured superhydrophobic metallic surfaces and their chemical sensing applications. *Appl. Surf. Sci.* 357:248–254.

Ta VD, Dunn A, Wasley TJ, Li J, Kay RW, Stringer J, Smith PJ, Esenturk E, Connaughton C, Shephard JD (2016) Laser textured superhydrophobic surfaces and their applications for homogeneous spot deposition. *Appl. Surf. Sci.* 365:153–159.

Tam AC, Leung WP, Zapka W, Ziemlich W (1992) Laser-cleaning techniques for removal of surface particulates. *J. Appl. Phys.* 71(7):3515–3523.

Tan B, Venkatakrishnan K (2006) A femtosecond laser-induced periodical surface structure on crystalline silicon. *J. Micromechanics Microengineering* 16(5):1080.

Tang MK, Huang XJ, Guo Z, Yu JG, Li XW, Zhang QX (2015) Fabrication of robust and stable superhydrophobic surface by a convenient, low-cost and efficient laser marking approach. *Colloids Surf. Physicochem. Eng. Asp.* 484:449–456.

Tebby Z, Dellea O (2011) Method for Depositing a Layer of Organized Particles on a Substrate. (FR20100051496 20100302).

Theppakuttai S, Chen S (2003) Nanoscale surface modification of glass using a 1064 nm pulsed laser. *Appl. Phys. Lett.* 83(4):758–760.

Tian J, Lancry M, Yoo SH, Garcia-Caurel E, Ossikovski R, Poumellec B (2017) Study of femtosecond laser-induced circular optical properties in silica by Mueller matrix spectropolarimetry. *Opt. Lett.* 42(20):4103.

Tian Y, Pesika N, Zeng H, Rosenberg K, Zhao B, McGuiggan P, Autumn K, Israelachvili J (2006) Adhesion and friction in gecko toe attachment and detachment. *Proc. Natl. Acad. Sci.* 103(51):19320–19325.

Tichý V, Willingale R (2018) Optimization of mirror spacing or pore width of lobster eye optics. *Astron. Nachrichten* 339(5):363–366.

Tsibidis GD, Fotakis C, Stratakis E (2015) From ripples to spikes: A hydrodynamical mechanism to interpret femtosecond laser-induced self-assembled structures. *Phys. Rev. B* 92(4):041405.

Tsibidis GD, Skoulas E, Papadopoulos A, Stratakis E (2016) Convection roll-driven generation of supra-wavelength periodic surface structures on dielectrics upon irradiation with femtosecond pulsed lasers. *Phys. Rev. B* 94(8):081305.

Tsutsumi N, Fujihara A, Nagata K (2008) Fabrication of laser induced periodic surface structure for geometrical engineering. *Thin Solid Films* 517(4):1487–1492.

Valle J, Burgui S, Langheinrich D, Gil C, Solano C, Toledo-Arana A, Helbig R, Lasagni A, Lasa I (2015) Evaluation of Surface Microtopography Engineered by Direct Laser Interference for Bacterial Anti-Biofouling. *Macromol. Biosci.* 15(8):1060–1069.

Van Oss CJ, Ju L, Chaudhury MK, Good RJ (1989) Estimation of the polar parameters of the surface tension of liquids by contact angle measurements on gels. *J. Colloid Interface Sci.* 128(2):313–319.

Varlamova O, Costache F, Ratzke M, Reif J (2007) Control parameters in pattern formation upon femtosecond laser ablation. *Appl. Surf. Sci.* 253(19):7932–7936.

Varlamova O, Reif J, Varlamov S, Bestehorn M (2011) The laser polarization as control parameter in the formation of laser-induced periodic surface structures: Comparison of numerical and experimental results. *Appl. Surf. Sci.* 257(12):5465–5469.

Vella PC, Dimov SS, Brousseau E, Whiteside BR (2015) A new process chain for producing bulk metallic glass replication masters with micro- and nano-scale features. *Int. J. Adv. Manuf. Technol.* 76(1–4):523–543.

Vereecke G, Röhr E, Heyns MM (1999) Laser-assisted removal of particles on silicon wafers. *J. Appl. Phys.* 85(7):3837–3843.

Verho T, Bower C, Andrew P, Franssila S, Ikkala O, Ras RHA (2011) Mechanically Durable Superhydrophobic Surfaces. *Adv. Mater.* 23(5):673–678.

Vestentoft K, Olesen JA, Christensen BH, Balling P (2005) Nanostructuring of surfaces by ultra-short laser pulses. *Appl. Phys. A* 80(3):493–496.

Vigneron JP, Pasteels JM, Windsor DM, Vértesy Z, Rassart M, Seldrum T, Dumont J, Deparis O, Lousse V, Biró LP, Ertz D, Welch V (2007) Switchable reflector in the Panamanian tortoise beetle Charidotella egregia (Chrysomelidae: Cassidinae). *Phys. Rev. E* 76(3):031907.

Vignolini S, Rudall PJ, Rowland AV, Reed A, Moyroud E, Faden RB, Baumberg JJ, Glover BJ, Steiner U (2012) Pointillist structural color in Pollia fruit. *Proc. Natl. Acad. Sci.* 109(39):15712–15715.

Vilhena LM, Ramalho A, Cavaleiro A (2017) Grooved surface texturing by electrical discharge machining (EDM) under different lubrication regimes. *Lubr. Sci.* 29(7):493–501.

Völkermeyer F, Jaeschke P, Stute U, Kracht D (2013) Laser-based modification of wettablility for carbon fiber reinforced plastics. *Appl. Phys. A* 112(1):179–183.

Vorobyev AY, Guo C (2011) Antireflection effect of femtosecond laser-induced periodic surface structures on silicon. *Opt. Express* 19(105):A1031–A1036.

Vorobyev AY, Guo C (2013) Direct femtosecond laser surface nano/microstructuring and its applications. *Laser Photonics Rev.* 7(3):385–407.

Vorobyev AY, Guo C (2015) Multifunctional surfaces produced by femtosecond laser pulses. *J. Appl. Phys.* 117(3):033103.

Vukusic P, Sambles JR, Lawrence CR (2000) Structural colour: Colour mixing in wing scales of a butterfly. *Nature* 404(6777):457.

Vukusic P, Sambles R, Lawrence C, Wakely G (2001) Sculpted-multilayer optical effects in two species of Papilio butterfly. *Appl. Opt.* 40(7):1116–1125.

Wang D, Zhang X, Zhang D (2018) Fabrication of a Peristome Surface Structure of Nepenthes alata by Elliptical Vibration Cutting. *Nanomanufacturing Metrol.* 1(4):209–216.

Wang J, Guo C (2006) Formation of extraordinarily uniform periodic structures on metals induced by femtosecond laser pulses. *J. Appl. Phys.* 100(2):023511.

Wang N, Xiong D, Deng Y, Shi Y, Wang K (2015) Mechanically Robust Superhydrophobic Steel Surface with Anti-Icing, UV-Durability, and Corrosion Resistance Properties. *ACS Appl. Mater. Interfaces* 7(11):6260–6272.

Wang P, Yao T, Sun B, Ci T, Fan X, Han H (2017) Fabrication of mechanically robust superhydrophobic steel surface with corrosion resistance property. *RSC Adv.* 7(63):39699–39703.

Wang S, Liu K, Yao X, Jiang L (2015) Bioinspired Surfaces with Superwettability: New Insight on Theory, Design, and Applications. *Chem. Rev.* 115(16):8230–8293.

Wang ZB, Hong MH, Luk'yanchuk BS, Lin Y, Wang QF, Chong TC (2004) Angle effect in laser nanopatterning with particle-mask. *J. Appl. Phys.* 96(11):6845–6850.

Warrant EJ, Locket NA (2004) Vision in the deep sea. *Biol. Rev.* 79(3):671–712.

Watanabe K, Hoshino T, Kanda K, Haruyama Y, Matsui S (2004) Brilliant Blue Observation from a Morpho-Butterfly-Scale Quasi-Structure. *Jpn. J. Appl. Phys.* 44(1L):L48.

Watanabe O, Ikawa T, Hasegawa M, Tsuchimori M, Kawata Y (2001) Nanofabrication induced by near-field exposure from a nanosecond laser pulse. *Appl. Phys. Lett.* 79(9):1366–1368.

Watson GS, Green DW, Schwarzkopf L, Li X, Cribb BW, Myhra S, Watson JA (2015) A gecko skin micro/nano structure – A low adhesion, superhydrophobic, anti-wetting, self-cleaning, biocompatible, antibacterial surface. *Acta Biomater.* 21:109–122.

Welles W (2007) Wikimedia Commons: Humpback Whale, breaching, Stellwagen Bank National Marine Sanctuary. Retrieved (March 10, 2019), https://en.wikipedia.org/wiki/File:Humpback_stellwagen_edit.jpg.

Wenzel RN (1936) Resistance of solid surfaces to wetting by water. *Ind. Eng. Chem.* 28(8):988–994.

Wenzel RN (1949) Surface Roughness and Contact Angle. *J. Phys. Colloid Chem.* 53(9):1466–1467.

Whitehead KA, Colligon J, Verran J (2005) Retention of microbial cells in substratum surface features of micrometer and sub-micrometer dimensions. *Colloids Surf. B Biointerfaces* 41(2):129–138.

Wilts BD, Matsushita A, Arikawa K, Stavenga DG (2015) Spectrally tuned structural and pigmentary coloration of birdwing butterfly wing scales. *J. R. Soc. Interface* 12(111):20150717.

Wong TS, Kang SH, Tang SKY, Smythe EJ, Hatton BD, Grinthal A, Aizenberg J (2011) Bioinspired self-repairing slippery surfaces with pressure-stable omniphobicity. *Nature* 477(7365):443–447.

Wong WSY, Tricoli A (2018) Cassie-Levitated Droplets for Distortion-Free Low-Energy Solid–Liquid Interactions. *ACS Appl. Mater. Interfaces* 10(16):13999–14007.

Wu B, Zhou M, Li J, Ye X, Li G, Cai L (2009) Superhydrophobic surfaces fabricated by microstructuring of stainless steel using a femtosecond laser. *Appl. Surf. Sci.* 256(1):61–66.

Wu LYL, Ngian SK, Chen Z, Xuan DTT (2011) Quantitative test method for evaluation of anti-fingerprint property of coated surfaces. *Appl. Surf. Sci.* 257(7):2965–2969.

Wu W, Katsnelson A, Memis OG, Mohseni H (2007) A deep sub-wavelength process for the formation of highly uniform arrays of nanoholes and nanopillars. *Nanotechnology* 18(48):485302.

Wysocki G, Denk R, Piglmayer K, Arnold N, Bäuerle D (2003) Single-step fabrication of silicon-cone arrays. *Appl. Phys. Lett.* 82(5):692–693.

Xie G, Zhang G, Lin F, Zhang J, Liu Z, Mu S (2008) The fabrication of subwavelength anti-reflective nanostructures using a bio-template. *Nanotechnology* 19(9):095605.

Yang H, He H, Zhou L, Qian J, Hao J, Zhu H (2012) Sharp transition of laser-induced periodic ripple structures. *Opt. Appl.* 42(4):795–803.

Yang SM, Jang SG, Choi DG, Kim S, Yu HK (2006) Nanomachining by Colloidal Lithography. *Small* 2(4):458–475.

Yao J, Zhang C, Liu H, Dai Q, Wu L, Lan S, Gopal AV, Trofimov VA, Lysak TM (2012) Selective appearance of several laser-induced periodic surface structure patterns on a metal surface using structural colors produced by femtosecond laser pulses. *Appl. Surf. Sci.* 258(19):7625–7632.

Yasumaru N, Sentoku E, Kiuchi J (2017) Formation of organic layer on femtosecond laser-induced periodic surface structures. *Appl. Surf. Sci.* 405:267–272.

Yasumaru N, Sentoku E, Miyazaki K, Kiuchi J (2013) Femtosecond-laser-induced nanostructure formed on nitrided stainless steel. *Appl. Surf. Sci.* 264:611–615.

Ye C, Li M, Hu J, Cheng Q, Jiang L, Song Y (2011) Highly reflective superhydrophobic white coating inspired by poplar leaf hairs toward an effective "cool roof." *Energy Environ. Sci.* 4(9):3364–3367.

Yi G, Yuan Y, Li X, Zhang Y (2018) ZnO Nanopillar Coated Surfaces with Substrate-Dependent Superbactericidal Property. *Small* 14(14):1703159.

Yin K, Song YX, Dong XR, Wang C, Duan JA (2016) Underwater superoleophobicity, anti-oil and ultra-broadband enhanced absorption of metallic surfaces produced by a femtosecond laser inspired by fish and chameleons. *Sci. Rep.* 6:36557.

Yong J, Chen F, Yang Q, Jiang Z, Hou X (2018) A Review of Femtosecond-Laser-Induced Underwater Superoleophobic Surfaces. *Adv. Mater. Interfaces* 5(7):1701370.

Yoo YE, Kim TH, Choi DS, Hyun SM, Lee HJ, Lee KH, Kim SK, Kim BH, Seo YH, Lee HG, Lee JS (2009) Injection molding of a nanostructured plate and measurement of its surface properties. *Curr. Appl. Phys.* 9(2, Supplement):e12–e18.

Yoshioka S, Kinoshita S (2002) Effect of Macroscopic Structure in Iridescent Color of the Peacock Feathers. *Forma* 17:169–181.

Young JF, Preston JS, van Driel HM, Sipe JE (1983) Laser-induced periodic surface structure. II. Experiments on Ge, Si, Al, and brass. *Phys. Rev. B* 27(2):1155–1172.

Young T (1805) An essay on the cohesion of fluids. *Philos. Trans. R. Soc. Lond.* 95:65–87.

Yuan Y, Lee TR (2013) Contact Angle and Wetting Properties. Bracco G, Holst B, eds. *Surf. Sci. Tech.* Springer Series in Surface Sciences. (Springer Berlin Heidelberg), 3–34.

Yue L, Monks JN, Yan B, Wang Z (2017) Large-area formation of microsphere arrays using laser surface texturing technology. *Appl. Phys. A* 123(5):318.

Zhang G, Zhang J, Xie G, Liu Z, Shao H (2006) Cicada Wings: A Stamp from Nature for Nanoimprint Lithography. *Small* 2(12):1440–1443.

Zhang Y, Zou G, Liu L, Zhao Y, Liang Q, Wu A, Zhou YN (2016) Time-dependent wettability of nano-patterned surfaces fabricated by femtosecond laser with high efficiency. *Appl. Surf. Sci.* 389:554–559.

Zhang Z, Gu Q, Jiang W, Zhu H, Xu K, Ren Y, Xu C (2019) Achieving of bionic super-hydrophobicity by electrodepositing nano-Ni-pyramids on the picosecond laser-ablated micro-Cu-cone surface. *Surf. Coat. Technol.* 363:170–178.

Zheng YW, Luk'yanchuk BS, Lu YF, Song WD, Mai ZH (2001) Dry laser cleaning of particles from solid substrates: Experiments and theory. *J. Appl. Phys.* 90(5):2135–2142.

Zhou Y, Hong MH, Fuh J, Lu L, Luk'yanchuk BS, Wang ZB, Shi LP, Chong TC (2006) Direct femtosecond laser nanopatterning of glass substrate by particle-assisted near-field enhancement. *Appl. Phys. Lett.* 88(2):023110.

Zisman WA (1964) Relation of the Equilibrium Contact Angle to Liquid and Solid Constitution. *Contact Angle Wettability Adhes.* Advances in Chemistry. (American Chemical Society), 1–51.

Zorba V, Stratakis E, Barberoglou M, Spanakis E, Tzanetakis P, Anastasiadis SH, Fotakis C (2008) Biomimetic Artificial Surfaces Quantitatively Reproduce the Water Repellency of a Lotus Leaf. *Adv. Mater.* 20(21):4049–4054.

Zuhlke CA, Anderson TP, Alexander DR (2013) Formation of multiscale surface structures on nickel via above surface growth and below surface growth mechanisms using femtosecond laser pulses. *Opt. Express* 21(7):8460–8473.